

Università degli Studi di Torino  
Scuola di Dottorato

---

Dottorato in Fisica ed Astrofisica

**Study of strangeness production  
in pp collisions at  $\sqrt{s} = 5.02$  TeV at the LHC  
and the upgrade of the ALICE muon trigger  
for high luminosity**

**Silvia Delsanto**

**Tutor: Ermanno Vercellin  
Co-tutor: Livio Bianchi**

**Study of strangeness production  
in pp collisions at  $\sqrt{s} = 5.02$  TeV at the LHC  
and the upgrade of the ALICE muon trigger  
for high luminosity**

**Silvia Delsanto**

A thesis submitted to the Faculty of Science,  
University of the Witwatersrand, in fulfilment of  
the requirements for the degree of  
Doctor of Philosophy.

## Declaration of Authorship

I, Silvia Delsanto, declare that this thesis titled, “Study of strangeness production in pp collisions at  $\sqrt{s} = 5.02$  TeV at the LHC and the upgrade of the ALICE muon trigger for high luminosity” and the work presented in it are my own.

I confirm that:

- This work was done wholly or mainly while in candidature for a research degree at this University.
- Where any part of this thesis has previously been submitted for a degree or any other qualification at this University or any other institution, this has been clearly stated.
- Where I have consulted the published work of others, this is always clearly attributed.
- Where I have quoted from the work of others, the source is always given. With the exception of such quotations, this thesis is entirely my own work.
- I have acknowledged all main sources of help. Where the thesis is based on work done by myself jointly with others, I have made clear exactly what was done by others and what I have contributed myself.

Signature:

Date:

## Abstract

The ultimate aim of the ALICE (A Large Ion Collider Experiment) detector is to study relativistic heavy-ion collisions (A-A) provided by the CERN Large Hadron Collider (LHC). In these collisions, extraordinary conditions of temperature and energy density occur. Under these extreme conditions, the standard nuclear matter undergoes a transition from hadronic phase to an interacting quantum state called Quark-Gluon Plasma (QGP), where quarks and gluons are not confined anymore into hadrons but they are asymptotically free. The LHC also provides proton-proton (pp) and proton-nucleus (p-A) collisions considered reference colliding systems for A-A collisions because the formation of the QGP is not expected.

Since the short-lived QGP cannot be observed directly, signatures affected by its formation are analyzed in order to provide information on its characteristics. The so-called strangeness enhancement was one of the first QGP signatures proposed. Strangeness enhancement predicts an enhanced production of strange hadrons in A-A collisions with respect to pp collisions. However, recent experimental observations showed also an increase in strangeness production in high-multiplicity pp and p-Pb collisions at LHC energies. These results, together with other typical features of the heavy-ion collisions normally associated to the QGP, were recently observed also in the reference colliding systems. These unexpected developments have prompted unresolved questions about the nature of high-multiplicity pp and p-A collisions.

The goal of this PhD thesis is to present the ALICE measurement performed for the analysis of strange and multi-strange hadrons production as a function of charged-particle multiplicity in pp collisions at  $\sqrt{s} = 5.02$  TeV. The results obtained are compared to other ALICE measurements obtained in pp collisions at  $\sqrt{s} = 7$  and  $\sqrt{s} = 13$  TeV as well as to those obtained in p-Pb collisions at  $\sqrt{s_{NN}} = 5.02$  TeV. The  $\sqrt{s} = 5.02$  TeV pp results shown here are found to be in agreement within uncertainties either with  $\sqrt{s} = 7$  and  $\sqrt{s} = 13$  TeV pp analyses both with  $\sqrt{s_{NN}} = 5.02$  TeV p-Pb analysis. This kind of studies is crucial in order to understand details of the strangeness production mechanism and the evolution of pp and p-A colliding systems.

In addition, as part of the PhD service task and in the context of the ALICE upgrade for high luminosity, a new set of Resistive Plate Chambers (RPCs) of the ALICE muon trigger system was tested. The RPCs installed in ALICE in 2007 might present some ageing effects during the next operation period foreseen in 2021 onwards. Therefore, in order to guarantee the best performance of the muon trigger, some of the RPCs need to be replaced before the next ALICE activity Run. The new set available for tests showed

major structural problems and/or low efficiency levels compared to the first RPCs group. These issues could be identified during the tests on the new RPCs. Hence, these defects were communicated to the company responsible for their production. A new set of RCPs was produced and it will be tested in the upcoming months.

# Contents

<b>1</b>	<b>Introduction</b>	<b>1</b>
1.1	The Standard Model . . . . .	1
1.2	The quark-gluon Plasma . . . . .	4
1.2.1	QGP in heavy-ion collisions . . . . .	6
1.2.2	The space-time evolution of a collision . . . . .	8
1.2.3	Small systems . . . . .	10
1.3	Strangeness enhancement . . . . .	11
1.3.1	The evolution of strangeness enhancement . . . . .	14
1.3.2	Microscopic models . . . . .	17
<b>2</b>	<b>The ALICE detector and the RPC tests</b>	<b>22</b>
2.1	The ALICE detector . . . . .	24
2.1.1	Central Barrel . . . . .	26
2.1.2	Forward detectors . . . . .	31
2.1.3	The ALICE Muon Spectrometer . . . . .	34
2.2	Resistive Plate Chambers . . . . .	41
2.3	Operating Mode . . . . .	43
2.3.1	Streamer mode . . . . .	43
2.3.2	Avalanche mode . . . . .	43
2.3.3	Rate capability . . . . .	45
2.4	Working parameters . . . . .	46
2.4.1	Efficiency . . . . .	46
2.4.2	Spatial resolution and cluster size . . . . .	48
2.4.3	Time resolution . . . . .	48
2.4.4	Noise rate . . . . .	49
2.4.5	Current . . . . .	49
2.5	Ageing . . . . .	49
2.6	Muon trigger system RPCs . . . . .	50
2.7	Characterization of the new detectors . . . . .	51
2.8	Tests of the new RPCs . . . . .	52
2.8.1	Preliminary tests . . . . .	53

2.8.2	Efficiency measurement . . . . .	54
2.8.3	Noise map . . . . .	62
2.9	Results and discussion . . . . .	63
<b>3</b>	<b>Data analysis</b>	<b>66</b>
3.1	Introduction . . . . .	66
3.1.1	Event Selection Criteria . . . . .	71
3.1.2	Charged-particle multiplicity Selection Criteria . . . . .	71
3.1.3	Analysis Framework . . . . .	74
3.1.4	Data and Monte Carlo (MC) samples . . . . .	75
3.2	Analysis Details . . . . .	77
3.2.1	Additional cuts . . . . .	79
3.2.2	Signal extraction . . . . .	81
3.2.3	Raw Spectra . . . . .	85
3.2.4	Normalization correction . . . . .	85
3.2.5	Feed-down subtraction for $\Lambda$ and $\bar{\Lambda}$ . . . . .	89
3.2.6	Acceptance times efficiency . . . . .	94
3.2.7	Effect due to MC $p_{\mathbf{T}}$ shape on the $A \times \epsilon$ . . . . .	99
3.3	Systematic uncertainties . . . . .	106
3.3.1	Cut studies . . . . .	106
3.3.2	Cut variation and systematic uncertainties . . . . .	115
3.3.3	Uncorrelated systematic uncertainties . . . . .	122
3.3.4	Corrected Spectra and yield extraction . . . . .	130
3.3.5	Systematic uncertainty on extrapolation . . . . .	134
<b>4</b>	<b>Results and discussion</b>	<b>137</b>
4.1	$p_{\mathbf{T}}$ -integrated yields and $\langle p_{\mathbf{T}} \rangle$ . . . . .	139
<b>5</b>	<b>Summary, conclusions and outlook</b>	<b>147</b>
5.1	Service task on muon trigger RPCs . . . . .	147
5.2	Strangeness analysis . . . . .	148
5.3	Outlook . . . . .	149
5.3.1	The ALICE upgrade for high luminosity . . . . .	149
5.3.2	Strangeness analysis next steps . . . . .	151
<b>A</b>	<b>Invariant Mass Spectra</b>	<b>152</b>
<b>B</b>	<b>Cut studies</b>	<b>160</b>
<b>C</b>	<b>Systematic uncertainties</b>	<b>168</b>
	<b>Bibliography</b>	<b>177</b>





# Chapter 1

## Introduction

### 1.1 The Standard Model

The Standard Model of particle physics (SM) [1], theorized in the 1970s, describes the universe in terms of forces and matter. Specifically, matter is described as made of 12 point-like elementary particles, quarks with 6 flavors and 6 leptons together with their antiparticles. Figure 1.1 shows that quarks and leptons are divided into three generations with similar properties. Firstly, they are all characterized by spin 1/2 (fermions). Up and down quarks and the electron belong to the first generation of matter and they constitute most of the ordinary matter. The other quarks and leptons have very short lifetimes and they are only produced in environments of extremely high energies (as it will be explained in the next sections). According to their mass values, up ( $u$ ), down ( $d$ ) and strange ( $s$ ) are defined as light quarks, while charm ( $c$ ), top ( $t$ ) and bottom ( $b$ ) are defined as heavy quarks.

The SM [1] is a Yang-Mills theory based on the non-Abelian group  $U(1) \times SU(2) \times SU(3)$ . It includes the strong force which is mediated by eight gluons, the weak force mediated by three weak bosons and the electromagnetic force mediated by the photon. Figure 1.1 gives also an overview of the interaction carriers. All charged particles can interact electromagnetically; quarks and leptons can interact weakly. However, only quarks (and gluons) are able to interact strongly because they carry a property called *color* which plays a similar role as the charge for the electromagnetic interaction. The quantum field theory that describes the interaction between quarks and gluons is known as Quantum Chromo-Dynamics (QCD). This theory was developed after the success of the theory of Quantum Electro-Dynamics (QED) in the 1940s, which describes the interactions between light and matter.

As mentioned, quarks are characterized by the color charge. There are

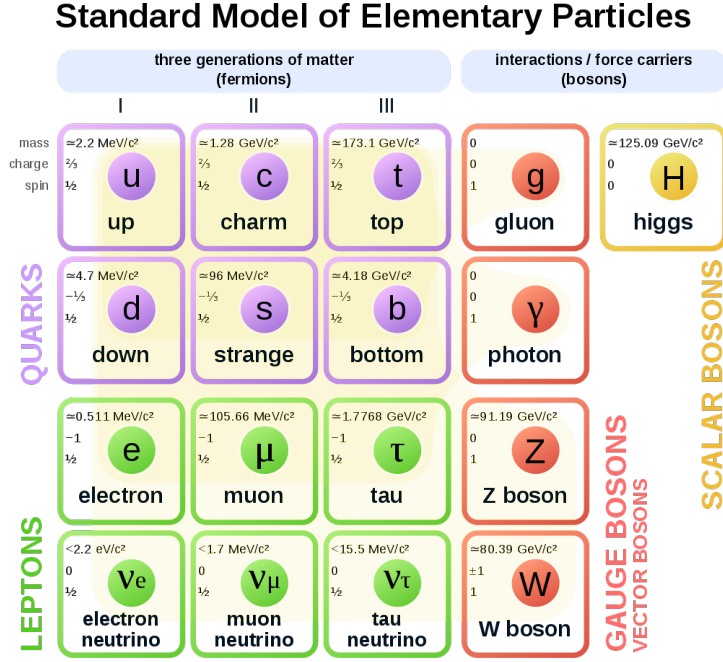


Figure 1.1: Overview of the Standard Model of Elementary Particles [2].

three pure states of color charge: red, blue and green. They were introduced in the theory to describe the compositions of hadrons (mesons and baryons). The color interaction is based on the non-Abelian SU(3) symmetry which is mediated by the eight massless gluon fields. These are also equipped with color charges and are able to interact.

All forces mentioned before are characterized by a coupling constant which identifies the level of intensity of the interaction depending on the energy scale. The coupling constant for the strong interaction  $\alpha_s$  depends on the four-momentum  $Q^2$  transferred. A first order perturbative QCD [3] calculation (valid at very large  $Q^2$ ) gives [4]:

$$\alpha_s(|Q|^2) = \frac{12\pi}{(33 - 2n_{flavor}) \ln(\frac{|Q|^2}{\Lambda_{QCD}^2})}, \quad |Q^2| \gg \Lambda_{QCD}^2 \quad (1.1)$$

where  $n_f$  is the number of quark flavors (6) and  $\Lambda_{QCD}$  is a parameter  $\sim 220$  MeV (depending on  $n_f$ ) which defines the limit on the application of the perturbative QCD approach. Figure 1.2 shows the theoretical curve according to perturbative QCD which represents the evolution of  $\alpha_s$  as a function of the transferred momentum and the measurements of the coupling constant from various physical processes [5].

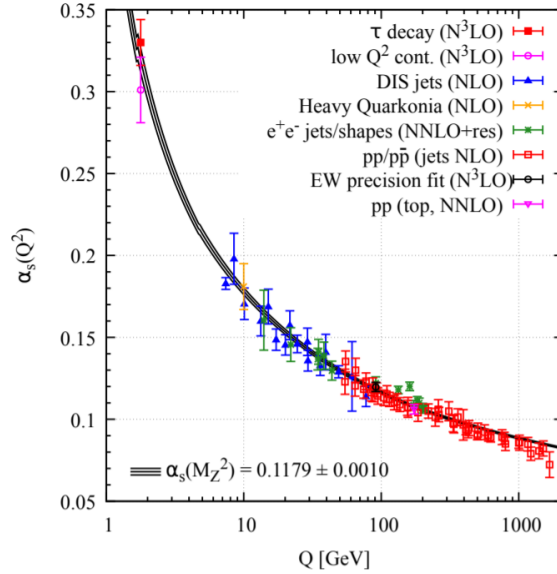


Figure 1.2: The curve represents the theoretical QCD calculation of the coupling constant  $\alpha_s$  as a function of the transferred momentum, while the points show the experimental values of  $\alpha_s$  obtained from different physical processes.[5]

As a consequence, the shape of the potential associated to the strong interaction  $V_{QCD}$  is different compared to the other interactions. It can be approximated with the following equation:

$$V_{QCD} = -\frac{4}{3} \frac{\alpha_s(r) \hbar c}{r} + kr \quad (1.2)$$

where  $r$  is the distance between two quarks and  $k \approx 1$  GeV/fm. The first term models a Coulomb-like interaction and the second one represents the confinement potential (see below).

Equations 1.1 and 1.2 imply that:

- when the distance from the color quark increases or the transferred momentum decreases, the coupling constant  $\alpha_s$  becomes larger and the force associated is strong enough to confine gluons and quarks (commonly defined as partons) in bound states. In particular, the second term of the potential of strong interaction  $V_{QCD}$  (Eq. 1.2) which increases with the distance between the two partons, avoids that a single gluon or quark detaches from the others, preserving the **confinement**. The confinement regime cannot be described by perturbative QCD [3] because of the large value of the strong coupling constant. A successful

approach can be to solve the equation of the system discretizing the space. This technique is defined as lattice QCD [6] and is built on Monte Carlo integration.

- when the distance decreases from the color quark or the transferred momentum increases, the coupling constant  $\alpha_s$  becomes smaller and gluons and quarks are deconfined. This phenomenon is defined as **asymptotic freedom**.

The asymptotic freedom leads to a quantum state of matter where quarks and gluons are not confined into hadrons: the so-called **Quark-Gluon Plasma (QGP)** [7][8], described as a strongly interacting fluid where the mean free path between partons is almost zero.

## 1.2 The quark-gluon Plasma

The QGP is one of the first stages of the early universe in the Big Bang theory [9]. It is believed that the QGP existed a few microseconds following the Big Bang and persisted until the early universe temperature dropped to about 160 MeV. This is the critical temperature at which the nucleons genesis set in.

Today, similar conditions of temperature and energy density persist only in some astrophysical phenomena such as neutron stars and supernova explosions. As far as it is known, these are the only cases where the QGP can be formed naturally: in the first case, the energy density levels are so elevated that nucleons cannot survive as entities while in the second case, the temperatures increase well above 200 MeV thereby forming a hot deconfined medium.

Since this state of matter can hardly be found in nature, its study requires it to be reproduced in the laboratory under controlled conditions. One way to obtain the QGP is to increase the density of hadrons until the distance between them is around 1 nucleon radius. In this case the density becomes 8 times larger than ordinary matter. Under these conditions, quarks inside hadrons are deconfined and they can interact with each other. On the other hand, this state of matter can also be achieved by increasing the temperature of the system of hadrons. As the temperature increases, the kinetic energy associated to the quarks increases as well. At a critical temperature (more details are provided below) the hadrons boundaries dissolve and the quarks and gluons are deconfined.

This second case can be described more in detail with a simplified model called the Bag model [10]. The energy density can be calculated as a function

of the temperature ( $T$ ) associated to a gas of free pions at low  $T$  (Eq. 1.3) and a gas of free quarks and gluons at high  $T$  (Eq. 1.4). Quarks and gluons are considered as non-interacting mass-less particles in a bag of finite dimension which mimics the hadron (the “Bag”). The confinement of quarks and gluons is represented by an external pressure that needs to be introduced “ad hoc” in the model and to balance the internal pressure coming from the kinetic energy of the quarks:

$$\epsilon_\pi = n_{dof} \frac{\pi^2}{30} T^4 \quad (1.3)$$

$$\epsilon_{QGP} = n_{dof} \frac{\pi^2}{30} T^4 + B \quad (1.4)$$

where  $n_{dof}$  are the degrees of freedom. For a gas of pions  $n_{dof}$  are the three isospin states ( $\pi^+$ ,  $\pi^-$ ,  $\pi^0$ ). For the quark-gluon gas,  $n_{dof}$  is:

$$n_{dof} = n_g + \frac{7}{8}(n_q + n_{\bar{q}}) \quad (1.5)$$

where the degrees of freedom for gluons are  $n_g = 8 \times 2$  (8 gluons, 2 polarizations) and the degrees of freedom for quark/anti-quark are  $n_q = n_{\bar{q}} = 3 \times 2 \times 2$  (3 colors, 2 spins, 3 flavors). In Eq 1.4  $B$  is the bag constant which is related to the external pressure. The pressure ( $P$ ) of the system is related to the energy density  $\epsilon = P/3$  (for a quark-gluon gas  $\epsilon = P/3 - B$ ). Figure 1.3 shows a diagram of the pressure as a function of  $T^4$ : according to the Bag model a phase transition from a gas of pions to a quark-gluon gas is expected at a critical temperature  $T_c$ . Lattice QCD [6] gives a more refined and accu-

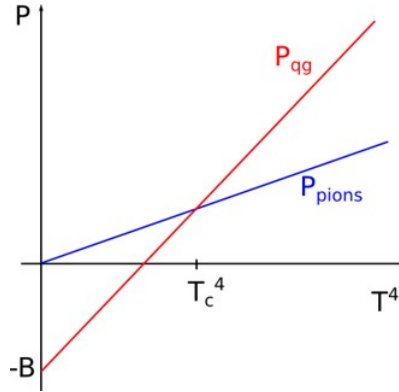


Figure 1.3: Schematic view of the pressure in a two-phase ideal gas.

rate description compared to this phenomenological model and identifies the  $T_c$  at which the deconfinement occurs around 155 MeV corresponding to an

energy density of  $1 \text{ GeV}/\text{fm}^3$  (the standard nuclear matter energy density is  $\epsilon_{\text{nuclear}} = 0.15 \text{ GeV}/\text{fm}^3$ ).

A phase diagram (Figure 1.4) can be calculated to show the relation between two important thermodynamic variables: the temperature  $T$  (y-axis) and the net baryon density (x-axis).

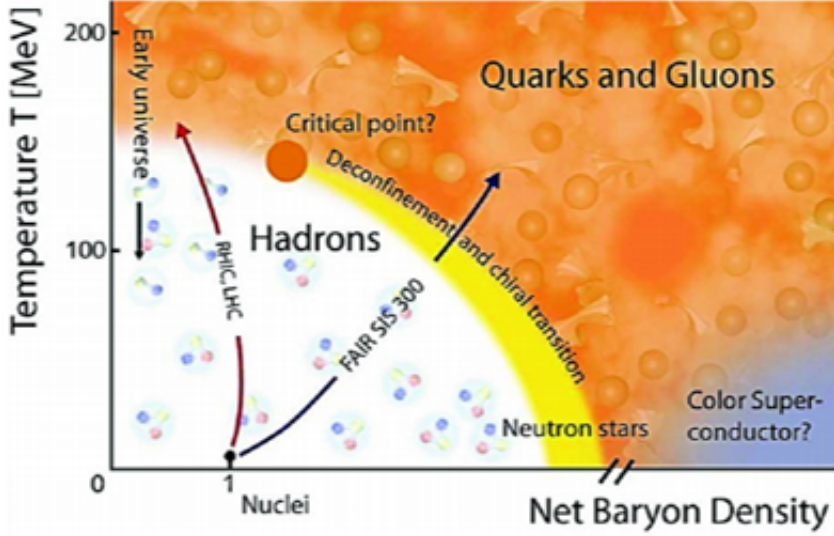


Figure 1.4: Schematic view of the QCD phase diagram [11].

Here, it is evident that the transition from a hadron gas to the QGP can be obtained in several ways: by increasing  $T$  and/or changing the net baryon density. The region, corresponding to the primordial universe at net baryon density close to 0 and at a temperature higher than  $T_c \simeq 160 \text{ MeV}$  [12], can be investigated in ultra-relativistic heavy-ion collisions at a collider facility such as the LHC [13] at CERN. In the next section, the reason why heavy-ion collisions were chosen will be discussed.

### 1.2.1 QGP in heavy-ion collisions

To produce tiny amounts of the QGP, a strongly nuclear interacting environment under the following conditions, is necessary:

- The temperature of the system has to overcome the critical temperature in order to reach the equilibrium phase, so that the system can be analyzed through the thermodynamic equations. As a consequence, the typical strong interaction time-scale ( $1 \text{ fm}/c$ ) is exceeded;

- In order to reach energy densities sufficiently high enough ( $> 1 \text{ GeV}/\text{fm}^3$ ) to realize a phase transition from a hadronic phase to the QGP, the nuclear system needs to be composed of a large amount of nucleons and its size needs to largely overcome the scale of the strong interaction (1 fm). In addition, if the two requirements are met, statistical macroscopic variables can be used to study the evolution of this system.

Collisions such as  $e^+e^-$  or proton-proton are not sufficient to fulfill the requirements especially because only few tens of particles are produced during a collision even if the centre-of-mass energies are hundreds GeV [14]. It is necessary to use colliding systems of larger dimensions such as relativistic and ultra-relativistic heavy-ion collisions.

If the centre-of-mass energy  $\sqrt{s_{NN}}$  is around 10 GeV per nucleon pair, protons and neutrons are stopped in the collision area right after the collision. So, looking at Figure 1.4, due to these type of collisions with high net baryon density, it is possible to investigate the phase diagram along the net baryon density axis. On the contrary, if the centre-of-mass energy per nucleon pair exceeds 100 GeV, nuclei become “transparent” to each other and after the collision they proceed to leave a region where the net baryon number is almost zero at a high energy density.

For instance, at RHIC (Relativistic Heavy Ion Collider) [15], in Au-Au collisions at  $\sqrt{s_{NN}} = 200 \text{ GeV}$ , the energy density is estimated to be around  $5 \text{ GeV}/\text{fm}^3$  [16] while at the LHC at centre-of-mass energies of the order of TeV the energy density is around  $15 \text{ GeV}/\text{fm}^3$  [17].

In the next section the dynamics of a relativistic heavy-ion collision will be described. First of all, before the collision, the nuclei are travelling in two beams in opposite directions at velocities close to the speed of light  $c$ . Due to Lorentz boost, the nuclei appear to be contracted. A schematic representation is shown in Figure 1.5.

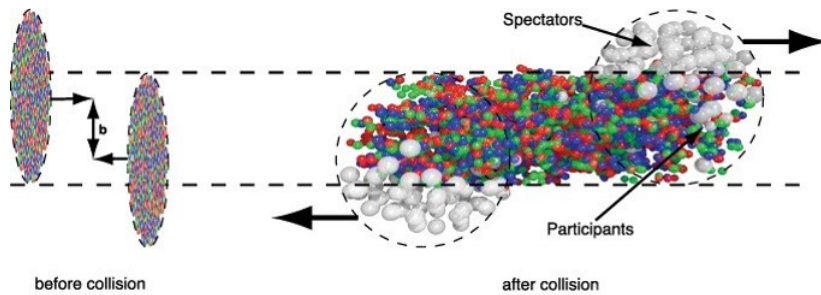


Figure 1.5: A schematic view of a heavy-ion collision [18].

The geometry of the collision influences the total energy released in the

centre-of-mass since the colliding nuclei are extensive objects and the number of nucleons involved in a collision depends on how the two beams collide. The impact parameter  $b$  is defined as the distance between the centres of the two nuclei measured in the perpendicular plane with respect to the colliding axis (see Fig. 1.5). Nucleons involved in the collisions are defined as *participants* whereas the others are called *spectators*. The spectators are almost unperturbed and fly along the original trajectory at the beam velocity. If the impact parameter is small then the collisions are classified as **central** and are characterized simultaneously by a large number of participants and a small number of spectators. If  $b$  is large the collisions are **peripheral** with a small number of participants and a large number of spectators. It is not possible to measure directly the impact parameter of a collision. Therefore, one way to determine central or peripheral collisions is to measure the number of spectators with calorimeters located along the direction of the beam. At the LHC heavy ion (or nucleus) usually used is lead (Pb).

### Charged-particle multiplicity

Another fundamental variable related to the geometry of the collision is the charged-particle multiplicity. It is defined as simply the number of charged particles per event produced in a defined kinematic region. It is rather important because it can provide information on the global characteristics of a collision specifically on the dynamics of particle production and its connection to the geometry of the initial collision. In addition, charged-particle multiplicity can be measured in every colliding system (from proton-proton to Pb-Pb) and by studying different observables as a function of charged-particle multiplicity it allows to compare several colliding systems at the same time.

## 1.2.2 The space-time evolution of a collision

A space-time evolution of a relativistic collision is represented in Figure 1.6. The right-hand side of the figure considers the case where the QGP phase is present after the collision. It can be described schematically in three main steps [19]:

- **Pre-equilibrium** ( $t < 1 \text{ fm}/c$ ): the collision starts at  $t = 0 \text{ fm}/c$ . In the region of overlap between the two nuclei, parton-parton hard scatterings take place depositing a great amount of energy. This pre-equilibrium stage is described by perturbative QCD models since the thermal equilibrium is not reached yet. This stage is predicted to last around  $1 \text{ fm}/c$  or less;



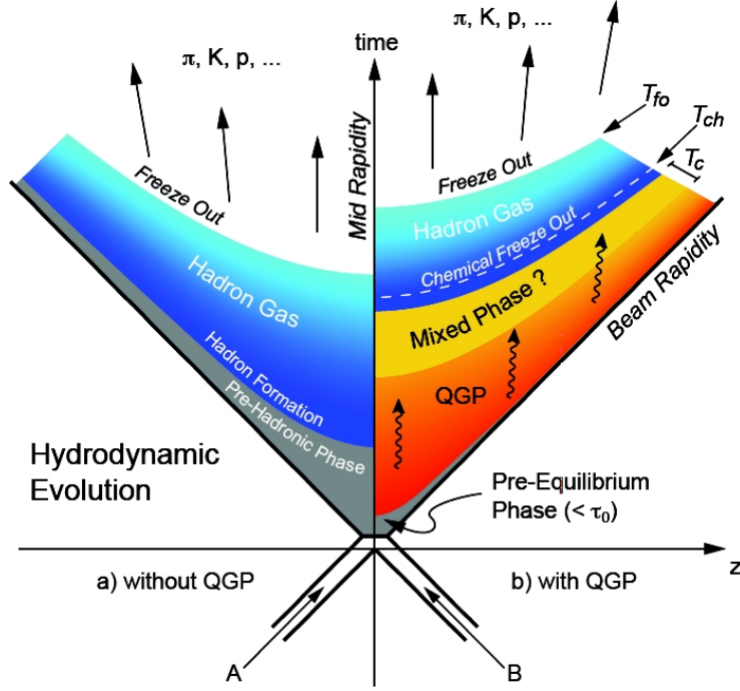


Figure 1.6: Collision space-time evolution [20].

- **QGP phase** ( $t \approx 1 \text{ fm}/c$ ): the system thermalizes and after reaching equilibrium, thermodynamics observables can be estimated. A plasma of quarks and gluons is created. Subsequently, the system evolves by expanding and cooling down through inelastic and elastic internal collisions between partonic constituents;
- **Hadronization** ( $t \approx 10 \text{ fm}/c$ ): during the expansion phase the energy density and the temperature of the system decrease. Once the temperature drops below  $T_c$ , the hadrons are recreated. The system becomes a gas of hadrons which interact inelastically. As soon as the energy of the internal collisions does not allow inelastic interactions anymore, the *chemical freeze-out* is reached at  $t \approx 10 \text{ fm}/c$ . Therefore, the relative abundances of the hadron species, which define the hadrochemistry of the system, are fixed. Elastic interactions between hadrons altering their kinematic properties are still occurring. Moreover, when the distances between the hadrons are larger than the interaction range, also all the kinematic interactions stop (**kinetic freeze-out**) and the kinematics of the hadrons are also fixed. Finally, the hadrons emerge for detection.

The left-hand side of Figure 1.6 shows the evolution of a collision if the QGP phase is not present. After a pre-hadronic phase the system evolves directly into a hadronic phase.

The QGP stage only lasts for a very short period of time and it can only be studied indirectly since it is not possible to detect free quarks from the space-time evolution steps. In order to examine this hot and dense medium, features that are early established during a collision or that can be reliably back-extrapolated are studied. These so-called signatures can experimentally probe the existence of the QGP phase because they are influenced by its formation.

At LHC energies heavy-ion collisions create conditions very close to the early universe ones. Four experiments at the LHC participate in the heavy-ion physics program: LHCb [21], CMS [22], ATLAS [23] and ALICE [24]. This thesis focuses on the ALICE experiment since it was designed to study the properties of the QGP.

There are several probes of the QGP formation which are studied in the context of the ALICE physics. They are briefly listed below:

- **Hard probes:** they concern processes at high transferred momentum which are only possible at the beginning of the collision. Their production rates are described in terms of perturbative QCD [3]. Some examples of hard probes are electroweak bosons [25][26], jet quenching and heavy quark productions. In particular heavy quark bound states like charmonium ( $c\bar{c}$ ) and bottomonium ( $b\bar{b}$ ) are extensively studied [27].
- **Soft probes:** they are characterized by low transferred momenta. Some examples are the anisotropic flow [28], energy and momentum distributions, light hadron productions [29] and strangeness enhancement. Particularly relevant for this work is the latter which is described in Section 1.3.

### 1.2.3 Small systems

Two other types of collisions are also being studied at the LHC: proton-proton (pp) and proton-lead (p-Pb). Because of the relatively smaller size of these collisions with respect to heavy-ion collisions, they are traditionally referred to small system collisions. One of the goals of pp collisions is to provide reference measurements for heavy-ion physics. During a pp collision, the partons formed emerge without interactions up to the final state and

they are not affected by the formation of a strongly interacting medium (see left-hand side of Figure 1.6). This means that any differences observed in the heavy-ion environment with respect to the pp colliding system could be associated with the formation of the QGP. However, initial state effects that might emerge from interactions of gluons inside the nuclei during the first stages of a collision, could persist throughout the entire system evolution and influence the final observations. This phenomenon can happen either in pp or in p-Pb collisions, an asymmetric hybrid system in which a proton and a heavy-ion collide, is studied to find these cold nuclear matter effects and to disentangle them from the pure QGP.

In recent times, this simple and well-defined classification of small systems was questioned. Recent unexpected observations in pp and p-Pb collisions showed typical behaviour normally seen only in heavy-ion collisions. This brought about a lot of questions about how to interpret these new data and even the hypothesis of a possible QGP formation in small systems [30]-[40].

This work specifically focuses on one of these new measurements in pp collisions: the production of strangeness. In the next sections, first the so-called **strangeness enhancement** will be defined as a signature of the QGP. Then, in the light of these new discoveries, its evolution observed in small systems will be discussed.

### 1.3 Strangeness enhancement

Strange hadrons are classified as follows. If they contain at least one strange quark and  $u$  and  $d$  quarks are called hyperons. In particular, for the purpose of this thesis, examples are  $\Lambda$  ( $uds$ ),  $\Xi^-$  ( $dss$ ) and  $\Omega^-$  ( $sss$ ) together with their anti-particles  $\bar{\Lambda}$  ( $u\bar{d}\bar{s}$ ),  $\bar{\Xi}^+$  ( $d\bar{s}\bar{s}$ ) and  $\bar{\Omega}^+$  ( $s\bar{s}\bar{s}$ ). If they contain two or three strange quarks, they are called multi-strange baryons. In addition, there are also mesons characterized by the presence of strange quarks e.g.  $K_S^0((d\bar{s} - s\bar{d})/\sqrt{2})$  or  $\phi$  ( $s\bar{s}$ ).

Before the collision, there is no presence of net strangeness, because the two beams are only constituted by ordinary nuclear matter ( $u$  and  $d$  quarks) and  $s$  quarks potentially exist only as sea quarks. All strangeness detected is produced during the collision. In addition, the energy cost to generate a strange quark is low since it has the third lightest mass as can be seen in Figure 1.1. It is, therefore, abundantly created during the collision. For these two reasons, strangeness production studies always played an important role in any colliding system.

In 1982 Johann Rafelski and Berndt Müller suggested that strangeness production is a probe of the QGP in heavy-ion collisions [41]. The production

mechanism of  $s$  quarks was analyzed in two systems:

- **QGP**: quarks and gluons are deconfined and the degrees of freedom are partonic;
- **Gas of Hadrons (HG)**: quarks and gluons are confined and the degrees of freedom are hadronic.

It was calculated that the energy required to generate hyperons or strange mesons inside the QGP, is significantly lower than the energy needed to produce them in a HG in thermal equilibrium. In the QGP, the density of gluons is considerably higher and gives access to new generation mechanisms represented by Feynman diagrams as shown in Figure 1.7. The first three diagrams show the processes of gluon fusion which provide 80% of the  $s\bar{s}$  pairs produced. In HG, in order to conserve the strange and baryon number, strange particles need to be generated together with their anti-particles requiring more energy if compared to the first case.

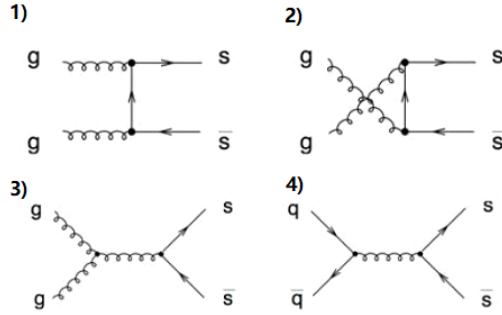


Figure 1.7: Feynman diagrams for the  $s\bar{s}$  production in QGP. The first three diagrams represent the gluon-fusion reactions. The last one represents  $q\bar{q}$  annihilation.

In addition, the equilibration times of hadronic processes are longer with respect to the ones of partonic processes (especially the gluon fusion reactions). According to these findings, the strangeness production is favoured in the QGP with respect to the HG and an enhanced production of strange hadrons is expected in heavy-ion collisions while a suppression should be seen in pp collisions. The signature conceived by Rafelski and Müller is the so-called **Strangeness Enhancement (SE)**. It is based on the fact that in the QGP (heavy-ion collisions) the strangeness production is expected to be more abundant with respect to the case of a hadron gas (in principle, pp collisions). The **strangeness enhancement** in heavy-ion (AA) collisions

relative to pp collisions at mid-rapidity ( $|y| < 0.5$ ), for a hadron specie  $h$  is defined as follows:

$$E(h) = \frac{dN/dy(h)^{AA}}{N_{evt}^{AA} \langle N_{part} \rangle^{AA}} \frac{N_{evt}^{pp} \langle N_{part} \rangle^{pp}}{dN/dy(h)^{pp}} \quad (1.6)$$

where:

- $dN/dy(h)^{AA}$  and  $dN/dy(h)^{pp}$  are the production yields at mid-rapidity of the hadron  $h$  in AA and pp collisions, respectively;
- $N_{evt}^{AA}$  and  $N_{evt}^{pp}$  are the numbers of event in AA and pp collisions, respectively;
- $\langle N_{part} \rangle^{AA}$  and  $\langle N_{part} \rangle^{pp}$  are the average numbers of participating nucleons in the AA and pp collisions, respectively. For pp collisions this number is simply two whereas in AA it depends on the centrality of the collision.
- It is also important to define the particle rapidity  $y$ :

$$y = \frac{1}{2} \ln \left( \frac{E + p_z c}{E - p_z c} \right) \quad (1.7)$$

where  $E$  is the energy and  $p_z$  is the momentum along the beam axis. The rapidity  $y$  is related to another important variable, the pseudorapidity  $\eta$  which is defined as:

$$\eta = -\ln [\tan(\theta/2)] \quad (1.8)$$

where  $\theta$  is the emission angle of a particle w.r.t. the beam axis. The relation between  $y$  and  $\eta$  is:

$$y = \ln \left( \frac{\sqrt{m^2 + p_T^2} \cosh^2 \eta + p_T \sinh \eta}{m^2 + p_T^2} \right) \quad (1.9)$$

where  $m$  is the mass of the particle and  $p_T = \sqrt{p_x^2 + p_y^2}$  the transverse momentum (with  $p_x$  and  $p_y$  the momenta in the plane perpendicular the beam axis). Experimentally, it is easier to measure the pseudorapidity because only the angle of emission of a particle needs to be known, while the direct measurement of  $E$  and  $p_z$  is not always possible.

Historically, strangeness enhancement has been studied in different heavy-ion systems and at different centre-of-mass energies [42]. Figure 1.8 shows the strangeness enhancement as a function of  $\langle N_{part} \rangle^{AA}$  of the (multi-)strange hadrons  $\Lambda$ ,  $\Xi^-$  and  $\Omega^- + \bar{\Omega}^+$ : the left panel shows the SE measured by ALICE in Pb-Pb collisions at  $\sqrt{s_{NN}} = 2.76$  TeV [42] while the right panel shows the comparison with the measurements from STAR [43] in Au-Au collisions at  $\sqrt{s_{NN}} = 200$  GeV and from NA57 [44] in Pb-Pb collisions at  $\sqrt{s_{NN}} = 17.2$  GeV. An enhanced production of strange particles is observed in heavy-ion collisions in every collision energy with respect to the reference system as a function of  $\langle N_{part} \rangle^{AA}$  (centrality of the collision). In addition, it was noticed that the trend rises more steeply with the content of strangeness of the hyperons and the steepness of the SE as a function of  $\langle N_{part} \rangle^{AA}$  is higher at lower collision energies. This trend was justified, in the context of the thermodynamical evolution of the system, with the canonical suppression removal from the p-p colliding system [45] [46].

These results were interpreted as a confirmation of the Rafelski and Müller prediction that expected a suppression of strange particle production in pp collisions (hadron gas) and an enhancement in heavy-ion collision when the QGP is formed.

### 1.3.1 The evolution of strangeness enhancement

As explained, strangeness enhancement was originally considered as a signature of the formation of the QGP in heavy-ion collisions. Recent observations showed that enhanced production of (multi-)strange hadrons are also present in pp and p-Pb collisions [47]. In order to compare strangeness production in all colliding systems, the original formulation of strangeness enhancement has to be redefined. Therefore, a more meaningful way is to study the strange hadron particle yields as a function of charged-particle multiplicity. Thus, a study of the yield vs charged-particle multiplicity would shed light about the influential mechanisms involved in particle production. Such study can be seen in Figure 1.9, the variable analyzed is the integrated yield of strange hadrons, relative to pions ( $\pi^+ + \pi^-$ ), as a function of the event charged-particle multiplicity ( $\langle dN_{ch}/d\eta \rangle$ ) in the pseudorapidity interval  $|\eta| < 0.5$ . In the same figure a comparison of the yield ratios of  $K_S^0$  (in black),  $\Lambda + \bar{\Lambda}$  (in blue),  $\Xi^- + \bar{\Xi}^+$  (in green) and  $\Omega^- + \bar{\Omega}^+$  (in red) with respect to the pions is shown. Results are reported for three colliding systems at different energies:

- in pp collisions at  $\sqrt{s} = 7$  TeV;
- in p-Pb collisions at  $\sqrt{s_{NN}} = 5.02$  TeV;

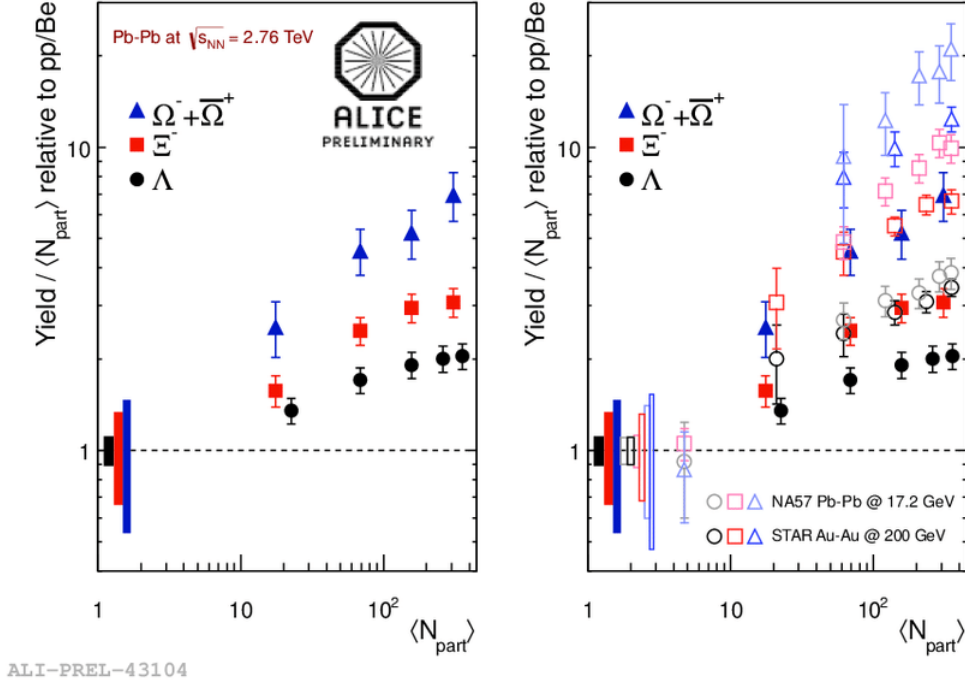


Figure 1.8: The left panel shows the mid-rapidity  $E(h)$  as a function of  $\langle N_{part} \rangle^{AA}$  for  $\Lambda$ ,  $\Xi^-$  and  $\Omega^- + \bar{\Omega}^+$  measured by ALICE in Pb-Pb at  $\sqrt{s_{NN}} = 2.76$  TeV while the right panel shows the comparison with the measurements from STAR [43] in Au-Au at  $\sqrt{s_{NN}} = 200$  GeV and from NA57 [44] in Pb-Pb at  $\sqrt{s_{NN}} = 17.2$  GeV. Figure found in [42].

- in Pb-Pb collisions at  $\sqrt{s_{NN}} = 2.76$  TeV;

A considerable enhancement in the production of strange to non-strange particles with charged-particle multiplicity can be seen in pp and in p-Pb collisions. The ratios of yields reach a plateau at higher multiplicities which correspond to the Pb-Pb collision data. It can be observed that the trend followed by the measured data evolves smoothly as a function of charged-particle multiplicity. This suggests that at the LHC regime, the strangeness production is not dependent on the type of colliding system or on the centre-of-mass energy but that the driving observable is the charged-particle multiplicity: focusing on  $\langle dN_{ch}/d\eta \rangle$  between 5 and 10, similar values of particle yields ratios for all particles analyzed in pp and in p-Pb collisions at different centre-of-mass energies, are produced. Furthermore, Figure 1.10 focuses on the yields of ratios at low charged-particle multiplicity (pp and p-Pb collisions) showing that they increase as a function of  $\langle dN_{ch}/d\eta \rangle$  more rapidly as their content of strangeness grows ( $\Omega$  has the steepest trend since it has

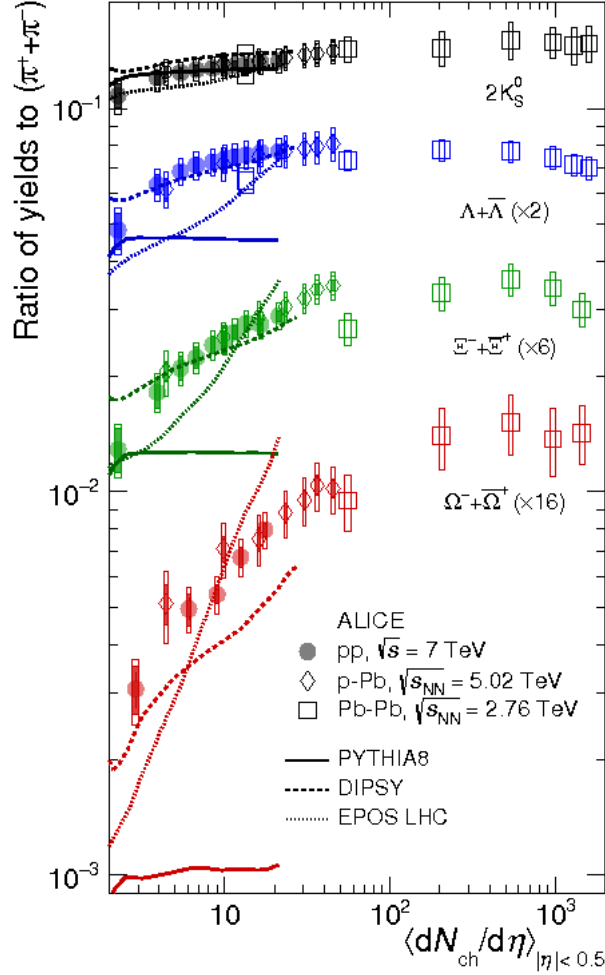


Figure 1.9: Ratios of integrated yields of  $K_S^0$ ,  $\Lambda + \bar{\Lambda}$ ,  $\Xi^- + \Xi^+$  w.r.t. pions as a function of  $\langle dN_{ch}/d\eta \rangle$  in the mid-rapidity region measured by ALICE in different colliding systems. These results are compared with three Monte Carlo models: PYTHIA 8, DIPSY and EPOS LHC [47].

three  $s$  quarks, while  $K_S^0$  has the flattest trend since it has one  $s$  quark). This Figure also shows that the trend for protons is constant as a function of  $\langle dN_{ch}/d\eta \rangle$  as expected since it does not have strangeness.

The next section will be dedicated to the description of the microscopic models applied in Figure 1.9.



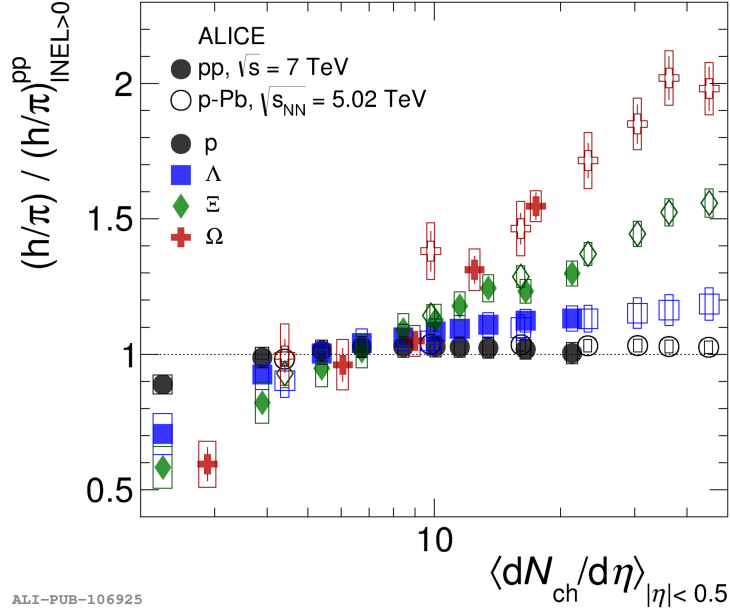


Figure 1.10: Particle yield ratios to pions normalized to the values measured in the inclusive INEL>0 (see Chapter 3) pp sample. The results are shown for pp and p–Pb collisions both normalized to the inclusive INEL>0 pp sample [47].

### 1.3.2 Microscopic models

At the moment, a unique theory which describes parton and hadron interactions in all kinematic and energy intervals is not available. In general, it is very challenging to develop models and to obtain an acceptable and consistent description of all results extracted from the different colliding systems. First of all, perturbative QCD [3] can be applied to describe hard processes with a large four-momentum transferred but it fails to describe soft processes where the four-momentum transferred is low. Therefore, several phenomenological models were applied to describe particle production. For instance, the ratios of yields shown in Figure 1.9 are compared to three microscopic phenomenological models: PYTHIA 8 [48], DIPSY [49], EPOS LHC [50] which are described below:

- **PYTHIA 8** [48] is based on a combination of several elements. First of all, hard scattering processes are implemented and evaluated with approximations of perturbative QCD [3]. The Lund string model [51] is also applied to describe hadronization. It is a phenomenological model built on high-tension “string” which represents a potential growing linearly with the distance between two quarks mimicking the gluon-

field between color charges. At a certain distance, depending on the string tension ( $k_0 \sim 1$  GeV/fm), it is energetically favorable to fragment the string into a quark and anti-quark pair and subsequently into hadrons. In addition, multiple parton-parton interactions (MPIs) in the same events are necessary in order to have a qualitatively good description of the charged-particle multiplicity distributions in PYTHIA 8 [48]. However, another experimental observable, the increase of the average transverse momentum as a function of charged-particle multiplicity, needs another mechanism, called Color Reconnection (CR), to be reproduced. It takes place after a parton shower and takes into account all SU(3) permitted: the final partons are color reconnected in such a way that the total string length becomes as short as possible. The left panel of Figure 1.11 shows that, implementing CR in PYTHIA 8 [48], allows to describe the rise of the average  $p_T$  as a function of charged-particle multiplicity.

- **DIPSY** [49] is also based on the same physics effects as PYTHIA 8 but with some additions. In particular, color ropes are implemented in a high string density environment: a color rope is a dense pack of color strings. The hadronization of a color rope happens string-by-string with an effective string tension  $k > k_0$ . This implementation implies that more baryons and mesons, characterized by heavier quarks (different flavours from  $u$  and  $d$ ), are produced. This mechanism is necessary to describe baryon-over-meson as a function of charged-particle multiplicity (see the right panel of Figure 1.11).

In Fig. 1.9 PYTHIA 8 fails to describe the ratios of yields for all strange hadrons except for  $K_S^0$  and the baryon-over-meson ratios while DIPSY seems to be in quantitative agreement with all particle yield ratios and it is able to qualitatively reproduce the  $\Lambda/K_S^0$  ratio within uncertainty in Figure 1.11. In order to improve the description of the recent experimental observations, the color rope mechanism is also implemented in the last versions of PYTHIA 8 [52].

- **EPOS LHC** [50] uses a hybrid approach incorporating hydrodynamic and parton model descriptions. As described previously, during a collision that involves the QGP formation, the system reaches the thermal equilibrium after a pre-equilibrium phase and then cools down and expands. Since the system is in equilibrium, its evolution can be described with the laws of hydrodynamics. In EPOS LHC [50] a double-regime scenario is implemented. At time  $\tau_0$  (before hadronization) strings are distinguished from each other: string segments in high-density re-

gions form the *core*, while string segments in low density areas form the *corona*. From time  $\tau_0$  the *core* evolves as a viscous hydrodynamic system and the hadronization stage happens statistically at a common temperature  $T_H$ . In the *corona*, strings can hadronize as in the Lund approach. The hadron evolution is explained by core-to-corona ratio changing in events with a different final state charged-particle multiplicity.

EPOS LHC [50] qualitatively describes the pattern for the ratios of particle yields seen in Figure 1.9.

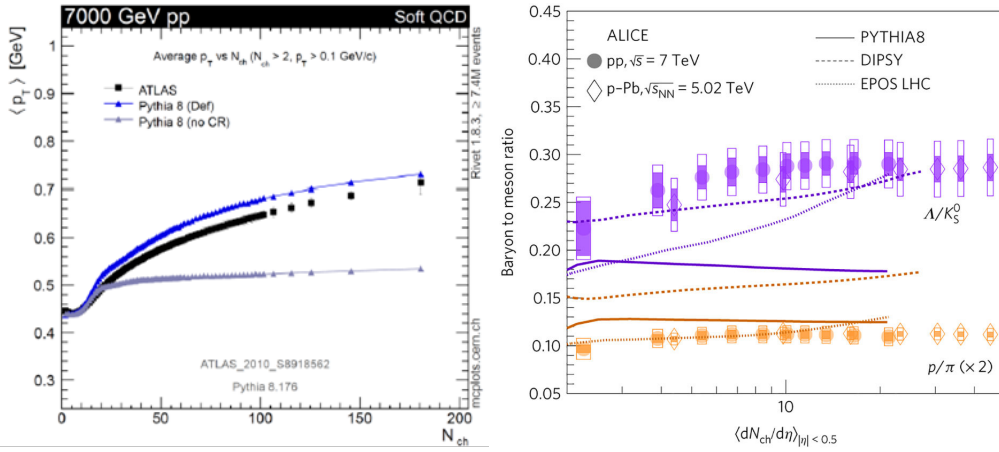


Figure 1.11: The left panel [53] shows the average transverse momentum as a function of charged-particle multiplicity compared to PYTHIA 8 with color reconnection and without color reconnection(CR). The right panel [47] shows the baryon-to-meson ratios for  $\Lambda/K_S^0$  and for  $p/\pi$  as a function of  $\langle dN_{ch}/d\eta \rangle$  at midrapidity in comparison with PYTHIA 8, DIPSY and EPOS LHC.

The best model description is provided by DIPSY [49] but none of the Monte Carlo (MC) models are able to fully explain the data. It is very challenging for MC models to reproduce all the strangeness experimental observations since the microscopic mechanism of strangeness production during a collision, is not fully understood.

Figure 1.12 shows the most updated ALICE measurements of the ratios of yields of (multi-)strange hadrons in pp, p-Pb, Pb-Pb, Xe-Xe at several centre-of-mass energies. The smooth evolution as a function of charged-particle multiplicity is evident.

The new features observed in small systems brought a change of perspective on what may happen in pp and p-Pb collisions, suggesting even the

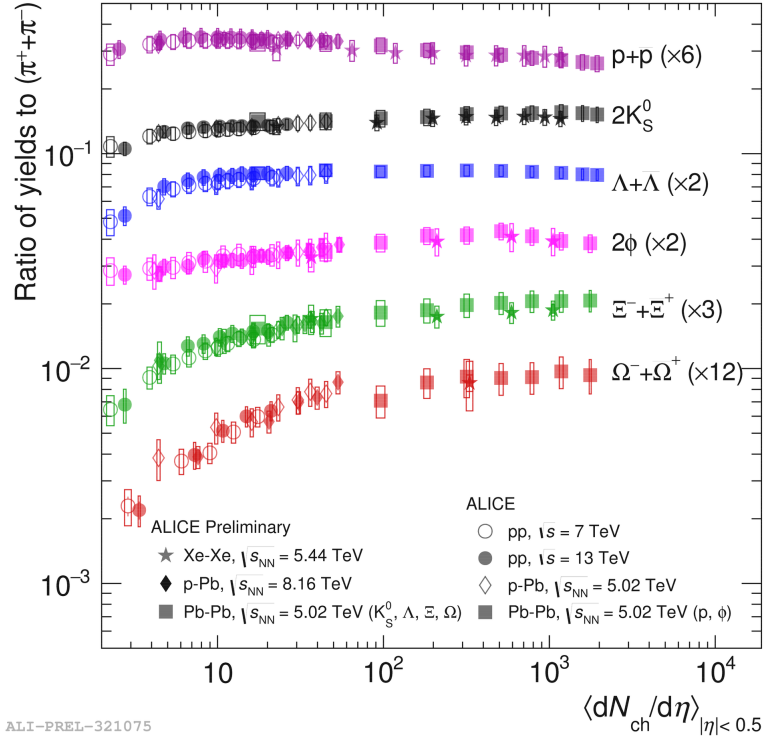


Figure 1.12: Ratio of integrated yields of  $K_S^0$ ,  $\Lambda + \bar{\Lambda}$ ,  $\Xi^- + \bar{\Xi}^+$ ,  $\Omega^- + \bar{\Omega}^+$ ,  $\phi$  and  $p$  w.r.t. pions as a function of  $\langle dN_{ch}/d\eta \rangle$  at mid-rapidity measured by ALICE in different colliding systems [54].

possibility of QGP formation. In addition, the traditional interpretation of pp collisions as reference for heavy-ion collisions has been reviewed in view of the fact that in the highest portion of the charged-particle multiplicity, strangeness enhancement effects were also seen in this colliding system. As a consequence, production yields studies of strange hadrons as a function of charged-particle multiplicity became more relevant compared to the classical definition of strangeness enhancement in Eq.1.6.

So to summarize, it is crucial to extend the studies in pp collisions especially at high charged-particle multiplicity to contribute towards the understanding of the microscopic strangeness production mechanism and to explain the remarkable and unexpected observations of an enhanced strange particle production in small systems.

### Motivation of this study

The main topic of this work is to study (multi-)strange hadron production as a function of charged-particle multiplicity at midrapidity in pp collisions

at  $\sqrt{s} = 5.02$  TeV with ALICE. The study focuses on  $K_S^0$ ,  $\Lambda + \bar{\Lambda}$ ,  $\Xi^- + \bar{\Xi}^+$  and  $\Omega^- + \bar{\Omega}^+$ . The goal of the analysis is to extend the observation in pp collisions at  $\sqrt{s} = 7$  TeV [55] and  $\sqrt{s} = 13$  TeV [56] to a lower energy and to compare the experimental results obtained. The most critical areas of the analyses are at high and low charged-particle multiplicity. The maximum and the minimum values of charged-particle multiplicity (the numerical values are presented in Chapter 3) are related to the statistics available for the analysis. The present data sample available offers large statistics ( $\sim 1.1$  billions events) and it was collected in a short period of time during which very stable detector conditions were experienced. The results are then compared to the analyses of the same particles in pp collisions at  $\sqrt{s} = 7$  [55] and  $\sqrt{s} = 13$  TeV [56] and in p-Pb collisions at  $\sqrt{s} = 5.02$  TeV [57] in order to check the consistency of the experimental data at different centre-of-mass energies and in a different colliding system (p-Pb).

The outline of this PhD thesis is the following:

- **Chapter 2:** an overall description of the ALICE experiment is given focusing in particular on the muon trigger. The PhD Service task which concerned the Resistive Plate chambers (RPCs) of the muon trigger, is also presented.
- **Chapter 3:** the analysis strategy of (multi-)strange hadrons in pp collisions at  $\sqrt{s} = 5.02$  TeV as a function of charged-particle multiplicity is described in full details.
- **Chapter 4:** the results obtained are shown and compared with other analyses in pp collisions at  $\sqrt{s} = 7$  TeV and  $\sqrt{s} = 13$  TeV and in p-Pb collisions at  $\sqrt{s} = 5.02$  TeV.
- **Chapter 5:** the service task and the analysis procedure are summarized. Conclusions on the results obtained and the next steps in the analysis are discussed. The outlook on the ALICE experiment for the data taking campaigns during Run 3 and Run 4 is also presented.

# Chapter 2

## The ALICE detector and the RPC tests

In this chapter, the experimental apparatus of ALICE will be described with a particular emphasis on the Muon Spectrometer and its muon trigger detector. In addition, this PhD service task that involved the testing of the new muon trigger Resistive Plate Chambers is discussed in detail.

### CERN accelerators and main experiments

The LHC is the main particle accelerator at CERN and it is the final and the most powerful ingredient at the end of a chain of accelerator facilities as depicted in Figure 2.1.

The LHC and the entire accelerator complex are designed to accelerate protons and nuclei up to the highest energy ever reached. Table 2.1 shows the maximum centre-of-mass energy and the nominal luminosity for every colliding system.

<b>Colliding system</b>	centre-of-mass energy	Luminosity
<b>pp collisions</b>	$\sqrt{s} = 13 \text{ TeV}$	$10^{34} \text{ s}^{-1} \text{ cm}^{-2}$
<b>p-Pb collisions</b>	$\sqrt{s_{NN}} = 8.16 \text{ TeV}$	$10^{29} \text{ s}^{-1} \text{ cm}^{-2}$
<b>Pb-Pb collisions</b>	$\sqrt{s_{NN}} = 5.02 \text{ TeV}$	$10^{27} \text{ s}^{-1} \text{ cm}^{-2}$
<b>Xe-Xe collisions</b>	$\sqrt{s_{NN}} = 5.44 \text{ TeV}$	$10^{27} \text{ s}^{-1} \text{ cm}^{-2}$

Table 2.1: Maximum centre-of-mass energy and luminosity for collisions provided provided by the LHC so far.

The acceleration process involves several steps. In the case of proton-proton collisions, protons come from a bottle of hydrogen gas (ion source);

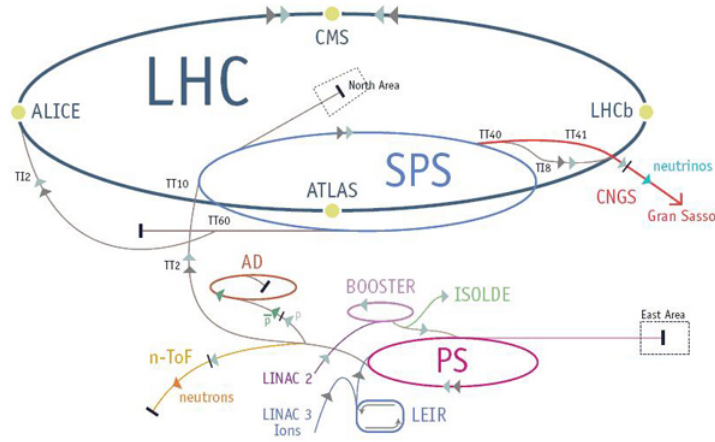


Figure 2.1: LHC and CERN accelerator complex [59].

in an electric field, electrons are stripped off hydrogen atoms to form a positively charged plasma of protons. Then they are pre-accelerated by the linear accelerator LINAC and boosted in bunches by the proton Synchrotron Booster, after which they are injected into the Proton Synchrotron (PS). Here they reach a maximum energy of 25 GeV; at this point protons are delivered to the Super Proton Synchrotron (SPS), where their energy increases up to 450 GeV. At this stage, the protons are ready to be injected into the LHC ring where they finally reach the maximum energy. The LHC [13] is housed between 45 m and 170 m underground in a tunnel with a circumference of 26.7 km.

The two counter-rotating beams circulate in two separated pipes inside superconducting dipoles and quadrupoles, and can collide at four different points, where the four largest CERN experimental detectors are located:

- LHCb [21]: Large Hadron Collider beauty; it is designed to study b-physics and, in particular, to measure the CP violation parameters with the purpose of explaining matter-antimatter asymmetry.
- CMS [22]: Compact Muon Solenoid; it is a general purpose experiment aimed at studying primarily the Higgs Boson, but also extra dimensions or supersymmetry.
- ATLAS [23]: A Toroidal LHC ApparatuS; same program as CMS.
- ALICE [24]: A Large Ion Collider Experiment; it is a different detector with complementary goals; ALICE is the only LHC experiment pri-

marily designed to study heavy-ion collisions and to characterize the QGP, as described in the next section.

## 2.1 The ALICE detector

### Physics program

The ALICE detector, shown in Figure 2.2, is devoted to study the physics of strongly interacting matter and the properties of the QGP at high energy densities, through its experimental probes. Even if the main goal is to study Pb-Pb collisions, measurements related to the other colliding systems are crucial for different reasons: therefore, as alluded to in Chapter 1, the ALICE physics program also includes data taking with different colliding configurations:

- Data-taking in Pb-Pb collisions provides the highest energy density regime ever accessed before in a laboratory;
- Data-taking in collisions with ions lighter than Pb allows to cover a wider range of luminosities;
- Data-taking in p-p collisions provides a baseline to be compared with heavy-ion data and offers interesting physics in its own right;
- Data-taking in p-Pb collisions allows to disentangle cold nuclear matter effects from genuine QGP effects.

### Experimental apparatus

The main technological challenge for a heavy-ion experiment performed at such a high centre-of-mass energies is to deal with the large multiplicity of charged particles produced in each ion-ion collision. During the design phase of the ALICE detector, the multiplicity predictions were of the order of 8000 charged particles per unit of pseudorapidity. Therefore, all the ALICE sub-detectors were designed with a high granularity to cope with a charged-particle multiplicity of 8000 [58].

The interaction rate for Pb-Pb collisions at a nominal luminosity ( $L=10^{27}$  s<sup>-1</sup>cm<sup>-2</sup>) is  $R=L \sigma$  (cross-section  $\sigma = 8$  b) $\approx 10$  kHz which allows for the use of relatively slow detectors. Therefore, ALICE is able to detect, track and reconstruct many different particles in a wide momentum range from 100 MeV/ $c$  to about 100 GeV/ $c$  and is also sensitive to short-lived states such as open heavy flavour and hyperons. In addition, ALICE utilizes all available



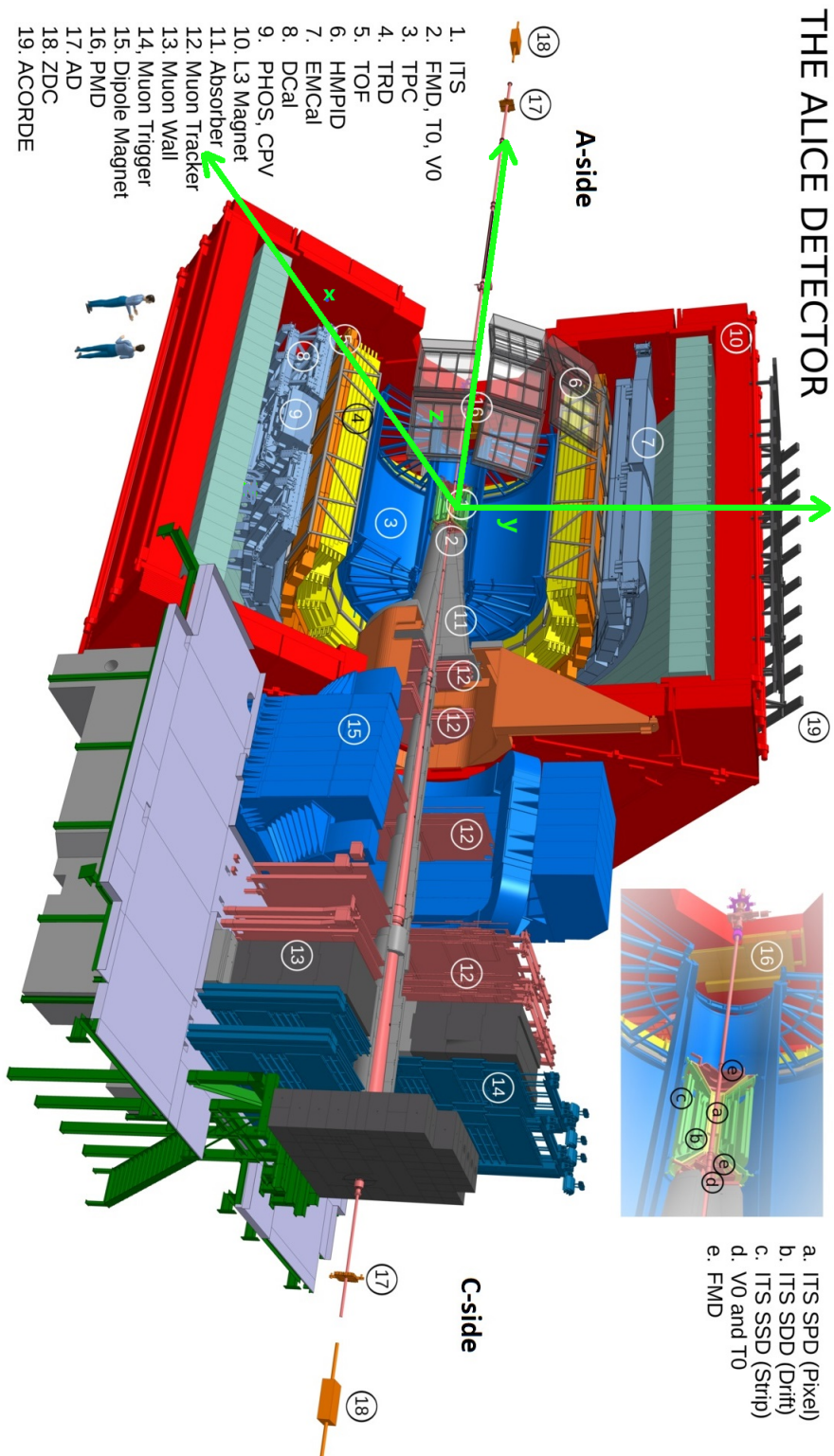


Figure 2.2: The ALICE detector during Run 1 and Run 2 [60].

detector technologies to achieve excellent particle identification. ALICE is therefore equipped with several different detector groups, mainly divided into:

- A central barrel where hadrons, electrons and photons are reconstructed;
- A set of forward detectors whose main goal it is to measure luminosity, centrality and multiplicity;
- The muon spectrometer.

Figure 2.2 shows the ALICE apparatus and the ALICE coordinate system. The A-side refers to the side that points to the ATLAS experiment whereas the C-side to the CMS experiment.

The detectors that are of specific interest in the data analysis presented in this thesis are the Inner Tracking System (ITS), the Time Projection Chamber (TPC), the Time of Flight (TOF) and the V0A and V0C detectors. They are all described in the next sections.

### 2.1.1 Central Barrel

The central barrel consists of several detectors, with a cylindrical arrangement around the Interaction Point (IP), encapsulated inside a solenoid, which provides a field up to 0.5 T, resulting in bent particle tracks for the momentum measurements of charged particles.

Unless specified otherwise, the pseudorapidity coverage of the detectors in the central barrel is  $|\eta| < 0.9$ .

#### ITS

The Inner Tracking System (ITS) [62] is the detector closest to the beam pipe and the Interaction Point(IP).

The ITS is made up of six cylindrical layers of silicon micro-pattern detectors with two-dimensional read-out. The innermost layers, for which a higher granularity is required, are made of Silicon Pixel Detectors (SPD). The next two layers are covered by Silicon Drift Detectors (SDD), while the outer layers consist of Silicon Strip Detectors (SSD). The innermost layers of the SPD cover a larger pseudorapidity range ( $|\eta| < 1.7$ ).

The main goals of the ITS are:

- primary and secondary vertex reconstruction;
- reconstruction and identification of low transverse momentum,  $p_{\mathbf{T}}$ , tracks ( $p_{\mathbf{T}} < 20$  MeV/ $c$ ) which are too bent to be reconstructed by the TPC.

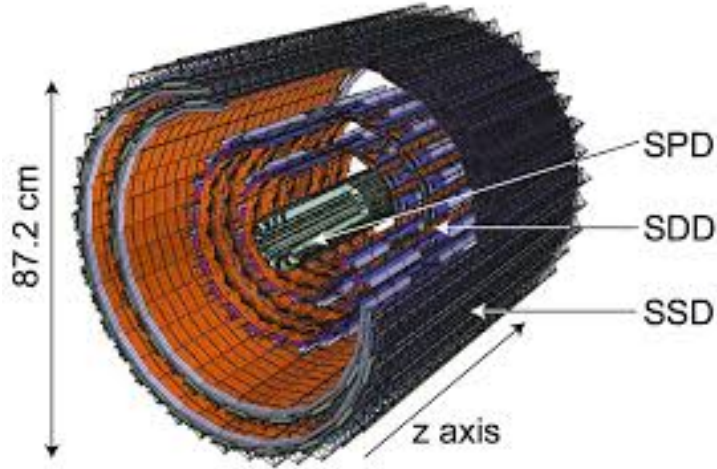


Figure 2.3: The ITS detector [61].

- improve the momentum resolution for high  $p_T$  particles.

The ITS is designed to obtain a spatial resolution better than  $100 \mu\text{m}$ . A view of the ITS is given in Figure 2.3.

## TPC

The Time Projection Chamber (TPC) [63] is the main tracking detector in ALICE. It is a cylindrical gaseous detector with an internal volume of  $88 \text{ m}^3$  filled with a mixture of 90% Ne and 10%  $\text{CO}_2$ , divided in two halves by a central high voltage electrode. The charged-particle ionisation liberates electrons from the gas, which migrate towards the end plates due to a  $400 \text{ V/cm}$  drift electrical field. The TPC end-plates are segmented into 18 trapezoidal sectors each equipped with Multi-Wire Proportional Chambers (MWPC) with cathode pad read-out, covering an overall active area of  $32.5 \text{ m}^2$ . The timing and spatial information are combined to determine the particle track and to perform momentum measurements.

Its inner radius (about  $90 \text{ cm}$ ) is determined by the maximum particle density that can be tolerated while its outer radius (about  $250 \text{ cm}$ ) by the path length needed to achieve the desired resolution (7%) on the energy loss ( $dE/dx$ ) for particle identification. The mean momentum of tracked particles is about  $500 \text{ MeV}/c$ . The electron drift time over the whole path is about  $95 \mu\text{s}$ . Even if the TPC is a slow detector, it can cope with the minimum bias collision rate in Pb-Pb which is around  $8 \text{ kHz}$  at nominal luminosity. The detector provides more than 90% efficiency in track finding, with a resolution of about 2% for charged particle momentum measurements.

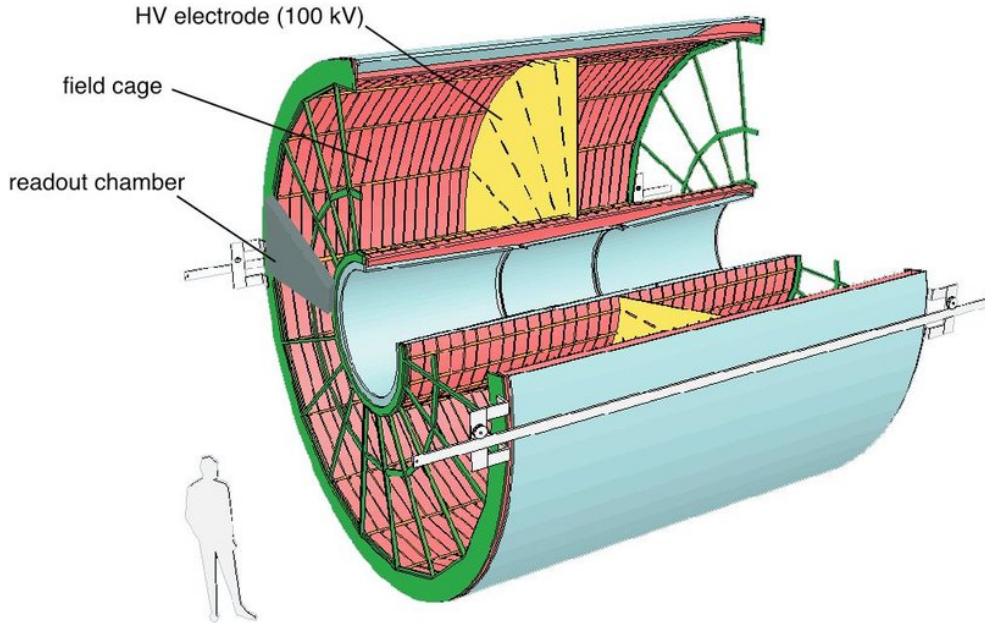


Figure 2.4: The ALICE TPC detector [64].

In combination with ITS, TOF and TRD (see below), the TPC can also provide particle identification by  $dE/dx$  measurements in a momentum interval, from the low-momentum region up to few tens of  $\text{GeV}/c$ , with a resolution better than 10%. A schematic view of the TPC is given in Figure 2.4.

## TRD

The Transition Radiation Detector (TRD) [66] is the main electron detector in ALICE and is used when the particle identification through the ionization energy loss after the TPC is no longer efficient on PID.

The TRD is composed of 540 modules divided into 18 sectors, for a total of 7 m in length and  $750 \text{ m}^3$  in active volume. Every module is basically made up of a drift chamber with cathode pad read-out combined with a fibre/foam sandwich radiator in front. It can provide electron identification for momenta up to  $100 \text{ GeV}/c$ . The detector is complementary to the muon spectrometer, since it allows the study of quarkonia and open heavy flavoured mesons in the electronic channel. It can exploit ITS vertex information to identify primary  $J/\psi$  from the ones that originate from B-meson decays. A layout of the TRD is given in Figure 2.5.

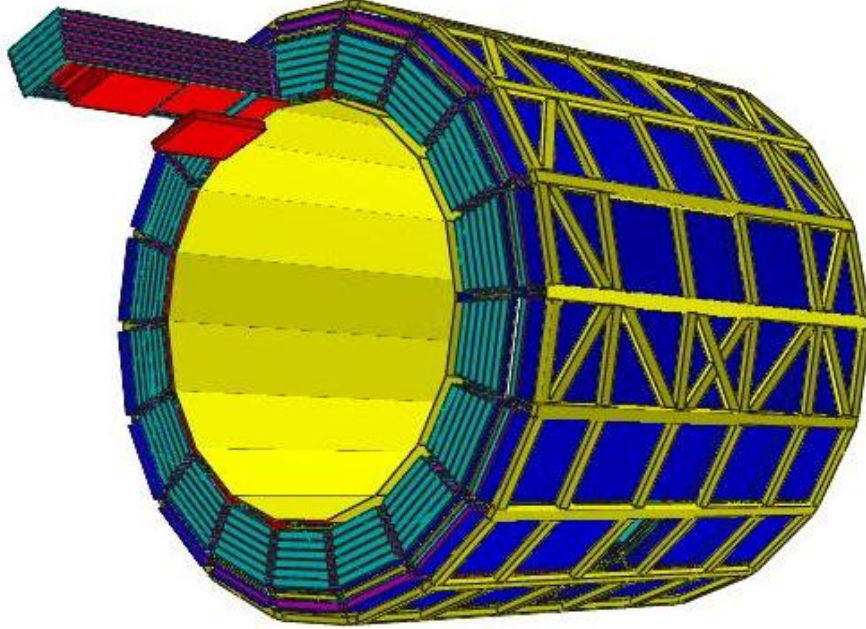


Figure 2.5: The TRD detector [66] with a TRD module highlighted in red.

## TOF

The Time Of Flight (TOF) [68] detector is important for the identification of pions, kaons and protons in an intermediate  $p_{\mathbf{T}}$  region (0.2 GeV/ $c$  - 2.5 GeV/ $c$ ) and in the  $e/\pi$  separation in the momentum range between 140 and 200 MeV/ $c$ .

It is basically an array of Multigap Resistive Plate Chambers (MRPC), a relatively cheap device with which it is possible to cover the required area of 160 m<sup>2</sup>. The MRPCs are ten layers of double-stack (resistive glass plates interleaved with gas layers) detectors; they cover an active area of 7.4 x 120 cm<sup>2</sup> and are organized in 18 sectors in a cylindrical shell at radial distance of 3.7 m from the beam pipe. Charged particles ionize the gas which fills the detector gaps, and the high electric field amplifies this ionization with an electron avalanche. TOF provides the time information for each charged particle able to reach it, with an intrinsic resolution of 50 ps. A layout of the TOF together with HMPID and PHOS is given in Figure 2.6.

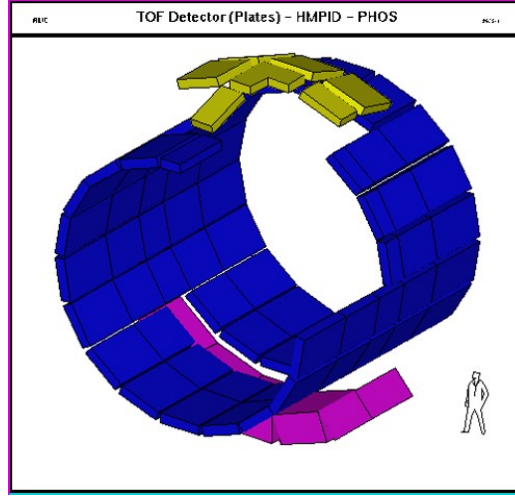


Figure 2.6: The TOF (blue), HMPID (yellow) and PHOS (purple) detectors [90].

## HMPID

The High Momentum Particle Identification Detector (HMPID)[71] is made up of Ring-Imaging Cherenkov counters and consists of seven modules mounted on an independent support cradle. A fast particle which crosses the 15 mm thick layer of liquid  $C_6F_{14}$  produces Cherenkov photons, detected by a photon counter.

This detector is used to improve the particle identification capability of ALICE by extending the momentum range, making it possible to identify particles and discriminate between different particles up to higher momenta:  $\pi/K$  and  $K/p$  discrimination is therefore possible up to 3 GeV/ $c$  and 5 GeV/ $c$ , respectively.

## PHOS

The Photon Spectrometer (PHOS) [73] is a high resolution photon calorimeter, from  $PbWO_4$  crystals. The PHOS covers a pseudorapidity interval of  $|\eta| < 0.12$  and an azimuthal range of  $100^\circ$ .

The PHOS measures both direct photons and decay photons, mainly from high  $p_T$   $\pi^0$  and  $\eta$  mesons. Through its optimal position resolution, it is possible to distinguish between the two particles. The measurements of single photon and di-photon spectra and Bose-Einstein correlations of direct photons allow to test and characterize the properties of the initial phase of the collisions, while the detection of high  $p_T$   $\pi^0$  allows the investigation of

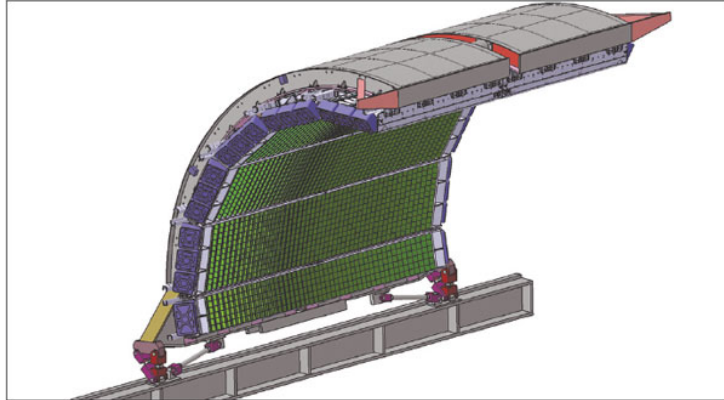


Figure 2.7: The EMCal detector [75].

jet quenching as one of the probes of deconfinement.

### EMCal

The Electromagnetic Calorimeter (EMCal) [74] is the outermost detector in the central barrel of ALICE and is mounted just in front of the L3 magnet. The EMCal is a lead-scintillator sampling calorimeter that covers the pseudorapidity range  $|\eta| < 0.7$  and an azimuthal angular range of  $100^\circ$ . This detector improves the ALICE capability in  $p_{\mathbf{T}}$  reconstruction of jet, direct photons and electrons from heavy flavour decay.

### Solenoidal Magnet

The large solenoidal magnet was adapted from the L3 experiment at LEP [69]. It provides a uniform and relatively weak field (0.5 T) parallel to the beam axis. The relative weak magnetic field allows charged particles down to  $p_{\mathbf{T}} = 100 \text{ MeV}/c$  to be tracked in the TPC.

## 2.1.2 Forward detectors

The forward part of the ALICE set-up is composed of different kinds of detectors: ZDC, FMD, PMD, V0, T0. A description of these detectors is given in the following.

### ZDC

The Zero Degree Calorimeter (ZDC) [79], shown in Figure 2.8, is used during p-A and A-A collisions and measures the energy deposited by the spectator

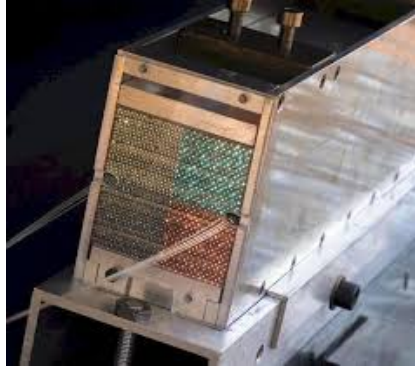


Figure 2.8: Front view of the ZDC detector [80].

nucleons to estimate the interaction centrality and to determine the reaction plane for flow analyses. There are four ZDCs, two for neutrons (ZN) and two for protons (ZP). A pair of ZP and ZN is mounted adjacent to the beam pipe, at a distance of 116 m on either side of the IP; at such a distance, protons and neutrons are spatially separated by the LHC magnetic elements.

The ZDCs are “spaghetti”-like calorimeters, composed of a dense absorber (brass for ZP, a tungsten alloy for ZN) in which quartz fibers are interspersed. Quartz fibers are selected instead of scintillating ones because of the requirements in terms of radiation-hardness (the daily dose for ZN during Pb-Pb operation is of the order of about  $10^4$  Gy).

### FMD

The Forward Multiplicity Detector (FMD) [76], shown in Figure 2.9, consists of 51200 silicon strip channels distributed over 5 ring counters of two types, internal and external. The internal type is divided into 20 different arrays, with 512 strips each, while the external ones have 40 arrays of 256 strips each.

The main goal of this detector is to provide precise charged-particle multiplicity information in its covered pseudorapidity range of  $2.5 < \eta < 3.5$ , on both sides of the IP, useful among others, for the flow analysis.

### PMD

The Photon Multiplicity Detector (PMD) [78] measures the multiplicity of charged particles and photon spatial distribution in the forward region for every event.

It covers a pseudorapidity region of  $2.5 < \eta < 3.5$  and is located on the A-side 360 cm away from the interaction point. It is made up of two layers



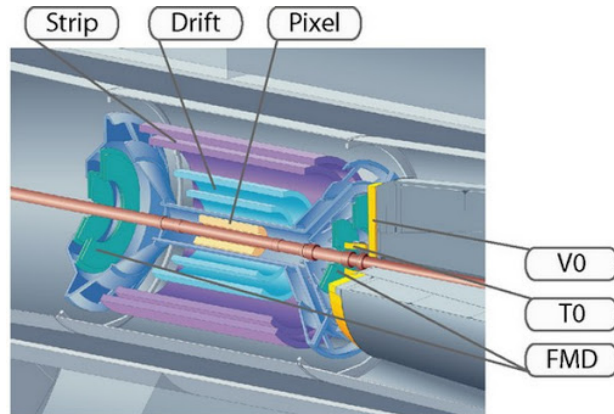


Figure 2.9: The V0, T0 and FMD detectors [77].

of multi-wire proportional counters with a lead converter (thickness of 3 radiation lengths) in between. The front plane is used as a vetoing detector for charged particles.

### T0

The T0 detector [76], shown in Figure 2.9, provides the ALICE first trigger level, and it delivers a start trigger with a resolution of 50 ps to the TOF particle identification system.

Moreover, it can measure the vertex position with a resolution of the order of one centimeter, enough to discriminate against beam-gas interactions: this is needed for triggering purposes.

The T0 consists of two arrays of Cherenkov counters, asymmetrically mounted at distances of 72.2 cm on the C-side and 375 cm on the A-side from the IP, respectively.

### V0

The V0 detector [76], shown in Figure 2.9, is made up of two scintillator hodoscopes located at 90 cm (V0C, C-side) and 340 cm (V0A, A-side) from the IP. It provides a minimum-bias trigger for the central barrel detectors and is needed for the identification and rejection of beam-gas events. In addition, V0 can also measure the charged-particle multiplicity and provides centrality estimation for p-A and A-A colliding systems.

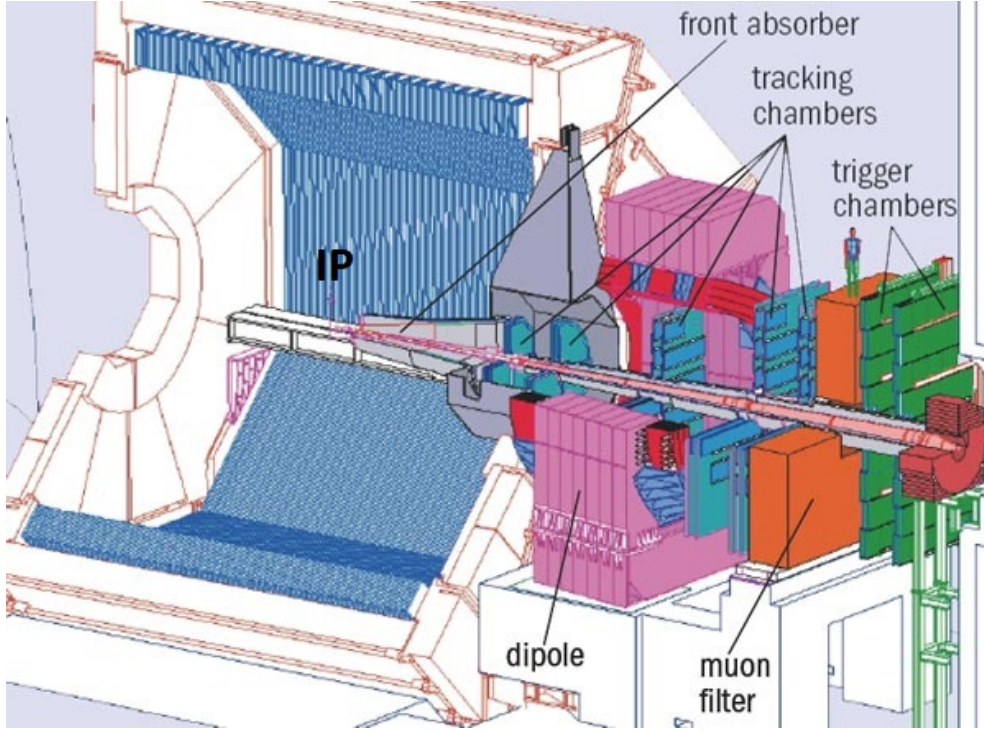


Figure 2.10: The Muon Spectrometer [82].

### 2.1.3 The ALICE Muon Spectrometer

The goal of the Muon Spectrometer [89] is to measure the open heavy flavour production, heavy quarkonia production ( $J/\Psi$ ,  $\Psi'$  and  $\Upsilon$ ,  $\Upsilon'$ , and  $\Upsilon''$ ), low-mass vector mesons (such as  $\rho$ ,  $\eta$  and  $\phi$ ) and electroweak bosons ( $W$  and  $Z$ ) via their muonic or semi-muonic decay channels. It is able to measure the quarkonia (both  $J/\Psi$  and  $\Upsilon$ ) production in central Pb-Pb collisions at LHC energies, vanishing down to  $0 p_{\text{T}}$ . It was built with the requirement of a mass resolution of around  $100 \text{ MeV}/c^2$  at  $10 \text{ GeV}/c^2$ , which is necessary to separate the different  $\Upsilon$  resonances in the high background environment typical of central Pb-Pb collisions.

It is located on the C-side and is composed of a dipole magnet, three absorbers, a tracking system and a trigger system (Figure 2.10). It covers a polar range of  $2^\circ < \theta < 9^\circ$ , corresponding to the pseudorapidity interval of  $-4 < \eta < -2.5$ .

The muon spectrometer components are described in the following section with more emphasis on the muon trigger because these trigger detectors are a subject of this thesis.

### Front absorber

It is located inside the L3 magnet, 90 cm away from the IP, is 4 m long and defines the acceptance of the muon spectrometer. It is made of carbon and concrete to limit the multiple scattering and the energy loss of the muons and backscattering into the TPC. Lower Z materials such as carbon are located nearer to the vertex in order not to deteriorate the mass resolution of measured states. The front absorber suppresses and filters out most particles except muons coming from the interaction vertex. In particular, it stops most hadrons, thus reducing the particle flux on the detectors by two orders of magnitude.

### Beam shield

The inner beam shield is built all around and along the beam pipe and protects the chambers from background originating from particles at small angles. It is made of tungsten, lead and stainless steel to also minimize the background arising from primary particles emitted in the collision and from their showers produced in the beam pipe and in the shield, itself.

### Dipole magnet

The dipole magnet is positioned at about 7 m from the interaction vertex and is one of the biggest warm dipoles in the world. It is 5 m long and weighs about 850 tons.

The magnetic field is defined by the requirements on the mass resolution and the nominal field is 0.7 T (or 3 Tm) in the x-direction (i.e perpendicular to the beam). The bending plane is defined as the xy plane and the non-bending plane as the xz plane (z indicates the coordinate along the beam line).

### Tracking system

The tracking system [81] is made up of 5 stations of two detection planes each consisting of multi-wire proportional chambers with segmented cathode plane (cathode pad chamber, CPC) and a 5 mm gap filled with an Ar/CO<sub>2</sub> (80/20) gas mixture. Each station consists of detector elements defining a bending and a non-bending plane. The thickness of each chamber is below 3% of the radiation length. The first two stations are located in front of the dipole magnet at a distance of 5.4 m and 6.8 m, respectively, from the IP. Each of their detector planes consists of four CPCs, each with a quadrant design. Stations 3, 4 and 5 are situated at a distance of 9.7 m (inside the

dipole magnet), 12.6 m and 14.2, respectively, from the IP. A modular design was chosen for these stations, consisting of rectangular CPC. Muon transverse momenta in the bending plane ( $p_{xy}$ ) are determined by tracking muons along the magnetic field. A momentum resolution of 1% is needed to achieve the required resolution in the  $\Upsilon$  invariant mass region ( $100 \text{ MeV}/c^2$ ), which is, together with its resonances, the most challenging particle to detect. The tracking chambers are required to tolerate a high hit density. A very fine segmentation of the detection elements is needed: readout pads near the beam pipe in the first station are  $4.2 \times 6 \text{ mm}^2$  in area.

The muon tracking system consists of  $10^6$  read-out channels. The chambers in station 1 and 2 have read-out electronic on the surface, while the CPC slats of stations 3, 4 and 5 are equipped with read-out electronics mounted on the top and bottom end of each slat. Each front-end read-out card, so called MANU board (64 channels), consists of 4 MANAS chips (pre-amplifier and shaper chip) several ADCs and the controller chip (Muon Arm Read-out).

The data flow is gathered with the help of 100 front-end CROCUS boards placed in 20 crates. Each crate has its concentrator board which communicates with the ALICE-DAQ. Figure 2.11 shows an example of the quadrant-type tracking chamber installed in the Muon Spectrometer.

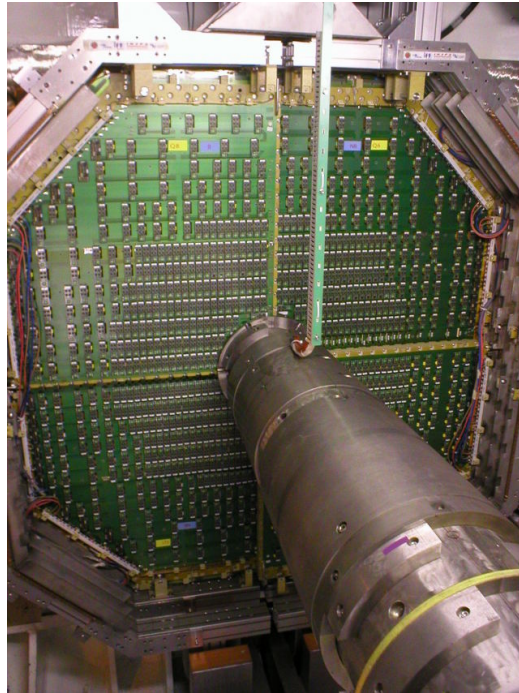


Figure 2.11: Example of Muon Tracking Chamber, here of the quadrant type [82].

### Muon filter

Another absorber is located between the tracking and the trigger stations, with the purpose of reducing the residual background of hadrons and low  $p_{\mathbf{T}}$  ( $p_{\mathbf{T}} < 0.5 \text{ GeV}/c$ ) muons in the trigger system. It is a 120 cm thick iron wall, 14.5 m away from the IP. The combined effect of the front absorber and the muon filter prevents muons with  $p < 4 \text{ GeV}/c$  from reaching the trigger system.

### The ALICE muon trigger system

The aim of the muon trigger system is to identify unlike-sign muon pairs from the decay of resonances, like sign muon pairs for combinatorial background studies and single muons from open heavy flavours and electroweak bosons. The collision rate in Pb-Pb at nominal luminosity is about 8 kHz. The DAQ system can tolerate a trigger rate of the order of 1 kHz.

In central Pb-Pb collisions, the average background in the muon spectrometer acceptance consists of eight muons emitted per event from pion and kaon decays. This background has a predominantly low-momentum  $p_{\mathbf{T}}$  distribution. The muon trigger is designed to apply a hardware transverse momentum cut in order to minimize the probability of triggering on background muons and to select high- $p_{\mathbf{T}}$  muons from heavy flavours and quarkonium decays.

To fulfill these requirements, Resistive Plate Chambers (RPCs) are chosen. RPCs are rectangular position-sensitive gaseous detectors with a spatial resolution of the order of cm, which can cover large areas and provide fast signals.

In this section, the design of the trigger system as well as the trigger principle are described.

### The trigger system design

The muon trigger system consists of 72 RPCs arranged in two stations called MT1 and MT2, located, respectively, at 16.1 m and 17.1 m away from the IP.

Each station is composed of two detection planes (MT11 and MT12 for MT1, MT21 and MT22 for MT2-see Figure 2.12 left). Each plane covers a large area (about  $5.5 \times 6.5 \text{ m}^2$ ) and consists of 18 chambers. In the trigger system, there are three kinds of detector elements Long, Cut and Short (L, C, S) in order to allow the beam pipe to cross the central part of each plane.

Each half plane is composed of six L-type chambers, two C-type chambers with cut-corners and one S-type. In addition, the detector size increases from

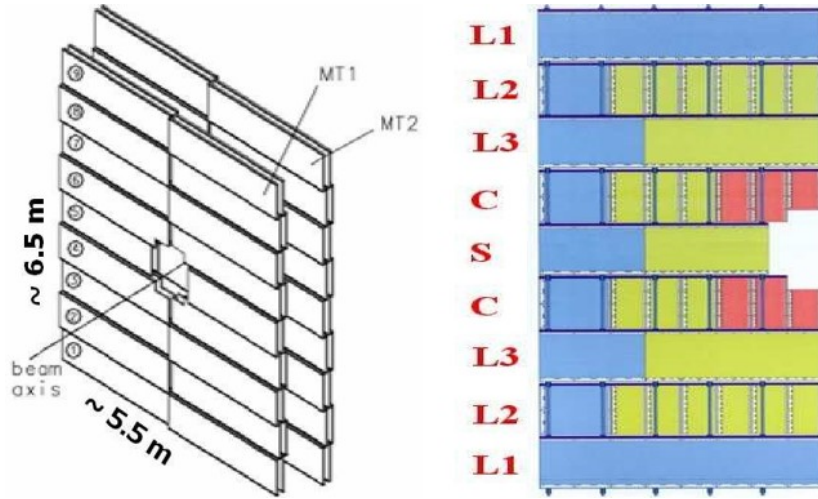


Figure 2.12: Schematic 3D view of the ALICE muon trigger system and the detector composition of a half plane [104].

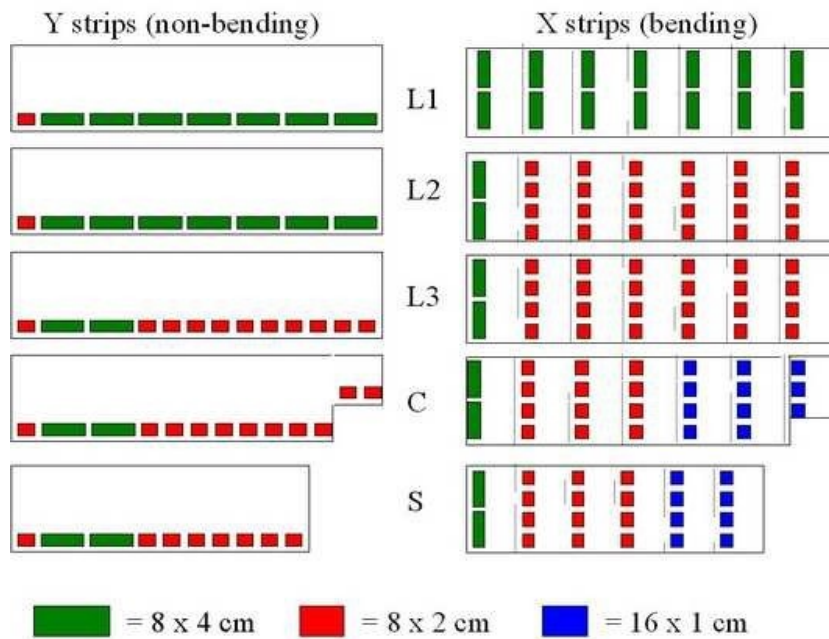


Figure 2.13: Strip segmentation of the detectors in the ALICE muon trigger [104].

MT1 to MT2 to cover the same angular acceptance. Each RPC is equipped with orthogonal strips and can be read-out on both sides, providing spatial information in both x and y directions (Figure 2.13). The vertical strips (also called Y-strips) measure the coordinate along the x-direction, while the horizontal strips (also called X-strips) measure the y-coordinate. The strip segmentation of the detectors is optimized to provide an almost flat occupancy throughout the surface plane, and the required spatial resolution. The particle density is expected to be maximum near the beam pipe, and become lower with increasing angle. Hence the strip pitch and length increase with the radius from the beam axis.

For horizontal strips, the detector needs a better spatial resolution because they determine the particle deviation in the bending plane. In the innermost regions the horizontal strip pitch is 1 cm while in the most peripheral regions, the pitch reaches 4 cm. Vertical strips have widths of 2 and 4 cm, respectively, since the resolution requirements in the non-bending plane are less stringent.

The RPCs are equipped with the ADULT (A DUaL Threshold) front-end electronics [103]. The digital signals are sent from ADULT to the local trigger electronics which has two main aims: firstly, the front-end produces the level 0 single muon trigger to implement the  $p_{\mathbf{T}}$  cut on single tracks and subsequently, the input bit patterns are stored in a pipe lined memory which is read out by the ALICE central trigger processor (CTP).

### Trigger principle

The trigger principle is implemented on the deviation of the muon trajectory in the magnetic field. As it was explained before, a momentum cut is necessary: two different  $p_{\mathbf{T}}$  cuts are defined, which represent a compromise between efficiency and background rejection: a low- $p_{\mathbf{T}}$  cut (0.5 GeV/ $c$ ) optimized for  $J/\Psi$  detection and a high- $p_{\mathbf{T}}$  cut (2 GeV/ $c$ ) optimized for  $\Upsilon$  detection. For single muons, the muon trigger provides two trigger modes, a low- and a high- $p_{\mathbf{T}}$  single muon trigger with a threshold of 0.5 GeV/ $c$ , and 4.2 GeV/ $c$ , respectively. A low- $p_{\mathbf{T}}$ (high- $p_{\mathbf{T}}$ ) dimuon trigger signal is issued when two opposite-sided muons with  $p_{\mathbf{T}} \leq 0.5$  (2 GeV/ $c$ ) are detected in the same event. The required  $p_{\mathbf{T}}$  cut is provided according to the following method: a muon generated at the IP is bent by the dipole and crosses the two trigger stations in  $(x_1, y_1, z_1)$  and  $(x_2, y_2, z_2)$ . The deviation introduced along the y-direction by the dipole magnet is defined as:

$$\delta y_2 = y_2 - y_{2,\infty} \quad (2.1)$$

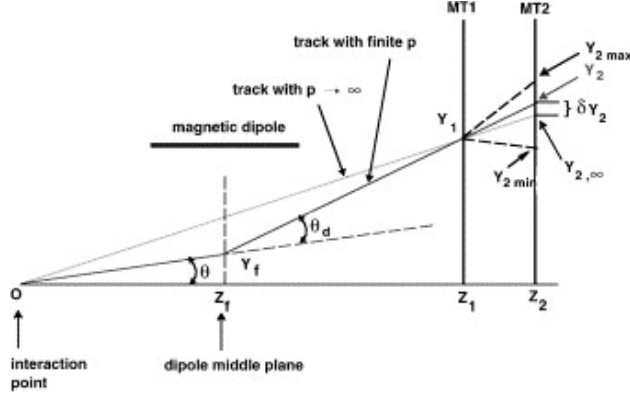


Figure 2.14: The ALICE muon trigger principle: projection in the  $yz$ -plane [90].

Where  $y_{2,\infty}$  is the position in which a muon with infinite momentum firing MT1 in  $y_1$  would cross MT2. For small deviations (less than  $10^\circ$ ), with reasonable approximation,  $\delta y_2$  can be written in terms of the particle  $p_T$ :

$$\delta y_2 = (z_2 - z_1) \frac{eBL R_F}{z_1 p_T}, \quad (2.2)$$

where  $z_1$  and  $z_2$  are the positions of MT1 and MT2 along the beam axis ( $z$ -direction),  $B$  is the magnetic field, which acts in a region of length  $L$  corresponding to the dipole length, and  $R_F$  is the radial position of the particle in the dipole mid-plane. It is evident that, according to this approximation, a cut applied on the deviation  $\delta y_2$  corresponds to a cut on transverse momentum. Moreover, positively and negatively muons can be distinguished according to the sign of the deviation. The values of  $\delta y_2$  (expressed through the number of strips) correspond to the values of  $p_T$  cut to be implemented. They are estimated through simulations and stored in Look-Up Tables (LUT), which are compared to the measured deviations in the strips.

The trigger algorithm also applies to the non-bending plane by checking that the tracks point back to the Interaction Point. In order to perform the above functionality, it is required that at least three out of four detection planes are fired. This allows one to reconstruct the track and to estimate the  $p_T$ .



## 2.2 Resistive Plate Chambers

The next sections will be dedicated to describing in detail the characteristics and the operation of the Resistive Plate Chambers (RPCs) [90] installed in the muon trigger.

An RPC is a gas-filled detector with a planar geometry. Figure 2.15 shows the cross section of a typical RPC element.

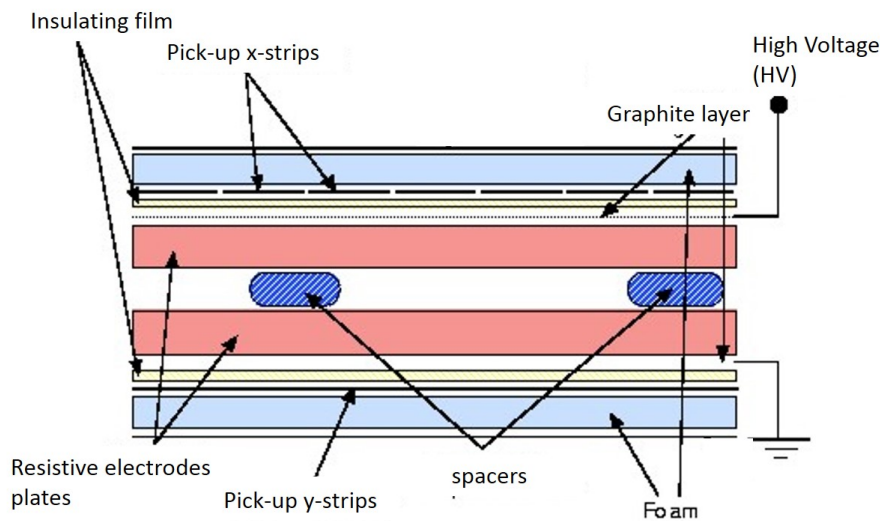


Figure 2.15: Cross section of a resistive plate chamber [90]

It is made up of two parallel electrode plates that confine a volume of gas: the gas gap. The special characteristic that differentiates this type of detector from a common gaseous counter is the resistive material that constitutes the electrodes. The two electrode plates are produced in bakelite covered with phenol resins and they are 2 mm thick. The separation between the plates is also 2 mm and is kept constant throughout the chamber with plastic spacers placed at regular intervals between the electrodes. A layer of graphite, which is a conductive material, connects the plates to ground and to the high voltage (HV) on the external surfaces, respectively, and guarantees that the HV is transmitted homogeneously over the entire surface. In this way, a uniform electric field is ensured inside the gap. Moreover, the uniformity of the electric field inside the gap is also determined by the smoothness of the internal surfaces which is guaranteed by treating them with linseed oil. The voltage needed for the working mode is of the order

of 4-5 kV/mm. The signal is picked-up by two sets of orthogonal strips made with conductive material that collect the signal inductively. A cover on a Mylar basis electrically insulates the strips from the graphite layer and from the electrodes. In order to equalize the strip impedance, the strip and ground planes are connected via a  $50 \Omega$  resistor at one end. Finally, the RPC is surrounded by a frame of polycarbonate equipped with four pipes to allow the gas to flow at atmospheric pressure into and out of the detector.

The RPC design allows the detector to be operated in different modes which are related to the gas composition and the operation parameters. The principle on which RPC detects particles relies on gas ionization: a particle travels through the gas gap ionizing a few gas atoms. In the presence of an electric field the freed electrons move to the anode while the corresponding ions drift to the cathode. The electrons have enough energy to cause a secondary ionization with other gas molecules on their way to the anode. This multiplication effect leads to an amplified signal which is inductively collected by the strips. In principle this phenomenon could generate a discharge on the anode. In general the RPC has quenching components which limit the discharge and provide a manageable signal. These components can be described as follows:

- Resistive electrodes: they cause a sudden drop in the discharge area of the local electric field. The discharge lasts around 10 ns, while the electrodes relaxation time is around 10 ms. This means that the resistive electrodes insulate the discharge production and evolution, avoiding that the signal multiplies over a small area of the order of  $0.1 \text{ cm}^2$ .
- Organic gas: its presence ensures that UV photons are captured and do not produce secondary electrons through photo ionization.
- Electronegative gas: this allows the low-energy electrons to be absorbed thereby reducing the size of the discharge. Only a small quantity (around 2-3 %) is necessary in order to avoid that also primary electrons are captured and the signal is suppressed.

The orthogonal read-out strips provide information on the position where the particle crossed the RPC with a spatial resolution in the range of 1 cm and time resolution of 1-3 ns.

## 2.3 Operating Mode

The main working modes for the RPCs are characterized in the next two sections: the streamer and avalanche mode.

### 2.3.1 Streamer mode

The study of a suitable gas mixture was carried out in the R&D phases of the ALICE experiment and the selected gas mixture has been used all along for qualifications and validation tests of the ALICE RPCs.

This gas composition for the streamer mode consists of four elements: argon, freon ( $C_2H_2F_4$ ) and iso-butane ( $i-C_4H_{10}$ ) are quenchers while  $SF_6$  is the electronegative gas. In the presence of an electric field between the electrode plates, the first electron freed during ionization drifts to the anode and generates a charge avalanche. At the same time the positively charged ions move towards the cathode. Since there are negative and positive charges moving inside the gas an internal and momentary electric field in the opposite direction to the operating field between the electrodes is generated (space-charge effect). Although the signal progression stops as soon as the two electric fields are equal, charges present at the bottom or at the top of the avalanche may form secondary avalanches. Moreover, photons produced during electron-ion recombinations may ionize other molecules of the gas and generate new avalanches while electrons knocked out from the gas can cause the same effect. These three phenomenons could induce a spark and generate a streamer signal.

Figure 2.16 shows an example of streamer signal: the signal amplitude of around 100 mV, is indicated by a lower signal around few mV which is associated with the avalanche created by primary and secondary electrons. Because the amplitude of the streamer signal is large a high preset threshold can be set: this lowers the background and the noise rate. A good spatial resolution is obtained because the signal develops quickly while the widening of the discharge is controlled. In streamer mode, due to the higher gain, a large amount of charge is deposited on the plates.

### 2.3.2 Avalanche mode

The main characteristic of the gas composition used for the avalanche mode is a larger percentage of quencher in order to avoid that the signal becomes a streamer. In this case  $C_2H_2F_4$  gas is used: it is an organic gas which

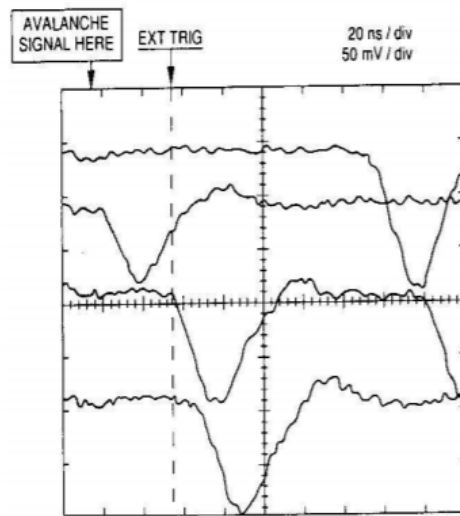


Figure 2.16: Example of a few streamer signals (pay attention to the scale) [94].

substitutes argon because the ionization happens more easily and it has better quenching features. Other gases used in the mixture that suppress the streamer, are iso-butane and  $\text{SF}_6$ . An example of a signal in avalanche mode is given in Figure 2.17.

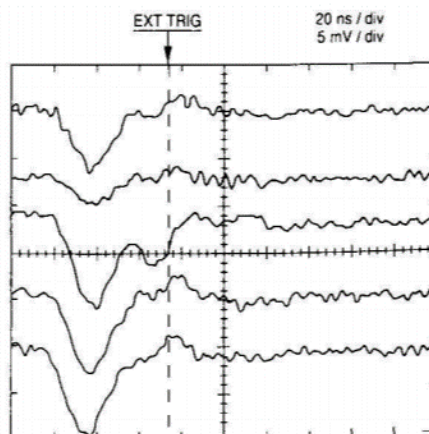


Figure 2.17: Example of a few avalanche signals (pay attention to the scale) [94].

A lower threshold is required because of the lower signal amplitude compared to streamer mode: the noise background is more relevant than in streamer mode.

The eventual working mode is chosen according to the experimental requirements. In Section 2.8.2 the choices made specifically for the muon trigger RPCs are described.

### 2.3.3 Rate capability

When a particle crosses the RPC, the average charge deposited on the electrodes is of the order of 50 pC for streamer mode and around 10 pC for avalanche mode.

As a consequence of the development of the avalanche or the streamer, the voltage and hence, the electric field between the electrodes is locally reduced. Therefore, the chamber is not efficient in this specific area for a short period called recovery time. The recovery time is the time needed to restore the nominal voltage between the electrodes. Should a particle cross the RPC in that very moment, the detector cannot detect it; thus its efficiency is reduced. The recovery time can be evaluated by considering that the chamber can be thought to work similarly to an RC circuit in that area. After the voltage drop due the passage of a particle, the capacitor recovers the initial voltage  $V_0$  [94] according to

$$V = V_0(1 - e^{-\frac{t}{\tau}}) \quad (2.3)$$

where  $\tau = RC$  is the relaxation time. Such a circuit can be considered and its equivalent in Fig 2.18. Its parameters (resistance  $R_p$  and capacitors  $C_p$ ,  $C_g$ ) are :

$$R_p = \frac{\rho d}{S}; \quad C_p = \epsilon_r \epsilon_0 \frac{S}{d}; \quad C_g = \epsilon_0 \frac{S}{g}; \quad (2.4)$$

where  $d$ ,  $S$ ,  $\rho$  and  $\epsilon_r$  are, respectively, the thickness, surface area, resistivity of the electrode and relative dielectric constant of the electrode.  $\epsilon_0$  is the vacuum dielectric constant and  $g$  is the width of the gas gap. If  $d = g$ , the relaxation time  $\tau$  becomes:

$$\tau = RC = 2R_p(\frac{C_p}{2} + C_g) = \epsilon_r \epsilon_0 \rho (1 + \frac{2}{\epsilon_r}) \quad (2.5)$$

For  $\rho$  around  $10^{-11}$   $\Omega\text{cm}$  and common value of  $\epsilon_r$  of 5 F/m, the recovery time is around 10 ms. As stated in using this basic RC model, the detector rate capability only depends on the resistivity and dielectric constant of the electrodes. There are other relevant features that can influence the rate

capability such as the surface resistivity of the electrodes and the spatial distribution of the signal. It is not possible to improve the rate capability by choosing materials for the electrodes with a resistivity lower than  $10^{-9} \Omega\text{cm}$  as the RPC would draw too much current and the noise rate will increase. Finally, also the choice of the streamer mixture influences the rate capability. In streamer mode the capacitor is fully discharged compared to avalanche mode where a smaller charge is deposited. This means that the capacitor recovery of the initial voltage  $V_0$  takes less time in avalanche mode leading to a better rate capability.

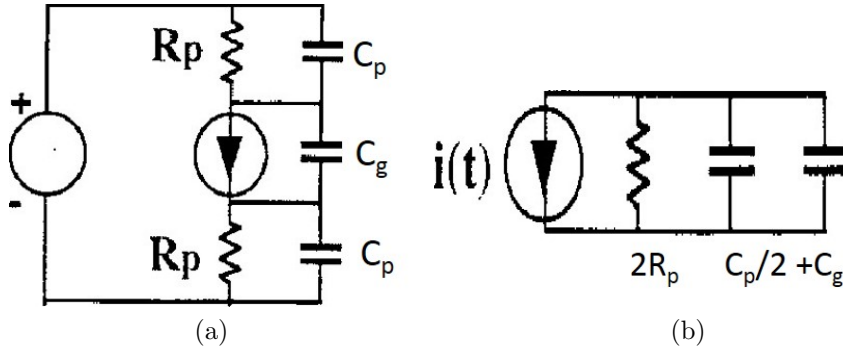


Figure 2.18: RC circuit modeling the recharging of electrodes of the RPC (left side) and the equivalent circuit of the RPC (right side) [90].

## 2.4 Working parameters

### 2.4.1 Efficiency

The high voltage (HV) applied to the chamber needs to be tuned to ensure maximum efficiency. In particular, the HV has to be high enough to generate the necessary electron multiplication to produce a signal greater than a certain threshold. Here a description is given of what happens when a particle crosses the detector: the multiplication process begins when the first atom is ionized in the gas-filled gap. Then free electron is accelerated by the electric field and acquires enough energy to ionize another atom while it is driven to the anode. Electrons travel over an average free path defined by  $\lambda$ . The energy gained by the electron during its motion needs to be greater than the ionization energy:

$$eE\lambda = e \frac{V}{d} \lambda > I \quad (2.6)$$

where  $I$  is the ionization energy,  $V$  is the voltage applied to the RPC,  $d$  is the gas gap width and  $e$  is the electron charge. In this case  $\lambda$  is written as a function of temperature  $T$  and pressure  $P$ :

$$\lambda = \frac{1}{\sigma N} = \frac{k T}{\sigma \bar{V} P} \quad (2.7)$$

where  $N$  is the gas atom density,  $\sigma$  is the electron-atom cross section,  $k$  is the Boltzmann constant and  $\bar{V}$  is the volume of the gas. The atom density can be defined using the ideal gas law so that the multiplication condition is related to  $V \frac{T}{P}$ .

An effective voltage  $V_{eff}$  can then be written as:

$$V_{eff} = V \frac{T}{T_0} \frac{p_0}{p} \quad (2.8)$$

where  $T_0$  and  $p_0$  are reference values of the temperature and pressure, respectively. At a HV of around 8 kV and atmospheric temperature and pressure, a change of  $5^\circ$  C in temperature or 20 mbar in pressure corresponds to a variation of around 150 V. For this reason, it is important to equip the HV power supplies of the RPC with a pressure and temperature gauge in order to ensure that the effective voltage remains stable. The RPC working voltage needs to be identified. Figure 2.19 shows an example of efficiency curve for the effective voltage produced in this work:

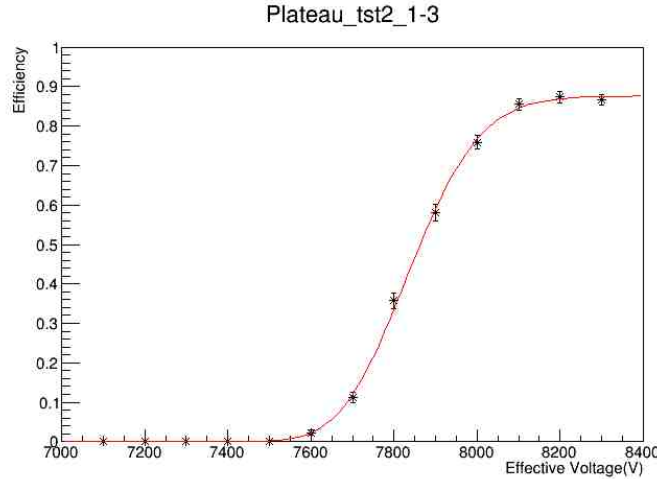


Figure 2.19: Example of efficiency curve as function of the effective voltage produced in this work (more details in Sec. ).

The Efficiency-HV curve of an RPC reaches the so-called knee after an increase in voltage of five hundred volts. Here the curve slope flattens off

and the curve becomes flat reaching a plateau. The operating high voltage used for the RPC is selected just after the knee at the beginning of the plateau. This choice is motivated by the fact that the HV cannot be set too high in order to limit the amplitude of the noise signal that may pass the preset threshold and be considered as a valid signal. If this preset threshold is higher, the shape of the curve remains the same but the curve shifts to a higher voltage.

Usually the RPC maximum efficiency is around 97-98%; it is limited by the spacers which reduce the actual active volume of the chamber. Other sources of the inefficiency include the non-equal distance between the internal layers or the internal surface which might not be completely smooth. These imperfections cause a variation of the electric field inside the chamber.

### 2.4.2 Spatial resolution and cluster size

The spatial resolution of a chamber is of the order of  $w/\sqrt{12}$  where  $w$  is the width of a strip. Effects due to the cluster size can modify the spatial resolution. The cluster size is defined as the number of adjacent strips in which a signal is induced. Firstly, the cluster size depends on the crossing point of the particle through the detector. For instance if the particle hit happens between two adjacent strips, the cluster size is 2. Another element that defines the cluster size is the threshold applied to the signal: as explained, in streamer mode the signal peak is tight and the signal amplitude allows to chose a high threshold which cuts off all the background. On the other hand, in avalanche mode the threshold is set according to the average amplitude of the signal but the spark is subject to fluctuations which may pass the threshold even if it is background. This means that the streamer mode is preferred if a good spatial resolution is required since the cluster size (around 1.5 with a strip width of 1 cm) is smaller compared to avalanche mode.

### 2.4.3 Time resolution

In the case of an RPC equipped with a small gap and parallel electrodes, there is no drift region and the electric field, which is uniform, can generate the electron multiplication everywhere inside the gap. This means that the time needed to generate the signal is quite small: the time resolution is around 1-3 ns, but is dependent on the HV applied. The time resolution is adequate for operating the RPC in the LHC environment. Typically the best performances in time resolution are obtained in avalanche mode, since sparking in streamer mode is a stochastic phenomenon.



### 2.4.4 Noise rate

The major source of background for these chambers is the noise caused by some imperfections that can affect the internal surfaces of the detector. These imperfections on the surfaces may lead to local increases of the electric field which produce discharges and the related noise signal. Alternatively, electrons escape from the cathode and drift to the anode, generating a discharge which gives a false signal. These anomalies need to be avoided in order to reduce the background and preserve the rate capability. Furthermore, the so-called cross-talk effect can occur: external electromagnetic fields can induce fake signals on the conductive strips, introducing another source of background. Finally, compared to the streamer mode, the avalanche mode shows a higher noise rate: the preset threshold needs to be lower because the amplitude of the signal is smaller causing more background.

### 2.4.5 Current

The current that flows between the two parallel plates needs to be monitored constantly. If the two layers are perfectly insulated, the only charge in the RPC is induced by particles crossing the gas gap without other contributions. When the chamber is not exposed to particles from the beam collisions, it is characterized by a so-called dark current which also includes the signals induced by cosmic rays. A current may flow between the electrodes if the insulation is not perfect generating a leakage current that can be seen at low values of the HV settings, at which contributions from ionization are negligible.

## 2.5 Ageing

During the LHC data taking, RPCs are exposed to a large number of particles which eventually may lead to ageing effects of the detectors [95]. Among these, the most frequent effect is a moderate increase of the dark current of the chamber, which in extreme cases potentially leads to inefficiencies. Ageing is a critical characteristic that needs to be checked regularly during the periods of LHC activity. In particular, the performance of RPCs may change during long periods of operation: for instance, high particle rates can lead to chemical reactions of the gas thereby contaminating it. These new polluting substances may deteriorate the electrodes' surface and change the resistivity of the bakelite or may even dissolve the linseed oil which covers the internal surface of the electrodes. Another effect is due to the ionizing and/or quenching properties of the gas mixture, since the energetic electrons drifting across

the gas gap might break the chemical bonds inside and between molecules of the gas mixture. For this reason, the lifetime of a chamber is considered to be potentially limited by the integrated current per surface unit drawn by the RPC when in operation. If the charge deposited on the electrodes per particle crossing the chamber is known, the integrated charge can be computed from the time integrated rate (hits/cm) [90]. In addition, ageing of the chambers can be caused by the diffusion of H<sub>2</sub>O molecules from the bakelite into the gas mixture. Consequently the electrodes gradually change their properties which results in a rise in their resistivity and mechanical failures. Hence it is important to maintain the correct water concentration in the gas.

## 2.6 Muon trigger system RPCs

RPCs are used in the muon trigger system since they fulfill the following characteristics:

- their rate capability is of a few hundred Hz/cm<sup>2</sup> and allows the utilization of these detectors in Pb-Pb and pp collisions;
- Since RPCs are not sensitive to neutrons and photons they are ideal detectors to operate in a radiation environment;
- the spatial resolution of about 1 cm is sufficient for the trigger selection;
- a time resolution of a few ns is enough to separate muons coming from different bunch crossings (bunch crossings are spaced 25 ns in time);
- the uniform electric field ensures a fast response and a high efficiency;
- since these chambers are made from affordable materials they are convenient in covering large areas of detection;
- RPCs have a compatible lifetime with respect to the LHC program.

In the preparation of LHC Run 1, all RPCs were completely installed in 2007: these were made of bakelite electrodes with a low resistivity of around 10<sup>9</sup> Ωcm according to the decision of the ALICE collaboration. Firstly, to accomplish the requirements during Pb-Pb collisions, a streamer gas mixture was selected. This (humidified) mixture consisted of:

$$50.5\% \text{ Ar} \quad 41.3\% \text{ C}_2\text{H}_2\text{F}_4 \quad 7.2\% \text{ } i - \text{C}_4\text{H}_{10} \quad 1\% \text{ SF}_6$$

On the other hand, for pp collisions a different gas mixture was chosen to safeguard the chambers against ageing in a high irradiation environment. A highly saturated and humidified avalanche gas mixture was used:

$$89.7\% C_2H_2F_4 \quad 10\% i - C_4H_{10} \quad 0.3\% SF_6$$

Such a gas mixture is used by applying a high voltage large enough to obtain signals of amplitude sufficient to be discriminated by the front end electronics (ADULT see below) without any amplification stage. For this reason, this working mode is defined as maxi-avalanche. The typical maxi-avalanche signal has an amplitude of around 10 mV instead of few mV. The HV applied is around 10400-10500 V at a temperature of 20 °C and a pressure of 940 mbar with a preset threshold of 7 mV. Because of its optimal performance also in Pb-Pb collisions, the maxi-avalanche mixture now is used for all types of collisions.

### Electronics

The ALICE muon trigger front-end electronics (FEE) were initially developed to be used in streamer mode. A DUaL Threshold (ADULT) [103] techniques is applied: the first threshold (10 mV) is set for the precursor avalanche peak while the second (80-100 mV) selects the streamer peak. The coincidence of the two output signals determines a hit on a strip. In maxi-avalanche mode operation, both thresholds are set at the same value.

## 2.7 Characterization of the new detectors

Since the installation in 2007, some RPCs (especially the ones placed closer to the beam pipe) have collected an integrated charge that is not negligible with respect to their life-time certified by the ageing tests [90]. Therefore, it was decided to replace these with new chambers. While the read-out strips and the mechanical structure will be kept, some of the gas gaps will be replaced by a new production batch during the LHC long shut-down 2 (LS2). The design of this new production is exactly the same as for the first batch.

This PhD service task was to perform a study on the RPCs with these new gas gaps in order to characterize them so that the ALICE collaboration can have access to all their features and to select the best ones to install in the muon trigger system before the next operation Run.

### Detector manufacturing

The resistivity of the sheets of bakelite was checked under controlled conditions ( $T = 20^\circ$  and relative humidity of 40 %). Then, these sheets were cut by milling to obtain the desired shape. The different components of the detector were assembled by an industrial company. First of all, the layer of graphite was painted on the external sides of the gas gap. It is important to leave a graphite-free frame 11 m wide on the gas gap to avoid discharges. Moreover, the two gas gap sheets are glued with internal spacers (arranged in a  $10 \times 10$  cm<sup>2</sup> matrix) and the final gas gap is insulated along the volume edges with a PET frame. Finally, the gas gaps were filled with a mixture of linseed-oil and n-pentane which was then drained out. In order to ensure a full linseed-oil coverage, this procedure was repeated twice.

The mechanical structures, the readout strip planes, the ground planes were produced in the Torino INFN Laboratory [104].

The tests on these new detectors were carried out using a streamer mixture even if they will work in maxi-avalanche mode as they can be compared to the tests done on the first chambers. After installation in ALICE, the current values will be closely monitored because the chambers will work at higher HV necessary with a maxi-avalanche mixture (around 10000 V instead of 8600 V).

## 2.8 Tests of the new RPCs

The next sections will describe in details the tests which were performed at the Torino INFN Laboratory in a dedicated station (see Figure 2.20). Here the complete list of the tests applied on every new RPCs is given:

- gas tightness of the detector;
- the current-HV curve (called ramp-up) and the detection of possible leakage and high levels of currents;
- the efficiency-HV curve and the efficiency map in cells of  $20 \times 20$  cm<sup>2</sup> to check the homogeneity of the detector and to identify the working HV;
- the efficiency map at working HV, with a granularity of  $2 \times 2$  cm<sup>2</sup> in order to detailed information on the local behaviour of the detector;
- the noise map of the detector, with the auto-trigger method.

The results presented here are for 10 RPCs and they were tested 2 at the time. In Table 2.2 all the new detectors names are listed together with their geometrical shape, referred to as RPC type.

RPC station 1	RPC type	RPC station 2	RPC type
413	Cut	369-11	Short
487	Long	485	Long
449-15	Cut	451-15	Cut
374-11	Long	369-11	Short
368-11	Cut	376-11	Long

Table 2.2: The list of all RPCs tested.

The types Long, Short and Cut depend on the position of the chamber in the detection planes of the muon trigger system as explained in Sec. 2.1.3.

## 2.8.1 Preliminary tests

### Gas-leakage test

Firstly, it was necessary to check the detectors for gas leakage. A blower equipped with a valve was linked to the gas inlet, while a U-shaped pipe containing water was connected to the gas outlet. The blower pumped air into the gap in order to rise the water level inside the pipe. If the level immediately decreases after shutting the valve, the RPC suffers of a gas leakage problem. If a detector presents this issue, it has to be discarded. All 10 RPCs passed this first preliminary test.

### Ramp-up

Secondly, the detector needed to be filled with the streamer mixture for at least 4-5 hours. Then, the HV was applied starting from a voltage of 1000 V. The current was monitored while increasing the HV every 10 minutes by 500 V up to 7000 V followed by 100 V up to 9000 V. This is, as a standard, the ramp-up procedure. Based on the previous tests on the first chambers [90], it was decided that the current should be less than 1  $\mu A$  at 7000 V. Since for a few chambers the current rose too fast, the HV was kept at the same value to check if the current would drop. Such a phenomenon is caused by the presence of impurities inside the gap that are burnt out the first time the detector is filled with the gas mixture and its HV is turned on. Finally, the ramp-up is successful when the current is around 1  $\mu A$  at 7000 V. The current

drawn by the RPC needs to be monitored during the test procedure because premature rises in the current levels can be the symptom of a malfunctioning. Should the current not stabilize, this could be caused by the following: the insulation of the mechanical structure or the electrodes might be deficient or the two electrodes layers might have an electric contact. If this kind of issues cannot be solved the detector has to be rejected.

All 10 chambers tested were monitored and presented acceptable values of current during the test procedure.

## 2.8.2 Efficiency measurement

### Set-up

The efficiency analysis was performed with cosmic rays and required a dedicated set-up in Torino at the INFN Laboratory. The set-up is illustrated in Figure 2.20 and is made up of:

- three planes consisting of nine scintillators each. Every plane covers an area of  $90 \times 150 \text{ cm}^2$  (Scint1, Scint2, Scint3);
- two tracking RPCs, that cover an area of  $172 \times 87 \text{ cm}^2$  each (TRK1, TRK2);
- four slots to install the RPCs for tests.

The two RPCs placed in position 2 and 3 were tested simultaneously while the ramp-up test was carried out on the ones placed in 1 and 4.

The area of the tracking chambers and the scintillators was not big enough to cover the detector area completely. So the testing apparatus was equipped with a moving structure with wheels in order to test two half-RPCs simultaneously: when the first two halves were tested, the apparatus is moved to repeat the test on the other two halves.

### Trigger and tracking systems

The trigger for when a cosmic ray crosses the apparatus requires at least one scintillator per plane and at least one strip per each plane of the two tracking RPCs to be hit. In addition, the maximum cluster size of the two tracking RPCs is required to be at most two in order to reject cosmic-ray showers. The layout of the trigger logic is shown in Fig. 2.21.

The tracking system is necessary to determine the cosmic ray impact coordinates of the RPCs under test and its corresponding local efficiency. The calculation is performed as follows: the detectors under test are placed

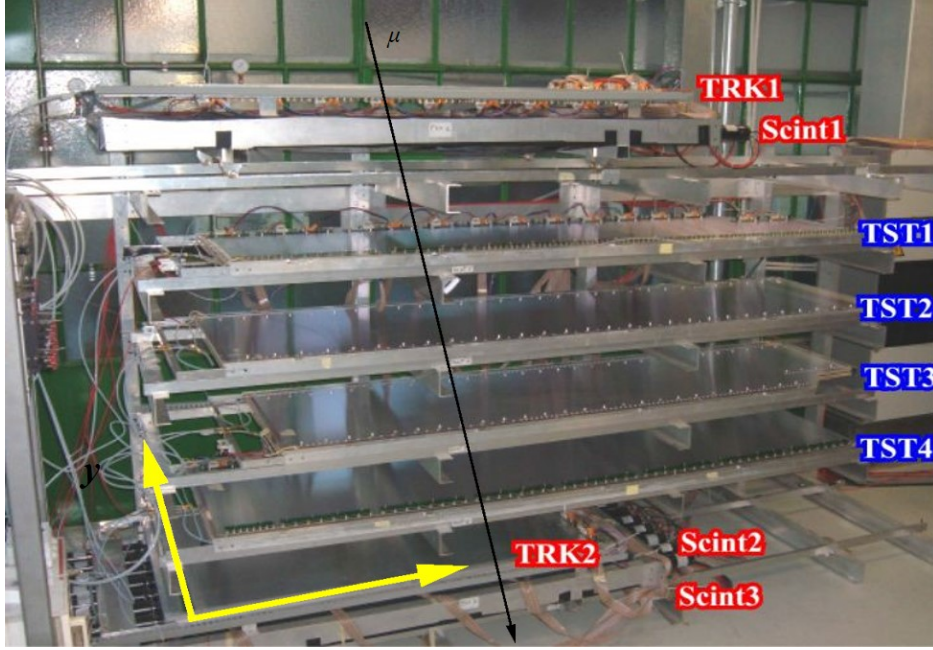


Figure 2.20: The test station at the Torino INFN laboratory.

at height  $z_{test,1}$  and  $z_{test,2}$ . The cosmic ray crosses the first tracking RPC at  $(x_1, y_1, z_1)$  while the second at  $(x_2, y_2, z_2)$ . The information on where the cosmic ray crosses the two tested RPCs need to be obtained, calculating  $(x_{test,i}, y_{test,i})$  where  $i=1,2$  :

$$x_{test,i} = x_1 + \frac{z_{test,i} - z_1}{z_2 - z_1}(x_2 - x_1); \quad y_{test,i} = y_1 + \frac{z_{test,i} - z_1}{z_2 - z_1}(y_2 - y_1); \quad i = 1, 2 \quad (2.9)$$

The reconstruction algorithm divides each tested RPC in a grid made up of cells. The area of a cell can be selected and the minimum option is  $2 \times 2$   $\text{cm}^2$ . Once the coordinates of the cosmic ray crossing point are calculated, for every event (which is a cosmic ray travelling through the chamber) the corresponding cell is associated. The efficiency is defined as the ratio of the number of events detected in that cell of the tested chamber ( $N_{detected}$ ) w.r.t. the number of cosmic rays associated to that cell ( $N_{associated}$ ).

$$\epsilon = \frac{N_{detected}}{N_{associated}} \quad (2.10)$$

The binomial distribution is used to calculate the statistical error on the RPC efficiency  $\epsilon$ . The second moment of the binomial distribution is  $np(1-p)$  so the efficiency statistical error  $\sigma_\epsilon$  becomes:

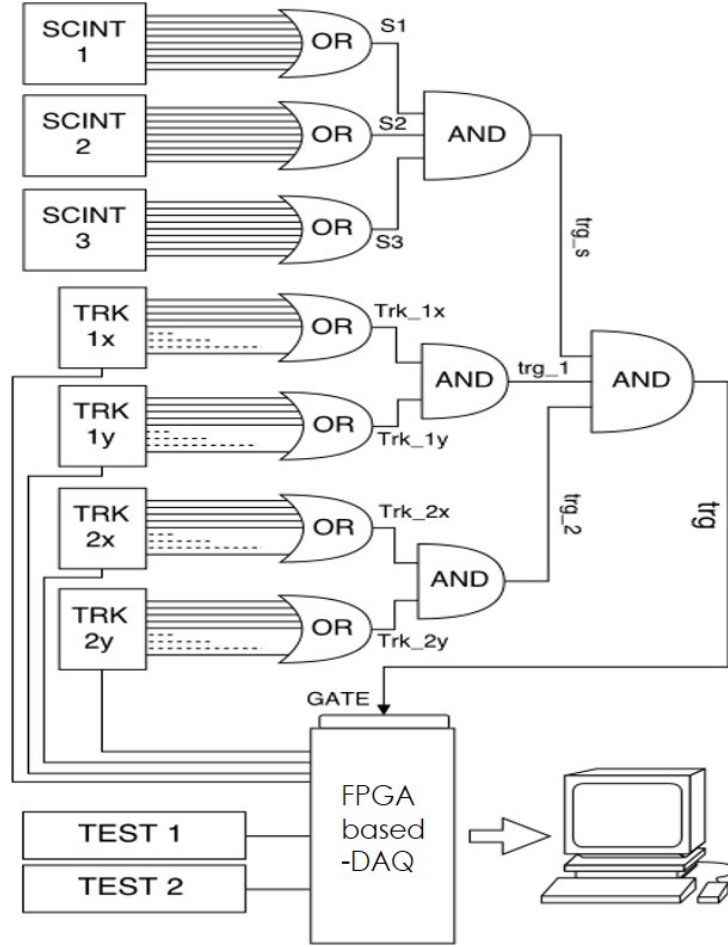


Figure 2.21: Trigger design to measure the efficiency.

$$\sigma_{\epsilon} = \frac{\sigma_{N_{detected}}}{N_{associated}} = \sqrt{\frac{\epsilon(1-\epsilon)}{N_{associated}}} \quad (2.11)$$

where  $p$  is  $\epsilon$  and  $n = N_{associated}$  in this context.

This formula accounts for the statistical fluctuations of the number of the detected particles for a given efficiency. When the statistical fluctuations decrease below the sensitivity error of the instrument, the statistical error calculated is no longer the main source of uncertainty: for example, if distances are measured with a resolution of 1 mm, the standard deviation of the distribution of the values should be quoted as an error only if it exceeds 1 mm.

In this case, the efficiency is measured by counting particles, i.e. with a resolution of  $\pm 1$  on  $N_{detected}$ , resulting in a resolution of  $\pm 1/n$  on the



efficiency. The quantity  $1/n$  can thus be taken as a sensitivity error on the measurement. The condition for the error, defined in the previous equation to be reliable can thus be written as:

$$1/n < \sqrt{\frac{\epsilon(1-\epsilon)}{n}} \quad (2.12)$$

Hence, for a certain RPC efficiency, above a threshold events number the sensitivity error of the detector becomes the dominant error.

### Efficiency-HV curves

As explained, 2 RPC halves are tested simultaneously. They were divided into a grid of  $7(\text{long side}) \times 3(\text{short side}) = 21$  cells. The area of every cell was around  $20 \times 20 \text{ cm}^2$ . The efficiency of all 21 cells was evaluated for 13 HV values in runs of 20000 events each. At the end of this test, 21 Efficiency-HV plots were evaluated, one for every cell. The integral of an asymmetric Gaussian distribution fits each Efficiency-HV plot:

$$\epsilon(HV) = \epsilon_{max} \frac{\int_{HV_{min}}^{HV} e^{-(t-\mu)^2/2\sigma^2(t)} dt}{\int_{HV_{min}}^{HV_{max}} e^{-(t-\mu)^2/2\sigma^2(t)} dt} \quad (2.13)$$

where  $\epsilon_{max}$  is the maximum efficiency and  $\sigma(t)$  is

$$\sigma(t) = \sigma_1 + \sigma_2 \frac{t - \mu}{\sigma_1} \quad (2.14)$$

$\sigma_1$ ,  $\sigma_2$  and  $\mu$  are parameters extracted from the fit. As an example Figure 2.22 shows 6 Efficiency-HV curves for the right half of RPC 487.

Some RPCs show internal disuniformities. In particular, some cells reached the maximum efficiency at a higher value of HV with respect of the majority. This phenomenon required to select a higher HV to provide suitable working conditions for every cell of the RPC. Table 2.3 summarizes the values of the working HV selected for every chamber under study.

Figure 2.23 shows an example of the efficiency map for half RPC 374-11 at the working HVs of 8600 V and 8300 V (top panels), together with the statistical error map (bottom panels).

### Efficiency maps

The efficiency map with high granularity cells was performed in order to detect inefficiency and internal disuniformities. Detectors selected to be installed in ALICE need to show a uniform behaviour over the entire RPC surface.

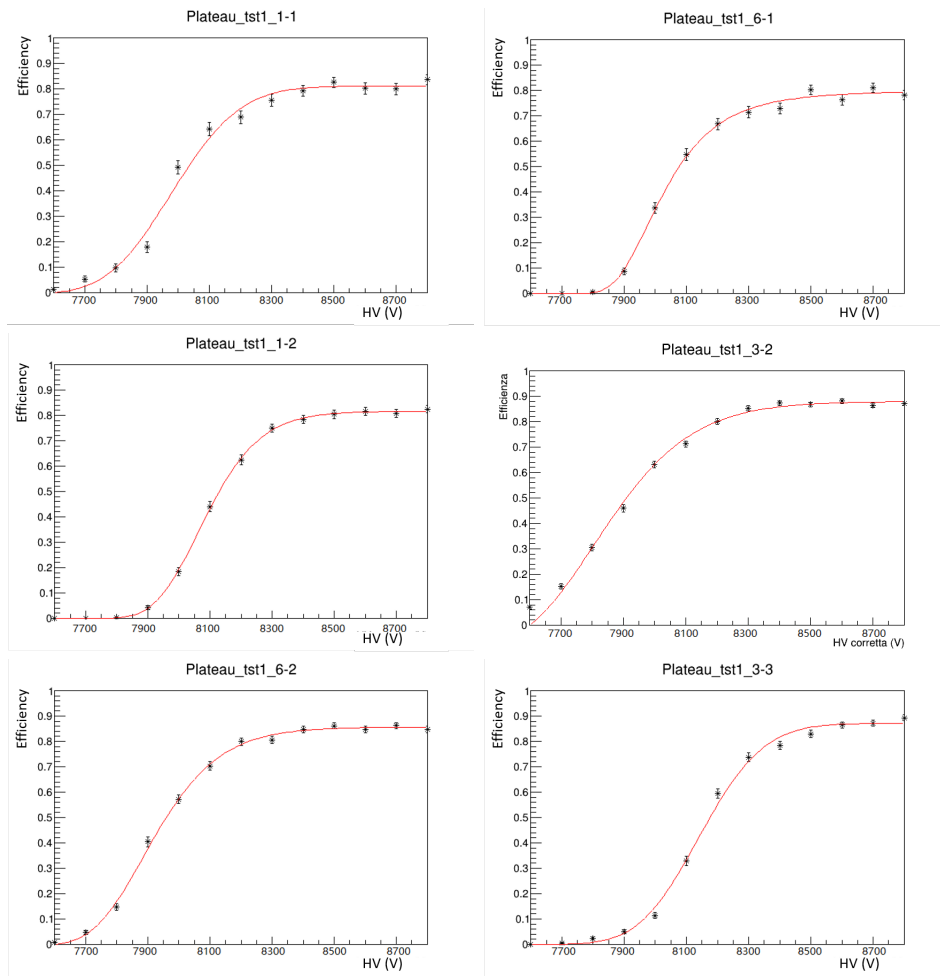


Figure 2.22: Example of 6 efficiency-HV curves together with the asymmetric Gaussian fit for the right half of RPC 487.

RPC	HV	RPC	HV
487	8600 V	485	8700 V
449-15	8800 V	451-15	9000 V
374-11	8600 V	369-11	8700 V
368-11	8700 V	376-11	8700 V
361-11	8700 V	362-11	8700 V

Table 2.3: The list of all HV selected for the detectors under study.

Each cell area is  $2 \times 2 \text{ cm}^2$  and for every run 1000000 events were collected: the rate in the central cells was around 500 events, in the peripheral cells

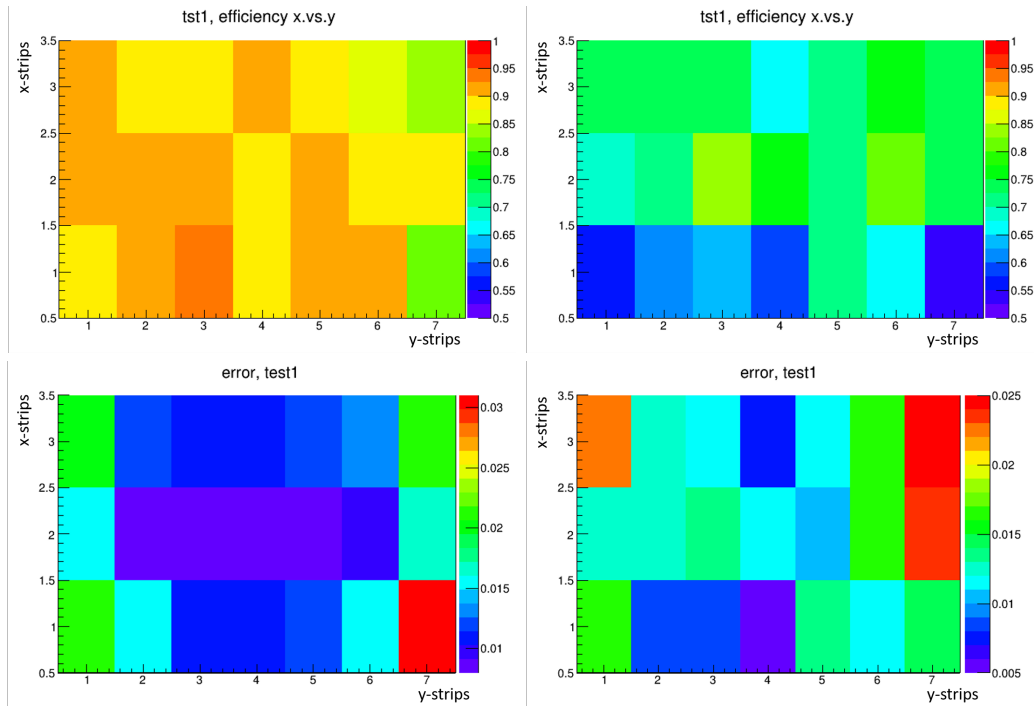


Figure 2.23: Efficiency maps of RPCs 374-11 at 8600 V (left-top panel) and at 8300 V (right-top panel) together with their statistical error maps (bottom panels).

around 100 events and in very peripheral cells around 50 events. In addition, the high granularity maps were evaluated at two high voltages: at the working HV and at 100 V below. Figure 2.24 shows three examples of high granularity efficiency maps for a half detector. Since the cell area is  $2 \times 2 \text{ cm}^2$ , the spatial resolution was high enough to see the spacers regular distances inside the RPC. The first panel shows a RPC type Cut as it can be seen from the shape. The second panel shows the best efficiency map obtained during these tests. Finally, the third panel shows an example of efficiency disuniformities on a RPC type Long.

Moreover, Figure 2.25 shows the corresponding statistical error maps of the three high granularity efficiency maps displayed in Fig. 2.24. The statistical errors are typically between 1% and 4% depending on the position on the detector.

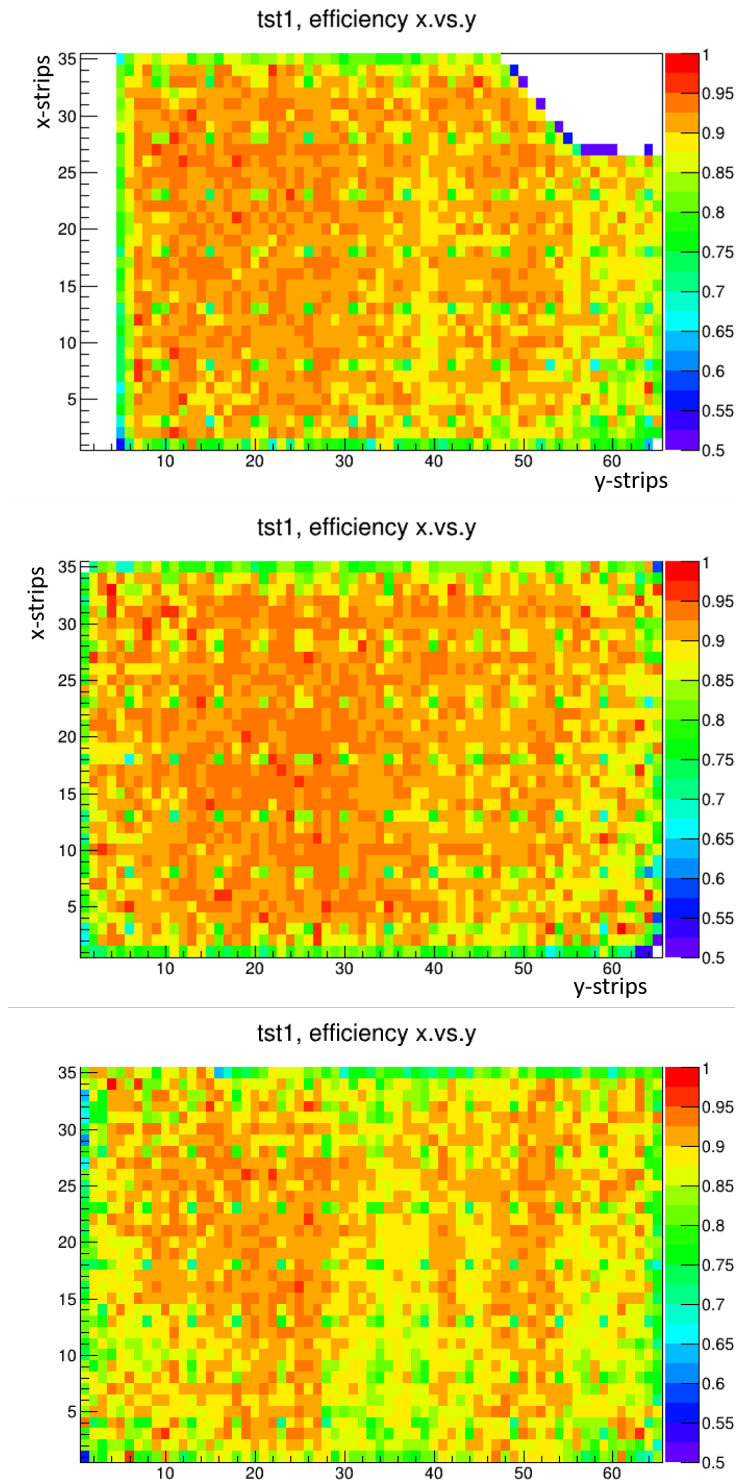


Figure 2.24: Efficiency maps of half RPCs 361-11 at 8700 V (first panel), 374-11 at 8600 V (second panel) and 368-11 at 8600 (third panel).

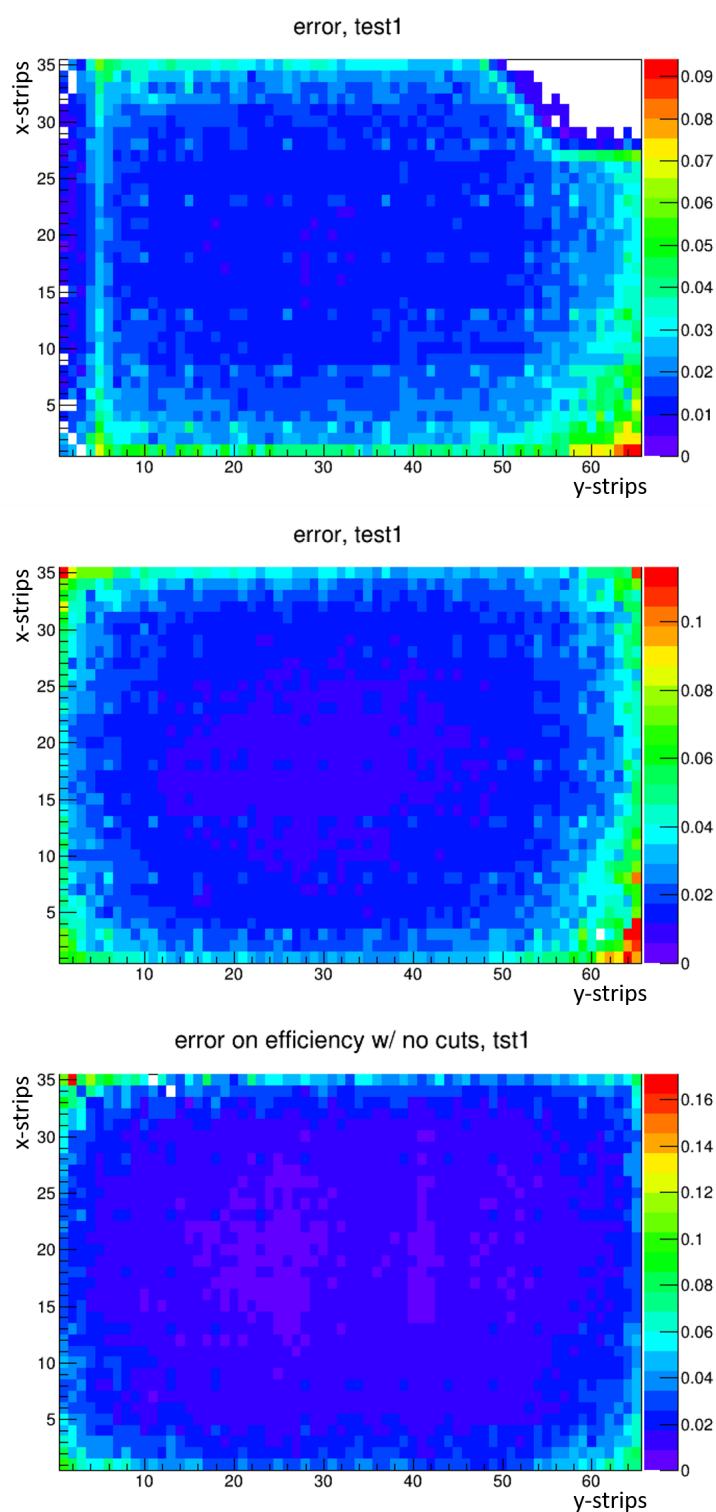


Figure 2.25: Efficiency Statistical error maps of half RPCs 361-11 at 8700 V (first panel), 374-11 at 8600 V (second panel) and 368-11 at 8600 V (third panel).

### 2.8.3 Noise map

The noise induced inside a RPC originates from the dark count rate which is defined as the count rate in the absence of external irradiation or beam but merely from the intrinsic noise and cosmic rays. The dark counting rate can be measured with the auto-trigger method; the RPC itself provides the trigger which requires events with at least one hit on both strip planes. The logic diagram of the electronic chain is shown in Fig. 2.26.

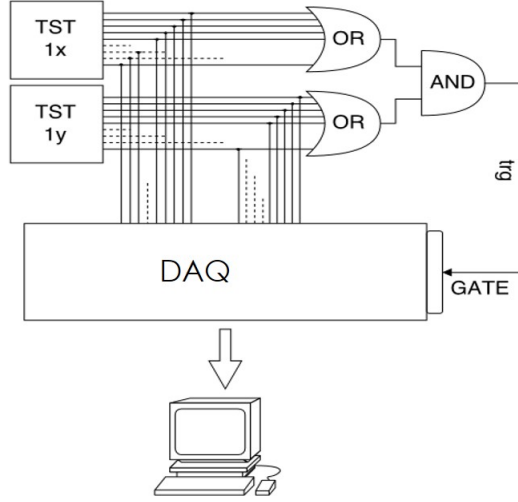


Figure 2.26: Logic scheme for the auto-trigger method.

A grid defined by the strips in the x and y directions divide the RPC in cells. To calculate the  $N_{ij}$  number of hits in every cell, it was counted how many times the i-strip in the x-direction and j-strip in the y-direction have been hit in the same event. The rate  $R_{ij}$  (Hz/cm<sup>2</sup>) associated with the  $(i, j)$  cell is:

$$R_{ij} = \frac{N_{ij} N_{non-vetoed}}{\Delta t N_{vetoed} A_{ij}} \quad (2.15)$$

where  $\Delta t$  refers to the acquisition time,  $A_{ij}$  to the area of the crossing between the i-strip and the j-strip,  $N_{vetoed}$  are the counts vetoed and  $N_{non-vetoed}$  are the counts non-vetoed by the Data Acquisition (DAQ) system, respectively. The dead time of the DAQ is consider as the ratio of non-vetoed to vetoed counts. Every cell rate was then displayed as a noise map (see Figure 2.27 as an example). RPC noise maps are important to detect noisy spots characterized by rates in access of around 10 Hz/cm<sup>2</sup>. Since these noisy spots can also be generated by the electronic read-out, the noise maps were produced at 10 different HV settings to establish that the noise originates from inside the

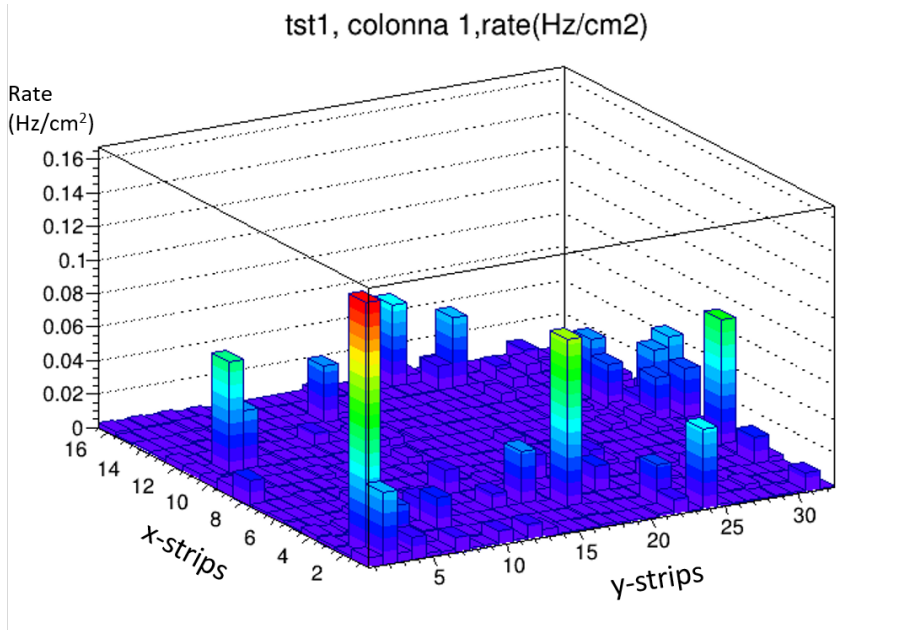


Figure 2.27: Noise map of RPC 374-11 at 8600 V.

RPC. If the noisy spot persists even when the HV is decreased, it is caused by the read-out.

All 10 RPCs under study did not present any noisy spots and their average rate was around 0.05-0.1 Hz/cm<sup>2</sup>.

## 2.9 Results and discussion

For this PhD service task, 10 newly produced RPCs were tested. They were meant to substitute the most exposed RPCs installed in ALICE since 2007. Table 2.4 below shows all the characteristics of the detectors tested.

According to the test, only 2 RPCs (374-11 and 361-11) can be considered for installation. Moreover, 12 other detectors of this new production were tested by the author during the master thesis and they also presented problems associated to the efficiency and to high current levels. In addition, comparing these results with the studies of the first detectors production [90], it can be seen that the average working HV was around 8100-8300 V while for the new RPCs the average working HV was around 8600-8800 V. The high granularity efficiency maps of the first group were also uniform and reached average values of 90-95 %. On the contrary most of the new chambers selected for the installation had an overall efficiency of 85-90 %.

RPC	HV	High Gran. Efficiency map	Noisy spots
487	8600 V	low overall (around 80%)	none
449-15	8800 V	map hole+low overall (around 80%)	none
374-11	8600 V	Good	none
368-11	8700 V	disuniformity	none
361-11	8700 V	Good	none
485	8700 V	low overall (around 80%)	none
451-15	9000 V	3 map holes	none
369-11	8700 V	1 map hole	none
376-11	8700 V	disuniformity+low overall (around 80%)	none
362-11	8700 V	1 map hole	none

Table 2.4: The list of the main characteristics of the detectors under study.

The characteristics of the new production led to further investigations: it was found that the chambers were built with structural problems. In particular, the gluing of the internal spacers and the two bakelite plates were irregular. For instance, if the amount of glue is too much (or too little) the 2 mm distance between the plates cannot be guaranteed and can cause disuniformities in the efficiency and differences in the working HV values through the chamber. This issue can even lead to holes in the efficiency maps as can be seen in Figure 2.28.

The industrial company was requested to improve the weak points of the chambers and to produce new RPCs. So far, three prototypes were tested showing promising results. Their average working HV is 8400-8500 V, they present a uniform efficiency map and acceptable noise rates [105]. Figure 2.29 shows an example of the high granularity efficiency map for one of the prototypes (RPC 682). The RPC mass production was then relaunched in March 2020 and the new RPCs will be delivered to the TORINO INFN Laboratory in the upcoming months.

The tests carried out in the context of the service task were not able to find suitable chambers for the installation in ALICE but they were crucial to diagnose the RPCs structural issues in order to give constructive feedback information to the industrial company in charge of the detectors construction.

The next chapter is dedicated to the main topic of this PhD work: the analysis of (multi-)strange hadrons production as a function of charged-particle multiplicity in pp collisions at  $\sqrt{s} = 5.02$  TeV.



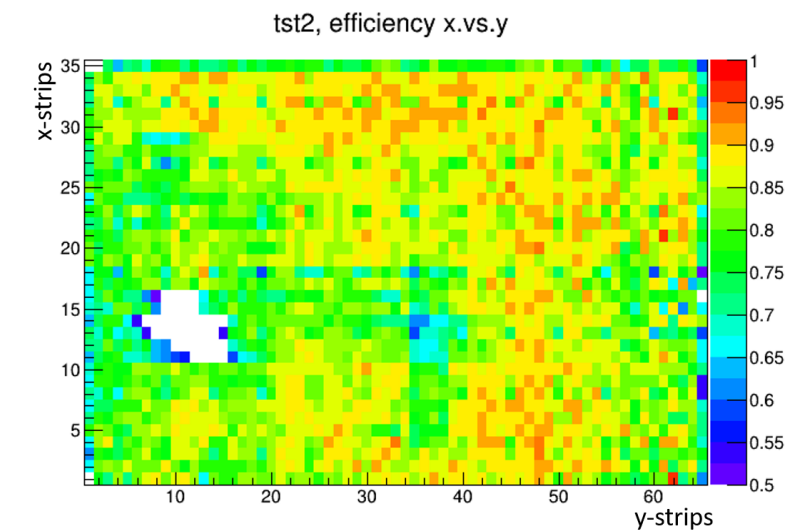


Figure 2.28: High granularity efficiency map for the left-half RPC 451-15 at 8900 V.

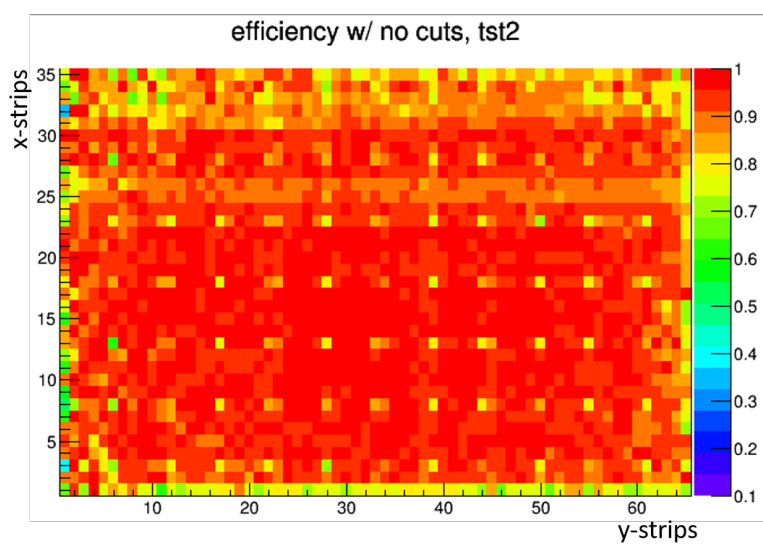


Figure 2.29: High granularity efficiency map for the left-half RPC 682 at 8500 V.

# Chapter 3

## Data analysis

This chapter is dedicated to the data analysis of (multi)-strange hadrons as a function of charged-particle multiplicity at midrapidity in pp collisions at  $\sqrt{s} = 5.02$  TeV. As described in Chapter 1, the analyses of strangeness production in pp collision are fundamental to understand the dynamics of small collision systems. This analysis is fully documented in an Analysis Note (<https://alice-notes.web.cern.ch/system/files/notes/analysis/959>) approved by the ALICE Collaboration. In order to access the Analysis Note the reader must have CERN-ALICE credentials.

### 3.1 Introduction

The focus of this data analysis is to study hadrons containing strange quarks. Those hadrons are divided here into two groups depending on the way they are reconstructed in the tracking detectors: V0s and Cascades.  $K_S^0$ ,  $\Lambda$  and  $\bar{\Lambda}$  are neutrally charged hadrons belonging to the V0s family and they are reconstructed through their weak decays into two oppositely charged particles. The V0 name comes from the V shape of the decay that characterizes the two daughter particles and because of the neutrality of the mother particle.  $\Xi^-$  and  $\Omega^-$  are baryons characterized by two and three strange quarks. Together with their antiparticles ( $\Xi^+$  and  $\bar{\Omega}^+$ ), they constitute the Cascades family because of their typical double-step weak decay that can be seen in Fig. 3.1. Table 3.1 illustrates the main characteristics of the V0s and Cascades under study: mass, decay mode, branching ratio (B.R.) and decay length ( $c\tau$ ) [106].

For instance, a  $\Xi^-$  particle can be followed through its decay. This baryon, after its formation, proceeds in free space for few centimeters. Then, its most probable decay mode is the one analyzed here since the branching ratio is

V0s	Mass MeV/c <sup>2</sup>	Decay	B.R.(%)	cτ (cm)
$K_S^0((d\bar{s} - s\bar{d})/\sqrt{2})$	497.611±0.013	$K_S^0 \rightarrow \pi^- + \pi^+$	69.2	2.684±0.001
$\Lambda(uds)$	1115.683±0.006	$\Lambda \rightarrow p + \pi^-$	63.8	7.89±0.06
$\bar{\Lambda}(\bar{u}\bar{d}s)$	1115.683±0.006	$\bar{\Lambda} \rightarrow \bar{p} + \pi^+$	63.8	7.89±0.06
Cascades	Mass MeV/c <sup>2</sup>	Decay	B.R.(%)	cτ (cm)
$\Xi^-(dss)$	1321.71±0.13	$\Xi^- \rightarrow \Lambda + \pi^-$	99.887	4.91±0.04
$\bar{\Xi}^+(\bar{d}\bar{s}s)$	1321.71±0.13	$\bar{\Xi}^+ \rightarrow \bar{\Lambda} + \pi^+$	99.887	4.91±0.04
$\Omega^-(sss)$	1672.45±0.29	$\Omega^- \rightarrow \Lambda + K^-$	67.8	2.46±0.04
$\bar{\Omega}^+(\bar{s}\bar{s}s)$	1672.45±0.29	$\bar{\Omega}^+ \rightarrow \bar{\Lambda} + K^+$	67.8	2.46±0.04

Table 3.1: Characteristics of V0s and Cascades.

99.887 %: it weakly decays into a  $\Lambda$  and a particle referred to as the bachelor, which, in this case, is a  $\pi^-$ . The distance traveled by the particles depend on its mean lifetime and momentum. The  $\Lambda$  daughter contains only one strange quark while the  $\Xi^-$  has two, but this change in strangeness is allowed since in a weak decay strangeness does not have to be conserved.

Afterwards,  $\Lambda$  also weakly decays with a probability of 63.8 % into two oppositely charged particles, a proton and a  $\pi$ . Similarly the other three cascades follow the same type of decay: for the  $\Omega$  the bachelor particle is a Kaon instead of a  $\pi$ . Also the V0 decay described for  $\Lambda$  is the same as for  $\bar{\Lambda}$  and  $K_S^0$ , except that for the latter the daughter particles are  $\pi^+$  and  $\pi^-$ .

As it was explained in the previous chapter, ITS and TPC are the main detectors used for tracking the particles under study. From Table 3.1 the Cascade decay lengths are too short in order to detect these particles directly. To be more specific, if their momentum is large enough Cascades might be able to hit the innermost layer of the SPD, but this information is not sufficient to reconstruct the particle. Furthermore, V0s are neutral particles which cannot be seen by the charge-sensitive tracking detectors of the ALICE central barrel. This means that only the charged-decay products of the V0s and bachelors can be tracked.

In ALICE a so-called topological reconstruction technique, based on geometrical and kinematic criteria to reconstruct V0s and Cascades, is used. In this section the reconstruction procedure is described for  $\Xi^-$  while the definition for the topological cuts together with their values will be given in the next section.

In order to reconstruct the V0 candidates, all secondary tracks with a positive charge are combined with the corresponding negatively charged tracks.

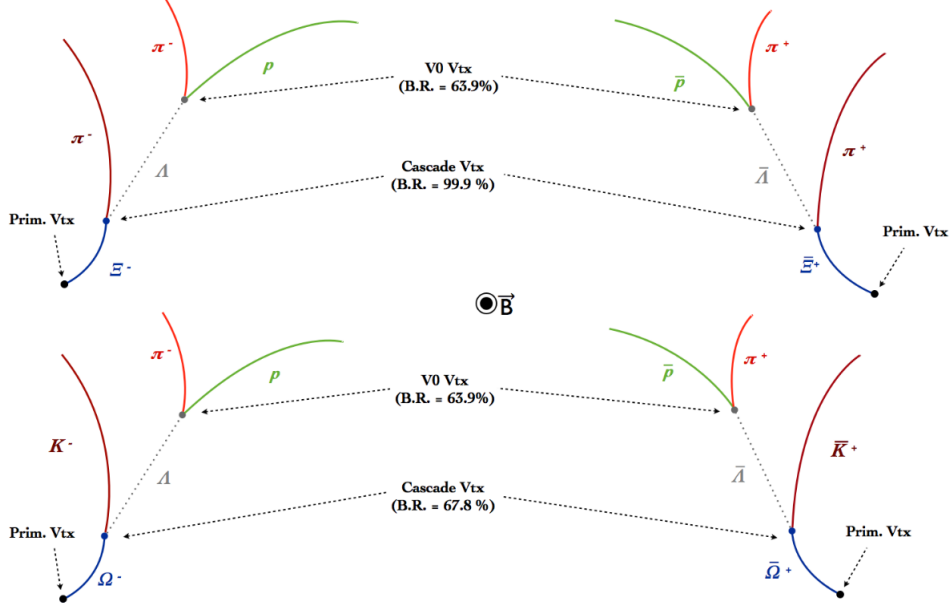


Figure 3.1: Cascade decay topologies, where **Prim.Vtx** represents the primary vertex position and  $\vec{B}$  denotes the magnetic field.

Then, a cut on the minimum value of the impact parameter for both tracks is required and a maximum cut is applied on the distance of closest approach (DCA) between the two to ensure that there are secondary particles as well as to identify the position of the V0 vertex. A selection on V0 vertexes is applied: only those inside a fiducial radius cut are accepted. Then, an inspection of the cosine of the pointing angle between a vector that connects the V0 vertex to the Cascade vertex and the V0 momentum vector is performed in order to ensure that the V0 candidate originates from a Cascade decay. Moreover, the invariant mass of the V0 particle is measured by calculating the squared-mass of the particle. In this case, it is considered the hypothesis that the V0 particle is a  $\Lambda$  particle. Theoretically, the  $\Lambda$  squared-mass is defined as:

$$M_{theor}^2(\Lambda) = (E_{\pi^-} + E_p)^2 - (\vec{p}_{\pi^-} + \vec{p}_p)^2, \quad (3.1)$$

where  $E$  is the energy and  $\vec{p}$  the momentum of the particle. Experimentally, the energy of the two daughters is not detected directly so that the equation becomes:

$$M_{exp}^2(\Lambda) = \left( \sqrt{m_{\pi^-}^2 + \vec{p}_{\pi^-}^2} + \sqrt{m_p^2 + \vec{p}_p^2} \right)^2 - (\vec{p}_{\pi^-} + \vec{p}_p)^2, \quad (3.2)$$

where  $m$  is the mass of the particle formulating the hypothesis in this case that the V0 daughters are a  $\pi^-$  and a  $p$ . The values of  $m$  used here are the nominal PDG masses [107]. The invariant mass distribution peaks around the nominal value of the  $\Lambda$  mass and has a width because of the limited resolution of the detector also because of the physics itself since the width of the distribution is inversely proportional to the life-time of the particle (ALICE is not sensitive enough to detect this contribution). A selection window on the  $\Lambda$  invariant mass is applied.

After the  $\Lambda$  reconstruction, all V0s are associated to all possible bachelor tracks. Then, cuts are applied to obtain the cascade candidate, as it was done for the V0s: the bachelor track impact parameter needs to be larger than a certain value to exclude that it is a primary particle. Hence, the DCA between the bachelor track and the line connecting the V0 and the  $\Xi^-$  vertex must be smaller than a certain value. Similarly, a selection on the cosine of the pointing angle of the cascade is applied to ensure that the candidate points back to the primary vertex. Further requirements on the selection are described in details in the next section together with all the variable cut values. After the three tracks pass all the selection cuts, it is possible to identify the  $\Xi^-$  through the invariant mass computation as it was for  $\Lambda$ :

$$M^2(\Xi^-) = \left( \sqrt{m_{\Lambda}^2 + \vec{p}_{\Lambda}^2} + \sqrt{m_{bach}^2 + \vec{p}_{bach}^2} \right)^2 - (\vec{p}_{\Lambda} + \vec{p}_{\pi^-})^2, \quad (3.3)$$

with  $\vec{p}_{\Lambda} = \vec{p}_p + \vec{p}_{\pi^-}$ . In this case the bachelor particle (*bach*) is  $\pi^-$ . The  $m$  values used here are the nominal PDG masses [107].

### Particle identification with the TPC

The particle identification (PID) can be obtained through the topology reconstruction just described, or through direct identification which in ALICE can be obtained with several detectors with different techniques. For this analysis, the TPC provides direct PID through the energy loss technique. Charged particles cross the TPC and ionize the gas losing energy. The energy loss per unit length ( $dE/dx$ ) needs to be measured: it is defined by the Bethe-Bloch Equation 3.4.  $dE/dx$  is calculated only from the velocity ( $\beta$ )

and the charge of the particle. Since the charge is usually unitary and  $\beta$  is related to the momentum which is calculated from the curvature of the track, the particle can be identified evaluating the mass from  $dE/dx$ . The Bethe-Bloch equation is:

$$-\left\langle \frac{dE}{dx} \right\rangle = k_1 \cdot z^2 \cdot \frac{Z}{A} \cdot \frac{1}{\beta^2} \left[ \frac{1}{2} \ln(k_2) \cdot m_e c^2 \cdot \beta^2 \gamma^2 \right] - \beta^2 + k_3 \quad (3.4)$$

where:

- $k_1, k_2$  and  $k_3$  are constants that depend on the gas ionized;
- $m_e$  is the mass of the electron;
- $z$  is the electric charge of the particle that ionizes the gas;
- $Z$  and  $A$  are the atomic and the mass number of the ionized gas, respectively;
- $\beta$  is the velocity divided by  $c$  of the particle that ionizes the gas. The velocity is  $\beta\gamma = p/Mc$  where  $p$  is the momentum and  $M$  is the mass of the particle that ionizes the gas;
- $\gamma = 1/\sqrt{1 - \beta^2}$  is the Lorentz factor.

Usually  $e^\pm, \mu^\pm, K^\pm, \pi^\pm$  and  $p(\bar{p})$  mass hypotheses are taken into account and they correspond to the particles that may live long enough to be detected by the TPC. They are also the main daughter particles for all kind of decays, so having this additional PID information from the TPC, helps to reduce the background. Figure 3.2 shows the energy loss  $dE/dx$  as a function of the momentum  $p$  for  $e^\pm, K^\pm, \pi^\pm$  and  $p$  for the TPC. The black lines represent the Bethe-Bloch prediction while the bands represent the statistical measured energy loss distributions around the predictions. Then, the difference between the  $dE/dx$  measured and the expected value is calculated for a certain track. This variable can be normalized by the TPC resolution on the measurement of  $dE/dx$ :

$$n_\sigma = \frac{[(dE/dx)_{measured} - (dE/dx)_{BB}]}{\sigma_{TPC}} \quad (3.5)$$

and it defines the number of  $\sigma_{TPC}$  ( $n_\sigma$ ) which can be chosen according to the strictness of the analysis. The resolution for the TPC is  $\sigma_{TPC} \sim 5\%$  for tracks with 159 clusters [113].

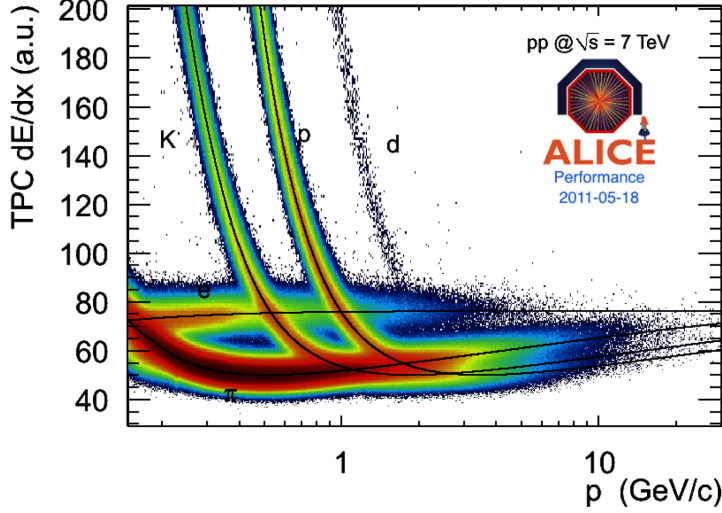


Figure 3.2:  $dE/dx$  as a function of the momentum  $p$  for  $e^\pm$ ,  $K^\pm$ ,  $\pi^\pm$  and  $p$  for TPC. The Figure is not yet available in pp collisions at  $\sqrt{s} = 5.02$  TeV so it is shown in pp collisions at  $\sqrt{s} = 7$  TeV [54].

### 3.1.1 Event Selection Criteria

Through the event selection, hadronic interactions are selected by reducing as much as possible the physical and machine-induced background but maintaining the highest possible efficiency. In this analysis basic event selection criteria were applied, following the ALICE convention for pp analysis:

- The events were selected based on the minimum-bias trigger asking at least one hit in the V0A or V0C or in the SPD detectors, in coincidence with two beam bunches crossing the IP region;
- Vertex z-position: only events with a primary vertex that lied within  $|z| < 10$  cm around the interaction point were selected for the analysis, where  $z$  is measured along the beam direction.

The results presented here, were measured for events with at least one charged particle generated in the pseudorapidity interval  $|\eta| < 1$  with  $p_T > 0$  (INEL>0), corresponding to about 75% of the total inelastic cross-section.

### 3.1.2 Charged-particle multiplicity Selection Criteria

From now on the author will refer to charged-particle multiplicity also as multiplicity.

The V0A and V0C detectors (together defined as V0M) are used to estimate the event multiplicity. The sum of V0A and V0C amplitudes are linearly proportional to the number of charged particles in pseudorapidity regions  $2.8 < \eta < 5.1$  and  $-3.7 < \eta < -1.7$ , respectively. The V0M amplitude distribution is divided into percentiles to define multiplicity classes. Figure 3.3 shows V0M amplitude classes for Minimum Bias and High-Multiplicity triggers in pp collision at  $\sqrt{s} = 13$  TeV [54]. The High-Multiplicity (HM) trigger is not relevant because HM triggers were not available for the data sample used in this analysis.

The actual multiplicity V0M percentile classes used for this analysis were

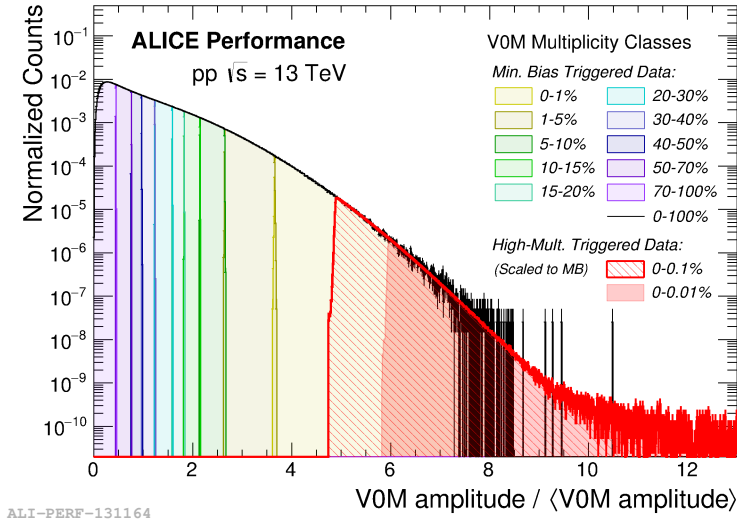


Figure 3.3: V0M amplitude classes at Minimum Bias and High-Multiplicity triggers in pp collision at  $\sqrt{s} = 13$  TeV. The Figure was not available in pp collisions at  $\sqrt{s} = 5.02$  TeV so it is shown in pp collisions at  $\sqrt{s} = 13$  TeV [54].

selected according to the available statistics. They are listed from high(i.e. [0 – 0.01]) to low(i.e. [70 – 100]) multiplicity:

- **V0 Analysis:** [0-0.01],[0.01-0.1],[0.1-1],[1-5],[5-10],[10-20],[20-30],[30-40],[40-50],[50-70],[70-100];
- **$\Xi$  Analysis:** [0-0.1],[0.1-1],[1-5],[5-10],[10-15],[15-20],[20-30],[30-40],[40-50],[50-70],[70-100];
- **$\Omega$  Analysis:** [0-1],[1-5],[5-10],[10-15],[15-30],[30-50],[50-70],[70-100];



Moreover, Table 3.2 reports the average number of charged particle  $\langle dN_{ch}/d\eta \rangle$  in the pseudorapidity interval  $|\eta| < 0.5$  (right column) for the different V0M event multiplicity percentile classes (central column). The left column represents the classification chosen for the multiplicity percentile intervals.

Class	Mult(%)	$\langle dN_{ch}/d\eta \rangle_{ \eta  < 0.5}$
I-A1	0.0-0.01	24.43 +0.72-0.69
I-A2	0.01-0.1	21.64 +0.38 -0.33
I-B	0.1-1	18.07+0.26 -0.22
II	1-5	14.47 +0.20-0.16
III	5-10	11.92 +0.16 -0.13
IV	10-15	10.29 +0.14 -0.11
V	15-20	9.11 +0.13 -0.10
VI	20-30	7.76 +0.13 -0.10
VII	30-40	6.34+0.09 -0.07
VIII	40-50	5.22+0.09 -0.07
IX	50-70	3.94+0.06 -0.05
X	70-100	2.43+0.04 -0.03
INEL>0	0-100	5.49 +0.08 -0.06

Table 3.2: The list of event multiplicity classes, percentile intervals and corresponding number of charged particles in  $|\eta| < 0.5$  at  $\sqrt{s} = 5.02$  TeV.

In other analyses like [118], events were not classified as in this work but using a direct counting of charged particles at central rapidity. The reason why a forward/backward multiplicity selection was used in this work, is because it was found [117] that if the selection in multiplicity is performed in the same pseudorapidity interval, where the signal under study is extracted, it might create a bias. Figure 3.4 shows an example in PYTHIA 8 simulations for Kaons [117] particularly how this phenomenon can affect the hadrochemistry of charged vs neutral particles. The left panel presents the case where multiplicity selection was estimated at mid-rapidity: charged kaon yields were higher than the neutral kaon ones at high multiplicity. On the contrary, if the multiplicity selection was not performed in the same pseudorapidity interval of the production rate measurements then  $K^\pm$  and  $K_S^0$  presented similar yields as a function of number of charged particle, as it is expected, since they have a comparable mass.

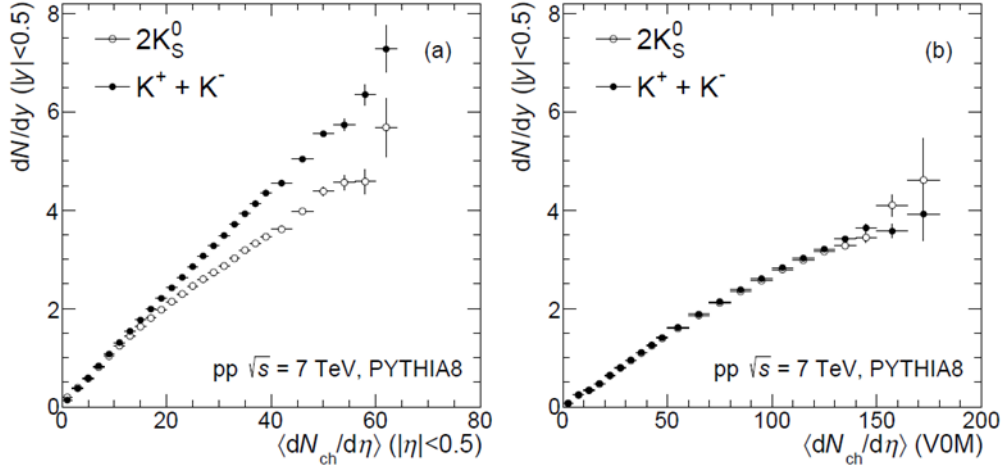


Figure 3.4: The left panel shows  $K^\pm$  and  $K_S^0$  as a function of multiplicity selected at mid-rapidity in PYTHIA 8 simulations of pp collisions at  $\sqrt{s} = 7 \text{ TeV}$ . The right panel shows  $K^\pm$  and  $K_0^S$  as a function of multiplicity selected at forward/backward pseudorapidity in PYTHIA 8 simulations of pp collisions at  $\sqrt{s} = 7 \text{ TeV}$  [117].

### 3.1.3 Analysis Framework

AliRoot [115] is the offline framework of ALICE. It was developed in C++ and it depends on ROOT [112] framework, which provides the setting for the production of the software package for detector simulation, event generator, reconstruction of events and data acquisition and analysis. In particular, thanks to the AliRoot framework, the physics data were reconstructed through a reconstruction chain which started from raw-data or from digits and ended with the creation of the track candidates. The final output was a root file called Event Summary Data (ESD) where the relevant physics information for the analysis was stored. Then, the ESDs were processed through a train of “analysis tasks” to obtain a root file containing only the information needed for this specific analysis. The following analysis tasks were employed to process specifically the strangeness analysis:

- **TaskStrangenessVsMultiplicityRun2.h(cxx)**
- **TaskStrangenessVsMultiplicityMCRun2.h(cxx)**

the first one on physics data while the second one on Monte Carlo simulations. Finally, the root files downloaded from the Grid were post processed with C++ custom programs to obtain the signals, the acceptance times efficiency (see the following sections).

### 3.1.4 Data and Monte Carlo (MC) samples

The analysis presented here used a pp data sample collected during 2017 and referred internally as period LHC17p (pass 1 reconstruction). For this data sample two data acquisition strategies were applied defined as CENT and FAST: for the first strategy the SDD was used in the reconstruction process, while for the second the SDD was excluded. The SDD is the slowest detector in the readout but it helps to improve the vertexing, especially the z-vertex coordinate determination. When this detector is included, the statistics is reduced by one half. In total 41 runs were selected for each data strategy, which means the runs passed the quality assurance, hence designated as “good runs” for the central barrel by the ALICE offline quality assurance and data preparation groups. The number of events analyzed was around 1.1 billion. The run numbers of the data sample for *LHC17p\_pass1\_CENT\_wSDD* and *LHC17p\_pass1\_FAST* are listed below.

- Runlist: 282343, 282342, 282341, 282340, 282314, 282313, 282312, 282309, 282307, 282306, 282305, 282304, 282303, 282303, 282247, 282230, 282229, 282227, 282224, 282206, 282189, 282147, 282146, 282127, 282126, 282125, 282123, 282122, 282120, 282119, 282118, 282099, 282098, 282078, 282051, 282050, 282031, 282025, 282021, 282016, 282008;

Since the acceptance times efficiency corrections cannot be estimated with data, the analysis needs to be repeated on Monte Carlo simulated data in order to calculate these corrections. Three productions of Monte Carlo events were used and they are described below:

- **LHC1713b**: minimum bias Monte Carlo produced using GEANT 3 transport code [108] and PYTHIA 8 generator [109]. It is a general purpose production and associated to the data production LHC17p. The full statistics available was about 290 million generated events while the number of events after event selection was about 196 million. The abbreviation to refer to this Monte Carlo is MC General Purpose.
- **LHC19\_e1strinj**: minimum bias Monte Carlo produced using GEANT 3 transport code [108] and PYTHIA 8 generator [109]. It was a general purpose production and associated to the data production LHC17p. For this second MC production, it was required that at least one  $\Xi^-$  or  $\bar{\Xi}^+$  and two  $\Omega^-$  or  $\bar{\Omega}^+$  per event were injected with a flat  $p_T$  distribution. The full statistics available was about 206 million generated events while the number of events after event selection was about 14 million. The abbreviation to refer to this Monte Carlo is MC Injection.

- **LHC17l4\_lastG4fix**: minimum bias Monte Carlo produced using GEANT 4 transport code [110] and PYTHIA 8 generator [109]. It is a general purpose production and associated to the data production LHC17p. The full statistics available was about 288 million generated events while after event selection was 197 million. The abbreviation to refer to this Monte Carlo is MC GEANT 4.

The final acceptance times efficiency corrections were evaluated from the MC Injection for Cascades because the statistics available was larger than for the other MCs. For  $K_S^0$ , the final acceptance times efficiency corrections were calculated from the MC General Purpose, while for  $\Lambda(\bar{\Lambda})$  from the MC GEANT 4. More details about these MC choices are given in Sec. 3.2.7.

MC type	Used for:	Final statistics
MC General Purpose	$K_S^0$	197 million
MC GEANT 4	$(\Lambda)\bar{\Lambda}$	197 million
MC Injection	Cascades	14 million

Table 3.3: The list of assigned MC samples used in this analysis together with their statistics.

In the next sections the analysis will be described in detail. The main steps for the analysis strategy are summarized in the following flow chart:

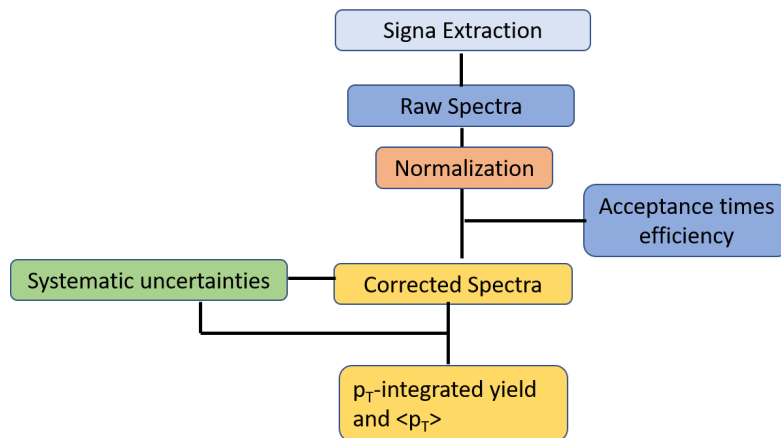


Figure 3.5: Major steps for the analysis strategy.

## 3.2 Analysis Details

The present analysis follows the same strategy used in previous pp analyses at  $\sqrt{s} = 7$  TeV [55] and  $\sqrt{s} = 13$  TeV [56]. The selection on cuts described below and shown in Table 3.4 was applied to the data and MC samples:

**Kinematic selection:** strange particles were reconstructed in the rapidity interval  $|y| < 0.5$ , while the pseudorapidity of the daughter tracks has to be within  $|\eta| < 0.8$ .

**Topological selection:** geometrical requirements were necessary to ensure that the tracks were confined in space according to the decay topology of the particle of interest.

- **Maximum DCA V0 Daughters:** It was required that the distance of closest approach between the two particle tracks associated with a V0 was smaller than a certain number of standard deviation of the resolution in order to guarantee that they originated from the decay of a  $K_S^0$  or a  $\Lambda$ .
- **Minimum DCA Negative/Positive to Primary Vertex (PV):** this variable is the distance of closest approach between tracks of the V0 daughters and the PV. It was used to avoid that tracks arising from the PV were mistaken as V0 daughters.
- **Minimum/Maximum V0 decay radius:** the background coming from randomly pairing of primary tracks could be minimized by applying a minimum cut on the V0 decay radius.
- **Minimum/Maximum Cascade decay radius:** the background coming from randomly pairing of primary tracks could be minimized by applying a minimum cut on the Cascade decay radius.
- **Maximum V0 pointing angle:** this is the angle between the decay path of the V0 (that connects the PV and the V0 decay point) and the reconstructed V0 momentum. A cut on this variable was necessary to ensure that V0s originated exactly from the PV.
- **Maximum Cascade pointing angle:** this is the angle between the decay path of the Cascade (that connects the PV, the Cascade decay point) and the reconstructed Cascade momentum. A cut on this variable was necessary to ensure that Cascades came exactly from the PV.
- **Maximum DCA cascade daughters:** this is the distance of closest approach (DCA) between the reconstructed V0 decay vertex and the

bachelor track. This cut required that the bachelor track and the  $\Lambda$  originated from the Cascade decay vertex.

- **Minimum DCA bachelor to PV:** this is the distance of closest approach between the PV and the bachelor track. This was used to discard primary tracks.
- **Minimum DCA V0 to PV:** this is the distance of closest approach between the reconstructed  $\Lambda$  trajectory and the PV.

**Proper Lifetime:** a cut on the proper lifetime of the cascade candidates, had to be applied to minimize the reconstruction of secondary V0s. The proper lifetime was calculated via  $mL/p$ , where  $m$  is the expected Cascade mass under the current hypothesis,  $L$  is the linear (3D) distance between the primary vertex and the Cascade decay vertex, and  $p$  is the total momentum of the candidate.

**Energy loss ( $dE/dx$ ) selection:** as explained in Sec. 3.1, PID was also performed by the TPC requiring  $4 n_\sigma$  on the daughter tracks to reduce their background.

**Daughter track quality selections:** it was applied to select only high-quality track candidates.

- the track was required to have at least 70 clusters in the TPC, in order to guarantee a good  $p_T$  resolution and a stable particle identification using the  $dE/dx$  in the TPC;
- V0 Daughter tracks were expected to have a number of crossed rows (which corresponds to the number of clusters reconstructed) divided by the number of findable clusters (which corresponds to the number of clusters that should have been reconstructed) of at least 0.8 [114]. This cut helped to exclude particle tracks which crossed the dead zones of the TPC.

**Primary selection and PDG association:** for the simulated data, it was required that the daughter and mother candidates belong to the correct species, i.e. to associate the right PDG code to the track of interest. In addition, only physical and primary candidates were accepted which means that only true V0s and Cascades were accepted and they are rejected if they came from a decay.

**Competing decay for  $\Omega$ :** the same decay topology characterizes both the  $\Xi$  and  $\Omega$  which means that a  $\Xi$  can be reconstructed as an  $\Omega$ . Since the production rate of  $\Omega$  was however 10 times smaller than the  $\Xi$ , this mismatch needed to be taken into account for  $\Omega$ . To avoid any fake contribution, the

$\Omega$  invariant mass was reconstructed within the  $\Xi$  hypothesis (considering the  $\pi$  mass for the bachelor) while a rejection window of  $8 \text{ MeV}/c^2$  around the PDG  $\Xi$  mass was applied.

**V0 mass window:** it was required that the difference between the V0 invariant mass and the PDG mass was smaller than a certain value. This was applied for V0 identification within the cascade reconstruction.

In Tables 3.4 and 3.5 the selection cuts are listed. These cuts were tuned not only to reduce the backgrounds but also not to compromise the signal.

<b>Topological Variable</b>	$K_S^0 (\Lambda)$
V0 transv. decay radius $R_2D$	$>0.5 \text{ cm}$
DCA Negative track to PV	$>0.06 \text{ cm}$
DCA Positive track to PV	$>0.06 \text{ cm}$
DCA V0 Daughters	$< 1.0 \sigma$
V0 cosine of Pointing Angle	$> 0.97(0.995)$
<b>Selection</b>	$K_S^0 (\Lambda)$
Rapidity Interval	$ y  < 0.5$
TPC $dE/dx$ selection	$< 4 \sigma$
Proper Lifetime ( $mL/p$ )	$<20 (30) \text{ cm}$
Daughter track Pseudorapidity Interval	$ \eta  < 0.8$
Daughter track $N_{crossed}/N_{findable}$	$\geq 0.8$
Daughter track $N_{crossedrows}$	70
ITS refit flag + TOF	kTRUE
Primary Selection (MC only)	AliStack::IsPhysicalPrimary()
MC association (MC only)	PDG code associated to Cascade

Table 3.4: The list of selection cuts applied in the V0 analysis.

### 3.2.1 Additional cuts

In this analysis there were other additional cuts.

**ITSRefit flag and TOF:** it was required that at least one daughter track had a hit in the TOF detector or that the track was reconstructed by both the ITS and TPC detectors. This requirement reduced the out-of-bunch pile-up effects. The out-of-bunch pile-up phenomenon occurs when additional pp collisions happen in bunch-crossings just before or after the collision of interest. More details are given in Sec. 3.2.6.

**DCA Bachelor to Baryon:** this topological cut was applied in the extraction of  $\Xi^-$  and  $\Xi^+$ . It was previously used in the p-Pb[57] and Pb-

Topological Variable	$\Xi$ ( $\Omega$ ) Cut
Cascade transv. decay radius $R_2D$	$>0.6(0.5)$ cm
V0 transv. decay radius $R_2D$	$>1.2(1.1)$ cm
DCA Negative track to PV	$>0.12(0.13)$ cm
DCA Positive track to PV	$>0.12(0.13)$ cm
DCA V0 Daughters	$< 1.3\sigma$
DCA Bachelor to PV	$>0.04$ cm
DCA V0 to PV	$>0.06$ cm
DCA Bachelor to V0	$>1.3$ cm
DCA Bachelor to Baryon (only $\Xi$ )	$>0.02$ cm
V0 cosine of Pointing Angle	$>0.97$
Cascade cosine of Pointing Angle	$> 0.97$
V0 invariant mass window	$0.008$ GeV/ $c^2$
Selection	$\Xi$ ( $\Omega$ ) Cut
Rapidity Interval	$ y  < 0.5$
TPC $dE/dx$ selection	$< 4 \sigma$
Proper Lifetime ( $mL/p$ )	$< 3 * 4.91(3 * 2.46)$ cm
Daughter track Pseudorapidity Interval	$ \eta  < 0.8$
Daughter track $N_{crossedrows}$	70
Competing Cascade Rejection (only $\Omega$ )	$ M(\Xi) - 1.321  > 8$ MeV/ $c^2$
ITS refit flag + TOF	kTRUE
Primary Selection (MC only)	AliStack::IsPhysicalPrimary()
MC association (MC only)	PDG code associated to Cascade

Table 3.5: The list of selection cuts applied in the Cascade analysis.

Pb[119] analyses in order to reduce the structure shown on the left-hand side of the invariant mass signal peak which complicates the background fit. This artifact results when the (truly)bachelor track is assigned as the  $\Lambda$  daughter. This can happen when the DCA value between the bachelor and baryon- $\Lambda$ -daughter (called from now on DCA Bachelor to Baryon) and/or when the decay length of the  $\Lambda$  are too small. These events could be discarded by applying a cut on the DCA Bachelor to Baryon.

This structure was also present in the invariant masses of  $\Xi^-$  and  $\Xi^+$  in this analysis in all  $p_{\mathbf{T}}$  bins (black histograms). The invariant mass histograms in Figure 3.6 refer to a low  $p_{\mathbf{T}}$  bin for  $\Xi^-$  and  $\Xi^+$ : the red ones show that it was possible to partially minimize this effect by applying a cut on the DCA Bachelor to Baryon. The cut was tuned to reduce this background structure



as much as possible without losing too much statistics on the signal peak (for instance in the two bins showed in Fig. 3.6 the structure was reduced of around 20% while the signal peak of  $\sim 10\%$ ).

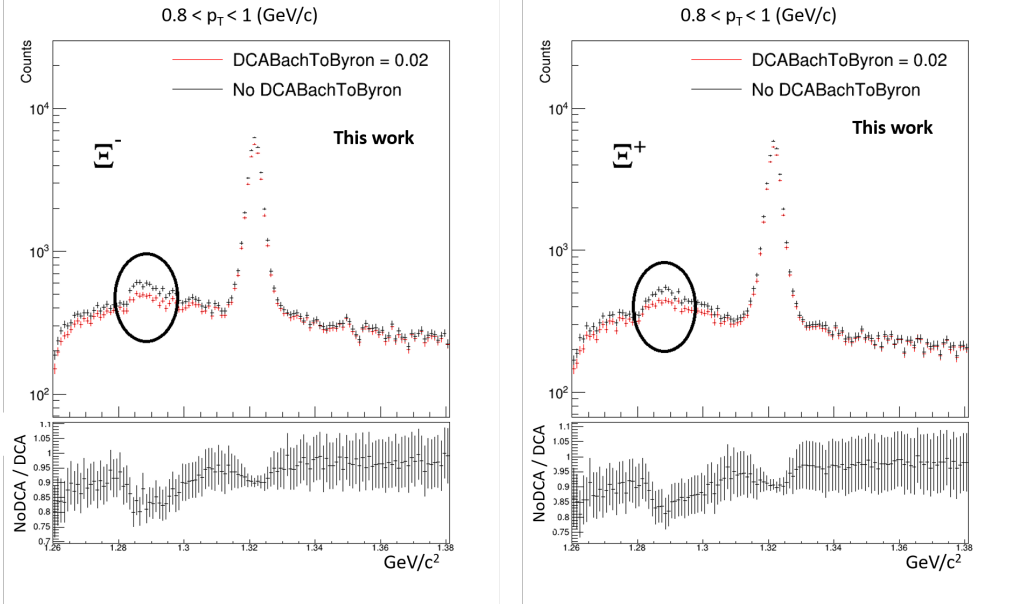


Figure 3.6: Examples of invariant Mass Spectra for  $\Xi^-$  (left figure) and  $\Xi^+$  (right figure) with and without the application of DCA Bachelor to Baryon cut. At the bottom, the ratios of the invariant mass spectra without the cut over the invariant mass spectra with the cut are shown. The vertical bars represent the statistical errors. The black circles highlight the structure.

### 3.2.2 Signal extraction

The signal extraction procedure is very similar to the one used in previous pp analyses at  $\sqrt{s} = 7$  [55] and  $\sqrt{s} = 13$  TeV [56].

After the selection cuts, candidates were divided according to  $p_T$  (GeV/c) and multiplicity intervals (see Sec. 3.1.2). The chosen  $p_T$  binning for V0s and Cascades are listed below:

- $K_S^0$  (GeV/c): {0.0,0.2,0.4,0.5,0.6,0.7,0.8,0.9,1.0,1.2,1.4,1.6,1.8,2.0,2.3, 2.6,2.9,3.2,3.4,3.7,4.0,4.5,5.5,6.5};
- $\Lambda$  ( $\bar{\Lambda}$ ) (GeV/c): {0.5,0.6,0.7,0.8,0.9,1.0,1.2,1.4,1.6,1.8,2.0,2.3,2.6,2.9, 3.2,3.4,3.7,4.0,4.5,5.5,6.5};
- $\Xi^-$  ( $\bar{\Xi}^+$ ) (GeV/c): {0.6,1.0,1.2,1.4,1.6,1.8,2.0,2.2,2.5,2.9,3.4,4.0,5.0,6.5};

- $\Omega^- (\bar{\Omega}^+)$  ( $\text{GeV}/c$ ):  $\{0.9, 1.6, 2.2, 2.6, 3.0, 3.8, 5.5\}$ ;

The binning was different for every particle according to the statistic available. For every  $p_{\mathbf{T}}$  bin and every multiplicity bin, the invariant mass distribution was produced.

Firstly, these invariant mass histograms were fitted with a second order polynomial function in background regions excluding the invariant mass window where the peak was present. This was done in order to perform a better estimation of the background shape.

Secondly, the full histogram was fitted with a combination of two functions: the peak was fitted with a Gaussian and the background with a second order polynomial. The parameters obtained in the first background fit were applied as initial parameters for the second fit.

Finally, the signal was extracted following the bin counting ( $BC$ ) procedure:

- the second fit of the spectra (convolution of Gaussian function for the peak and a second order polynomial for the background) provided the width ( $\sigma$ ) and mean ( $\mu$ ) of the peak;
- the invariant mass peak was integrated over the  $[\mu - 5\sigma, \mu + 5\sigma]$  window,  $(S + B)_{BC}$ ;
- the integrated fit of the background function  $B_{fit}$  in the  $[\mu - 5\sigma, \mu + 5\sigma]$  region was subtracted from the integrated of the peak to obtain the signal;

So in formula, the raw yield  $S_{raw}$  in each  $p_{\mathbf{T}}$  and multiplicity bin was calculated as follow:

$$S_{raw} = (S + B)_{BC} - B_{fit} \quad (3.6)$$

and the statistical uncertainty on  $S_{raw}$  was calculated by applying the standard propagation law, which in this case is:

$$\sigma_{S_{raw}} = \sqrt{\sigma_{(S+B)_{BC}}^2 + \sigma_{B_{fit}}^2} \quad (3.7)$$

In every figure produced in this work, the statistical uncertainties are always indicated with vertical bars and calculated following the standard uncertainty propagation (unless specified differently).

Figures 3.7-3.10 show examples of invariant mass spectra for  $K_S^0$ ,  $\Lambda$ ,  $\Xi^-$  and  $\Omega^-$  invariant mass spectra in different multiplicity and  $p_{\mathbf{T}}$  bins and together with the sum of the fitted peak and background together (red function). The compatibility between CENT and FAST data strategies (see Section 3.1.4) was checked so the all results shown were obtained by merging

them. The histograms for all  $p_T$  bins and for integrated multiplicity are reported in Appendix A.

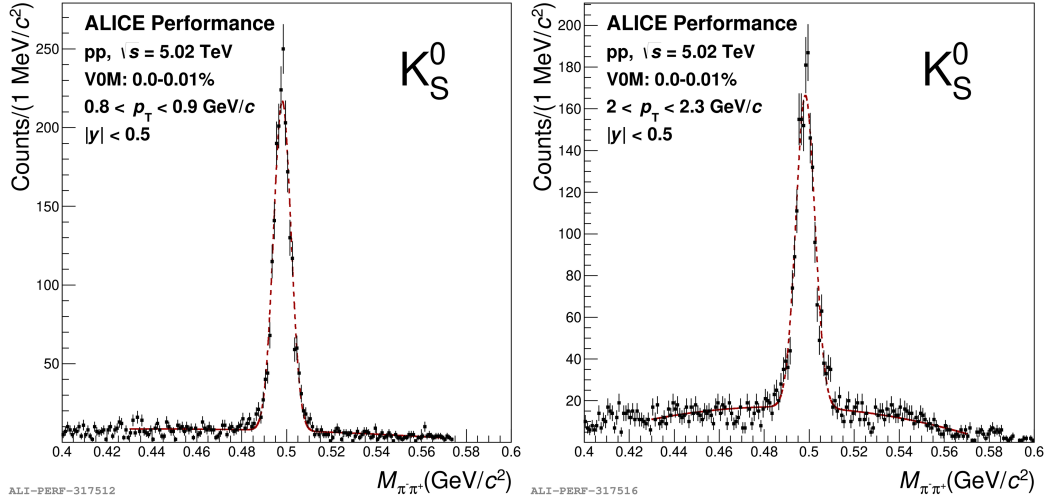


Figure 3.7:  $K_S^0$  invariant mass spectra in the multiplicity bin 0.0-0.01% in two  $p_T$  bins. The red function is the peak plus background function.

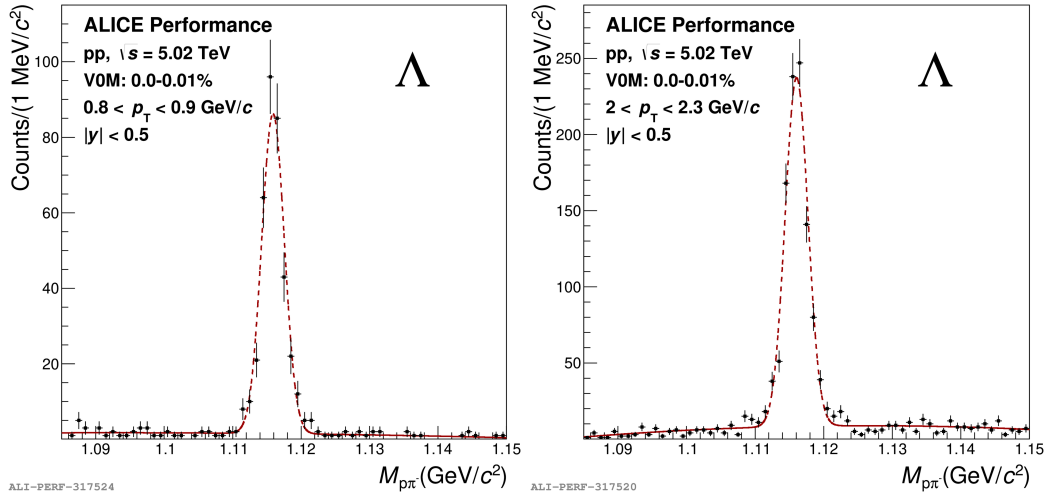


Figure 3.8:  $\Lambda$  invariant mass spectra in the multiplicity bin 0.0-0.01% in two  $p_T$  bins. The red function is the peak plus background function.

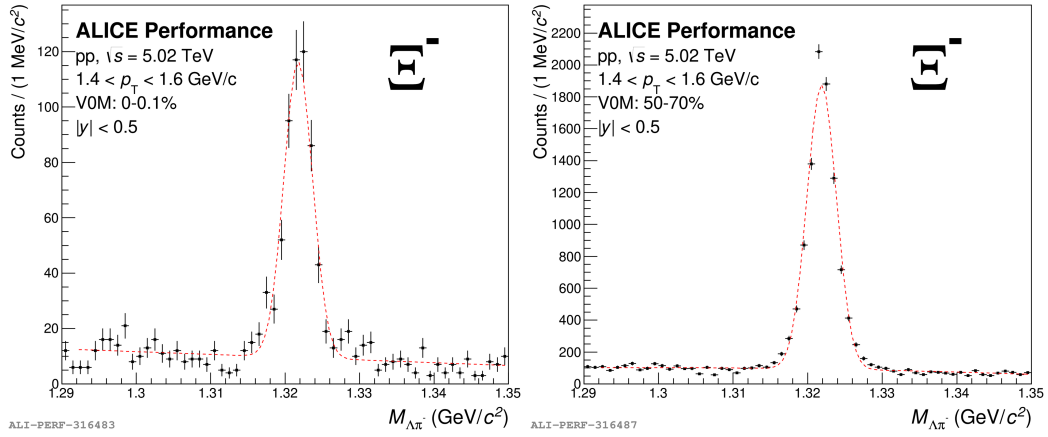


Figure 3.9:  $\Xi^-$  invariant mass spectra in two multiplicity bins in  $1.4 < p_{\mathbf{T}} < 1.6$  GeV/ $c$ . The red function is the peak plus background function.

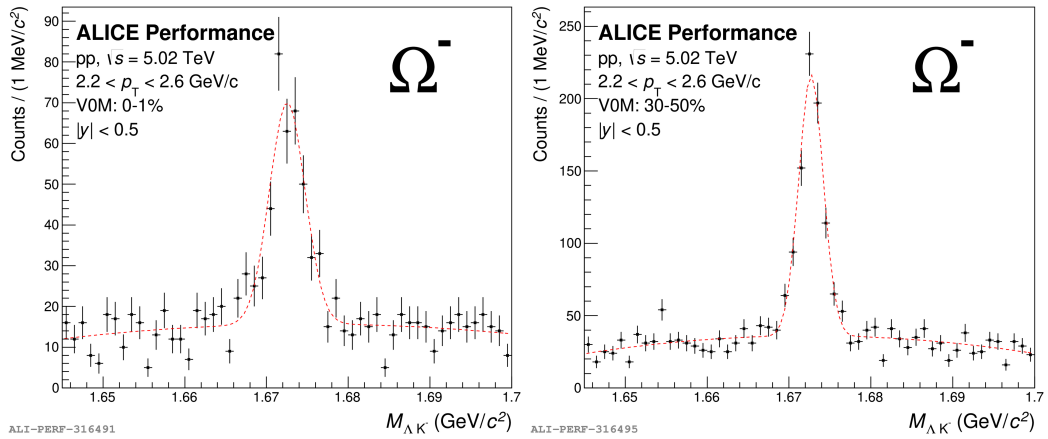


Figure 3.10:  $\Omega^-$  invariant mass spectra in two multiplicity bins in  $2.2 < p_{\mathbf{T}} < 2.6$  GeV/ $c$ . The red function is the peak plus background function.

### 3.2.3 Raw Spectra

After signal extraction, the raw transverse momentum spectra were obtained normalizing the extracted signal by the number of inelastic events  $INEL>0$  and the  $p_T$  bin width. Figures 3.11-3.14 show the raw spectra for V0s and Cascades in multiplicity classes and for integrated multiplicity.

The  $\Lambda$  and  $\bar{\Lambda}$  raw spectra were obtained after applying the  $\Lambda$  feed-down correction (see Sec. 3.2.5). Multiplicative factors indicated in the legend were used to better display the spectra. Due to the lack of statistics, some bins at high multiplicity and low/high  $p_T$  were discarded.

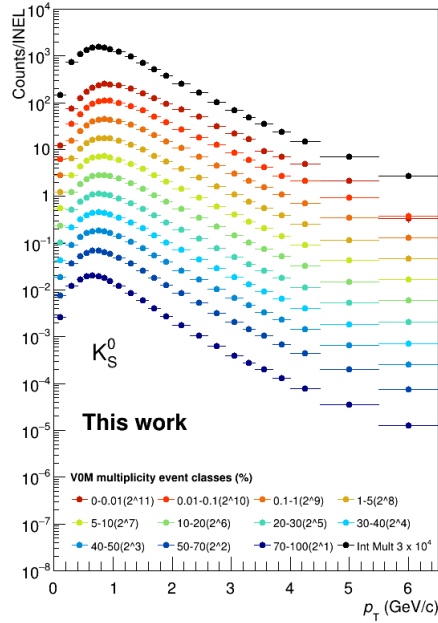


Figure 3.11:  $K_S^0$  raw spectra as a function of  $p_T$  in multiplicity classes and integrated multiplicity.

### 3.2.4 Normalization correction

The raw spectra needed further corrections described in the equation that follows:

$$\frac{1}{N_{events}^{true INEL>0}} \frac{dN_{part}^{true INEL>0}}{p_T} = \frac{1}{N_{events}^{accepted INEL>0}} \frac{dN_{part}^{accepted INEL>0}}{p_T} \frac{\epsilon_{event}}{\epsilon_{part}(p_T)} \quad (3.8)$$

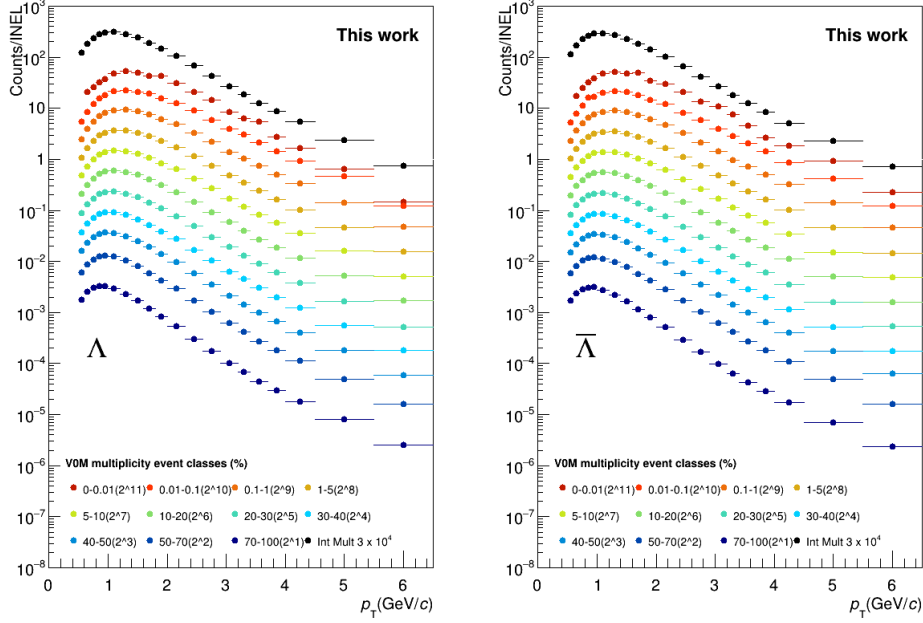


Figure 3.12:  $\Lambda$  and  $\bar{\Lambda}$  raw spectra as a function of  $p_T$  in multiplicity classes and integrated multiplicity.

The factors  $\epsilon_{event}$  and  $\epsilon_{part}(p_T)$  were obtained from Monte Carlo simulations and they depend on the multiplicity. The factor  $\epsilon_{event}$  is defined as:

$$\epsilon_{event} = \frac{N_{events}^{accepted \ INEL > 0}}{N_{events}^{true \ INEL > 0}} \quad (3.9)$$

This factor represents the event correction and it is the ratio between the number of events selected after applying all the cuts ( $N_{events}^{accepted}$ ) and the number of events with a “true” production vertex located within  $|Z_{vtx}^{true}| < 10$  cm and at least one charged primary particle produced in  $|\eta| < 1$  ( $N_{events}^{true}$ ). This factor is not particle dependent and it is taken from [111].

The correction factor  $\epsilon_{part}(p_T)$ , described by Eq 1.6, is particle dependent and takes into account the signal-loss fraction due to the event selection:

$$\epsilon_{part}(p_T) = \frac{\frac{dN_{part}^{Gen}}{p_T}(accepted \ INEL > 0)}{\frac{dN_{part}^{Gen}}{p_T}(true \ INEL > 0)} \quad (3.10)$$

It represents the ratio between the particle spectra at generated level after applying the event selection on the data and the generated particle spectra

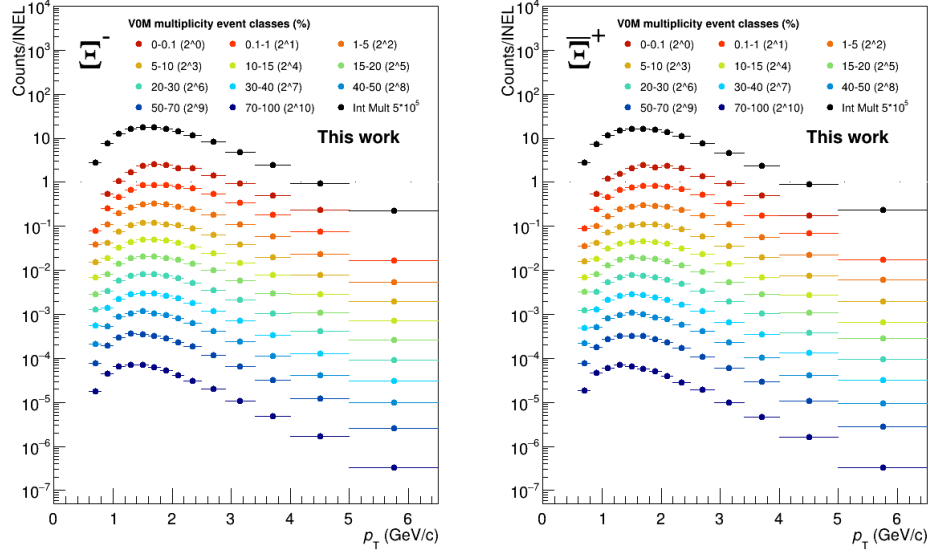


Figure 3.13:  $\Xi^-$  and  $\Xi^+$  raw spectra as a function of  $p_T$  in multiplicity classes and integrated multiplicity.

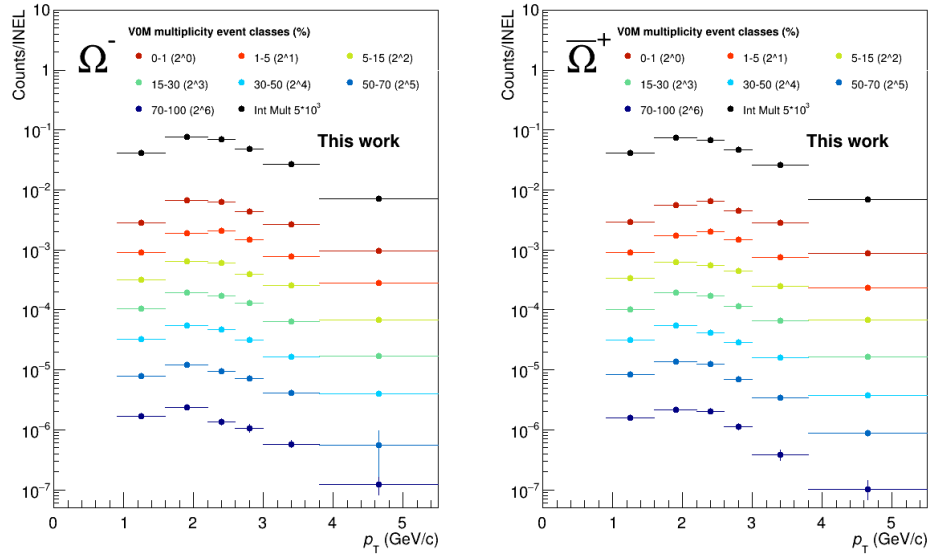


Figure 3.14:  $\Omega^-$  and  $\Omega^+$  raw spectra as a function of  $p_T$  in multiplicity classes and integrated multiplicity.

from “true” INEL>0 events. This factor was obtained by utilizing the MC General Purpose, however, since the statistics were poor the final value of  $\epsilon_{part}(p_T)$  was obtained from the fit with a sigmoid and linear function for  $K_s^0$  and an arctangent function for the other particles (see Figures 3.15).

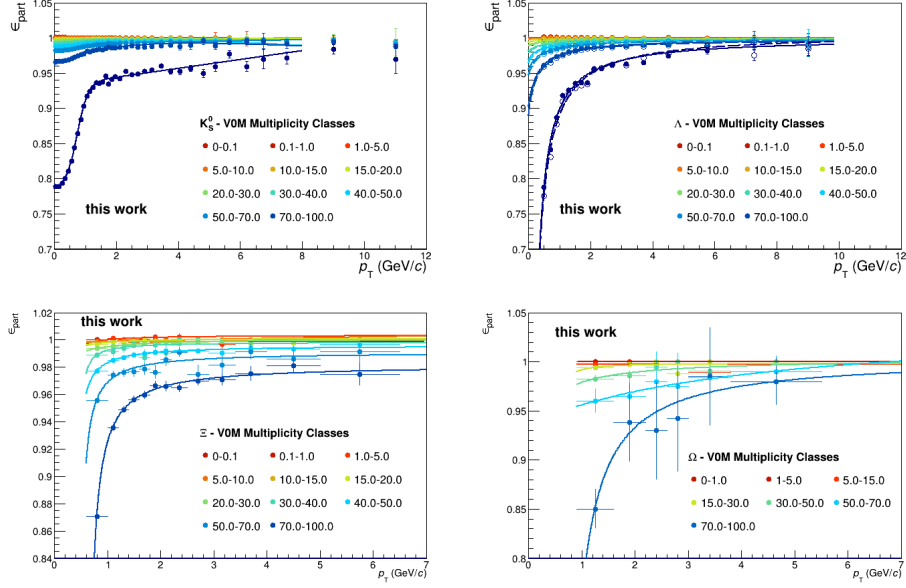


Figure 3.15: Values of  $\epsilon_{part}(p_T)$  for V0s (top panels) and Cascades (bottom panel) as a function of  $p_T$ .



### 3.2.5 Feed-down subtraction for $\Lambda$ and $\bar{\Lambda}$

In order to obtain the true number of  $\Lambda$  and  $\bar{\Lambda}$ , it was necessary to subtract the number of  $\Lambda$  and  $\bar{\Lambda}$  coming from the decay of  $\Xi^-$  and  $\bar{\Xi}^+$ , respectively, and  $\Xi^0$ . The feed-down contribution was computed as follows:

$$\Lambda_{primary}^{raw}(p_T) = \Lambda_{measured}^{raw}(p_T) - \sum_j F_{ij} \int_{p_T} \frac{dN}{dp_T}(\Xi^-) \quad (3.11)$$

where  $F_{ij}$  is the feed-down matrix and is defined as:

$$F_{ij} = \frac{N_{rec}(\Lambda)_{frombin-i}}{N_{gen}(\Xi)_{\Xi binj}} \quad (3.12)$$

In Figure 3.16 the feed-down matrix represents the fraction of reconstructed  $\Lambda(\bar{\Lambda})$  ( $N_{rec}(\Lambda)$ ) in a  $\Lambda(\bar{\Lambda})$   $p_T$  bin- $i$  which had decayed from a charged and neutral  $\Xi$  ( $N_{gen}(\Xi)$ ) in a  $\Xi$   $p_T$  bin- $j$  (Figure 3.16).

The numerator of the feed-down matrix is a 2D histogram where the x-axis represents the  $p_T$  bins of the reconstructed  $\Lambda(\bar{\Lambda})$  while the  $p_T$  bins of generated  $\Xi^-$  ( $\bar{\Xi}^+$ ) are on the y-axis. The 2D histogram was then normalized by the number of generated  $\Xi^-$  ( $\bar{\Xi}^+$ ) for every  $\Xi^-$  ( $\bar{\Xi}^+$ )  $p_T$  bin.

The denominator of this matrix was always filled with the charged  $\Xi$ , whereas two different methods were considered for the numerator to take the contributions from the neutral  $\Xi^0$  into account, which was not measured:

- **MC Ratio:** the numerator was filled with  $\Lambda$  (or  $\bar{\Lambda}$ ) from the decays of both charged and neutral  $\Xi$ . In this case, the ratio  $\Xi^-/\Xi^0$ , as provided by the Monte Carlo generator, was used to compute the feed-down matrix element  $F_{ij}$ , as defined in eq. 3.2.
- **Double Charged  $\Xi$ :** the numerator was filled with  $\Lambda$ (or  $\bar{\Lambda}$ ) from the decays of only charged  $\Xi$ , and the resulting feed-down was multiplied by a factor two.

The uncertainty on the matrix element  $F_{ij}$  was statistical only.

The feed-down correction was computed for integrated multiplicity and for every  $\Lambda$  multiplicity bin.

One of the main challenges when performing the analysis for different multiplicity class selections was to determine the  $\Xi^-/\bar{\Xi}^+$  corrected spectra for each multiplicity class used in the  $\Lambda$  analysis. In particular, three multiplicity classes for  $\Lambda$  did not match those used for  $\Xi^-/\bar{\Xi}^+$ .

An interpolation/extrapolation was performed between the corrected  $\Xi^-/\bar{\Xi}^+$  yields as a function of the charged-particle multiplicity (see Sec. 3.3.4), so

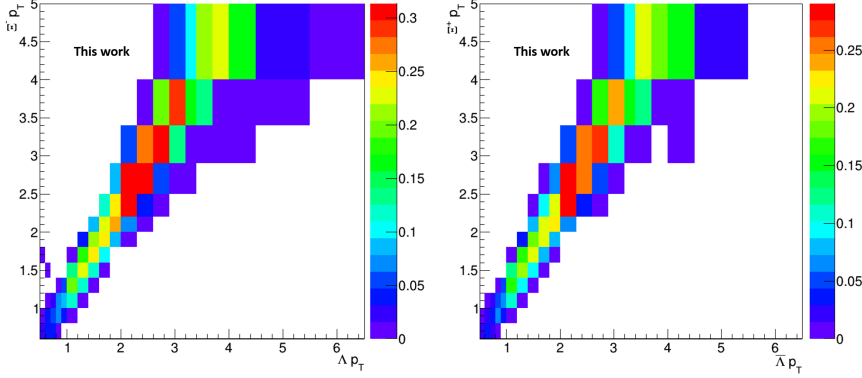


Figure 3.16:  $\Lambda$  (left panel) and  $\bar{\Lambda}$  (right panel) feed-down matrix.

that the required class selection for the  $\Lambda$  analysis could be satisfied. The procedure was applied independently for each  $p_{\mathbf{T}}$  bin of the  $\Xi^-/\bar{\Xi}^+$  analysis and yields as a function of charged-particle multiplicity were fitted using a second order polynomial function. (See Table 3.3 to check the equivalence between percentile classes and number of charged particles). Figures 3.17 and 3.18 show the results obtained for  $\Xi^-$  and  $\bar{\Xi}^+$  four  $p_{\mathbf{T}}$  ranges. In order to estimate the statistical uncertainties over the interpolated/extrapolated points, the polynomial fits were performed over the highest and lowest variations of the measured  $\Xi^-/\bar{\Xi}^+$  yields. Using the values extracted from this procedure it was possible to construct the  $\Xi^-/\bar{\Xi}^+$  corrected spectra at the required multiplicity selections for the  $\Lambda$  analysis (see Figure 3.19). Multiplicative factors, indicated in the legends, were applied in order to better display the  $\Xi^-$  and  $\bar{\Xi}^+$  distributions.

Then, the  $dN/dp_{\mathbf{T}}(\Xi)$  (see Eq. 3.11) could be obtained by fitting the  $\Xi$  spectra with a Levy-Tsallis function, and the integral was performed on the function itself. The integral was calculated over the Levy-Tsallis function fit in order to reduce statistical fluctuations. The final fractions which were subtracted from the  $\Lambda$  and  $\bar{\Lambda}$  spectra were shown in Fig. 3.20 as a function of  $p_{\mathbf{T}}$  and multiplicity classes, respectively. Moreover, Figure 3.21 compares the fraction of secondary  $\Lambda$  (left figure) and  $\bar{\Lambda}$  (right figure) obtained with the two methods in integrated multiplicity: **MC ratio** and **Double Charged  $\Xi$** . The bottom plot shows the ratio of the fraction calculated with the first method with respect to the one obtained with the second method.

The feed-down procedure is also repeated on the merging of  $\Lambda$  and  $\bar{\Lambda}$  and  $\Xi^-$  and  $\bar{\Xi}^+$  data.

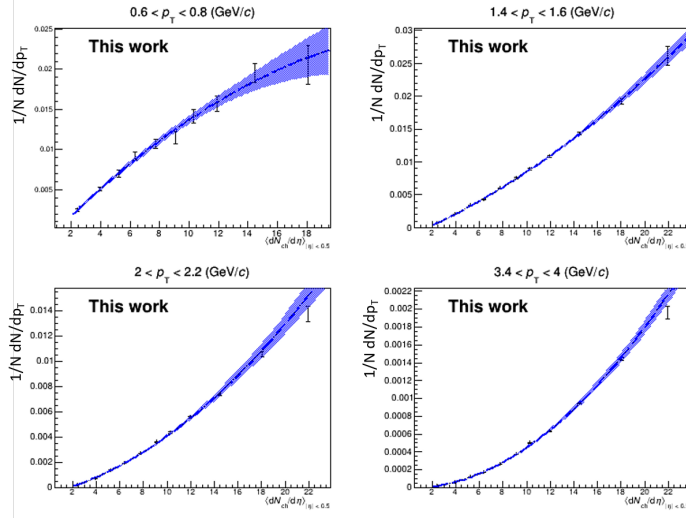


Figure 3.17:  $\Xi^-$  yields vs number of charged particles (multiplicity classes) in four  $p_T$  bins. They are fitted with a second order polynomial function and errors on fit are identified by the blue bands.

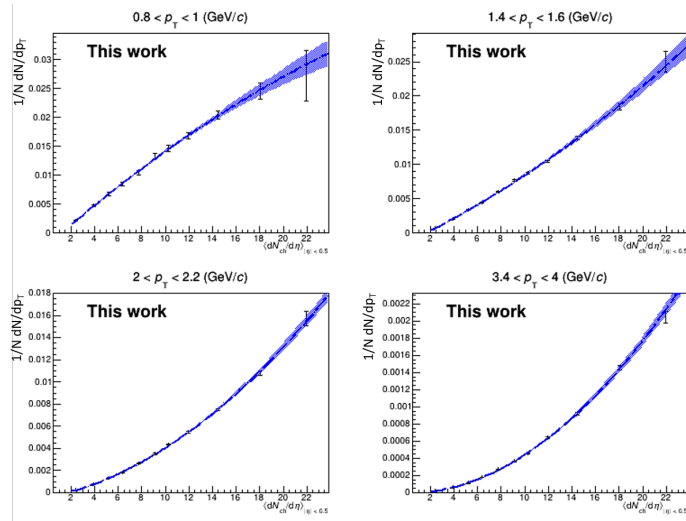


Figure 3.18:  $\Xi^+$  yields vs number of charged particles (multiplicity classes) in four  $p_T$  bins. They are fitted with a second order polynomial function and errors on fit are identified by the blue bands.

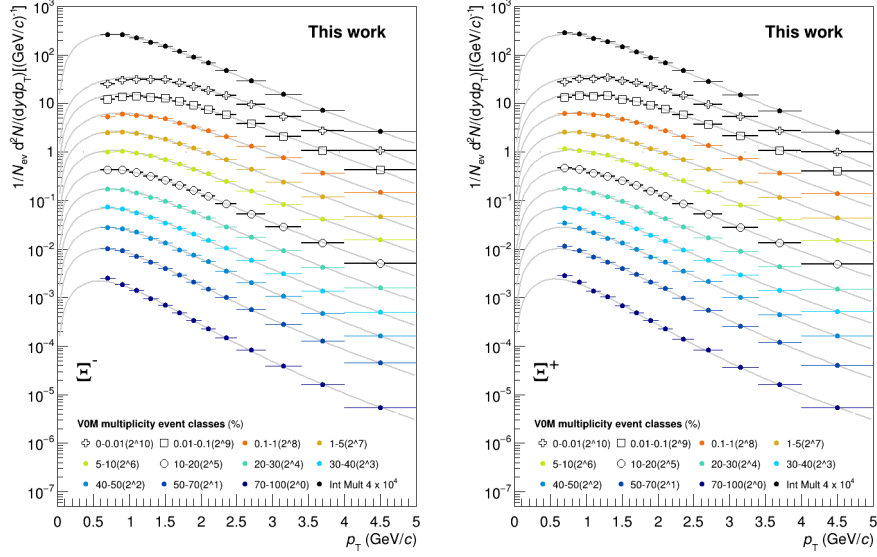


Figure 3.19:  $\Xi^-$  and  $\Xi^+$  corrected spectra in  $\Lambda$  multiplicity classes. Multiplicative factors were applied to the corrected spectra. See Section 3.3.4 for the description on how the colored corrected spectra were obtained.

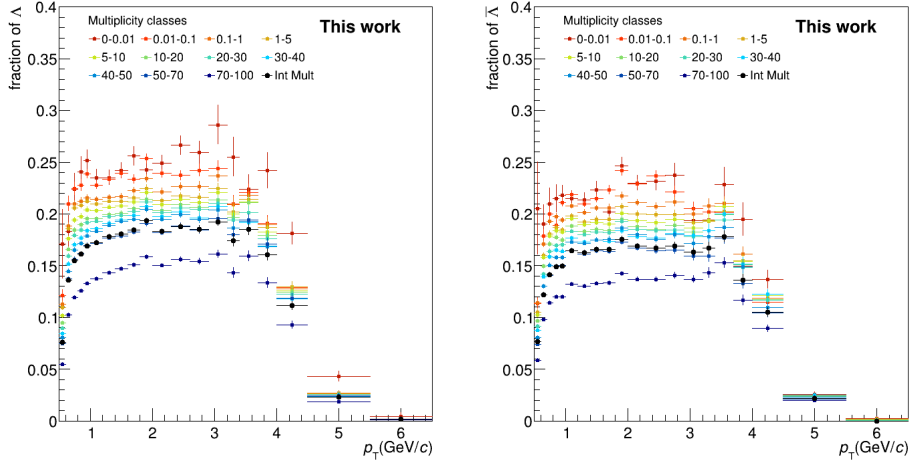


Figure 3.20: Yields fractions of  $\Lambda$  from  $\Xi^- + \Xi^0$  decays (left-handed panel) and  $\bar{\Lambda}$  from  $\Xi^- + \Xi^0$  decays (right-handed panel) that were subtracted from  $\Lambda$  and  $\bar{\Lambda}$  measured yields.

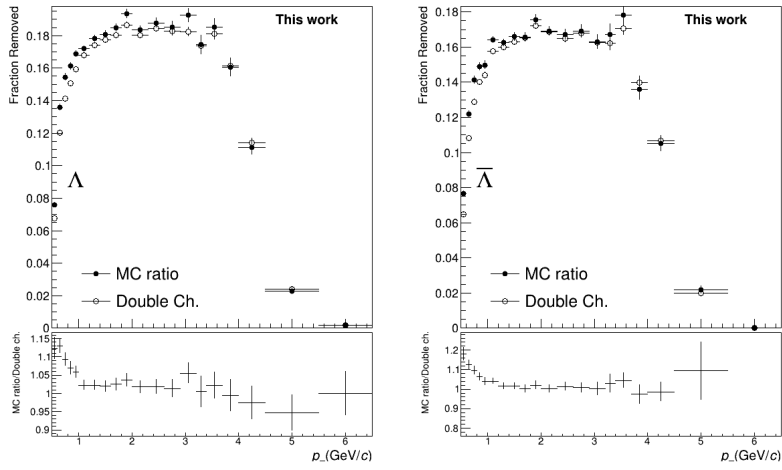


Figure 3.21: Comparison between the yields fractions from MC ratio and Double Charged  $\Xi$  methods in integrated multiplicity for  $\Lambda$  (left-handed panel) and  $\bar{\Lambda}$  (right-handed panel). The bottom panels show the ratio between the yields fractions obtained from MC ratio and Double Charged  $\Xi$  methods.

### 3.2.6 Acceptance times efficiency

To obtain the acceptance times efficiency, the analysis had to be performed on MC simulated data applying the same topological, geometrical and selection cuts discussed above.

In addition, the corresponding PDG code was used to identify daughter and mother tracks and it was checked, for all particle under study, the primary status in order to take only true ones and to reject them if they come from a decay.

The acceptance times efficiency ( $A \times \epsilon$ ) was defined as the ratio between the number of reconstructed particles ( $N(\text{particle})_{reconstructed}$ ) and generated primary particles ( $N(\text{particle})_{generated}$ ) in each  $p_{\mathbf{T}}$  bin:

$$A \times \epsilon = \frac{N(\text{particle})_{reconstructed}}{N(\text{particle})_{generated}} \quad (3.13)$$

The  $A \times \epsilon$  was produced for every multiplicity class and in integrated multiplicity as a function of  $p_{\mathbf{T}}$ .

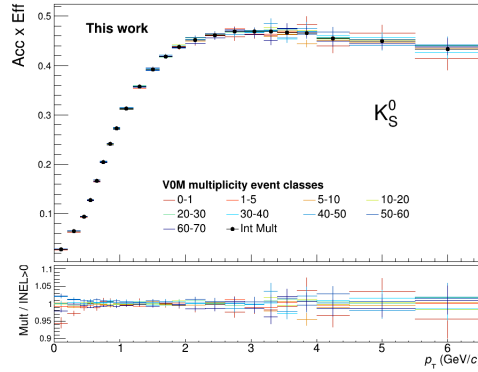


Figure 3.22: The top panel shows the acceptance times efficiency for  $K_S^0$  in multiplicity classes and for integrated multiplicity, while the bottom panel shows the ratio of  $A \times \epsilon$  for multiplicity bins over the integrated multiplicity one.

It is shown on the top panel of Figures 3.22–3.25 for every particle under study while the bottom panel shows the ratio of the  $A \times \epsilon$  for individual multiplicity classes over the integrated multiplicity  $A \times \epsilon$ .

Since there was no dependence on the multiplicity, it was decided to use the integrated multiplicity  $A \times \epsilon$  correction for every multiplicity bin.

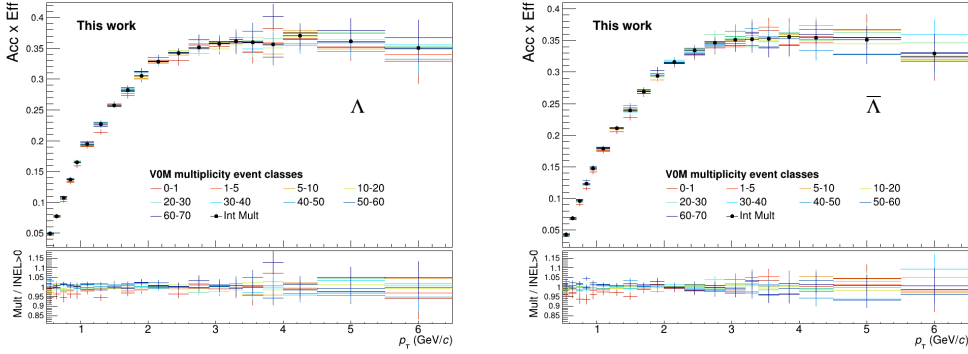


Figure 3.23: The top panels show the acceptance times efficiency for  $\Lambda$  and  $\bar{\Lambda}$  in multiplicity classes and for integrated multiplicity, while the bottom panels show the ratio of  $A \times \epsilon$  for multiplicity bins over the integrated multiplicity one.

In addition, Figures 3.26 and 3.27 show the effect of the ITS||TOF cut on the acceptance times efficiency. There were considered three conditions for V0s and Cascades: when only the ITSrefit flag was applied, when only TOF cut was applied and when either the ITSrefit flag or the TOF cut was used. In the first case (ITSrefit flag only) the  $A \times \epsilon$  was suppressed especially at high  $p_{\mathbf{T}}$ , while in the second case (TOF cut only) it was suppressed at in particular at low  $p_{\mathbf{T}}$ . Therefore, it was necessary to apply both cuts (with OR condition) to obtain a reasonable  $A \times \epsilon$ . At this stage, the corrected spectra are obtained dividing the raw spectra by  $A \times \epsilon$  (see Sec. 3.3.4).

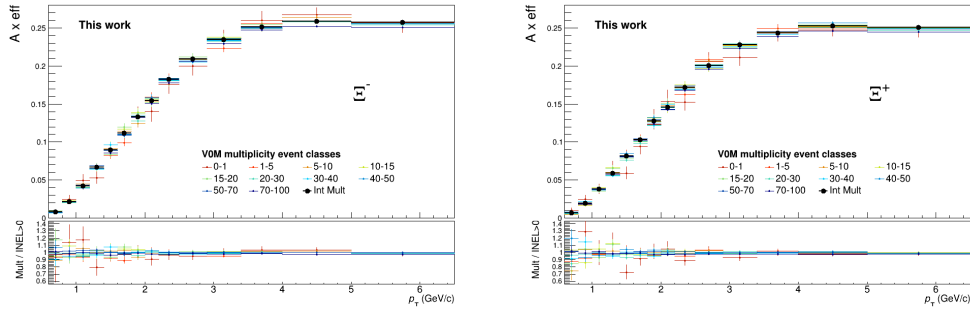


Figure 3.24: The top panels show the acceptance times efficiency for  $\Xi^-$  and  $\Xi^+$  in multiplicity classes and for integrated multiplicity, while the bottom panels show the ratio of  $A \times \epsilon$  for multiplicity bins over the integrated multiplicity one.

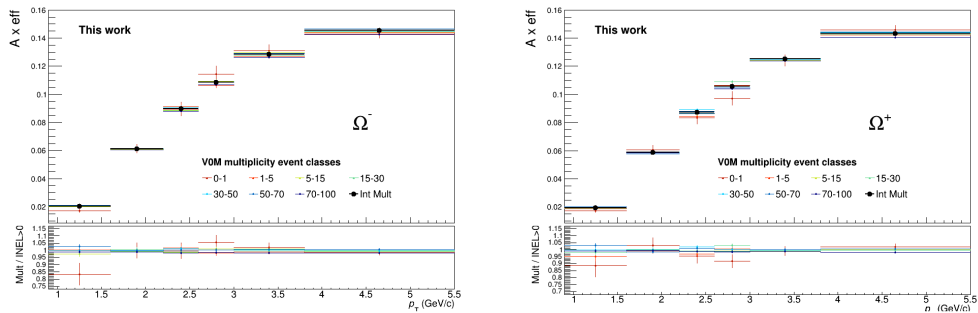


Figure 3.25: The top panels show the acceptance times efficiency for  $\Omega^-$  and  $\Omega^+$  in multiplicity classes and for integrated multiplicity, while the bottom panels show the ratio of  $A \times \epsilon$  for multiplicity bins over the integrated multiplicity one.



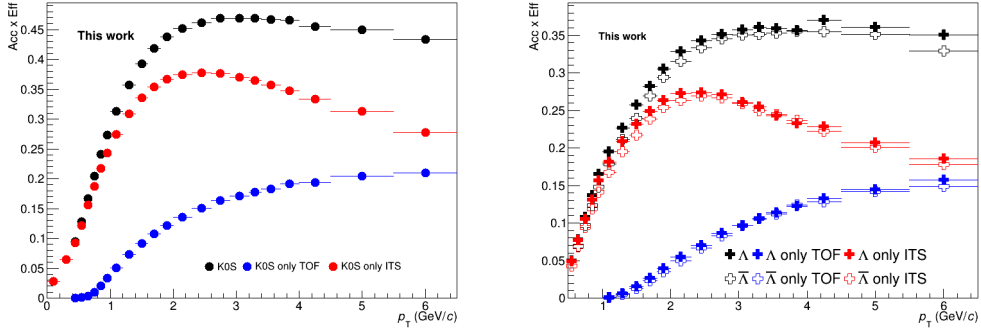


Figure 3.26: The left panel shows the  $A \times \epsilon$  as a function of  $p_T$  for  $K_S^0$  and the right panel shows  $\Lambda$  (full points) and  $\bar{\Lambda}$  (hollow points) when ITSrefit flag or TOF cut (color black points) is applied and when TOF cut only (color red points) and ITSrefit flag only (color blue points) are applied.

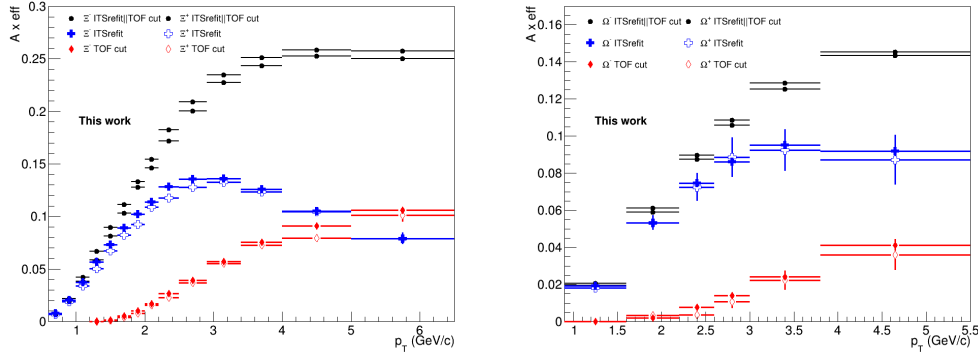


Figure 3.27: The left panel shows the  $A \times \epsilon$  as a function of  $p_T$  for  $\Xi^-$  (full points) and  $\Xi^+$  (hollow points) and the right panel shows  $\Omega^-$  (full points) and  $\Omega^+$  (hollow points) when ITSrefit flag or TOF cut (color black points) was applied and when TOF cut only (color red points) and ITSrefit flag only (color blue points) were applied.

### $A \times \epsilon$ correction for anti-particle

The MC General Purpose as well as the MC Injection productions were both produced using GEANT 3. Due to the fact that the description of the anti-proton absorption in the materials is not treated in GEANT 3 as accurately as in GEANT 4, the acceptance times efficiency corrections for anti-particles could be affected at low  $p_{\mathbf{T}}$ . Figure 3.28 shows the comparison for  $\Lambda$  (left panel) and  $\bar{\Lambda}$  (right panel) of  $A \times \epsilon$  calculated with MC General Purpose, for which was used GEANT 3, and  $A \times \epsilon$  calculated with MC GEANT 4. The ratios between the two cases show a difference of 5-10 % at low and high  $p_{\mathbf{T}}$  for  $\bar{\Lambda}$  so it was decided to use the MC GEANT4 to calculate the final Acceptance times efficiency for  $\Lambda$  and  $\bar{\Lambda}$ .

Figure 3.29 shows the same comparison for  $\Xi^-$  (left panel) and  $\bar{\Xi}^+$  (right panel). The difference between the two cases for  $\bar{\Xi}^+$  at low  $p_{\mathbf{T}}$  reaches 8 %. In this case, it was not possible to simply use the MC GEANT 4 for the final  $A \times \epsilon$  because the MC Injection offered a much higher statistics for Cascades. This is why, a  $A \times \epsilon$  correction was elaborated for  $\bar{\Xi}^+$ : as shown in Fig. 3.29's bottom panel, the  $\bar{\Xi}^+$  ratio between the two  $A \times \epsilon$  for  $\bar{\Xi}^+$  was fitted with five different functions up to  $p_{\mathbf{T}}$  2.9 GeV/c to see which one better describes the ratio and with a constant function from 2.9 GeV/c to 5 GeV/c. According to the  $\chi^2$  values written in the legend, the sigmoid function was the best option to calculate the correction factors in every  $p_{\mathbf{T}}$  bin up to 2.9 GeV/c while the constant function was used for the last three bins. Then, these factors were applied to normalize the  $\bar{\Xi}^+$  acceptance times efficiency distributions as a function of  $p_{\mathbf{T}}$ .

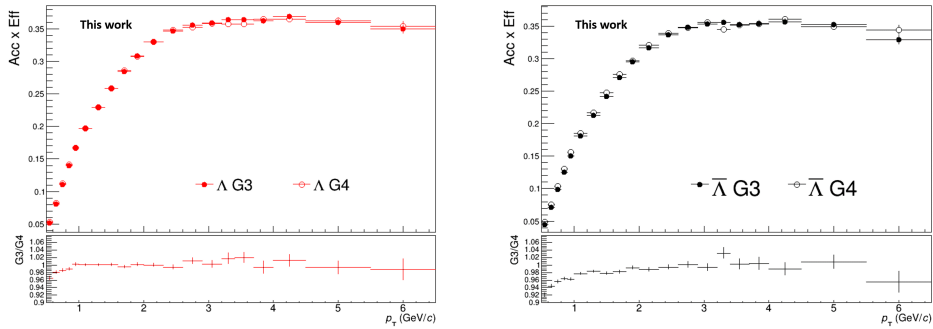


Figure 3.28: The left panel shows  $\Lambda$   $A \times \epsilon$  obtained from the MC General Purpose and MC GEANT 4 together with their ratio (bottom panel). The right panel shows  $\bar{\Lambda}$   $A \times \epsilon$  obtained from the MC General Purpose and MC GEANT 4 together with their ratio (bottom panel).

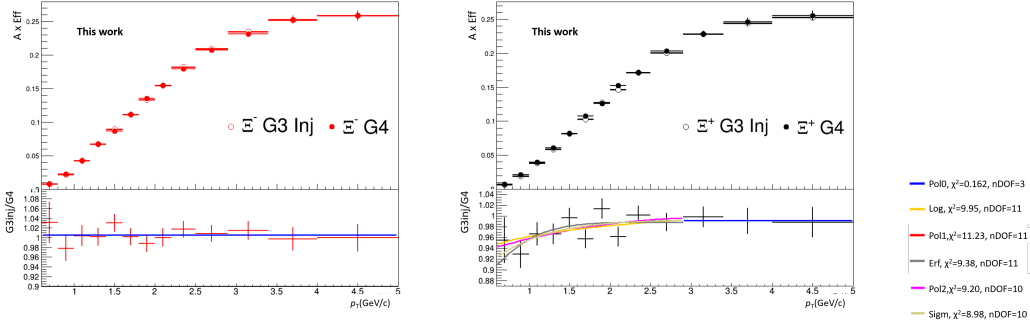


Figure 3.29: The left panel shows  $\Xi^- A \times \epsilon$  obtained from the MC General Purpose and MC GEANT 4 together with their ratio (bottom panel). The right panel shows  $\Xi^+ A \times \epsilon$  obtained from the MC Injected and MC GEANT 4 together with their ratio (bottom panel). The ratio is fitted with five functions up to 2.9 GeV/c and a constant function in the last three  $p_{\mathbf{T}}$  bins.

The left panel of Figure 3.30 shows for  $\Xi^+$  the same comparison shown in the right panel of Figure 3.29 but in this case the correction is applied to the  $A \times \epsilon$  calculated with MC injected. The ratio between the two  $A \times \epsilon$  demonstrates that the correction applied cured the issue at low  $p_{\mathbf{T}}$ . As it can be seen in the right panel of 3.30, this effect was not relevant for  $\Omega^+$  because, the spectrum starts at a higher value of  $p_{\mathbf{T}}$ .

Moreover, the systematic uncertainties with this factor was defined as the absolute maximum difference of the other four functions with respect to the sigmoid (contribution of  $\sim 2\%$  at low  $p_{\mathbf{T}}$ ).

### 3.2.7 Effect due to MC $p_{\mathbf{T}}$ shape on the $A \times \epsilon$

In order to reduce statistical fluctuations, large  $p_{\mathbf{T}}$  bins were chosen to evaluate the invariant mass spectra and, consequently, the raw and corrected  $p_{\mathbf{T}}$  spectra. This could introduce a bias in the corrected spectra because the input of the MC  $p_{\mathbf{T}}$  shape could be quite different from the measured one (data). In particular, the MC Injection had a flat  $p_{\mathbf{T}}$  distribution, which was very different from a Levy-Tsallis-like shape. A comparison between the data and MC shape is shown in Fig. 3.31 for  $K_S^0$ ,  $\Lambda$ ,  $\Xi$  and  $\Omega$ . The measured  $p_{\mathbf{T}}$ -spectra were fitted with a Levy-Tsallis function, then the  $p_{\mathbf{T}}$ -corrected spectra were randomly generated with a high granularity in  $p_{\mathbf{T}}$ .

The comparison of the  $p_{\mathbf{T}}$  corrected spectra for  $\Xi$  and  $\Omega$  clearly shows a substantial difference to the MC simulations both as a function of  $p_{\mathbf{T}}$ .

In order to reduce the bias introduced by the MC  $p_{\mathbf{T}}$ -shape on the corrected spectra, an iterative procedure was applied. It consisted of the follow-

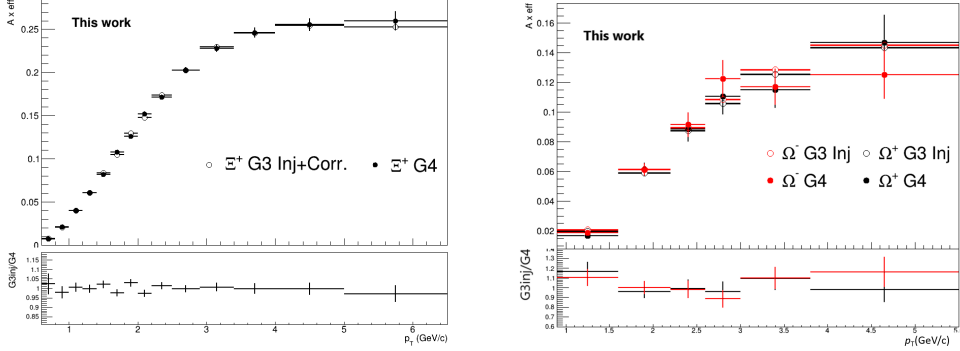


Figure 3.30: The left panel shows  $\Xi^+$   $A \times \epsilon$  calculated with MC injected after applying the correction and  $\Xi^+$   $A \times \epsilon$  calculated with MC GEANT4 together with their ratio (bottom panned). The right panel shows the  $A \times \epsilon$  calculated from MC Injection and MC GEANT 4 for  $\Omega^-$  and  $\Omega^+$  together with their ratio (bottom panel).

ing steps:

1. the ratios of the “fitted” shapes obtained from experimental data over Monte Carlo input  $p_T$ -shape were computed with a granularity much higher than the one used in the data analysis;
2. the ratios obtained from the step 1 were used to “re-weight” the reconstructed and generated spectra (computed with the same high granularity) used to compute efficiencies;
3. new efficiencies were recomputed by “re-binning” the  $p_T$ -spectra at the step 2 in the same  $p_T$  bins used in the analysis. In this way the “corrected” efficiencies were obtained;
4. the correction factors, which were the ratios of the new efficiencies with respect to the previous values, were finally applied to the measured corrected spectra.

At every new iteration, the corrected spectra used in step 1 were substituted with the ones obtained at step 4 of the previous iteration. Figures 3.32–3.35 show the V0s and Cascades correction factors together with the ratio of the corrected spectra over MC input  $p_T$ -shape for every iteration. The residual correction became negligible (the correction factors are 1 in every  $p_T$  and multiplicity bin and adding another iteration did not improve the correction) after the third iteration for  $\Xi$  and  $\Lambda$  and after the fourth iteration for  $K_S^0$  and  $\Omega$ .

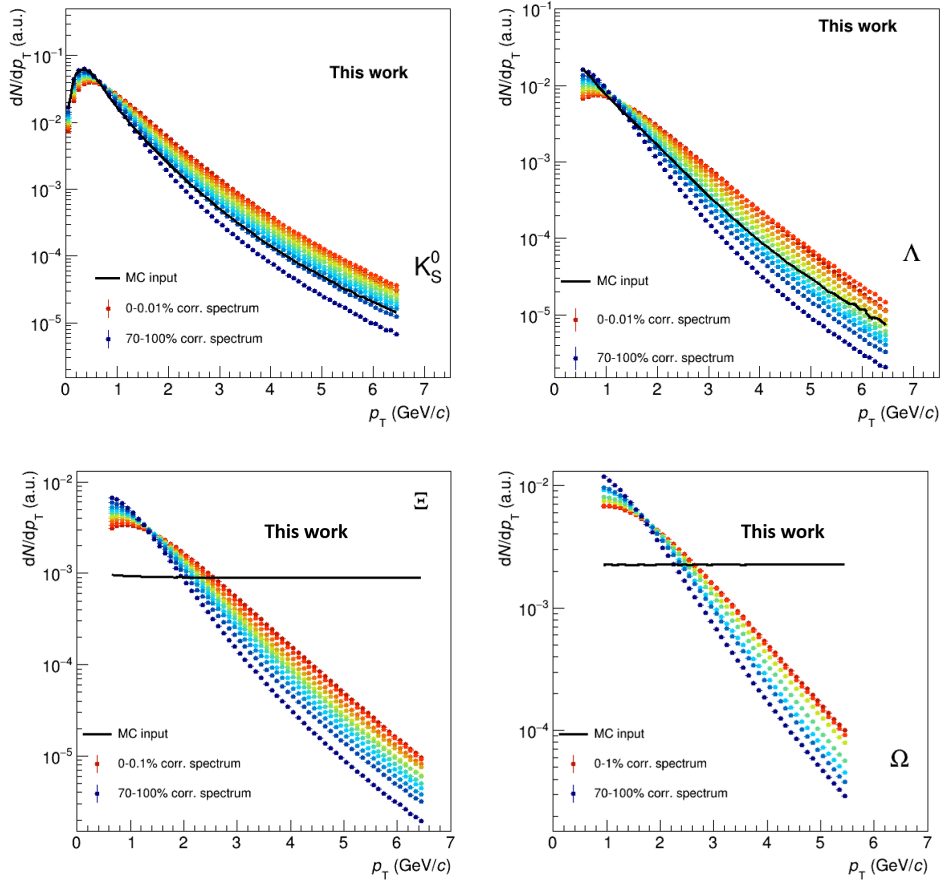


Figure 3.31:  $p_T$  shape for  $K_S^0$ ,  $\Lambda$ ,  $\Xi$  and  $\Omega$ . The black lines represent the Monte Carlo whereas the dotted-colored spectra are the  $p_T$ -shapes obtained from experimental data for all multiplicity classes. The legend indicates the first and the last multiplicity class.

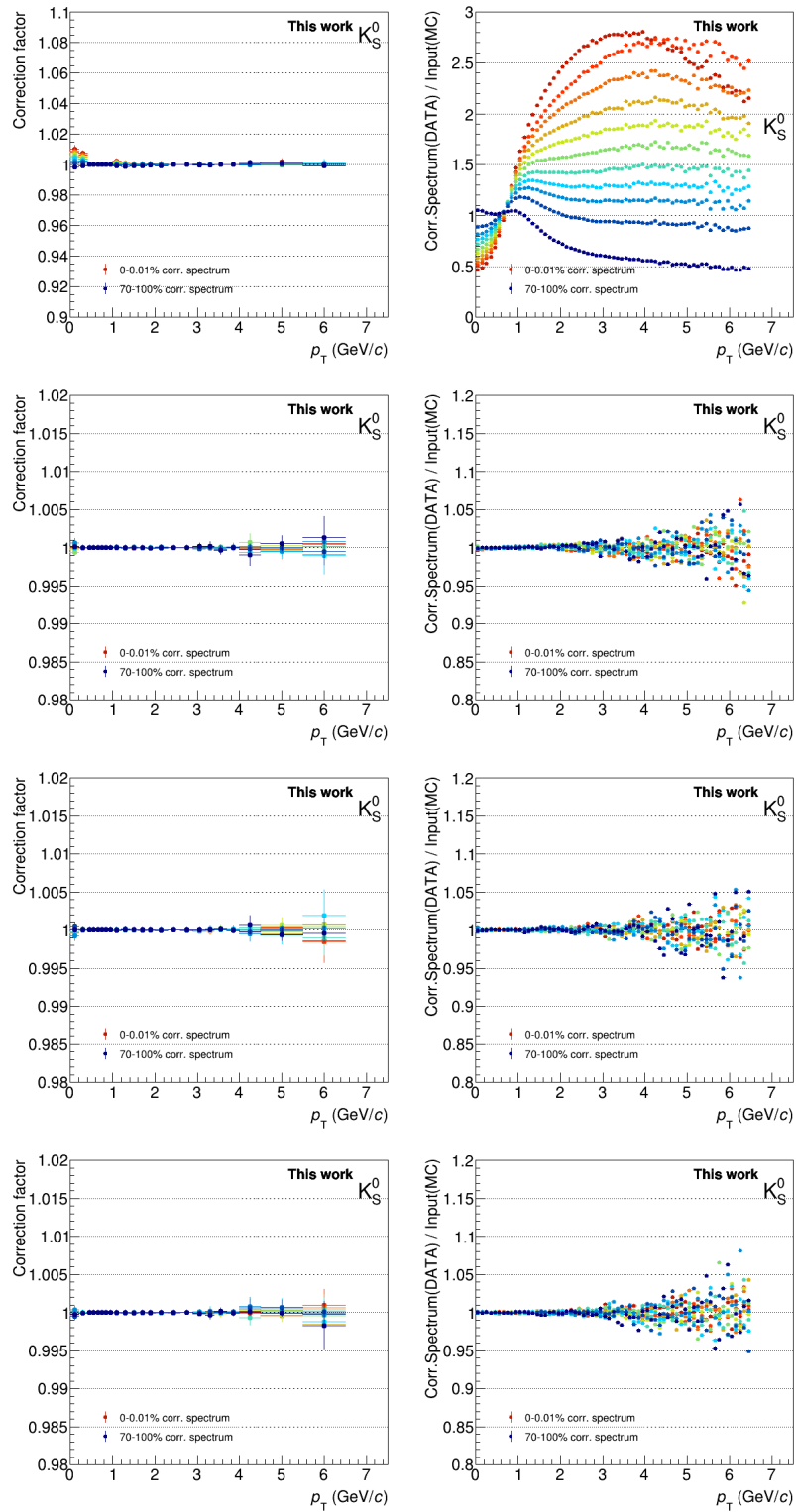


Figure 3.32:  $K_S^0$  Correction factors (left panels) and ratios of corrected spectra over the MC input  $p_T$ -shape (right panels) for all four iterations for all multiplicity classes. The legend indicates the first and the last multiplicity class.

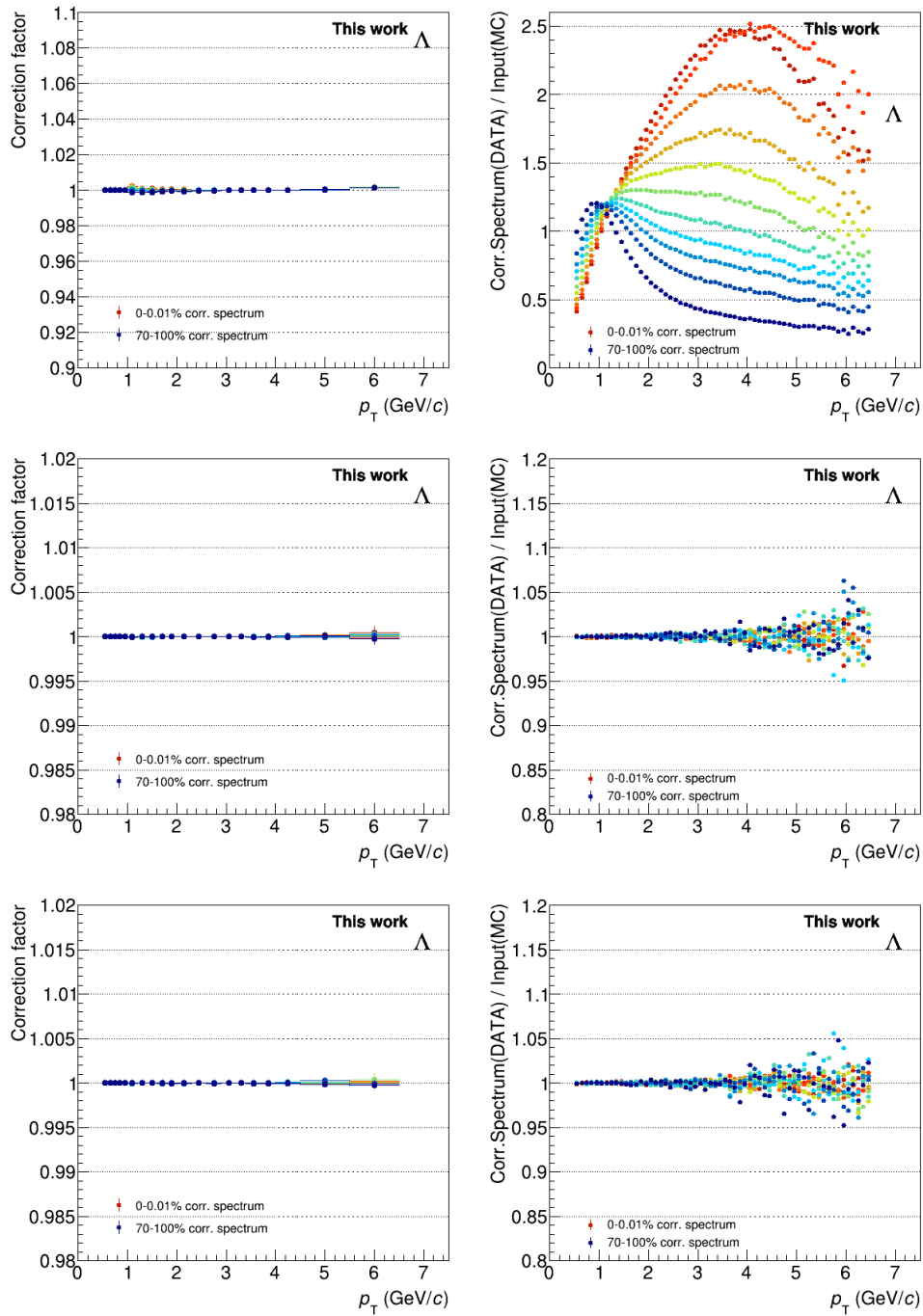


Figure 3.33:  $\Lambda$  Correction factors (left panels) and ratios of corrected spectra over the MC input  $p_T$ -shape (right panel) for all three iterations for all multiplicity classes. The legend indicates the first and the last multiplicity class.

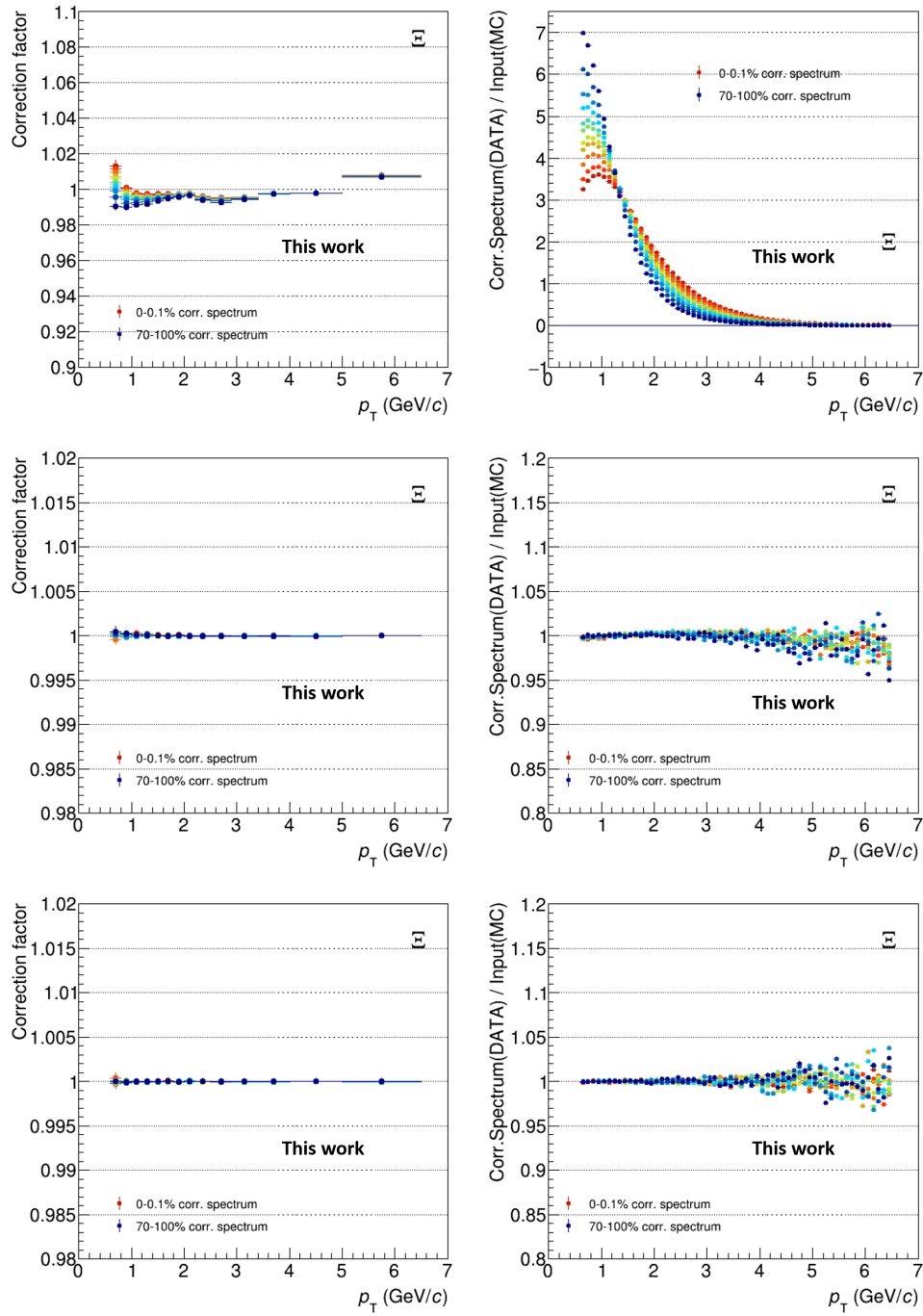


Figure 3.34:  $\Xi$  Correction factors (left panels) and ratios of corrected spectra over the MC input  $p_T$ -shape (right panel) for all three iterations for all multiplicity classes. The legend indicates the first and the last multiplicity class.



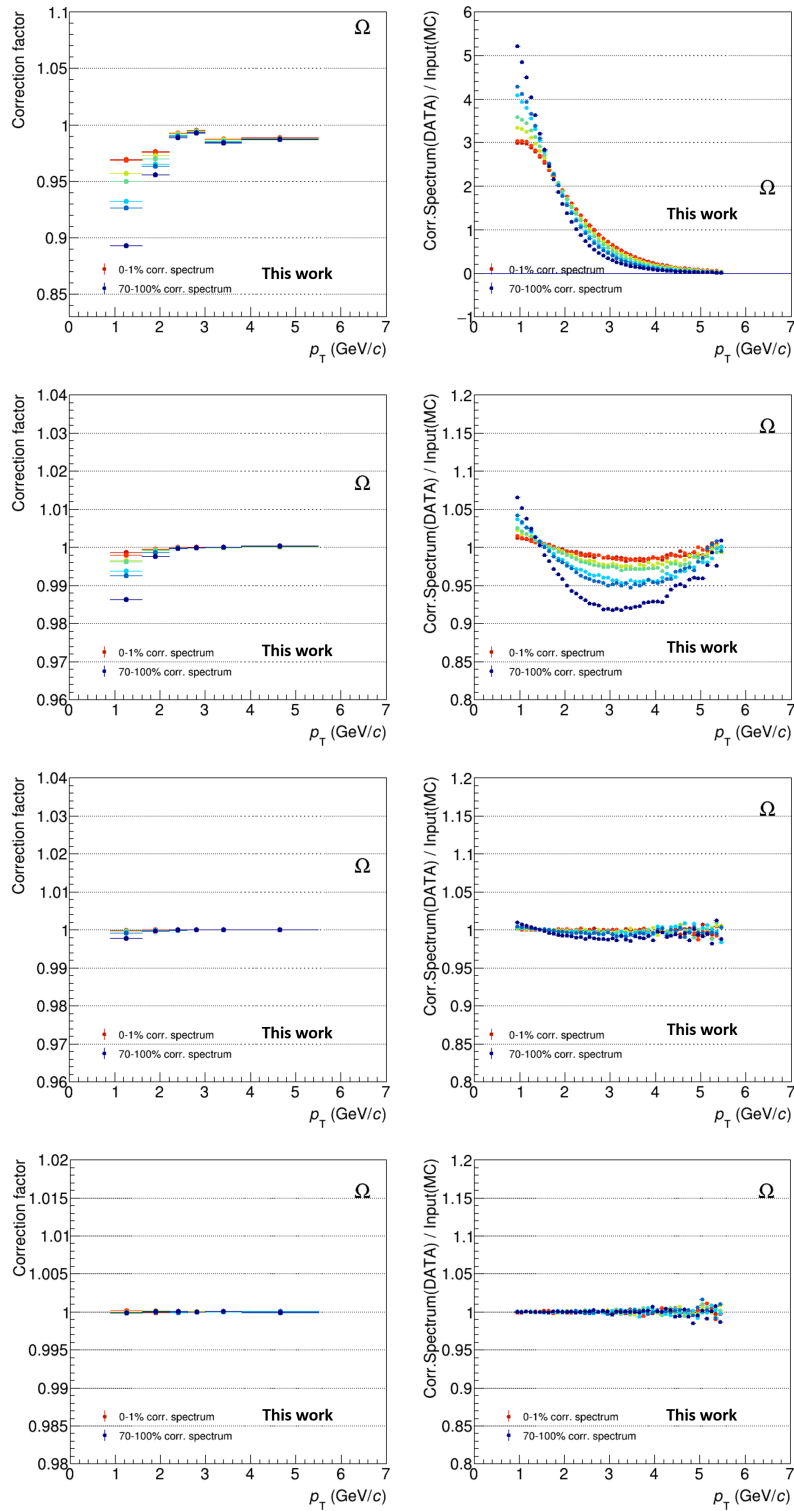


Figure 3.35:  $\Omega$  Correction factors (left panel) and ratios of corrected spectra over the MC input  $p_T$ -shape (right panel) for all four iterations for all multiplicity classes. The legend indicates the first and the last multiplicity class.

### 3.3 Systematic uncertainties

#### 3.3.1 Cut studies

The main sources of systematic uncertainties came from applying the same cuts on the topological and selection variables on MC and data. In particular, MC did not describe accurately every variable, so cutting at the same value data and MC, meant cutting different percentage of the signal. In order to select the cut values for the systematic uncertainties, a signal-loss study was performed for these variables. Every applied cut was varied, one at a time, 30 times per specific range defined in Table 3.6, while the other cuts maintained the default values applied in the analysis.

Topological Variable	range V0s	range $\Xi$	range $\Omega$
DCA Negative track to PV	0.0-0.15 cm	0.09-0.50 cm	0.09-0.50 cm
DCA Positive track to PV	0.0-0.15 cm	0.09-0.50 cm	0.09-0.50 cm
DCA Bachelor to PV	–	0.0-0.2 cm	0.0-0.2 cm
DCA V0 Daughters	0.1-1.5 cm	0.50-1.50 cm	0.50-1.5 cm
DCA Cascade Daughters	–	0.50-1.50 cm	0.20-1.5 cm
DCA V0 to PV	–	0.03-0.2 cm	0.03-0.20 cm
DCA Bachelor to Baryon	–	0.001-0.07 cm	–
V0 transv. decay rad. $R_{2D}$	0-5 cm	0-5 cm	0-5 cm
V0 cosine of point. angle	0.95-0.999	0.94-0.999	0.94-0.999
Casc. transv. decay rad. $R_{2D}$	–	0.2-2.0 cm	0.2-2.0 cm
Casc. cosine of point. angle	–	0.94-1.0	0.94-1.0
V0 mass (MeV/ $c^2$ )	–	0.002-0.01	0.002-0.01
Selection	range $\Lambda$	range $\Xi$	range $\Omega$
TPC $dE/dx$ selection	2-6 $\sigma$	2-7 $\sigma$	2-7 $\sigma$
Proper Lifetime ( $mL/p$ )	15-60 cm	1-20 cm	1-20 cm
TPC Crossed Rows	65-85	65-85	65-85
TPC CR/Findable	0.7-0.9	-	-
Comp. Casc. rej.	–	–	0.002-0.02

Table 3.6: Ranges of the variables that are varied. Default values were used for the open fields.

Then, the raw data and MC signals were extracted using the signal extraction procedure described in Section 2. The signal-loss fraction was performed as:

$$\text{Signal - loss fraction} = 1 - \frac{\text{Raw Signal}_{cut}}{\text{Raw Signal}_{default\ cut}}$$

where  $\text{Raw Signal}_{cut}$  was the signal extracted applying one varied cut keeping the others as default cuts and  $\text{Raw Signal}_{default\ cut}$  was the signal extracted with all default cuts.

The cut study was performed by:

- integrating over multiplicity and  $p_{\mathbf{T}}$
- integrating over multiplicity as a function of  $p_{\mathbf{T}}$  bins

the signal-loss fractions for all variables under study in integrated multiplicity and  $p_{\mathbf{T}}$  are shown in Appendix. In Figures 3.36-3.42 the signal-loss fraction is shown for all variables under study in integrated multiplicity for all  $p_{\mathbf{T}}$  bins. The data were represented by full points while the MC by cross points connected with a line. The dashed black line represents the default cut applied in the analysis. Moreover, four values were selected for every applied cut:

- loosest cut, corresponds to a 10% of the signal gain;
- loose cut, corresponds to a 5% of the signal gain;
- tight cut, corresponds to a 5% of the signal loss;
- tightest cut, corresponds to a 10% of the signal loss;

For some variables it was not possible to select two loose cuts with a signal loss of 5% and 10%. In most cases, this was due to the fact that, after a certain value of the variable under study, it was not possible to perform a further signal-loss (the default cut was already set to loosest).

The comparison between data and MC shows good agreement. The only exceptions were found for the V0 Cosine of Pointing Angle for all V0s and cascades at low  $p_{\mathbf{T}}$  and the TPC  $dE/dx$  selection for V0s where the MC did not follow the same trend of the data.

The signal-loss fraction of the V0 present a significant variation as a function of  $p_{\mathbf{T}}$  for the following variables: DCA V0 Daughter, V0 Cosine of Pointing Angle, V0 Radius. In addition, for  $\Xi^-$  and  $\bar{\Xi}^+$  also the signal loss fraction for Number of Crossed Rows, DCA Cascade Daughter and Cascade Radius shows a considerable spread as a function of  $p_{\mathbf{T}}$ .

While for  $\Omega^-$  and  $\bar{\Omega}^+$ , the dependence on  $p_{\mathbf{T}}$  was fairly constant but less so for DCA V0 Daughter, V0 Radius and Cascade Radius.

Four cuts were selected for every variable. The same values were applied to every  $p_{\mathbf{T}}$  bin. These cuts are listed in the next section.

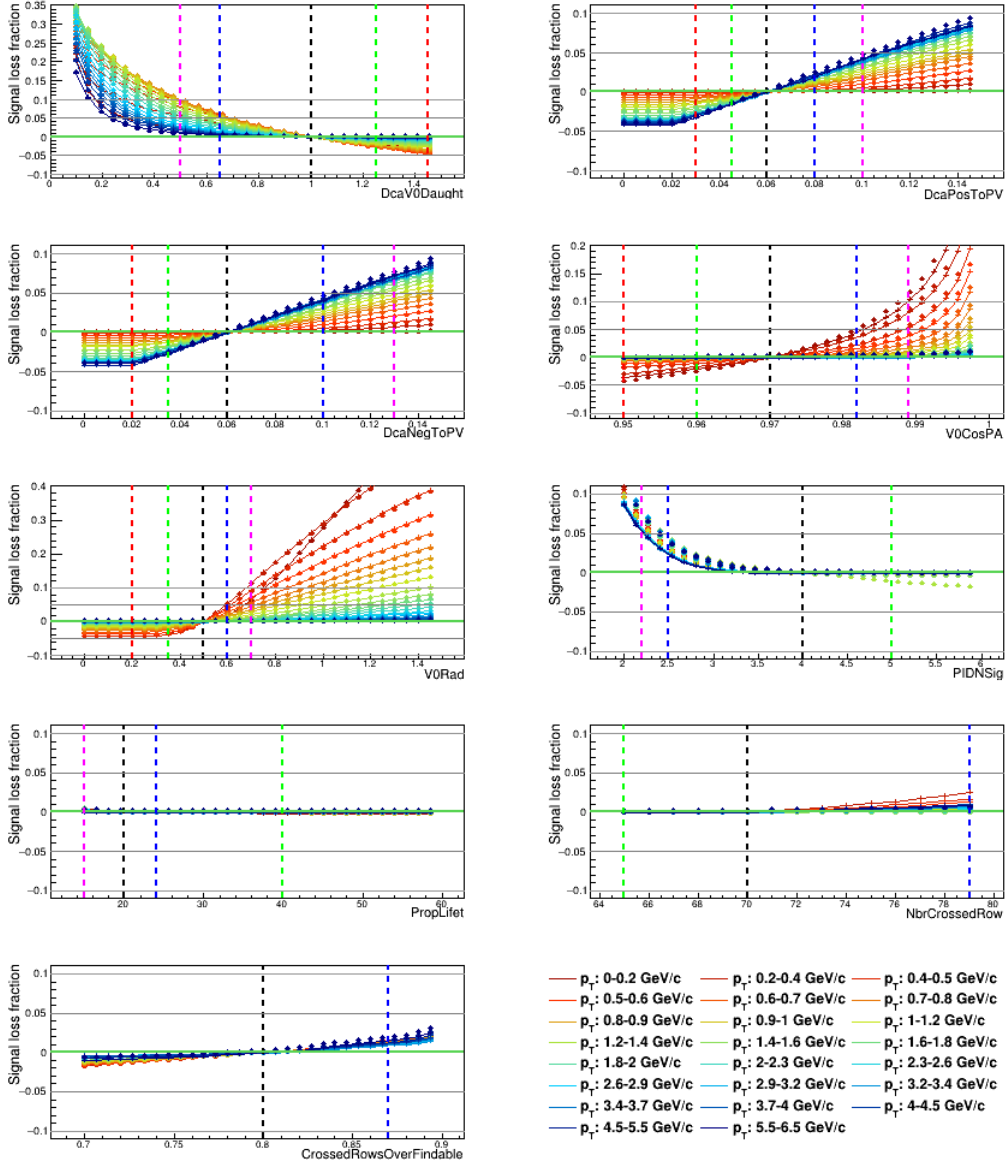


Figure 3.36: The signal-loss fractions for  $K_s^0$  in the 23  $p_T$  intervals (see legend) are shown. The data are the full points while the MC are the lines and cross points. The magenta, blue, green and red lines represent, respectively, the loosest, loose, tight and tightest cuts. The black dashed line corresponds to the default variable cut. These figures were obtained in this work.

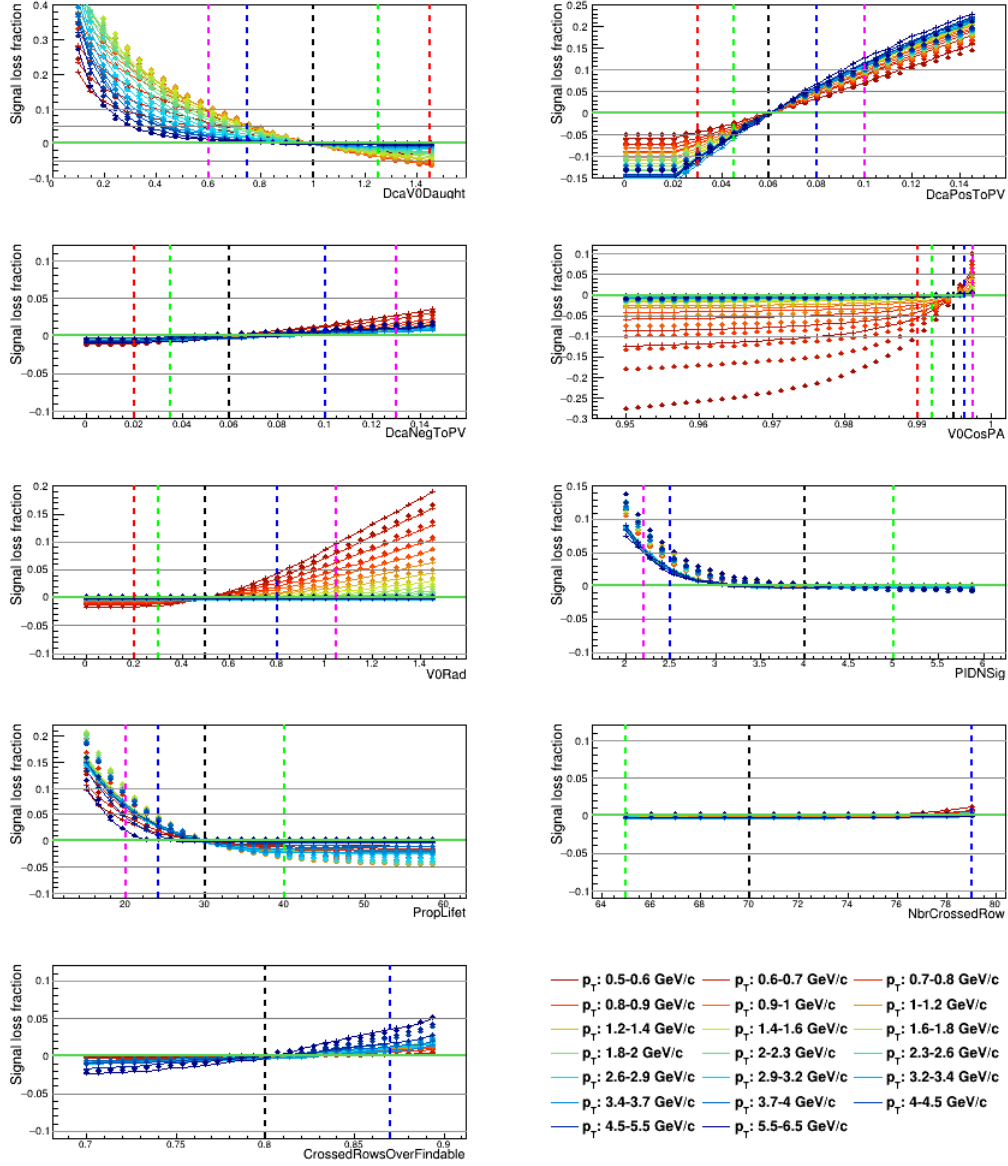


Figure 3.37: The signal-loss fractions for  $\Lambda$  in the 20  $p_T$  intervals (see legend) are shown. The data are the full points while the MC are the lines and cross points. The magenta, blue, green and red lines represent, respectively, the loosest, loose, tight and tightest cuts. The black dashed line corresponds to the default variable cut. These figures were obtained in this work.

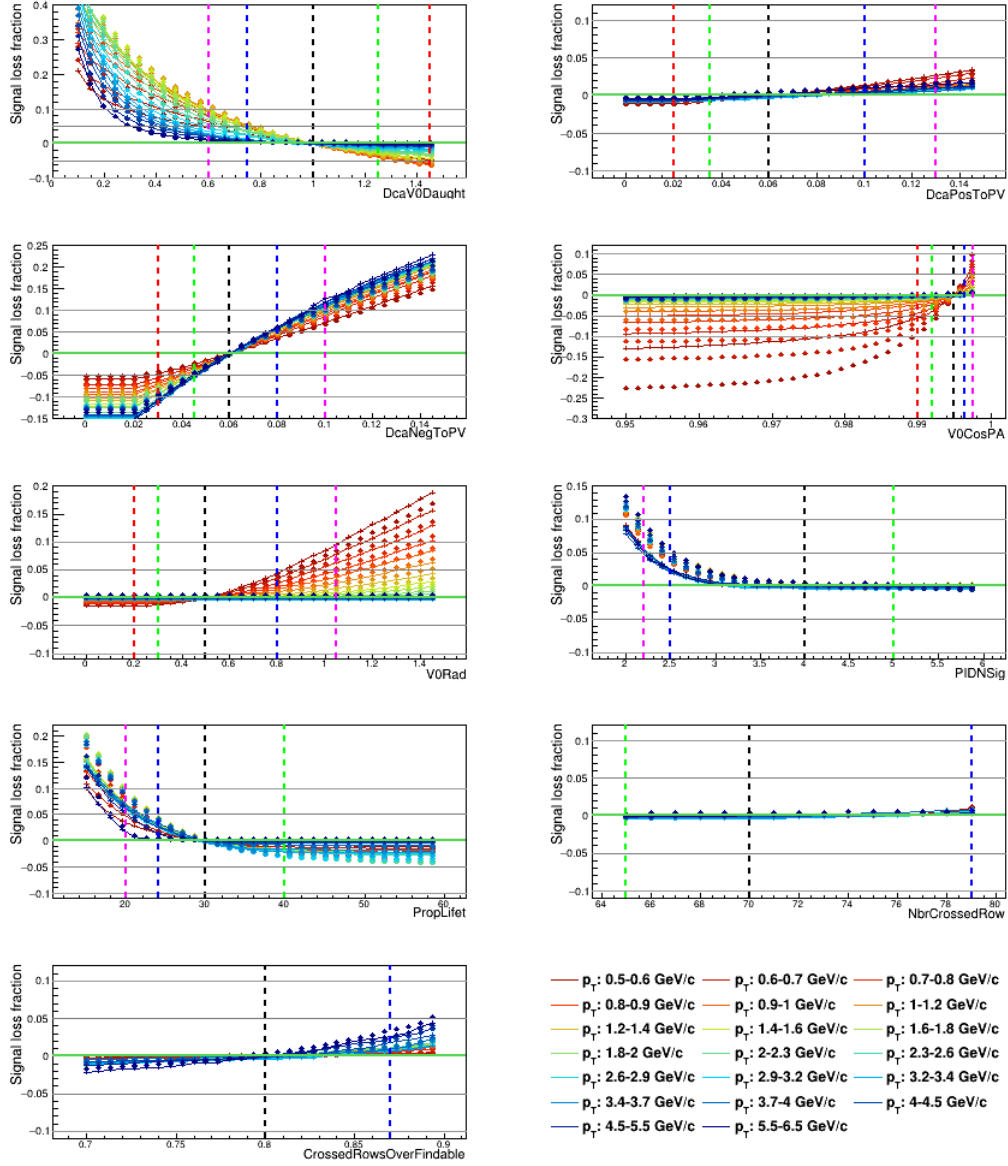


Figure 3.38: The signal-loss fractions for  $\bar{\Lambda}$  in the 20  $p_T$  intervals (see legend) are shown. The data are the full points while the MC are the lines and cross points. The magenta, blue, green and red lines represent, respectively, loosest, loose, tight and tightest cuts. The black dashed line corresponds to the default variable cut. These figures were obtained in this work.

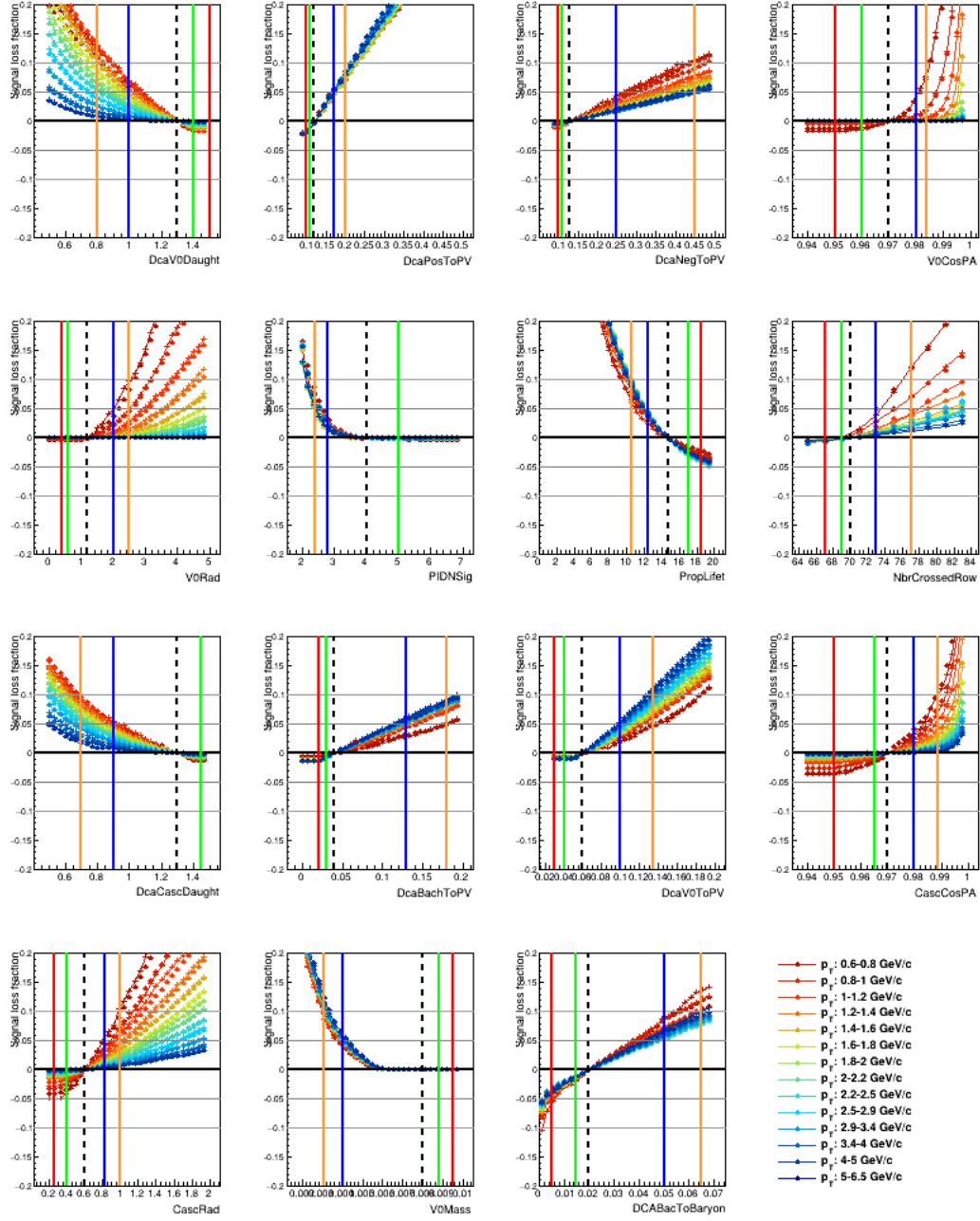


Figure 3.39: The signal-loss fractions for  $\Xi^-$  in the 14  $p_T$  intervals (see legend) are shown. The data are the full points while the MC are the lines and cross points. The Orange, blue, green and red lines represent, respectively, the loosest, loose, tight and tightest cuts. The black dashed line corresponds to the default variable cut. These figures were obtained in this work.

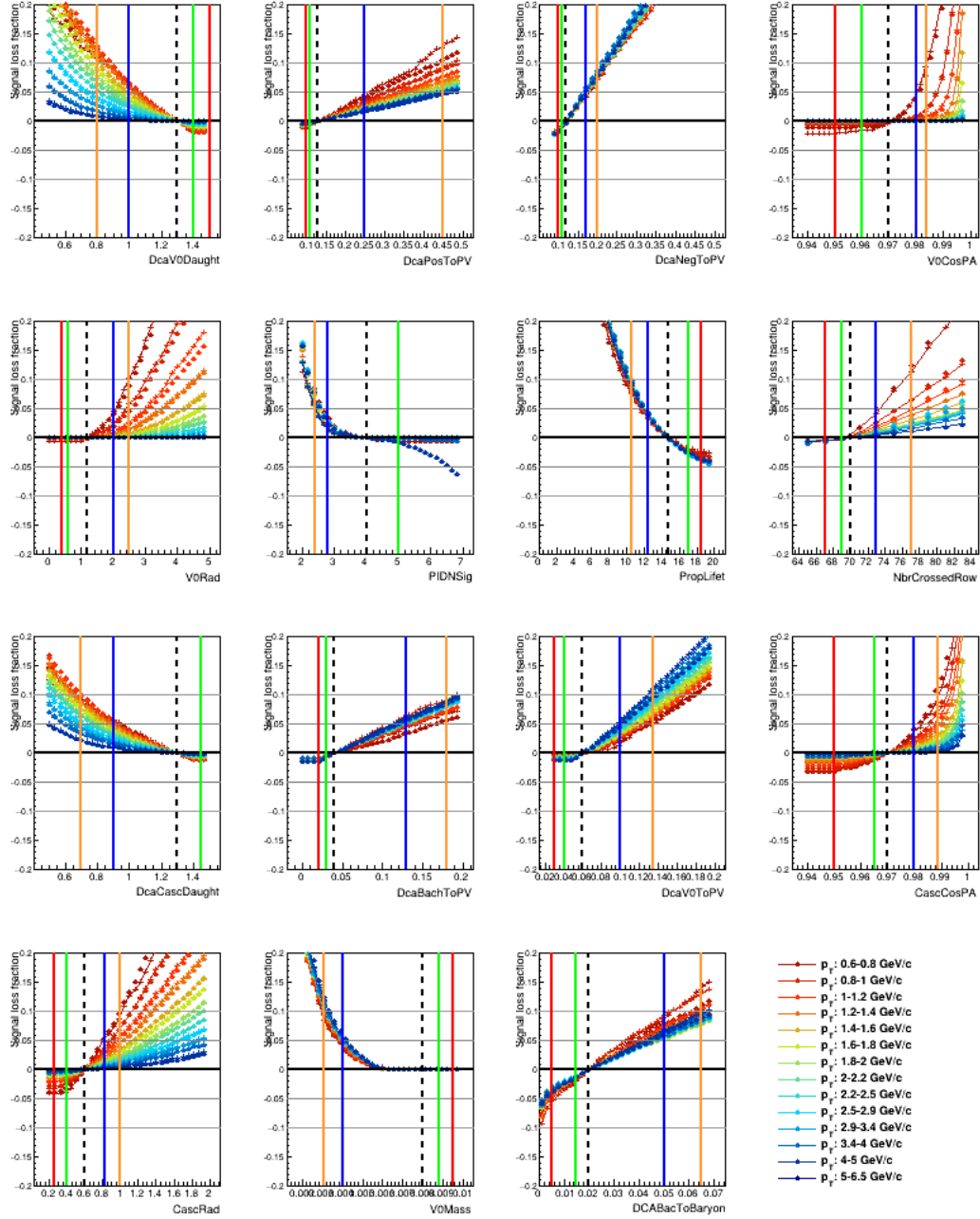


Figure 3.40: The signal-loss fractions for  $\Xi^{-+}$  in the 14  $p_{\mathbf{T}}$  intervals (see legend) are shown. The data are the full points while the MC are the lines and cross points. The orange, blue, green and red lines represent, respectively, the loosest, loose, tight and tightest cuts. The black dashed line corresponds to the default variable cut. These figures were obtained in this work.



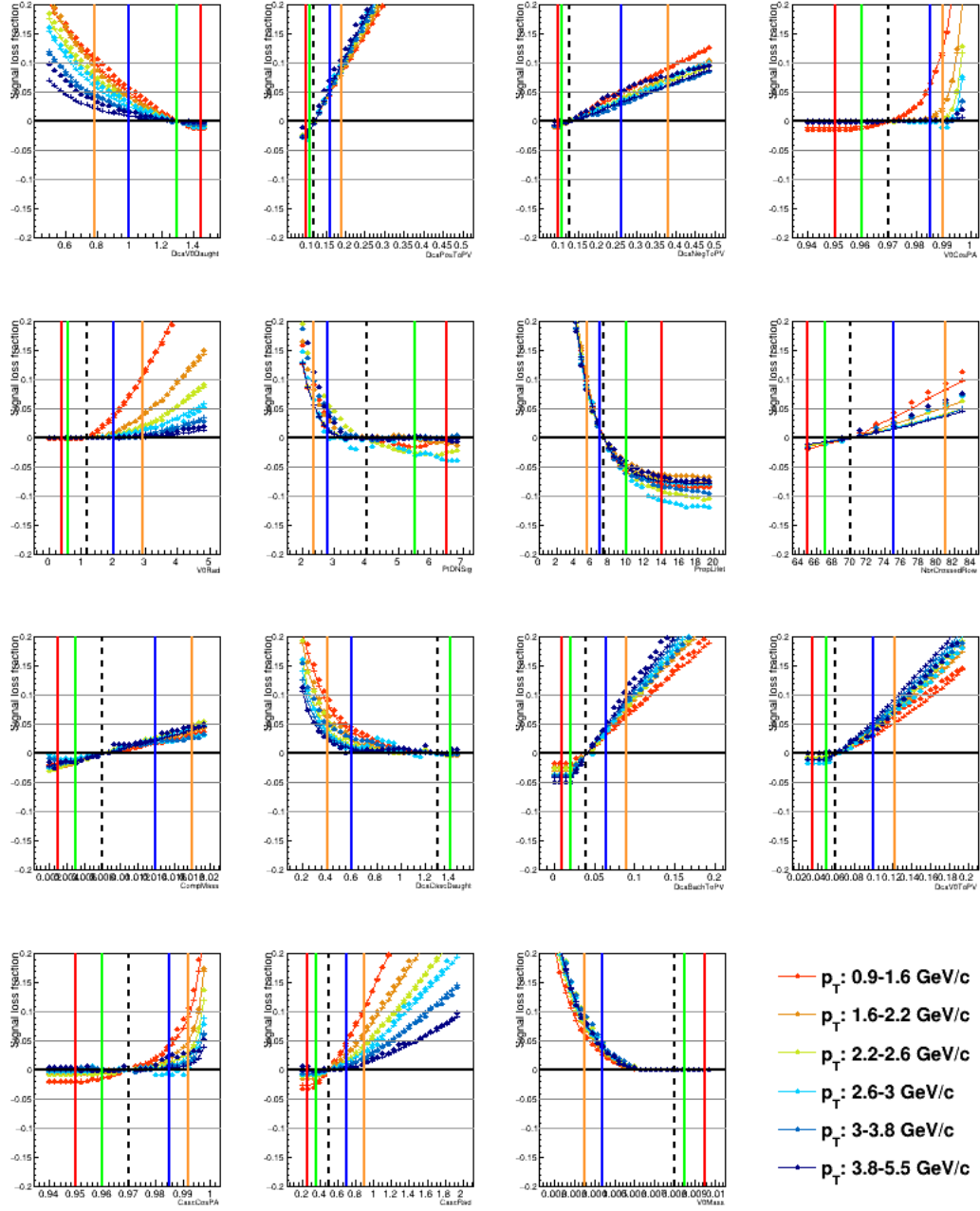


Figure 3.41: The signal-loss fractions for  $\bar{\Omega}^-$  in the 6  $p_T$  intervals (see legend) are shown. The data are the full points while the MC are the lines and cross points. The orange, blue, green and red lines represent, respectively, the loosest, loose, tight and tightest cuts. The black dashed line corresponds to the default variable cut. These figures were obtained in this work.

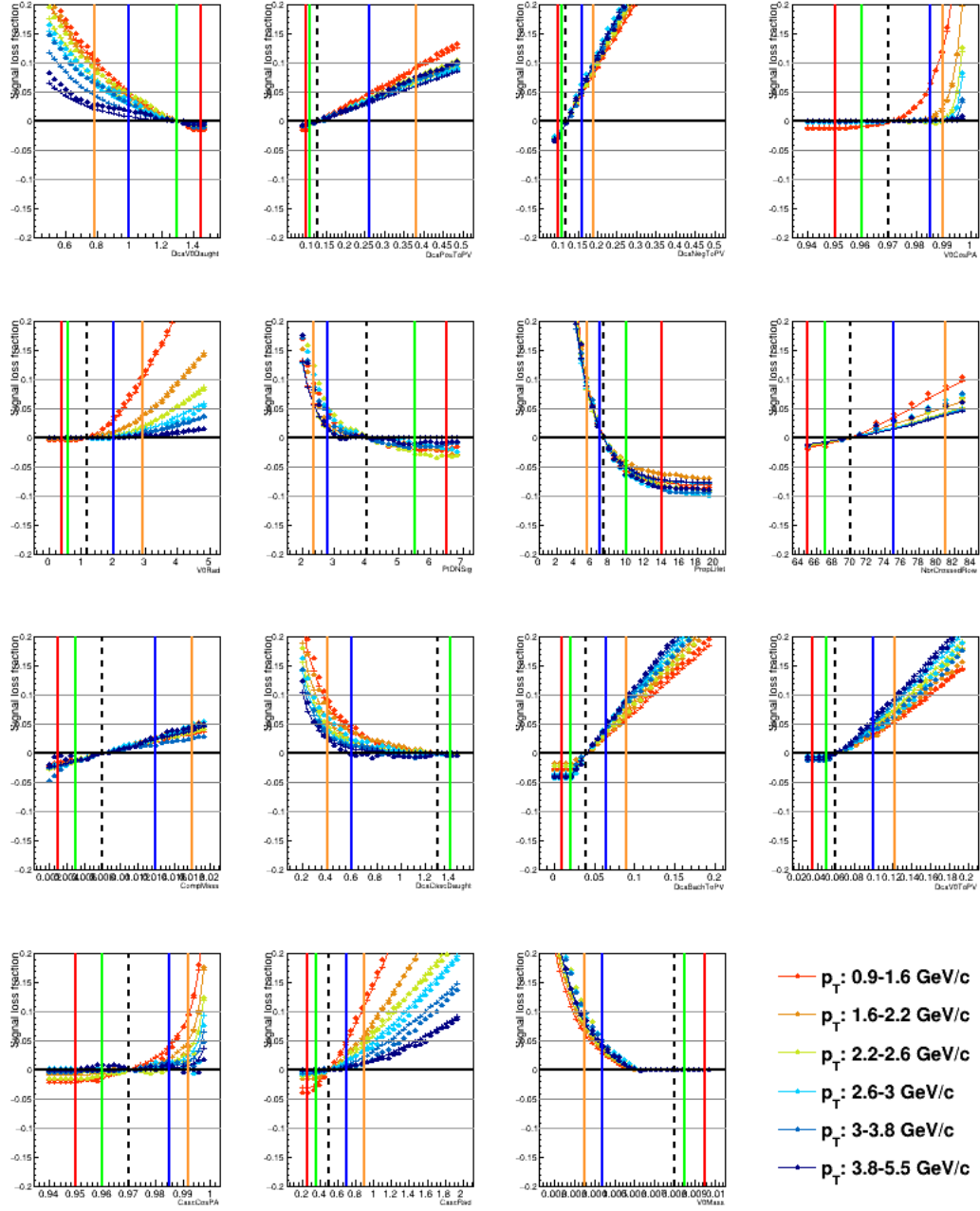


Figure 3.42: The signal-loss fractions for  $\bar{\Omega}^+$  in the 6  $p_T$  intervals (see legend) are shown. The data are the full points while the MC are the lines and cross points. The orange, blue, green and red lines represent, respectively, the loosest, loose, tight and tightest cuts. The black dashed line corresponds to the default variable cut. These figures were obtained in this work.

### 3.3.2 Cut variation and systematic uncertainties

Systematic uncertainties were evaluated taking into account the four cut values chosen during the signal loss fraction studies for every variable. The loosest, loose, tightest and tight cuts are listed in Tables 3.7-3.10 for V0s and Cascades.

In addition, the systematic error on the width of the signal window needed to be calculated. The signal extraction procedure was performed with a window of  $[\mu - 4\sigma, \mu + 4\sigma]$  and  $[\mu - 6\sigma, \mu + 6\sigma]$  in order to consider a signal loss and a signal gain.

The following procedure was applied:

- Corrected spectra were produced following the procedure described in Section 2 for all four selected cuts and for every variable;
- The absolute difference between the default corrected spectrum and the four spectra obtained with the varied cuts was calculated for every  $p_{\mathbf{T}}$  bin and for all variables;
- For each variable, the maximum absolute difference obtained for every  $p_{\mathbf{T}}$  bin was considered to be the systematic uncertainty;
- The total systematic error was obtained by adding in quadrature all those contributions only if the absolute maximum difference was larger than one Roger Barlow sigma described in the following;

The application of the Roger Barlow prescription [122] was used here since these are correlated quantities with multiplicity. The uncertainty  $\sigma_{\Delta}$  on the difference  $\Delta$  between two correlated quantities  $(a_1, a_2)$  measured with absolute uncertainties  $(\sigma_1, \sigma_2)$  was given by:

$$\Delta = a_2 - a_1, \quad \sigma_{\Delta} = \sqrt{|\sigma_2^2 - \sigma_1^2|}$$

The systematic uncertainties were evaluated in integrated multiplicity and in multiplicity classes.

#### Other sources of systematic uncertainties

- The systematic uncertainty associated to the material budget was estimated to be 4 % according to the approximation used in the analysis in pp collisions at  $\sqrt{s} = 13$  TeV[56]. For Cascades a more accurate study was available, to estimate the relative systematic uncertainty related

Topological Variable $K_s^0$	loosest cut	loose cut	tight cut	tightest cut
V0 transv. decay radius $R_2D$	$>0.2$ cm	$>0.35$ cm	$>0.6$ cm	$>0.7$ cm
DCA Negative track to PV	$>0.03$ cm	$>0.045$ cm	$>0.08$ cm	$>0.1$ cm
DCA Positive track to PV	$>0.02$ cm	$>0.035$ cm	$>0.1$ cm	$>0.13$ cm
DCA V0 Daughters	$< 1.45\sigma$	$< 1.25\sigma$	$< 0.65\sigma$	$< 0.5\sigma$
V0 cosine of Pointing Angle	$> 0.95$	$> 0.96$	$> 0.982$	$> 0.989$
<b>Selection</b>				
TPC $dE/dx$ selection	–	$< 5\sigma$	$< 2.5\sigma$	$< 2\sigma$
Proper Lifetime ( $mL/p$ )	–	$<40$ cm	$<24$ cm	$<15$ cm
Daughter track $N_{crossed}/N_{findable}$	$\geq 67$	$\geq 69$	$\geq 73$	$\geq 75$
TPC Crossed rows	–	–	$\geq 0.87$	–
Signal window	–	$4\sigma$	$6\sigma$	–

Table 3.7: The table shows for every variable the four cuts used to evaluate the systematic uncertainties for  $K_s^0$ .

Topological Variable $\Lambda$ ( $\bar{\Lambda}$ )	loosest cut	loose cut	tight cut	tightest cut
V0 transv. decay radius $R_2D$	$>0.2$ cm	$>0.3$ cm	$>0.8$ cm	$>1.05$ cm
DCA Negative track to PV	$>0.03(0.02)$ cm	$>0.045(0.035)$ cm	$>0.08(0.1)$ cm	$>0.1(0.13)$ cm
DCA Positive track to PV	$>0.02(0.03)$ cm	$>0.035(0.045)$ cm	$>0.1(0.08)$ cm	$>0.13(0.1)$ cm
DCA V0 Daughters	$< 1.45\sigma$	$< 1.25\sigma$	$< 0.75\sigma$	$< 0.6\sigma$
V0 cosine of Pointing Angle	$> 0.9$	$> 0.992$	$> 0.9965$	$> 0.9975$
<b>Selection</b>				
TPC $dE/dx$ selection	–	$< 5\sigma$	$< 2.5\sigma$	$< 2\sigma$
Proper Lifetime ( $mL/p$ )	–	$<40$ cm	$<24$ cm	$<20$ cm
Daughter track $N_{crossed}/N_{findable}$	$\geq 67$	$\geq 69$	$\geq 73$	$\geq 75$
TPC Crossed rows	–	–	$\geq 0.87$	–
Signal window	–	$4\sigma$	$6\sigma$	–

Table 3.8: The table shows for every variable the four cuts used to evaluate the systematic uncertainties for  $\Lambda$  ( $\bar{\Lambda}$ ).

Topological Variable $\Xi$	loosest cut	loose cut	tight cut	tightest cut
Cascade transv. decay radius $R_2D$	$>0.25$ cm	$>0.4$ cm	$>0.82$ cm	$>1.0$ cm
V0 transv. decay radius $R_2D$	$>0.4$ cm	$>0.6$ cm	$>2.0$ cm	$>2.5$ cm
DCA Negative track to PV	$>0.1$ cm	$>0.11$ cm	$>0.25(0.17)$ cm	$>0.45(0.25)$ cm
DCA Positive track to PV	$>0.1$ cm	$>0.11$ cm	$>0.17(0.25)$ cm	$>0.2(0.45)$ cm
DCA V0 Daughters	$< 1.5\sigma$	$< 1.4\sigma$	$< 1.0\sigma$	$< 0.8\sigma$
DCA Bachelor to PV	$>0.02$ cm	$>0.03$ cm	$>0.13$ cm	$>0.18$ cm
DCA V0 to PV	$>0.03$ cm	$>0.04$ cm	$>0.1$ cm	$>0.135$ cm
DCA Bachelor to V0	$>2$ cm	$>1.45$ cm	$>0.9$ cm	$>0.7$ cm
DCA Bachelor to Baryon	$>0.005$ cm	$>0.015$ cm	$>0.05$ cm	$>0.065$ cm
V0 cosine of Pointing Angle	$> 0.95$	$> 0.965$	$> 0.98$	$> 0.984$
Cascade cosine of Pointing Angle	$> 0.95$	$> 0.965$	$> 0.98$	$> 0.989$
V0 invariant mass window $\text{GeV}/c^2$	0.0095	0.0088	0.004	0.0031
<b>Selection</b>				
TPC $dE/dx$ selection	–	$< 5\sigma$	$< 2.8\sigma$	$< 2.4\sigma$
Proper Lifetime ( $mL/p$ )	$<18.5$ cm	$<17$ cm	$<12.5$ cm	$<10.5$ cm
Daughter track $N_{crossed}/N_{findable}$	$\geq 67$	$\geq 69$	$\geq 73$	$\geq 77$
Signal window	–	$4\sigma$	$6\sigma$	–

Table 3.9: The table shows for every variable the four cuts used to evaluate the systematic uncertainties for  $\Xi$ .

Topological Variable $\Omega$	loosest cut	loose cut	tight cut	tightest cut
Cascade transv. decay radius $R_2D$	$>0.25$ cm	$>0.35$ cm	$>0.7$ cm	$>0.9$ cm
V0 transv. decay radius $R_2D$	$>0.4$ cm	$>0.6$ cm	$>2.0$ cm	$>2.9$ cm
DCA Negative track to PV	$>0.1$ cm	$>0.11$ cm	$>0.26(0.16)$ cm	$>0.38(0.19)$ cm
DCA Positive track to PV	$>0.1$ cm	$>0.11$ cm	$>0.16(0.26)$ cm	$>0.19(0.38)$ cm
DCA V0 Daughters	$<1.45\sigma$	$<1.3\sigma$	$<1.0\sigma$	$<0.78\sigma$
DCA Bachelor to PV	$>0.01$ cm	$>0.02$ cm	$>0.065$ cm	$>0.09$ cm
DCA V0 to PV	$>0.035$ cm	$>0.04$ cm	$>0.1$ cm	$>0.122$ cm
DCA Bachelor to V0	-	$>1.4$ cm	$>0.6$ cm	$>0.4$ cm
V0 cosine of Pointing Angle	$>0.95$	$>0.96$	$>0.982$	$>0.99$
Cascade cosine of Pointing Angle	$>0.95$	$>0.96$	$>0.985$	$>0.992$
V0 invariant mass window $\text{GeV}/c^2$	0.0095	0.0088	0.0044	0.0035
<b>Selection</b>				
TPC $dE/dx$ selection	$<6.5\sigma$	$<5.5\sigma$	$<2.8\sigma$	$<2.35\sigma$
Proper Lifetime ( $mL/p$ )	$<14$ cm	$<10$ cm	$<7$ cm	$<5.5$ cm
Daughter track $N_{crossed}/N_{findable}$	$\geq 65$	$\geq 67$	$\geq 75$	$\geq 81$
Competing Cascade Rejection $\text{GeV}/c^2$	$>0.003$	$>0.005$	$>0.014$	$>0.018$
Signal window	-	$4\sigma$	$6\sigma$	-

Table 3.10: The table shows for every variable the four cuts used to evaluate the systematic uncertainties for  $\Omega$ .

to the material budget, the material budget was varied of  $\pm 4.5\%$  and  $A \times \epsilon$  recalculated. For  $\Xi^- + \bar{\Xi}^+$  the relative uncertainty followed a trend of a second order polynomial reaching values around 10% at low  $p_{\mathbf{T}}$ , 3% at medium  $p_{\mathbf{T}}$  and less than 1% at high  $p_{\mathbf{T}}$ . For  $\Omega^- + \bar{\Omega}^+$  this value was constant in  $p_{\mathbf{T}}$  around 2.5%.

- Another source of systematic uncertainty was the ITS||TOF cut used to reduce the out-of-bunch pile up. It was estimated to be 3% as done for the analysis in pp collision at  $\sqrt{s} = 13$  TeV [56].
- The systematic uncertainty associated to  $\epsilon_{part}(p_T)$  needed to be calculated by utilizing another MC production based on a different generator. However, such a MC production was not available for the data period of interest in this work. Given the fact that the  $\epsilon_{part}(p_T)$  factor for the  $\sqrt{s} = 7$  TeV [55] data set was compatible with the one from this study, i. e.  $\sqrt{s} = 5.02$  TeV data, it was therefore decided to interpolate the systematic uncertainties obtained from the  $\sqrt{s} = 7$  TeV analysis with a sigmoid function for V0s and an arctangent function for Cascades in order to obtain the values for the multiplicity and  $p_{\mathbf{T}}$  classes for the  $\sqrt{s} = 5.02$  TeV data for this study. The systematic was around 4% at low multiplicity and it rapidly decreases to 0% at high multiplicity.
- The systematic uncertainty on feed-down was defined as the absolute difference between the number of secondary  $\Lambda$  (or  $\bar{\Lambda}$ ) as calculated with the two methods **MC ratio** and **Double Charged  $\Xi$** . This contribution was only relevant at low  $p_{\mathbf{T}}$  where the relative systematic uncertainty is around 10%.

Figures 3.43-3.46 show the relative systematic uncertainties in integrated multiplicity for V0s and Cascades merging particles and antiparticles. In left panels, the total systematic errors are represented in black, the systematic uncertainties due to the contribution of the topological variables in blue and the systematic related to selection variables are given in red. In the same figure on the right panel, the contributions of every topological variable to the relative systematic uncertainty are shown.

Then, the total systematic uncertainties were applied to the corrected spectra. Since they were found to be compatible, it was decided to apply the systematic uncertainties calculated in integrated multiplicity also for all multiplicity classes in order to reduce statistical fluctuations. The systematic uncertainties calculated for particle and antiparticle separately are shown in Appendix C.

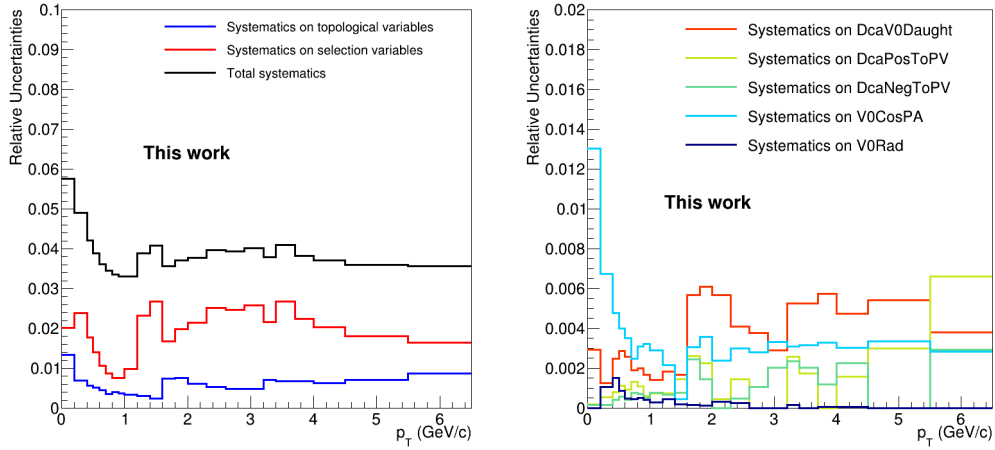


Figure 3.43: Left panel shows for  $K_s^0$  in integrated multiplicity as a function of  $p_T$  the total systematic uncertainties in black, the systematic uncertainties due to the topological cuts in blue and the ones from selection variables in red. The right panel shows for  $K_s^0$  the single contribution to the systematic uncertainties from every topological variable.

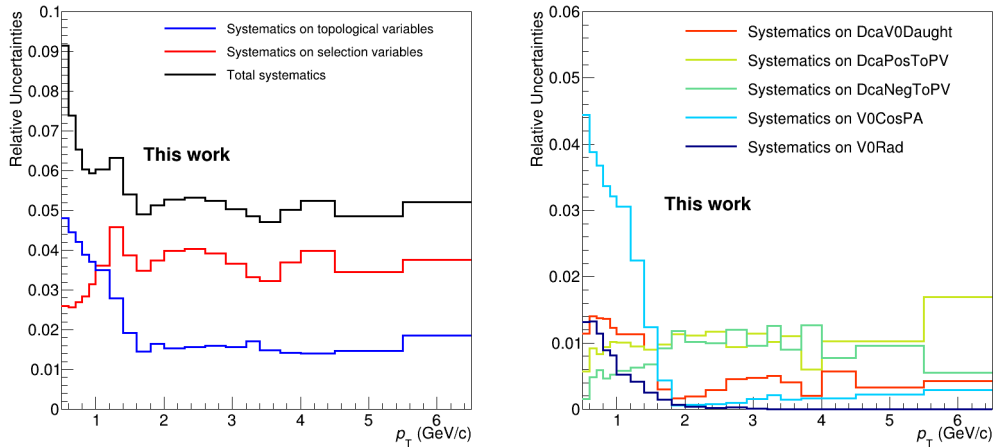


Figure 3.44: The left panel shows for  $\Lambda+\bar{\Lambda}$  in integrated multiplicity as a function of  $p_T$  the total systematic uncertainties in black, the systematic uncertainties due to the topological cuts in blue and the ones from selection variables in red. The right figure shows for  $\Lambda+\bar{\Lambda}$  the single contribution to the systematic uncertainties from every topological variable.



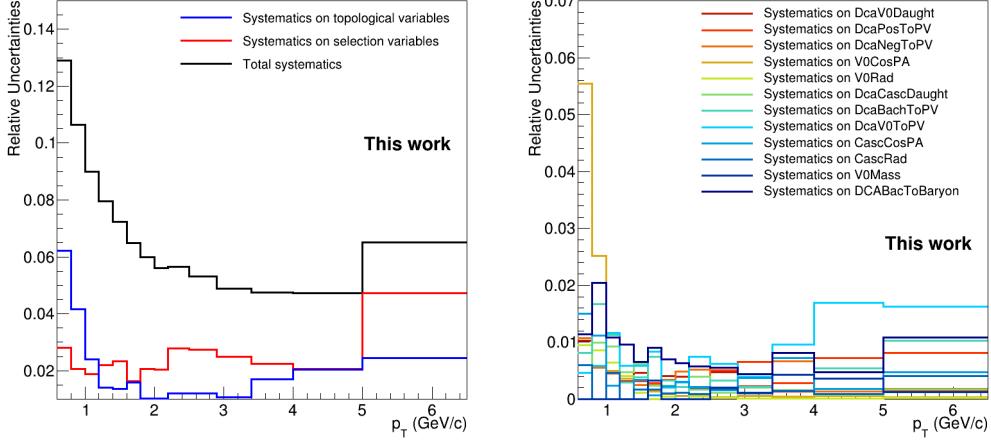


Figure 3.45: The left figure shows for  $\Xi^- + \Xi^+$  in integrated multiplicity as a function of  $p_T$  the total systematic uncertainties in black, the systematic uncertainties due to the topological cuts in blue and the ones from selection variables in red. The right panels shows for  $\Xi^- + \Xi^+$  the single contribution to the systematic uncertainties from every topological variable.

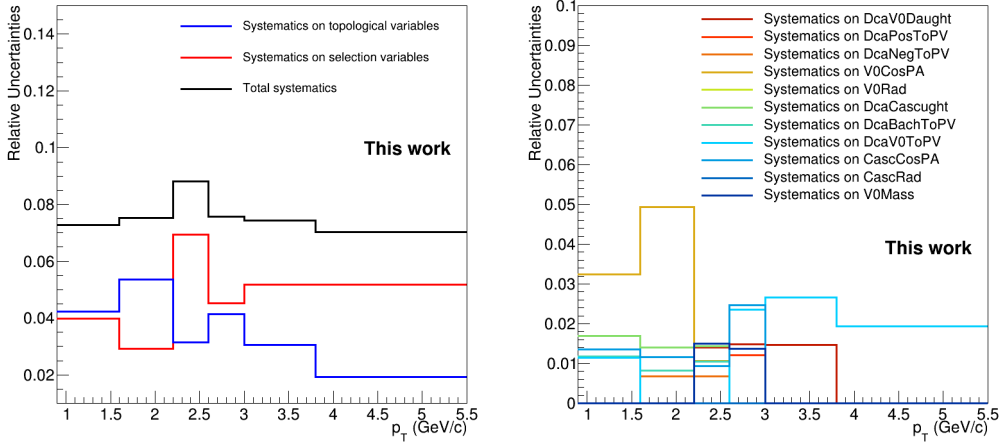


Figure 3.46: The left panel shows for  $\Omega^- + \bar{\Omega}^+$  in integrated multiplicity as a function of  $p_T$  the total systematic uncertainties in black, the systematic uncertainties due to the topological cuts in blue and the ones from selection variables in red. The right panel shows for  $\Omega^- + \bar{\Omega}^+$  the single contribution to the systematic uncertainties from every topological variable.

### 3.3.3 Uncorrelated systematic uncertainties

The uncorrelated (with multiplicity) systematic uncertainties were obtained with a similar procedure used in previous analyses in pp collisions at  $\sqrt{s} = 7$  TeV and  $\sqrt{s} = 13$  TeV. Firstly, the R-factor was calculated as defined by:

$$R = \frac{Y_{\text{modified-cut}}^{\text{mult-bin-}i}}{Y_{\text{default-cut}}^{\text{mult-bin-}i}} / \frac{Y_{\text{modified-cut}}^{0-100\%}}{Y_{\text{default-cut}}^{0-100\%}}; \quad (3.14)$$

where  $Y_{\text{modified-cut}}^{\text{mult-bin-}i}$  was a corrected spectrum with one modified cut in the  $i$ -multiplicity bin,  $Y_{\text{default-cut}}^{\text{mult-bin-}i}$  was a corrected spectrum with default cuts in the  $i$ -multiplicity bin,  $Y_{\text{modified-cut}}^{0-100\%}$  was a corrected spectrum with one modified cut in integrated multiplicity and  $Y_{\text{default-cut}}^{0-100\%}$  was a corrected spectrum with default cuts in integrated multiplicity.

This double ratio corresponds to the fraction of systematic uncertainty obtained for a specific variable in the multiplicity bin- $i$  with respect to the integrated one over multiplicity. The uncertainties associated with the ratio were computed according to the Roger Barlow prescription [122]. If  $Y_{\text{var}}$  and  $Y_{\text{def}}$  are two correlated quantities measured with absolute differences  $\sigma_{Y_{\text{var}}}$  and  $\sigma_{Y_{\text{def}}}$ , then the uncertainty associated with the difference between them is:

$$\Delta = Y_{\text{var}} - Y_{\text{def}}, \quad \sigma_{\Delta} = \sqrt{|\sigma_{Y_{\text{var}}}^2 - \sigma_{Y_{\text{def}}}^2|} \quad (3.15)$$

To calculate the uncertainty on the ratio, the relative difference can be considered as:

$$\frac{\Delta}{Y_{\text{def}}} = \frac{Y_{\text{var}} - Y_{\text{def}}}{Y_{\text{def}}} = \frac{Y_{\text{var}}}{Y_{\text{def}}} - 1 \quad (3.16)$$

The uncertainty on ratio is equal to the uncertainty on the relative difference. In order to obtain the uncertainty on the ratio, the propagation to the relative difference error is calculated:

$$\delta \left( \frac{Y_{\text{var}}}{Y_{\text{def}}} \right) = \delta \left( \frac{\Delta}{Y_{\text{def}}} \right) = \frac{\Delta}{Y_{\text{def}}} \sqrt{\frac{\sigma_{\Delta}^2}{\Delta^2} + \frac{\sigma_{Y_{\text{def}}}^2}{Y_{\text{def}}^2}} \quad (3.17)$$

If the R-factor was compatible with unity, it was considered independent of the multiplicity.

The R-factors versus multiplicity for every cut under study are shown in Figures 3.47–3.48 for  $K_s^0$  and  $\Lambda + \bar{\Lambda}$  and in Figures 3.49–3.50 for  $\Xi^- + \bar{\Xi}^+$  and  $\Omega^- + \bar{\Omega}^+$ , together with a fit with a first order polynomial function. These were computed over wider multiplicity and  $p_{\mathbf{T}}$  bins in order to reduce statistical fluctuations.

The fraction of uncorrelated systematic uncertainties were obtained by summing all  $|R - 1|$  in quadrature provided that the slope parameter of the fit function was not compatible with zero.

The fraction of uncorrelated systematic uncertainties for every multiplicity class was shown in Figures 3.51 and 3.52 together with the relative total systematic errors.

Since the uncorrelated systematic uncertainties changed with multiplicity and  $p_{\mathbf{T}}$ , the final value for the uncorrelated systematic uncertainty was the maximum between the multiplicity classes in every  $p_{\mathbf{T}}$  bin.

The fraction of the total systematic uncertainties which are uncorrelated is shown in Fig. 3.53 and 3.54. For V0s the fraction ranges from 20% to 40% at low  $p_{\mathbf{T}}$ , from 40% to 60% in the intermediate  $p_{\mathbf{T}}$  region and reaches 50 % for  $K_s^0$  and 60% for  $\Lambda + \bar{\Lambda}$  at high  $p_{\mathbf{T}}$ , respectively.

For  $\Xi^- + \bar{\Xi}^+$  the fraction of uncorrelated systematic uncertainty is about 40% in the intermediate  $p_{\mathbf{T}}$  region and increases to 65% at both high and low  $p_{\mathbf{T}}$ , while for  $\Omega^- + \bar{\Omega}^+$  it is around 70% at low  $p_{\mathbf{T}}$ , 45% at intermediate  $p_{\mathbf{T}}$  and 80% at high  $p_{\mathbf{T}}$ .

In order to obtain the uncorrelated systematic uncertainties in the  $p_{\mathbf{T}}$  bins used in the present analysis, the fractions of uncorrelated systematic uncertainties were multiplied by the total systematic uncertainty in each corresponding  $p_{\mathbf{T}}$  bins.

Finally, in order to further reduce the effect of statistical fluctuations, a procedure of “smoothing” was applied to the systematic uncertainties. In particular, the final systematic uncertainty applied to the corrected spectra was obtained for  $\Xi^- + \bar{\Xi}^+$  by fitting the relative uncertainties with a second order polynomial function up to 2.5 GeV/ $c$  followed by a zero order polynomial up to 5 GeV/ $c$ . For  $\Omega^- + \bar{\Omega}^+$  the final systematic uncertainty was obtained by fitting the relative uncertainties with a zero order polynomial function. Figure 3.56 shows the relative total systematic uncertainties together with the uncorrelated values and the smoothing functions.

The smoothing procedure was not applied to the V0s relative systematic uncertainties because their shape as a function of  $p_{\mathbf{T}}$  did not allow it.

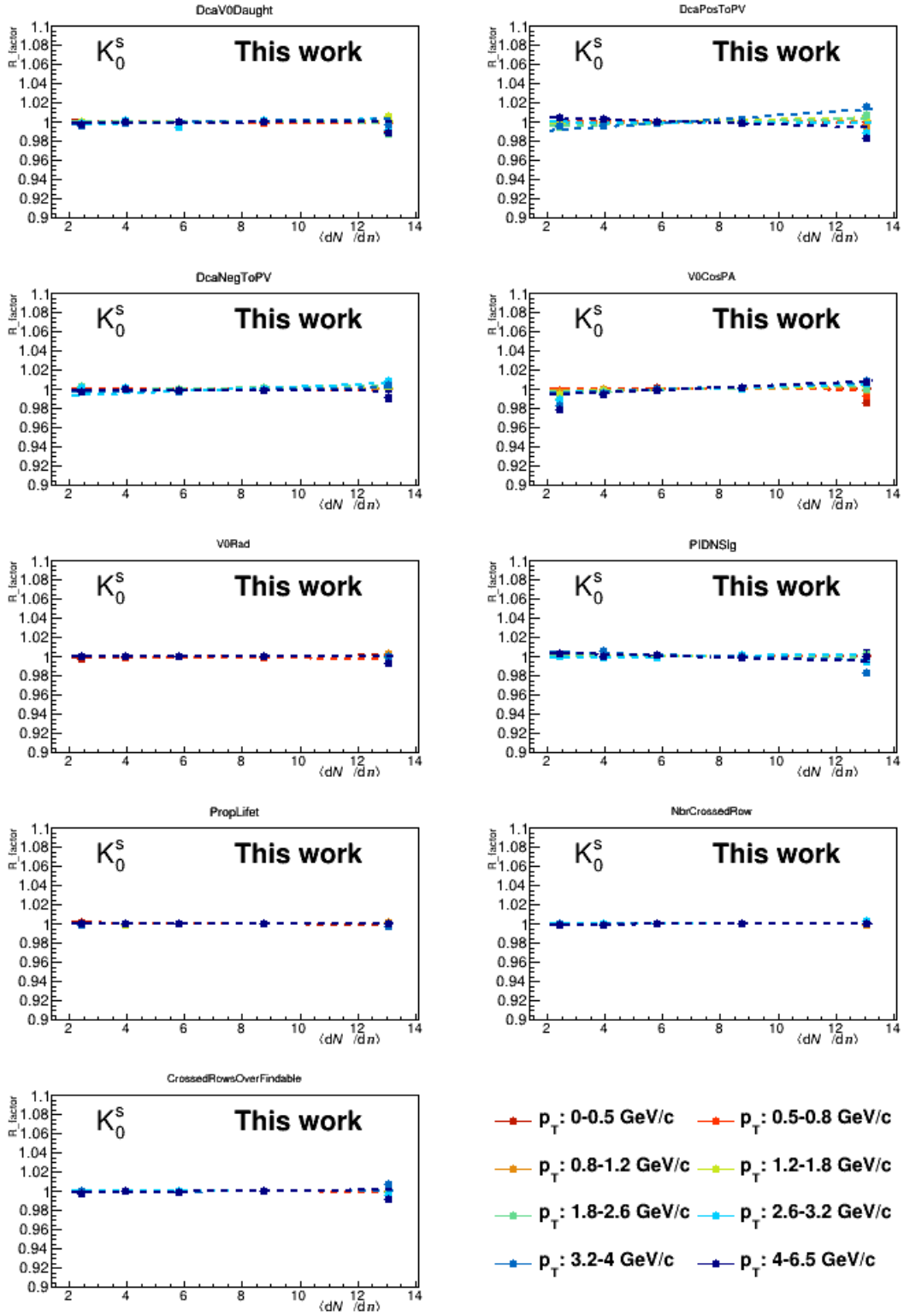


Figure 3.47: R-factors for  $K_s^0$  as a function of multiplicity in  $p_T$  intervals and for different variable cuts as indicated.

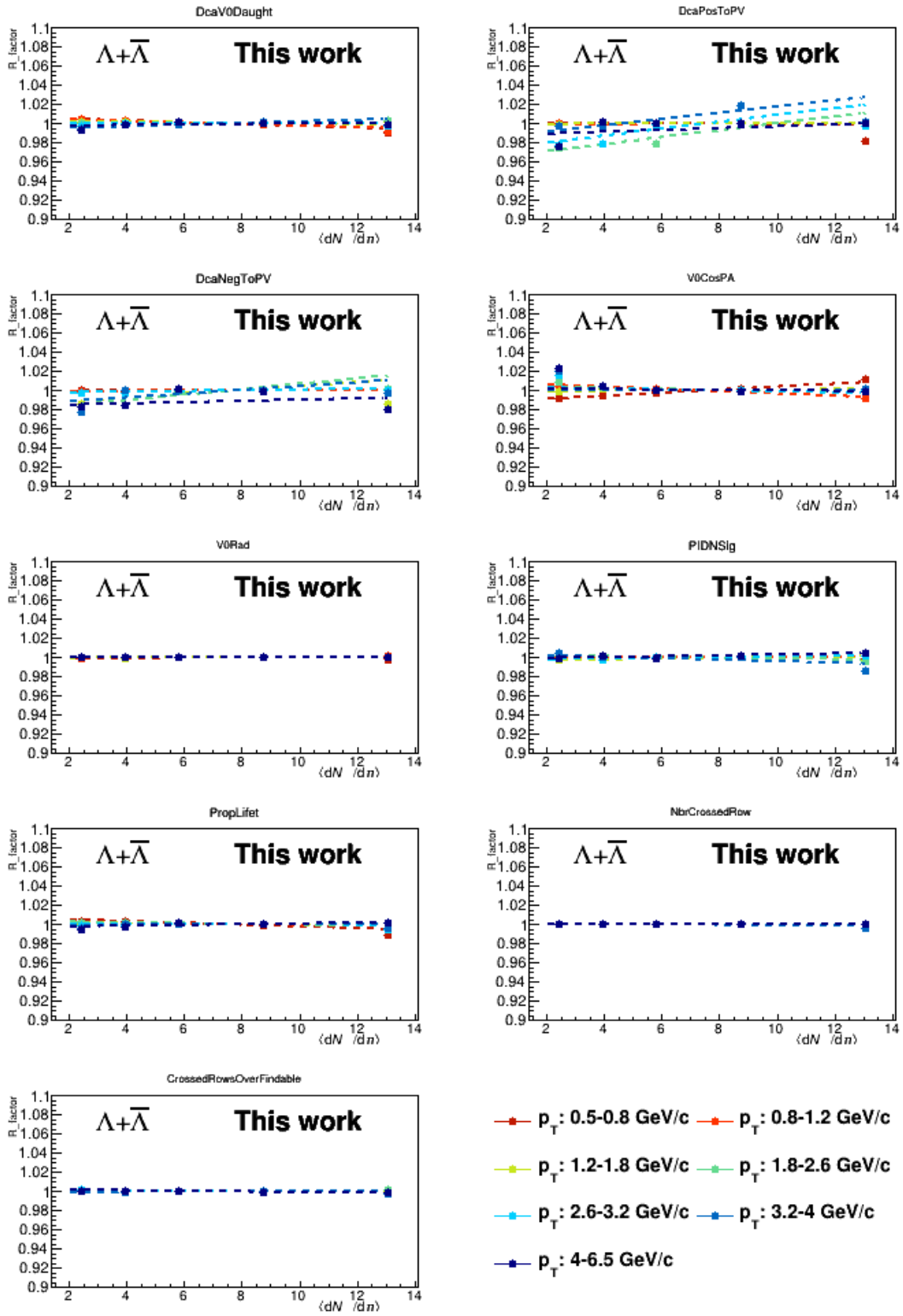


Figure 3.48: R-factors for  $\Lambda + \bar{\Lambda}$  as a function of multiplicity in  $p_T$  intervals and for different variable cuts as indicated.

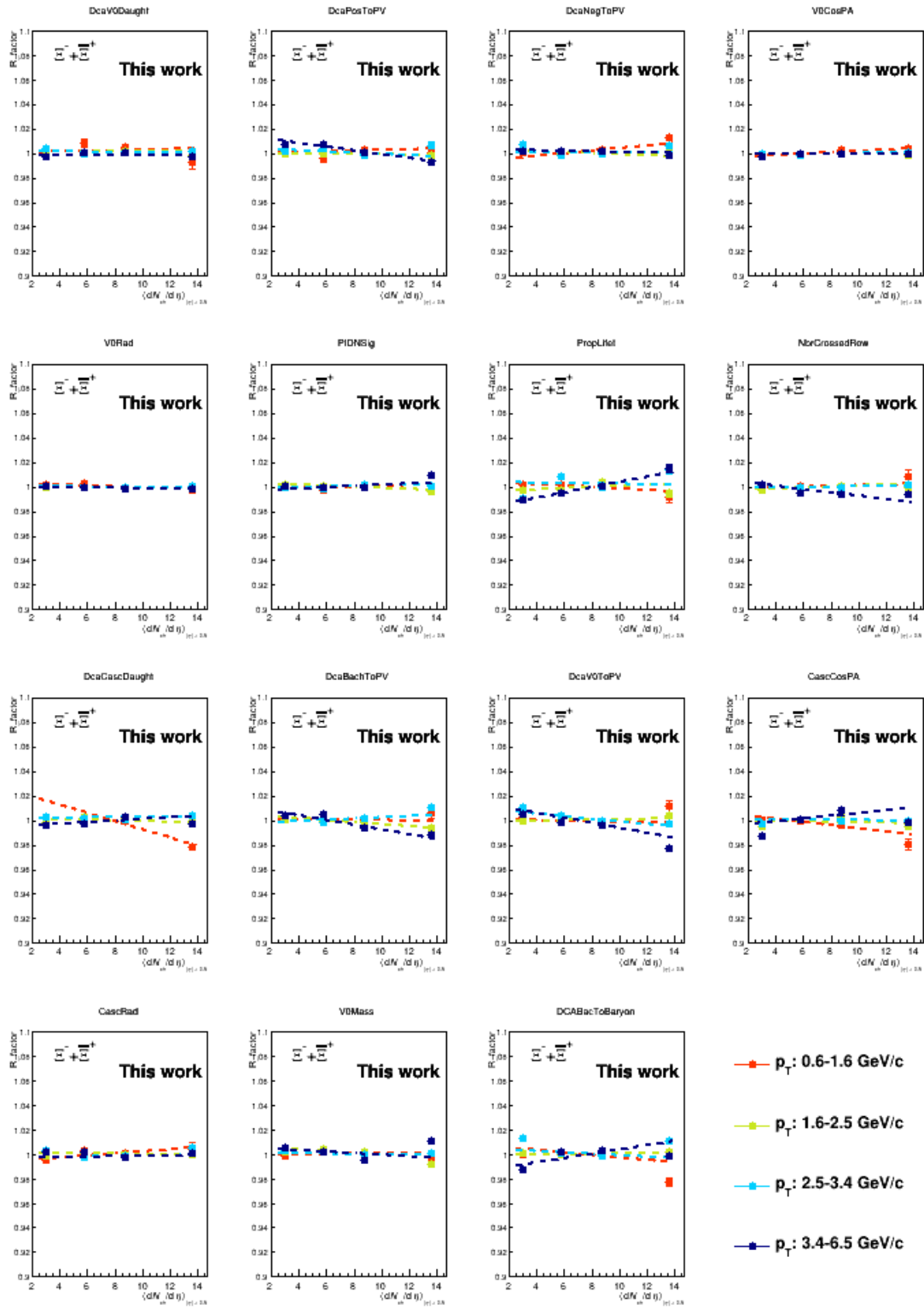


Figure 3.49: R-factors for  $\Xi^- + \Xi^+$  as a function of multiplicity in  $p_T$  intervals and for different variable cuts as indicated.

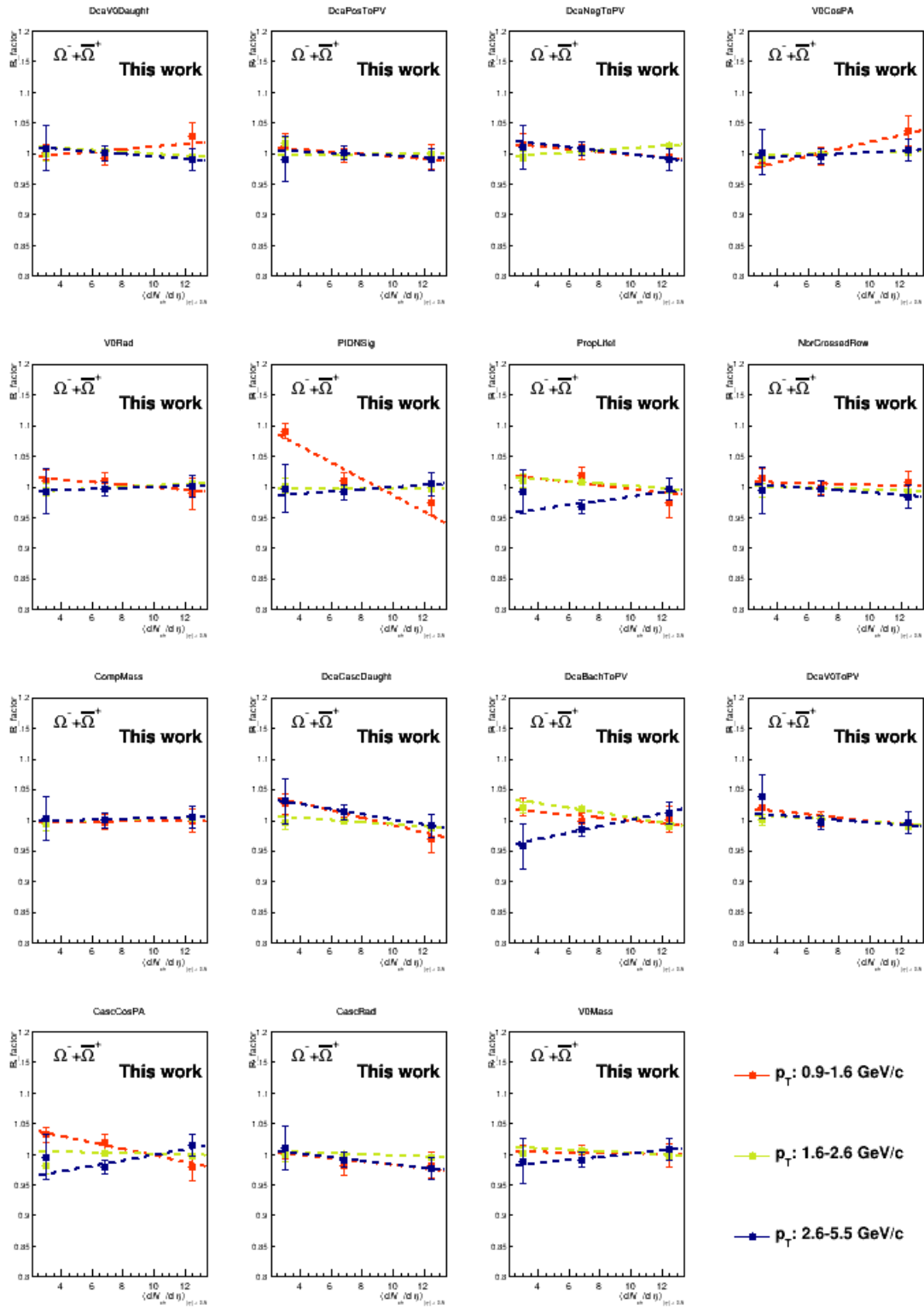


Figure 3.50: R-factors for  $\Omega^- + \bar{\Omega}^+$  as a function of multiplicity in  $p_T$  intervals and for different variable cuts as indicated.

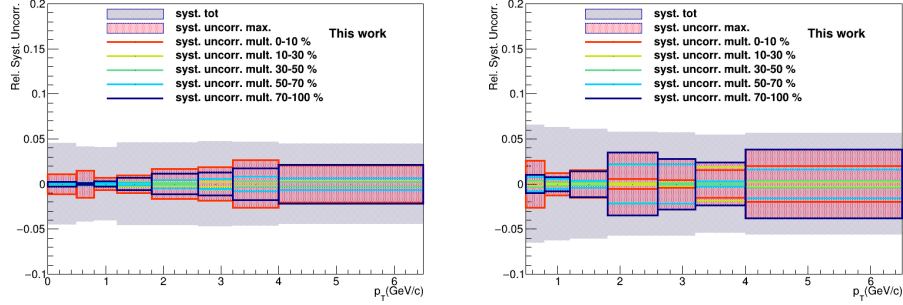


Figure 3.51: Fractions of uncorrelated systematic uncertainties for  $K_s^0$  (left panel) and  $\Lambda + \bar{\Lambda}$  (right panel) shown together with the relative uncorrelated systematic uncertainties.

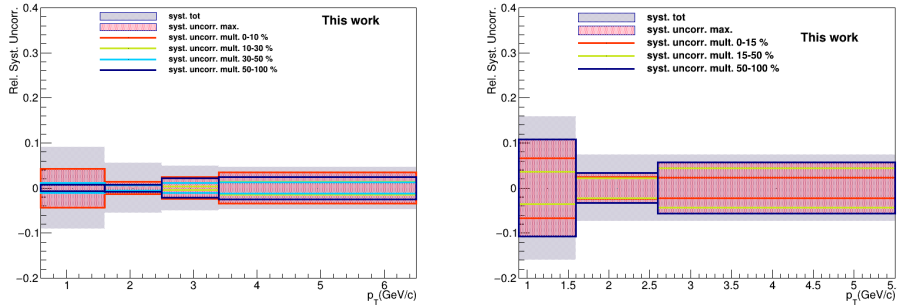


Figure 3.52: Fraction of uncorrelated systematic uncertainties for  $\Xi^- + \bar{\Xi}^+$  (left panel) and  $\Omega^- + \bar{\Omega}^+$  (right panel) shown together with the relative uncorrelated systematic uncertainties.

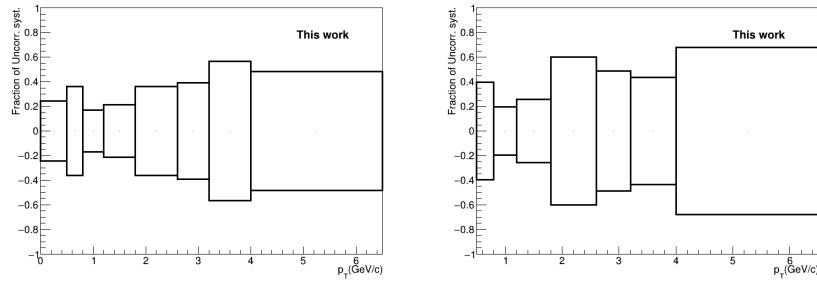


Figure 3.53: Fractions of the total systematic uncertainties which are uncorrelated for  $K_s^0$  (left panel) and  $\Lambda + \bar{\Lambda}$  (right panel).



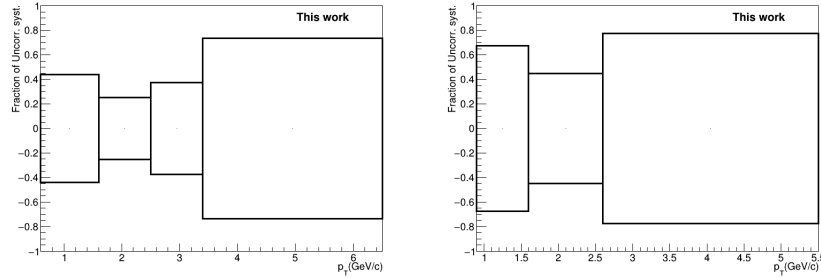


Figure 3.54: Fractions of the total systematic uncertainties which are uncorrelated for  $\Xi^- + \bar{\Xi}^+$  (left panel) and  $\Omega^- + \bar{\Omega}^+$  (right panel).

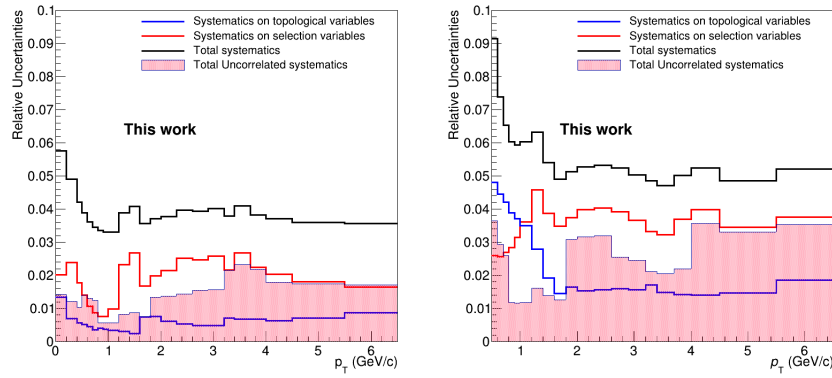


Figure 3.55:  $K_s^0$  (left panel) and  $\Lambda + \bar{\Lambda}$  (right panel) total relative systematic uncertainties together with uncorrelated uncertainties.

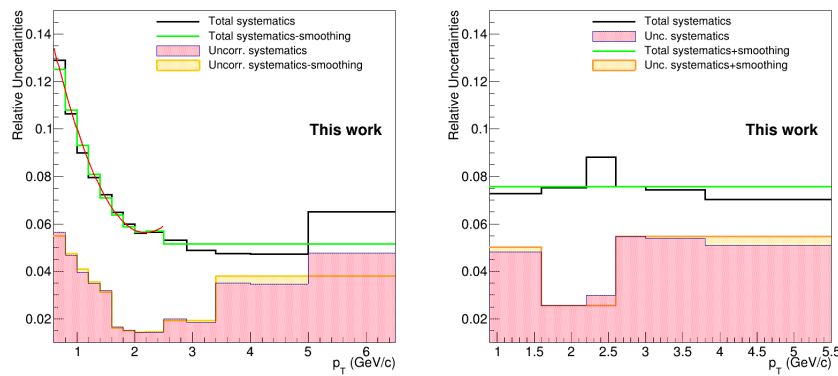


Figure 3.56:  $\Xi^- + \bar{\Xi}^+$  (left panel) and  $\Omega^- + \bar{\Omega}^+$  (right panel) total relative systematic uncertainties together with uncorrelated uncertainties and smoothing.

### 3.3.4 Corrected Spectra and yield extraction

The transverse momentum corrected spectra were obtained by dividing the raw spectra calculated in Sec. 3.2.3 by the acceptance times efficiency described in Sec. 3.2.6 and applying all the normalization and corrections described previously. The final transverse momentum spectra for  $\Lambda$  and  $\bar{\Lambda}$ ,  $\Xi^-$  and  $\bar{\Xi}^+$  and  $\Omega^-$  and  $\bar{\Omega}^+$  in all multiplicity classes and in integrated multiplicity (INEL>0) are shown in Figures 3.57-3.59 (the final transverse momentum spectra for  $K_s^0$  are shown in Chapter 4). Statistical uncertainties are identified by errors bars and the systematic ones by boxes. Scalar factors were applied in order to improve visibility. The bottom panels present the ratio of the corrected spectra for different multiplicity classes with respect to the INEL>0 case.

The next step consists of the calculation of the  $p_T$ -integrated yield: this is why the corrected spectra just shown were fitted with a Levy-Tsallis function (dashed-grey curves) [116]. Its equation is:

$$\frac{d^2N}{dp_T dy} = \frac{dN}{dy} p_T \frac{(n-1)(n-2)}{nT[nT + m(n-2)]} \left(1 + \frac{m_T - m}{nT}\right)^{-n} \quad (3.18)$$

where  $T$  is the kinetic freeze-out temperature,  $m_T$  is the transverse mass,  $n$  and  $m$  dimensionless parameters. The  $p_T$ -integrated yield was calculated summing the integral of the corrected spectra in the measured range to the integral of the Levy-Tsallis function [116] outside the measured range down to 0 in  $p_T$ . In addition, the average transverse momentum  $\langle p_T \rangle$  of the particle distributions was obtained averaging the corrected spectra in the measured range and complementing with the extrapolation with the Levy-Tsallis function outside the measured range down to 0 in  $p_T$ .

See Chapter 4 for the final momentum spectra for  $K_s^0$ ,  $\Lambda + \bar{\Lambda}$ ,  $\Xi^- + \bar{\Xi}^+$  and  $\Omega^- + \bar{\Omega}^+$  and for the  $p_T$ -integrated yield and the  $\langle p_T \rangle$  for  $K_s^0$ ,  $\Lambda$ ,  $\bar{\Lambda}$ ,  $\Lambda + \bar{\Lambda}$ ,  $\Xi^-$ ,  $\bar{\Xi}^+$ ,  $\Xi^- + \bar{\Xi}^+$ ,  $\Omega^-$ ,  $\bar{\Omega}^+$  and  $\Omega^- + \bar{\Omega}^+$ .

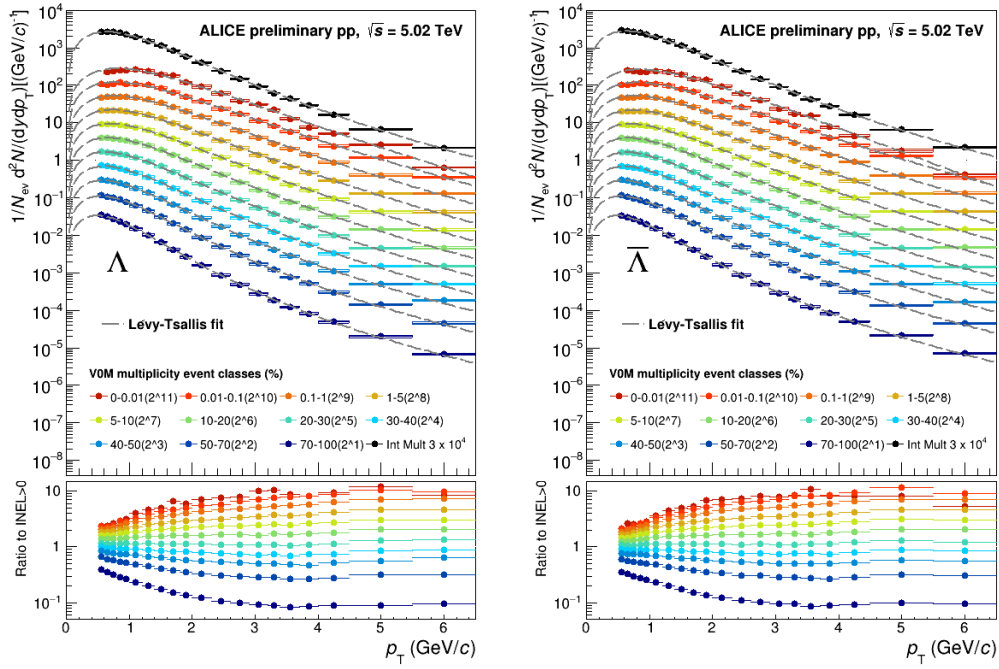


Figure 3.57:  $\Lambda$  and  $\bar{\Lambda}$  transverse momentum corrected spectra for all multiplicity classes and integrated multiplicity are shown. Statistical uncertainties are identified by errors bars and systematic ones by boxes. The bottom panel presents the ratio of the multiplicity dependent corrected spectra w.r.t. the integrated multiplicity spectrum. The dashed-grey curves show the Levy-Tsallis [116] fits to the transverse momentum distribution. Scalar factors, indicated in the legend, are applied in order to have a better display of the transverse momentum spectra.

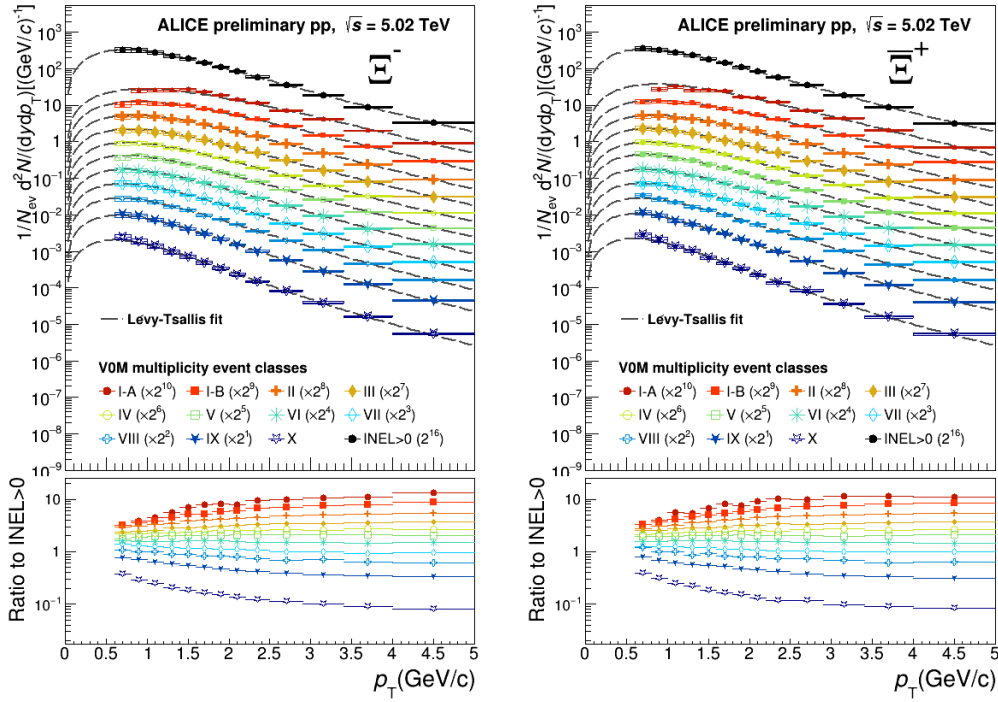


Figure 3.58:  $\Xi^-$  and  $\Xi^+$  transverse momentum corrected spectra for all multiplicity classes and integrated multiplicity are shown. Statistical uncertainties are identified by errors bars and systematic ones by boxes. The bottom panel presents the ratio of the multiplicity dependent corrected spectra w.r.t. the integrated multiplicity spectrum. The dashed-grey curves show the Levy-Tsallis [116] fits to the transverse momentum distribution. Scalar factors, indicated in the legend, are applied in order to have a better display of the transverse momentum spectra.

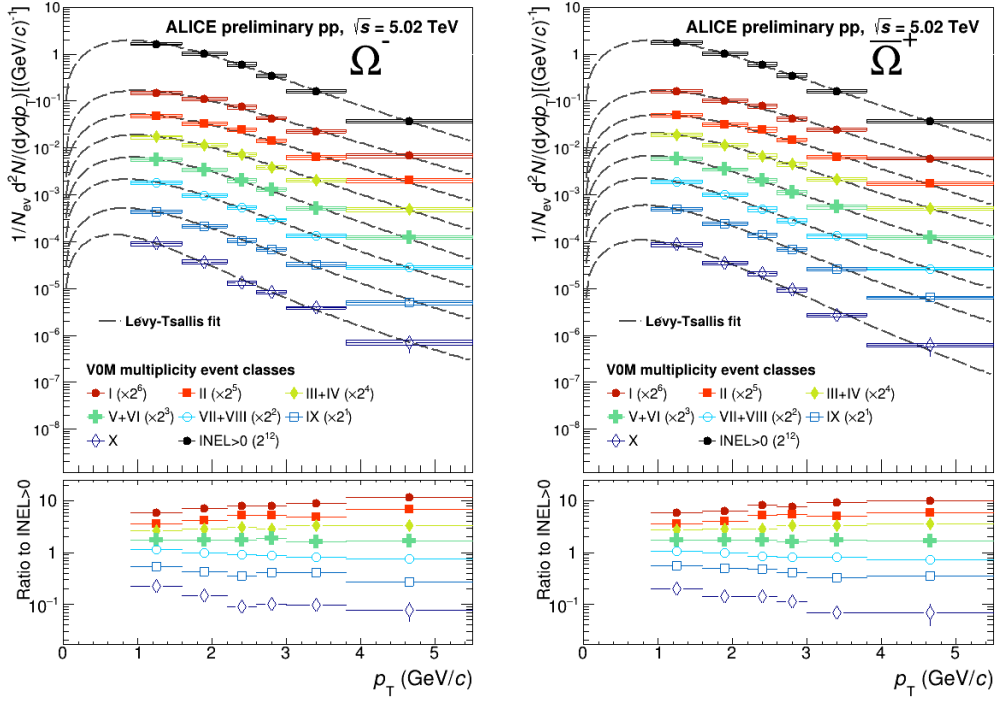


Figure 3.59:  $\Omega^-$  and  $\bar{\Omega}^+$  transverse momentum corrected spectra for multiplicity classes and integrated multiplicity are shown. Statistical uncertainties are identified by errors bars and systematic ones by boxes. The bottom panel presents the ratio of the multiplicity dependent corrected spectra w.r.t. the integrated multiplicity spectrum. The dashed-grey curves show the Levy-Tsallis [116] fits to the transverse momentum distribution. Scalar factors, indicated in the legend, are applied in order to have a better display of the transverse momentum spectra.

### 3.3.5 Systematic uncertainty on extrapolation

As explained in the previous section, the momentum distributions were fitted with the Levy-Tsallis function [116] to extrapolate the yield down to 0 in  $p_{\mathbf{T}}$ . The systematic uncertainties on extrapolation at low  $p_{\mathbf{T}}$  were calculated changing the fit function and applying the following procedure:

- The corrected spectra are fitted with four different functions: Boltzmann,  $m_T$ -exponential, Fermi Dirac and Blast-Wave distributions;
- The  $p_{\mathbf{T}}$ -integrated yield and  $\langle p_{\mathbf{T}} \rangle$  are measured in all four cases;
- the absolute difference between the default  $p_{\mathbf{T}}$ -integrated yield and  $\langle p_{\mathbf{T}} \rangle$  and the corresponding values obtained with the four functions is calculated;
- The absolute maximum difference is taken as the systematic uncertainty on the extrapolation.

In Figures 3.60, the spectra together with the fit of the five functions are presented for  $\Lambda + \bar{\Lambda}$ ,  $\Xi^- + \bar{\Xi}^+$  and  $\Omega^- + \bar{\Omega}^+$ . It was necessary to restrict the fit of the spectra to the lowest  $p_{\mathbf{T}}$  because at high  $p_{\mathbf{T}}$  the spectra were hard and the statistically-inspired functions deviate in this region.

Figure 3.61 shows the final relative systematic uncertainties for the extrapolation together with the contributions from the four functions on the  $p_{\mathbf{T}}$ -integrated yield and on  $\langle p_{\mathbf{T}} \rangle$  for  $\Lambda + \bar{\Lambda}$ ,  $\Xi^- + \bar{\Xi}^+$  and  $\Omega^- + \bar{\Omega}^+$ . The smallest contribution among all multiplicity classes defined the “correlated” with multiplicity uncertainty component and is identified by the black dashed line. The systematic uncertainties on extrapolation at low  $p_{\mathbf{T}}$  calculated for particle and antiparticle separately are shown in Appendix C.

The systematic errors related to the extrapolation were added in quadrature to the ones related to the  $p_{\mathbf{T}}$ -integrated yield and the average  $p_{\mathbf{T}}$  previously calculated (see section 3.3.2).

The final results on corrected transverse momentum distributions,  $p_{\mathbf{T}}$ -integrated yield and the average  $p_{\mathbf{T}}$  for all particle species are shown and discussed in the next chapter.

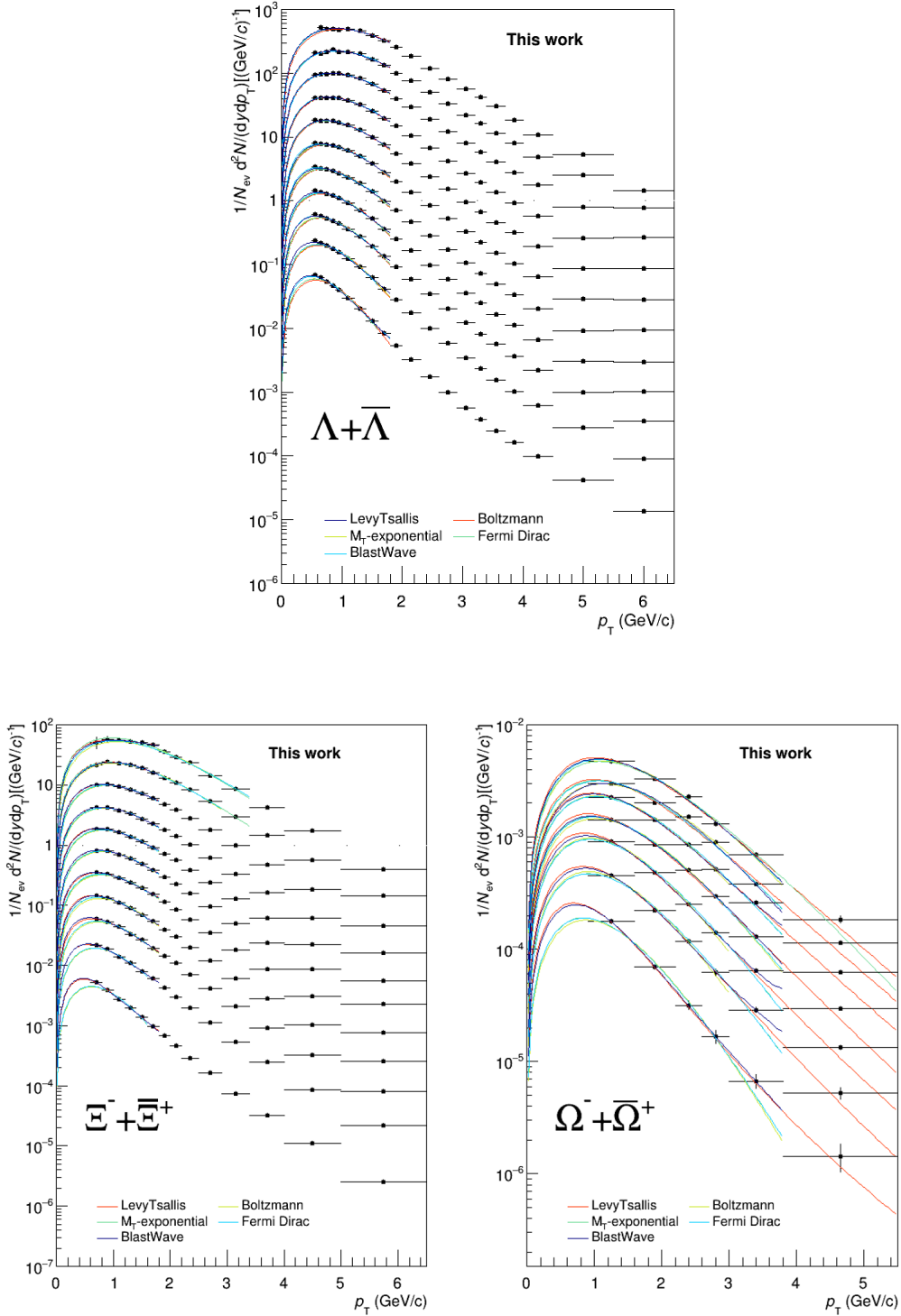


Figure 3.60: The corrected spectra for  $\Lambda + \bar{\Lambda}$ ,  $\Xi^- + \bar{\Xi}^+$  and  $\Omega^- + \bar{\Omega}^+$  are fitted with Levy-Tsallis, Boltzmann,  $m_T$ -exponential, Fermi Dirac and Blast Wave functions. For  $\Xi^- + \bar{\Xi}^+$  scalar factors are applied to better display the spectra. They are not indicated in a legend neither the multiplicity classes because the focus is on shape of the five fits.

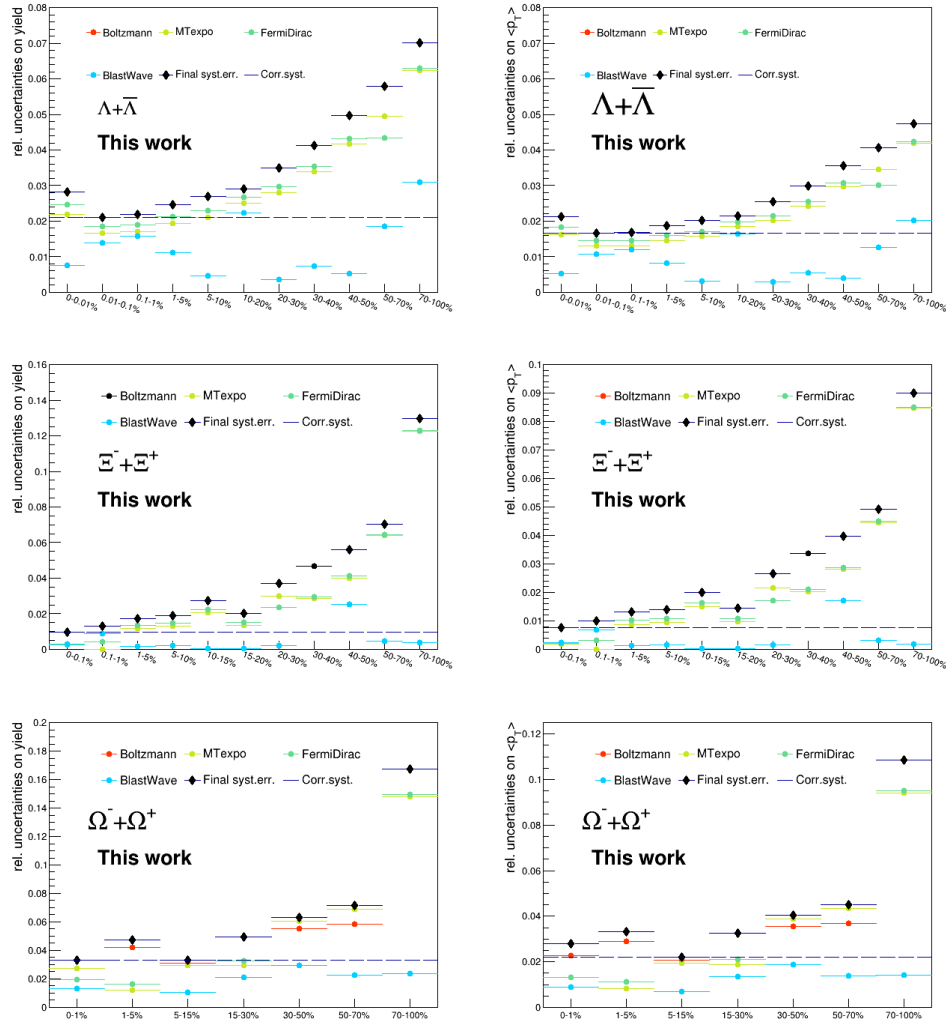


Figure 3.61: Relative systematic uncertainties on  $p_T$ -integrated yield (left panel) and  $\langle p_T \rangle$  (right panel) for  $\Lambda + \bar{\Lambda}$  (top panels),  $\Xi^- + \bar{\Xi}^+$  (middle panels) and  $\Omega^- + \bar{\Omega}^+$  (bottom panels). The “correlated” with multiplicity uncertainty component and is identified by the black dashed line.



# Chapter 4

## Results and discussion

In Chapter 3 the strategy to obtain the transverse momentum spectra, the  $p_{\mathbf{T}}$ -integrated yields and the average transverse momentum  $\langle p_{\mathbf{T}} \rangle$  together with their statistical and systematic uncertainties, was discussed. This Chapter is dedicated to the final results obtained from the data analysis in pp collisions at  $\sqrt{s} = 5.02$  TeV and to the comparison with the previous pp analyses at  $\sqrt{s} = 7$  TeV [55] and  $\sqrt{s} = 13$  TeV [56] as well as the p-Pb analysis at  $\sqrt{s_{NN}} = 5.02$  TeV [57].

Figure 4.1 shows the final transverse momentum spectra for  $K_S^0$ ,  $\Lambda + \bar{\Lambda}$ ,  $\Xi^- + \bar{\Xi}^+$  and  $\Omega^- + \bar{\Omega}^+$  in integrated multiplicity and for all multiplicity classes. Due to the lack in statistics, some bins at high multiplicity and low/high  $p_{\mathbf{T}}$  are discarded. The vertical bars indicate the statistical uncertainties while the boxes indicates the systematic uncertainties. Scalar factors were applied in order to improve visibility and they are indicated in the legend. The dashed grey curves correspond to the Levy-Tsallis function [116] fit which was used to calculate the  $p_{\mathbf{T}}$ -integrated yields and the  $\langle p_{\mathbf{T}} \rangle$ . Therefore, the bottom panels show the ratio of the multiplicity dependent transverse momentum distributions with respect to the integrated multiplicity transverse momentum spectrum. The systematic uncertainties on the ratio were evaluated only for the uncorrelated contributions through multiplicity.

The hardening of the spectra with multiplicity can be observed for all particle species under study and it could be quantified with the values of  $\langle p_{\mathbf{T}} \rangle$  (see Figures 4.7 and 4.8). The same phenomenon was also observed in other pp [55] [56] and p-Pb [57] analyses. It is relevant to mention that the ratios of  $p_{\mathbf{T}}$  spectra with respect to the  $p_{\mathbf{T}}$  spectrum in integrated multiplicity, reach a plateau for  $p_{\mathbf{T}} > 4$  GeV/c for all particle species under study.

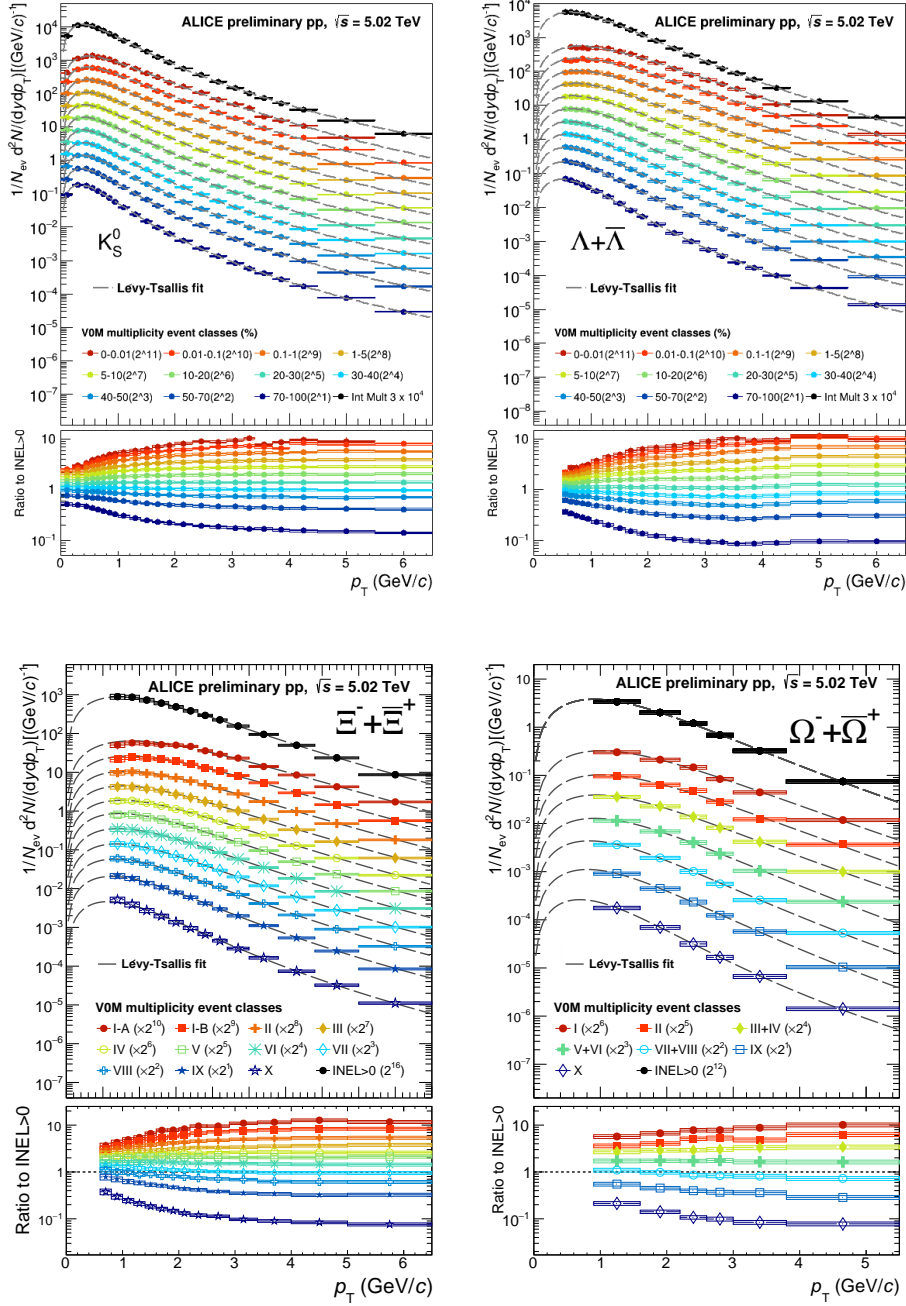


Figure 4.1:  $K_S^0$ ,  $\Lambda + \bar{\Lambda}$ ,  $\Xi^- + \bar{\Xi}^+$  and  $\Omega^- + \bar{\Omega}^+$  transverse momentum corrected spectra for all multiplicity classes (colored symbols) and in integrated multiplicity (black solid points). Statistical and systematic uncertainties are indicated by error bars and boxes, respectively. The bottom panels present the ratios of the multiplicity dependent corrected spectra w.r.t. the integrated multiplicity spectrum. The dashed-grey curves show the Levy-Tsallis [116] fits to the transverse momentum distributions. Scalar factors, indicated in the legend, are applied in order to have a better display of the spectra.

## 4.1 $p_{\mathbf{T}}$ -integrated yields and $\langle p_{\mathbf{T}} \rangle$

The  $p_{\mathbf{T}}$ -integrated yields ( $\langle dN/dy \rangle$ ) and the average  $p_{\mathbf{T}}$  ( $\langle p_{\mathbf{T}} \rangle$ ) as a function of the charged-particle multiplicity at midrapidity were calculated for V0s and Cascades.

Figures 4.2, 4.3 and 4.4 show the comparison of  $\langle dN/dy \rangle$  (left panel) and  $\langle p_{\mathbf{T}} \rangle$  (right panel) for  $\Lambda$  vs  $\bar{\Lambda}$ ,  $\Xi^-$  vs  $\bar{\Xi}^+$  and  $\Omega^-$  vs  $\bar{\Omega}^+$ , respectively. The statistical uncertainties are indicated with vertical bars while the total systematic uncertainties with boxes. Particle and antiparticle are in agreement within uncertainties for both observables.

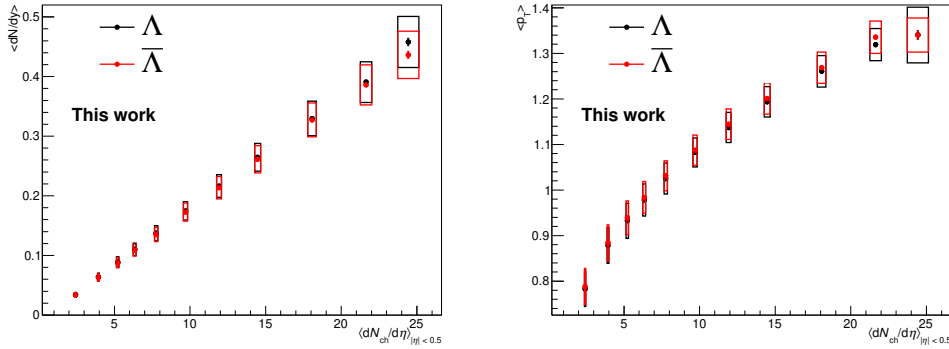


Figure 4.2:  $\Lambda$  and  $\bar{\Lambda}$   $p_{\mathbf{T}}$ -integrated yields (left panel) and  $\langle p_{\mathbf{T}} \rangle$  (right panel) as a function of charged-particle multiplicity are shown in red and black, respectively. Statistical and systematic uncertainties are indicated by vertical bars and boxes, respectively.

The  $p_{\mathbf{T}}$ -integrated yields and  $\langle p_{\mathbf{T}} \rangle$  as a function of charged-particle multiplicity were also calculated for the merged particle and antiparticle yields. Figures 4.5 and 4.7 show the  $\langle dN/dy \rangle$  and  $\langle p_{\mathbf{T}} \rangle$  for  $K_S^0$  and  $\Lambda + \bar{\Lambda}$  while, Figures 4.6 and 4.8 show the  $\langle dN/dy \rangle$  and  $\langle p_{\mathbf{T}} \rangle$  for  $\Xi^- + \bar{\Xi}^+$  and  $\Omega^- + \bar{\Omega}^+$  together with the statistical uncertainties (vertical bars), the total systematic uncertainties (boxes) and the uncorrelated across multiplicity systematic uncertainties (shadowed boxes). Results of the present study in pp collisions at  $\sqrt{s} = 5.02$  TeV are presented in green and they are compared with previous pp analyses at  $\sqrt{s} = 7$  TeV [55] and at  $\sqrt{s} = 13$  TeV [56] shown in blue and in red, respectively. The present  $\langle dN/dy \rangle$  of strange hadrons increases with the charged-particle multiplicity. In particular, the  $p_{\mathbf{T}}$ -integrated yields for  $K_S^0$ ,  $\Lambda + \bar{\Lambda}$  and  $\Xi^- + \bar{\Xi}^+$  follow a linear trend as it can be seen from the first order polynomial function fit while the  $\langle dN/dy \rangle$  for  $\Omega^- + \bar{\Omega}^+$  is fitted with a second order polynomial function. The  $p_{\mathbf{T}}$ -integrated yields obtained

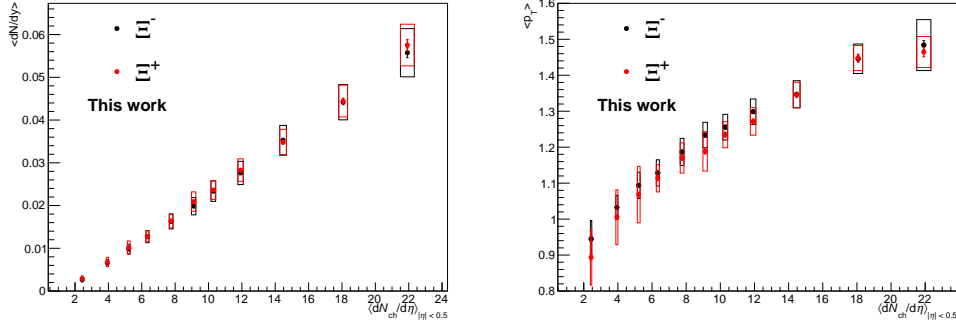


Figure 4.3:  $\Xi^-$  and  $\Xi^+$   $p_{\mathbf{T}}$ -integrated yields (left panel) and  $\langle p_{\mathbf{T}} \rangle$  (right panel) as a function of charged-particle multiplicity are shown in red and black, respectively. Statistical and systematic uncertainties are indicated by vertical bars and boxes, respectively.

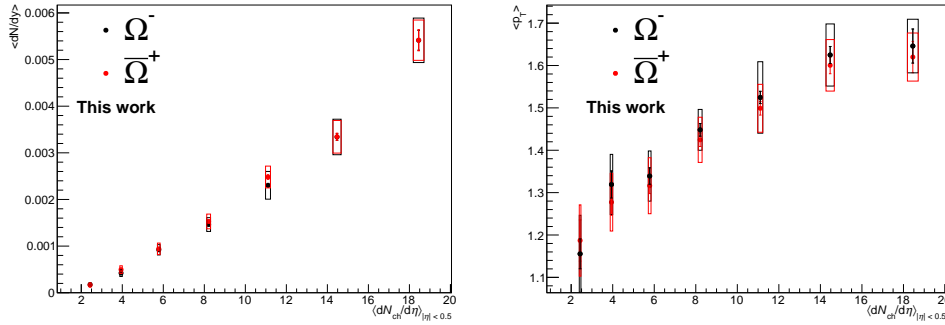


Figure 4.4:  $\Omega^-$  and  $\Omega^+$   $p_{\mathbf{T}}$ -integrated yields (left panel) and  $\langle p_{\mathbf{T}} \rangle$  (right panel) as a function of charged-particle multiplicity are shown in red and black, respectively. Statistical and systematic uncertainties are indicated by vertical bars and boxes, respectively.

in this work present a very good agreement within uncertainties with the results at higher centre-of-mass energies. The actual analysis confirms that the abundance of strange hadrons produced in pp collisions is invariant with respect to the collision energy and only depends on the charged particle density at the LHC high energy regime. Moreover, it can be noticed that the heavier the mass of the strange hadron is, the faster the  $p_{\mathbf{T}}$ -integrated yield increases as a function of charged particle multiplicity.

The  $\langle p_{\mathbf{T}} \rangle$  of strange hadrons increases as a function of  $\langle dN_{ch}/d\eta \rangle$  for all particles under study since the transverse momentum distributions become harder with multiplicity.

These results also follow the same trend as the previous results at higher centre-of-mass collision energies.

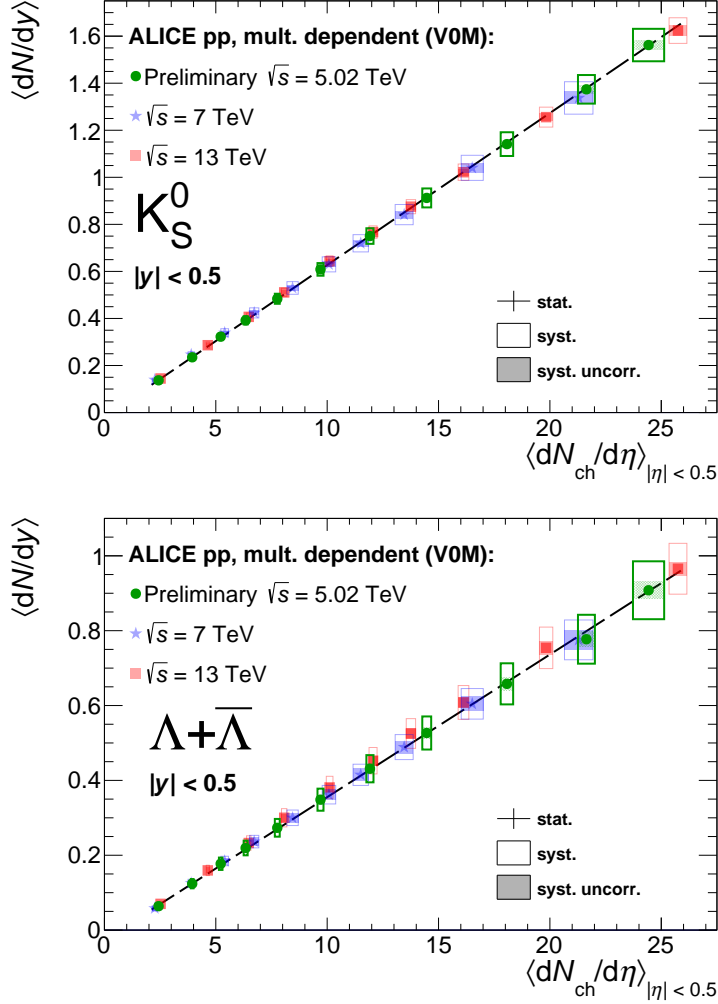


Figure 4.5:  $K_S^0$  (top panel) and  $\Lambda + \bar{\Lambda}$  (bottom panel)  $p_T$ -integrated yields as a function of charged-particle multiplicity at  $\sqrt{s} = 5.02$  TeV are represented in green. These present results are compared with the previous pp analyses at  $\sqrt{s} = 7$  TeV [55] (blue points) and  $\sqrt{s} = 13$  TeV [56] (red points). The statistical and total systematic uncertainties are represented by error bars and boxes, respectively. Shaded boxes show the uncorrelated systematic uncertainties across multiplicity. The black dashed lines represent the linear fit to the  $\langle dN/dy \rangle$ .

In addition, the relative statistical, total systematic and uncorrelated systematic uncertainties for the three analyses on  $p_T$ -integrated yields as a

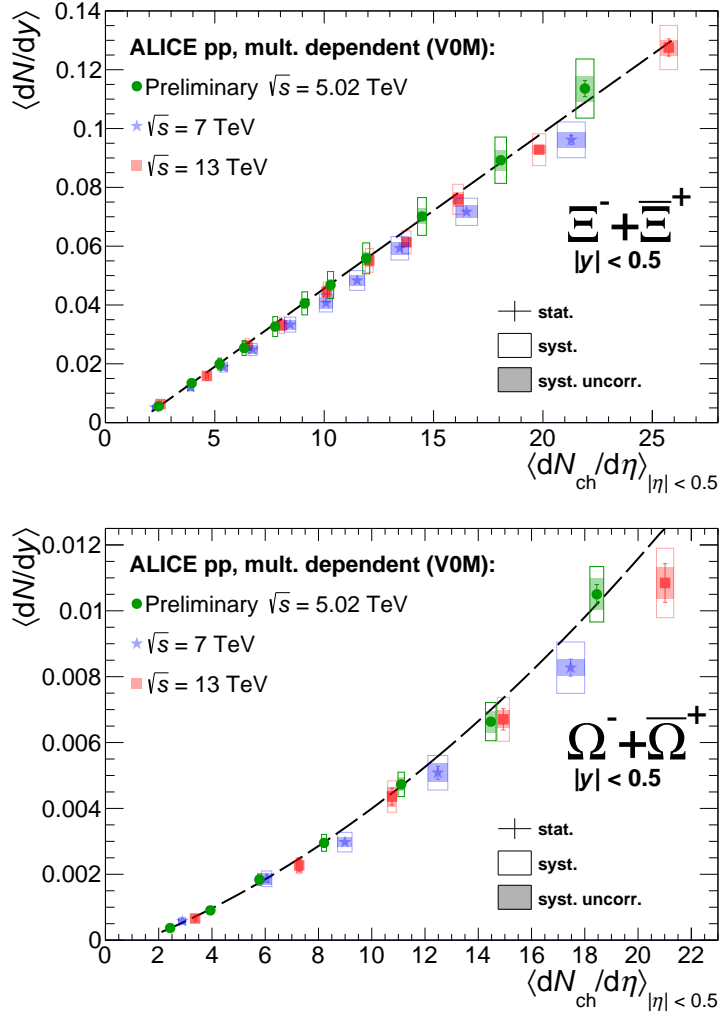


Figure 4.6:  $\Xi^{-} + \Xi^{+}$  (top panel) and  $\Omega^{-} + \Omega^{+}$  (bottom panel)  $p_{\mathbf{T}}$ -integrated yields as a function of charged-particle multiplicity at  $\sqrt{s} = 5.02$  TeV are represented in green. These present results are compared with the previous pp analyses at  $\sqrt{s} = 7$  TeV [55] (blue points) and  $\sqrt{s} = 13$  TeV [56] (red points). The statistical and total systematic uncertainties are represented by error bars and boxes, respectively. Shaded boxes show the uncorrelated systematic uncertainties across charged-particle multiplicity. The black dashed line represents for  $\Xi^{-} + \Xi^{+}$  the linear fit to the  $\langle dN/dy \rangle$  while for  $\Omega^{-} + \Omega^{+}$  the second order polynomial fit.

function of multiplicity classes were compared and found to be consistent and compatible for all particles under study (see Appendix C for more details).

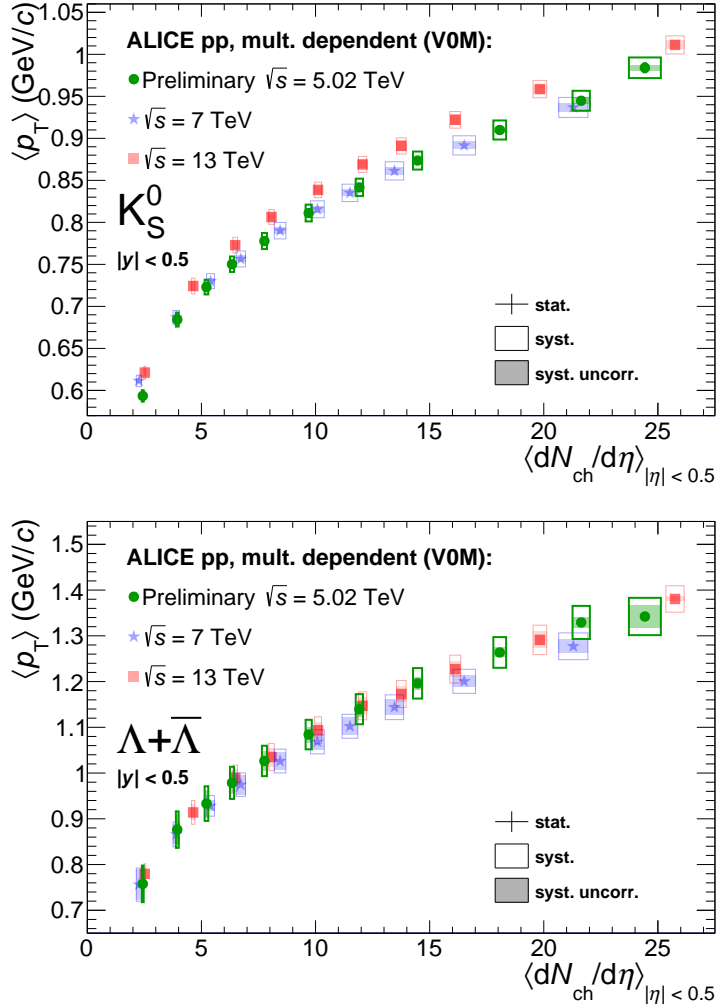


Figure 4.7:  $K_S^0$  (top panel) and  $\Lambda + \bar{\Lambda}$  (bottom panel)  $\langle p_T \rangle$  as a function of charged-particle multiplicity at  $\sqrt{s} = 5.02$  TeV are represented in green. These present results are compared with the previous pp analyses at  $\sqrt{s} = 7$  TeV [55] (blue points) and  $\sqrt{s} = 13$  TeV [56] (red points). The statistical and total systematic uncertainties are represented by error bars and boxes, respectively. Shaded boxes show the uncorrelated systematic uncertainties across charged-particle multiplicity.

Finally, it is also interesting to compare the  $p_T$ -integrated yield for pp at  $\sqrt{s} = 5.02$  TeV obtained in this work with the one obtained in p-Pb collisions at the same collision energy [57]. Figures 4.9 and 4.10 show a good agreement in the progression between pp and p-Pb collisions for all particles under study confirming that the  $p_T$ -integrated yields assume similar values

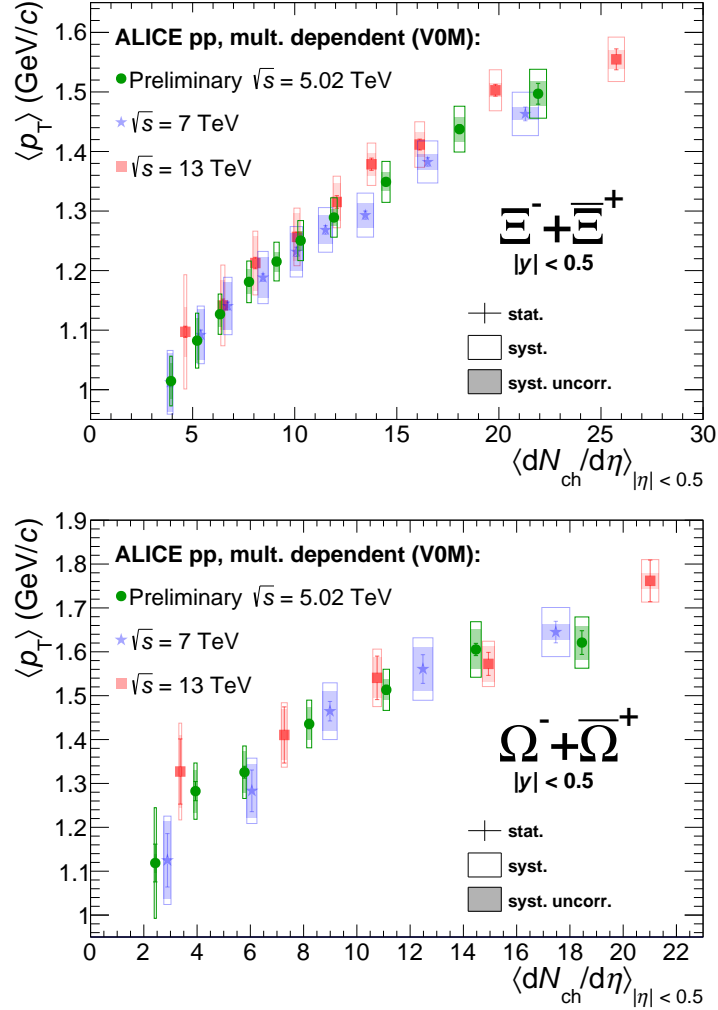


Figure 4.8:  $\bar{\Xi}^+ + \Xi^-$  (top panel) and  $\bar{\Omega}^+ + \Omega^-$  (bottom panel)  $\langle p_T \rangle$  at  $\sqrt{s} = 5.02$  TeV is compared with the previous results at  $\sqrt{s} = 7$  TeV [55] and  $\sqrt{s} = 13$  TeV [56]. The three analyses present compatible results.

at the same charged-particle multiplicity regardless of the colliding system involved.

The analysis of (multi-)strange hadrons as a function of charged-particle multiplicity in pp collisions at  $\sqrt{s_{NN}} = 5.02$  TeV was presented in this work. The hardening of the  $p_T$  distributions was observed. This phenomenon implies that the  $\langle p_T \rangle$  increases as a function of charged-particle multiplicity as it was already seen in previous pp analyses. In addition, the  $\langle dN/dy \rangle$  calculated here are in agreement with the  $p_T$ -integrated yields of analyses in pp collisions at higher colliding energies and in p-Pb collisions at the same col-



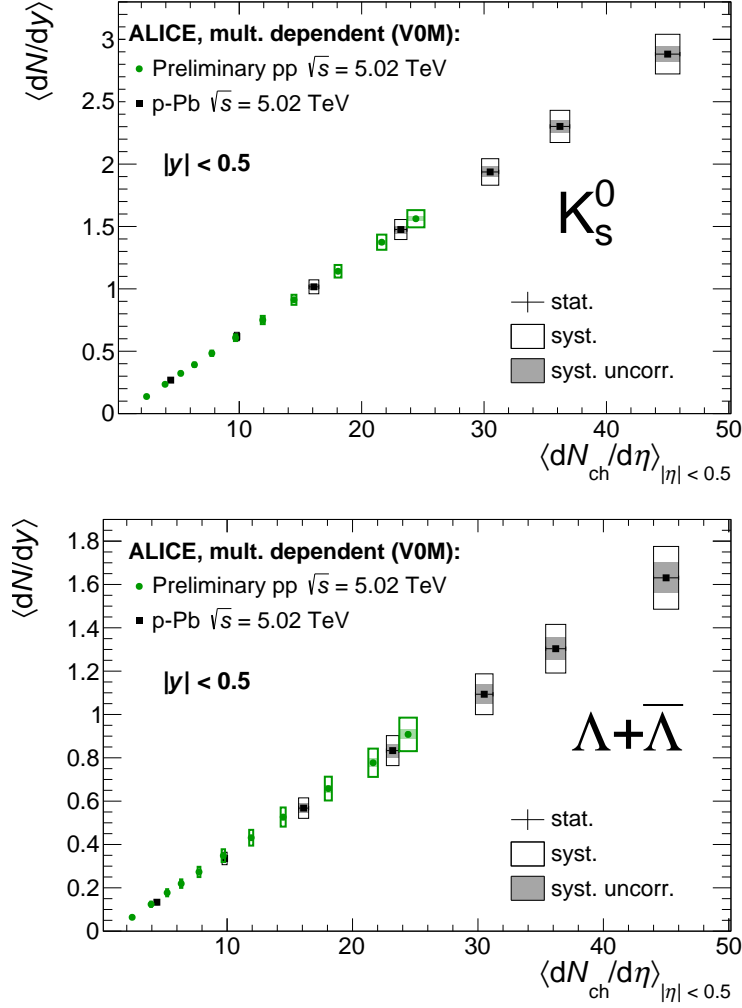


Figure 4.9:  $K_S^0$  (top panel) and  $\bar{\Lambda}^+ + \Lambda^-$  (bottom panel)  $p_T$ -integrated yields in pp collisions at  $\sqrt{s} = 5.02$  TeV (in green) are compared to  $p_T$ -integrated yields in p-Pb collisions at  $\sqrt{s_{NN}} = 5.02$  TeV [57] (in black). The statistical and total systematic uncertainties are represented by error bars and boxes, respectively. Shaded boxes show the uncorrelated systematic uncertainties across multiplicity.

liding energy, confirming that the driving observable is the charged-particle multiplicity and that the trend of the  $p_T$ -integrated yield does not depend on the energy of the system or on the colliding system.

The next and final chapter is dedicated to the summary, conclusions and outlook of this strangeness study and also of the muon trigger RPCs tests

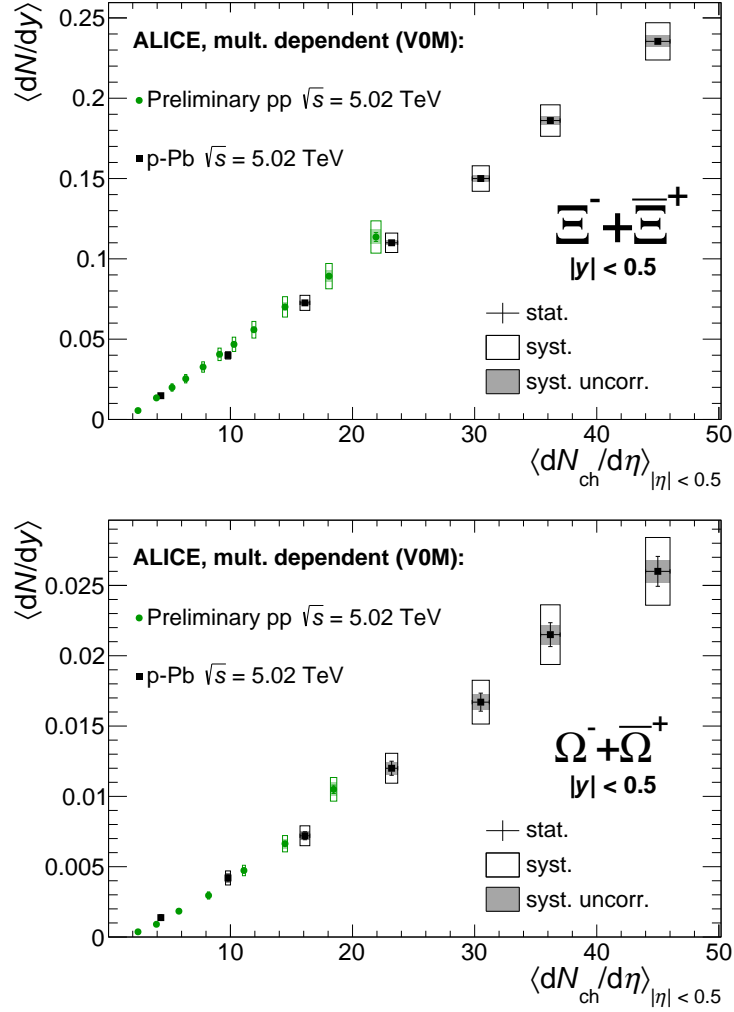


Figure 4.10:  $\Xi^- + \Xi^+$  (top panel) and  $\Omega^- + \Omega^+$  (bottom panel)  $p_T$ -integrated yields in pp collisions at  $\sqrt{s} = 5.02$  TeV (in green) are compared to  $p_T$ -integrated yields in p-Pb collisions at  $\sqrt{s_{NN}} = 5.02$  TeV [57] (in black). The statistical and total systematic uncertainties are represented by error bars and boxes, respectively. Shaded boxes show the uncorrelated systematic uncertainties across multiplicity.

described in Chapter 2.

# Chapter 5

## Summary, conclusions and outlook

This chapter is dedicated to briefly summarize the two studies presented in this PhD thesis. Moreover, conclusions on the results obtained and the analysis next steps are illustrated. Then, the outlook for the ALICE experiment, focusing on the muon trigger, is also described.

### 5.1 Service task on muon trigger RPCs

As part of the PhD service task, 10 RPCs were tested in view of the upgrade of the ALICE muon trigger for the data taking campaigns at higher luminosities. The actual RPCs were installed in ALICE in 2007 and after several years of operation, they started to show first signs of potential inefficiencies. In order to guarantee the best performance of the muon trigger during Run 3 and Run 4, it was decided to substitute some or even all of them. A new set of RPCs was ordered from an industrial company. They were built with the same components of the first set and also tested with cosmic rays using the same set-up at the INFN Laboratory in Turin. Similarly to the first tests the same streamer mixture was used in this work. In this way, it was possible to compare directly the results obtained from the two sets.

The main steps of the tests were: check for gas leaks, monitor the current drawn by the detectors, produce efficiency maps with cells of  $20 \times 20$  cm<sup>2</sup> in order to generate the efficiency-HV curve and to identify the working HV, produce the efficiency maps with high granularity (cell  $2 \times 2$  cm<sup>2</sup>) and extract the noise maps at 10 different values of HV to identify the noisy regions.

The results obtained from these tests have shown that only 2 out of 10 chambers may be considered for installation in the muon trigger detector

of ALICE. It was observed that 4 of them showed holes in efficiency, 2 of them presented disuniformities in the efficiency map with high granularity and 2 of them have an overall efficiency lower than 80 %. Compared to the first batch of RPCs, the new RPCs were found at a higher working HV of around  $\sim 400-500$  V (the first group works best at 8100-8300 V while the present batch at 8600-8800). The overall efficiency was always approximately 90-95 % for the old chambers, while the best of the new chambers reached an overall efficiency of maximum 85-90%. Closer inspections revealed that the new chambers were produced with structural imperfections. Hence, the company was contacted and requested to solve these issues and to produce a new set of RPCs. Three prototypes were tested at the beginning of 2020 and showed promising results in terms of overall efficiency, uniformity of the efficiency maps and noise rates.

The tests carried out in this work were nevertheless crucial in identifying the structural problems which prompted the manufacturing of the third set of chambers.

## 5.2 Strangeness analysis

The second and most important focus of the PhD work described and discussed in this thesis is the analysis of (multi-)strange hadron production as a function of charged-particle multiplicity at midrapidity in pp collisions at  $\sqrt{s} = 5.02$  TeV. In Chapter 1 the evolution of the concept of strangeness production is explained. The so-called strangeness enhancement was considered a signature of the formation of the QGP, since according to theoretical calculations, it was found that the production of strange particles is favored if the QGP phase is present (heavy-ion collisions), while it is suppressed when no QGP is formed (small systems). Recent observations showed also an enhanced production of strange hadrons in small systems (pp and p-Pb collisions) at high multiplicity (corresponding to LHC energies). Therefore, studies in pp collisions as a function of multiplicity are crucial in order to understand the dynamics of small colliding systems, the role of the strangeness formation mechanism and to compare the results with other analyses in different colliding systems performed as a function of multiplicity.

For this work (Chapter 3 and 4), two types of hadrons were analyzed: V0s and Cascades.  $K_S^0$ ,  $\Lambda$  and  $\bar{\Lambda}$  belonged to the first group while  $\Xi^-$ ,  $\bar{\Xi}^+$ ,  $\Omega^-$  and  $\bar{\Omega}^+$  to the second one. Topological, geometrical and kinematical cuts were applied in order to measure the invariant mass spectra in intervals of transverse momentum, in multiplicity classes and in integrated multiplicity. Signals were extracted by integrating the peak of the invariant mass distri-

butions in a defined window  $[\mu - 5\sigma, \mu + 5\sigma]$  (where  $\mu$  and  $\sigma$  are the mean and the width of the peak), and subtracting in the same window the background obtained from a polynomial function fit. Next, the signals were normalized by the number of inelastic events and the  $p_{\mathbf{T}}$  bin width to obtain the raw spectra. The corrected transverse momentum distributions were evaluated dividing the raw spectra by the acceptance times efficiency corrections which were calculated by applying the same cuts used for the data sample to the Monte Carlo samples. Several other corrections such as the Lambda feed-down were also applied and they are described in detail in Chapter 3. Another important aspect of the analysis, fully detailed in Chapter 3, was the systematic uncertainty due to the cuts applied during the analysis and on the extrapolation at low  $p_{\mathbf{T}}$ .

The  $p_{\mathbf{T}}$ -integrated yields and the average  $\langle p_{\mathbf{T}} \rangle$  as a function of charged-particle multiplicity were calculated from the corrected spectra for every particle under study. First of all,  $\langle dN/dy \rangle$  and  $\langle p_{\mathbf{T}} \rangle$  of particles and antiparticles were in agreement within uncertainties. Then,  $p_{\mathbf{T}}$ -integrated yields and  $\langle p_{\mathbf{T}} \rangle$  were produced for  $K_S^0$ ,  $\Lambda + \bar{\Lambda}$ ,  $\Xi^- + \bar{\Xi}^+$  and  $\Omega^- + \bar{\Omega}^+$  and compared to the results obtained in pp collisions at  $\sqrt{s} = 7$  TeV and  $\sqrt{s} = 13$  TeV and in p-Pb collisions at  $\sqrt{s} = 5.02$  TeV. The new  $\langle dN/dy \rangle$  confirmed an enhanced production of strange hadrons as a function of charged-particle multiplicity, following a linear trend for V0s and  $\Xi^- + \bar{\Xi}^+$  and a more than linear trend for  $\Omega^- + \bar{\Omega}^+$  (in Chapter 4 the trend is fitted with a second order polynomial function). The  $\langle p_{\mathbf{T}} \rangle$  increased as a function of charged-particle multiplicity as a consequence of the hardening of the transverse momentum spectra as it was also seen for the previous analyses in pp. Furthermore,  $p_{\mathbf{T}}$ -integrated yields showed a good agreement within uncertainties with the previous results in pp at higher energies and in p-Pb at the same energy confirming that the driving observable is the charged-particle multiplicity and that  $\langle dN/dy \rangle$  is not dependent on the centre-of-mass energy or on the colliding system for the high energy range at the LHC.

## 5.3 Outlook

### 5.3.1 The ALICE upgrade for high luminosity

The ALICE apparatus is undergoing an upgrade of its detectors [98] in order to be able to exploit the higher luminosities following the LHC upgrade. The upgrade strategy is based on the LHC plans to increase amongst other the luminosity of Pb-Pb collisions progressively after the second long shutdown, eventually reaching an interaction rate of about 50 kHz (from the

current 10 kHz), i.e. an instantaneous luminosity of  $L = 6 \cdot 10^{27} \text{ cm}^{-2} \text{ s}^{-1}$ . Based on this proposed plan, the ALICE detector is being upgraded to enable the read-out of all interactions and accumulate more than  $10 \text{ nb}^{-1}$  of Pb-Pb collisions during Run 3, corresponding to about  $10^{11}$  interactions. The requirements for Run 3 and Run 4 will be more stringent concerning the ALICE rate capability, vertex reconstruction, low transverse momenta resolution and data management. The planned upgrade includes:

- a new high-resolution ITS (Inner Tracking System) [123];
- the Muon Forward Tracker (MFT) [100], a new silicon detector which will be housed in front of the absorber and track muons close to the interaction point and will boost the Muon Spectrometer Physics program;
- the replacement of the read-out multi-wire proportional chambers of the TPC with GEM detectors (Gas Electron Multiplier), with new read-out electronics [124];
- the read-out electronics upgrade for TRD, TOF, PHOS and Muon spectrometer, equipped in view of higher data taking rate;
- upgrade of the online-offline data processing software;
- an upgraded beam pipe, with the reduction of its diameter in the collision zone, in order to improve the impact parameter resolution;
- upgrade of the forward trigger detectors and of the trigger system for higher rate operation. The muon trigger no longer provides the trigger and is named muon identifier (MID) [125].

For what concerns the muon trigger, while the RPCs are in principle able to sustain high rates of the order of  $100 \text{ Hz/cm}^2$ , the real limitation relates to their read-out speed and ageing effects. After the success of the tests on the prototypes, a new order of RPCs was requested from the industrial company and in the future months the new production will be tested at INFN Laboratory in Turin in order to select chambers suitable for the installation before Run 3. In addition to the substitution of some chambers, in order to make the detector lifetime comparable to the experiment data taking plans and to increase the RPCs counting rate capability, it was decided to use the same avalanche gas mixture at a lower gain and change the front-end electronics. The new front-end board will be based on the FEERIC ASIC (Front-End Electronics Rapid Integrated Circuit) developed at Clermont-Ferrand (France) [101]. Unlike ADULT, FEERIC performs amplification of

the analog signals from the RPC before discrimination. This should allow to operate the RPCs at a lower gain reducing the charge produced in the gas by a factor of 3-5, thereby limiting the potential aging effect. During Run 2 two muon trigger chambers were equipped with the new cards FEERIC in order to confirm their optimal behaviour.

### 5.3.2 Strangeness analysis next steps

The next step in the strangeness analysis in pp collisions at  $\sqrt{s} = 5.02$  TeV will be to compare the results obtained with Monte Carlo models such as EPOS LHC [50], PYTHIA8 [48] and DIPSY [49] (see Chapter 1). In addition, as soon as the pion production analysis in pp at  $\sqrt{s} = 5.02$  TeV will be completed, the ratios of yields over charged pions as a function of charged-particle multiplicity will be calculated in order to have similar results that can be added to the ones already obtained in pp, p-Pb, Pb-Pb, Xe-Xe collisions (see Figure 1.12). The ratios will be necessary for a comprehensive comparison between different collision systems over a wide range of energies.

These new results will also help to improve the model behaviours, to understand the strangeness production mechanism(s) which are still debated and to shed light on the dynamics of small collision systems.

Finally, it is important to mention that the Paper preparation is ongoing for publication, following the approval for the analysis by the ALICE Collaboration.

# Appendix A

## Invariant Mass Spectra



## V0 invariant mass spectra in integrated multiplicity

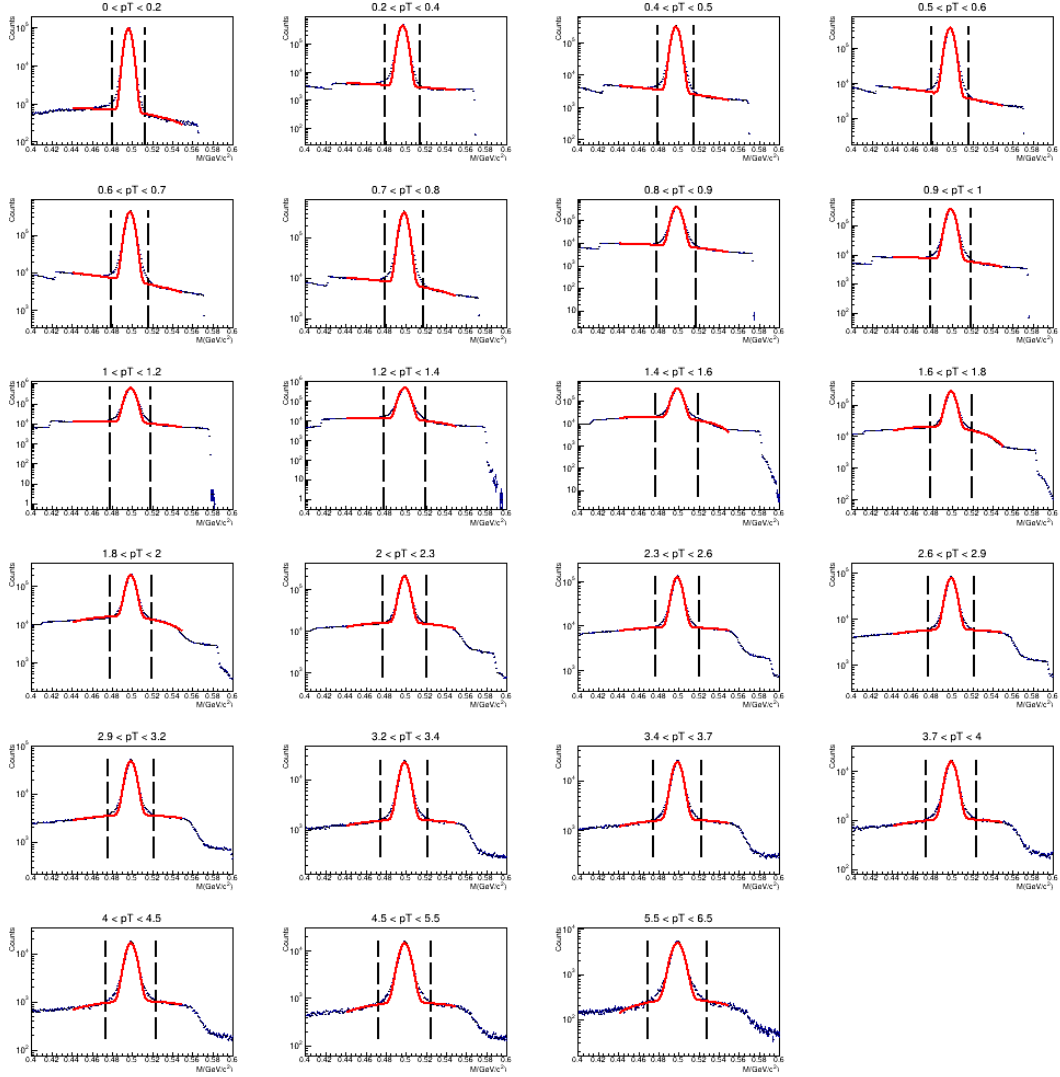


Figure A.1:  $K_S^0$  Invariant mass spectra for all  $p_T$  bins for integrated multiplicity. These figures were obtained in this work.

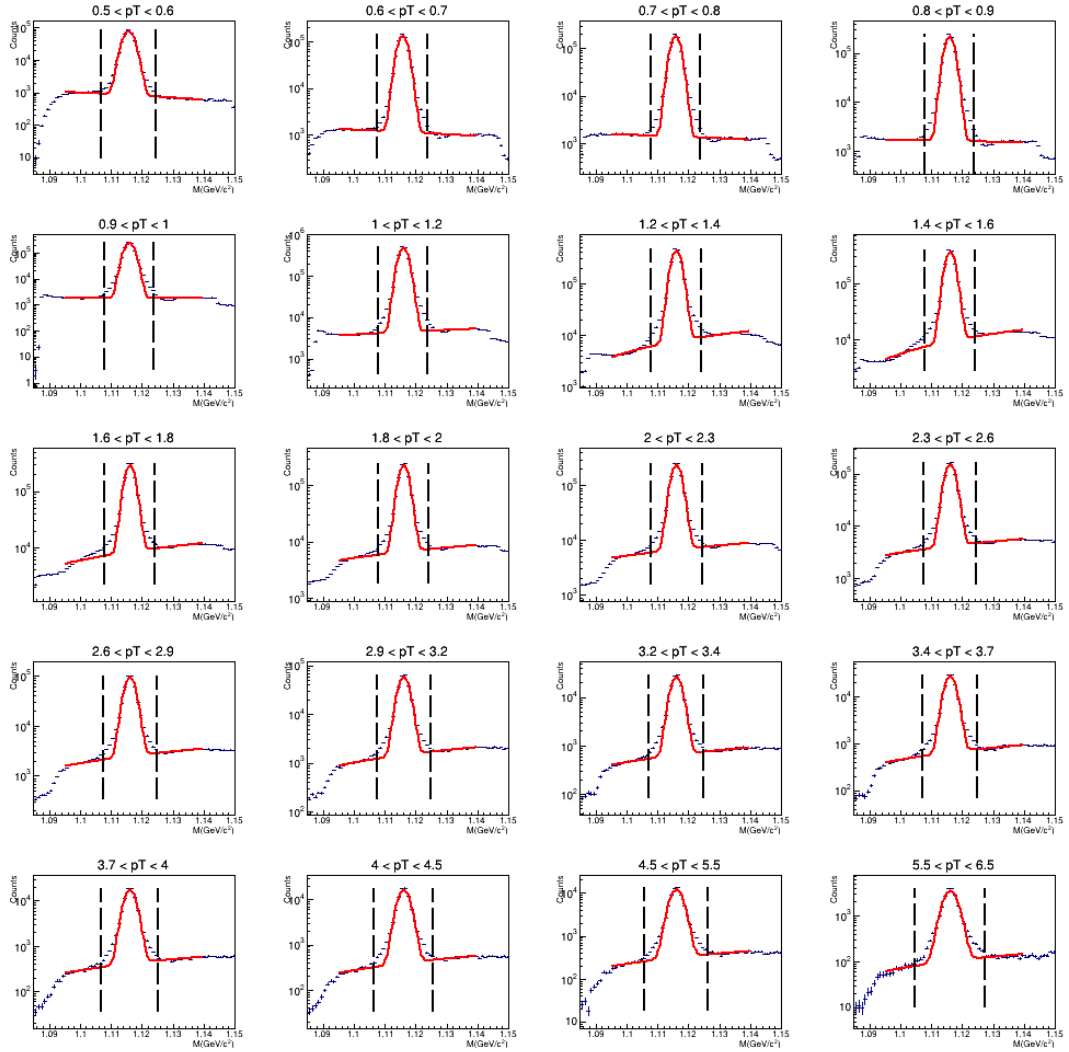


Figure A.2:  $\Lambda$  Invariant mass spectra for all  $p_T$  bins for integrated multiplicity. These figures were obtained in this work.

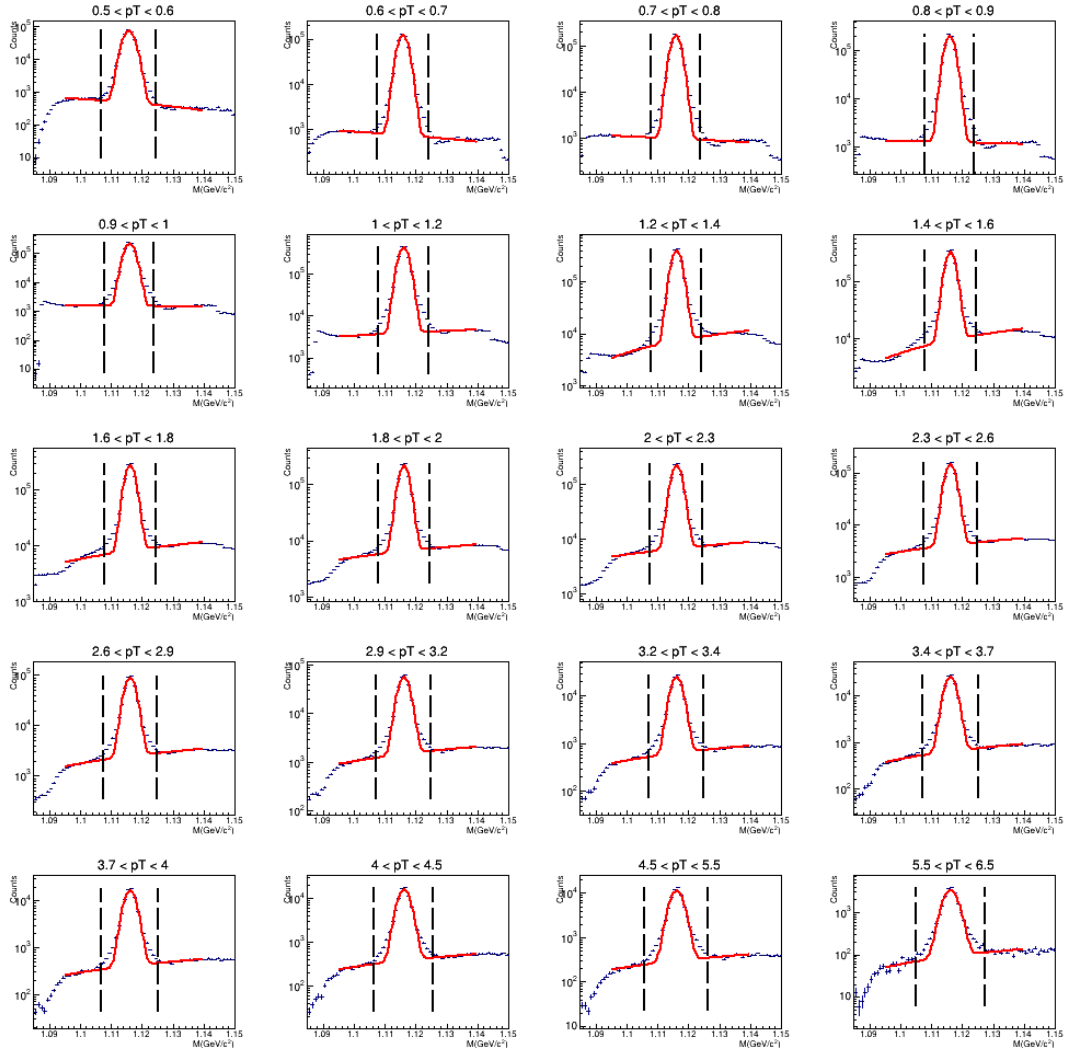


Figure A.3:  $\bar{\Lambda}$  Invariant mass spectra for all  $p_T$  bins for integrated multiplicity. These figures were obtained in this work.

## Cascade invariant mass spectra in integrated multiplicity

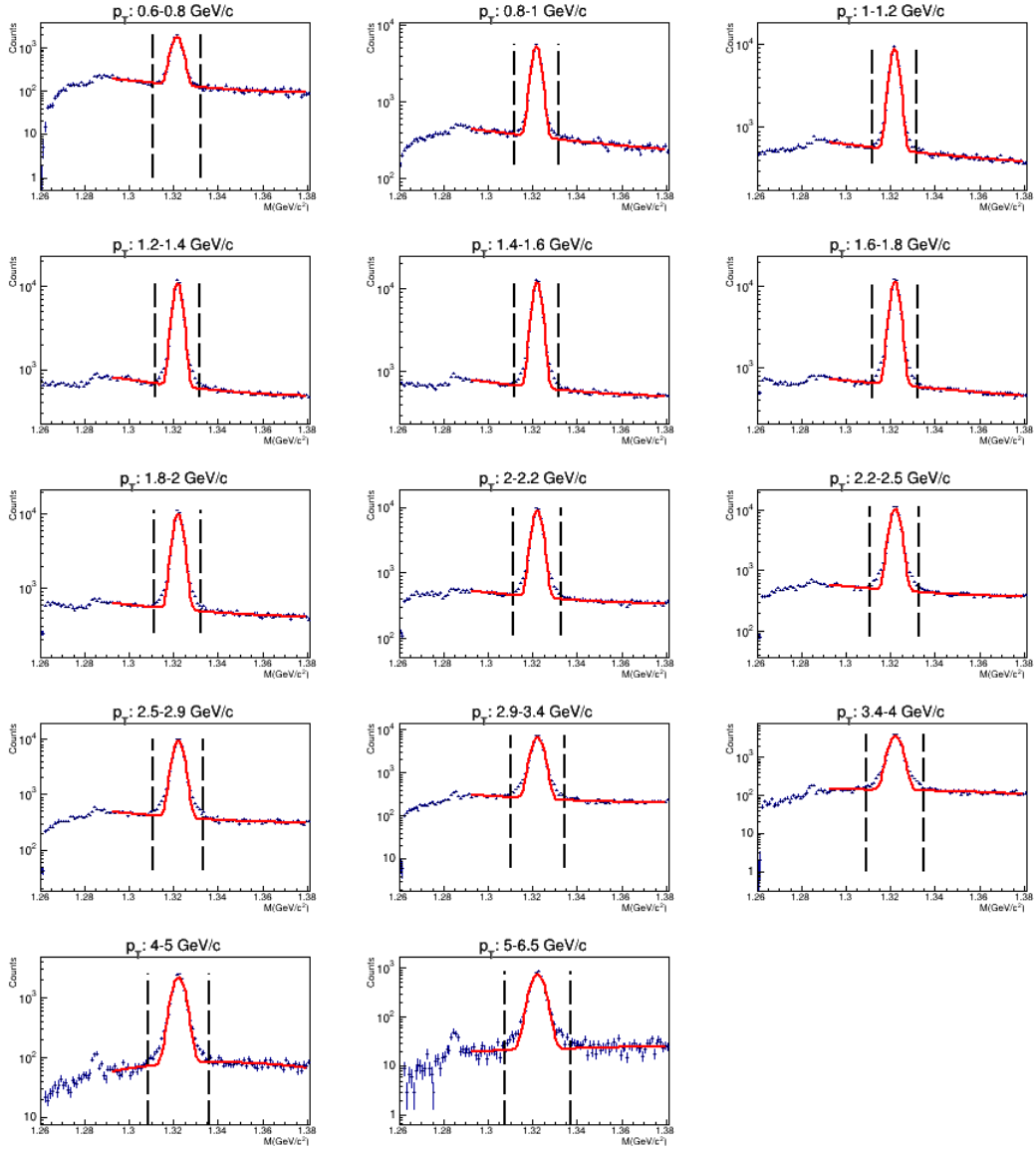


Figure A.4:  $\Xi^-$  Invariant mass spectra for all  $p_T$  bins for integrated multiplicity. These figures were obtained in this work.

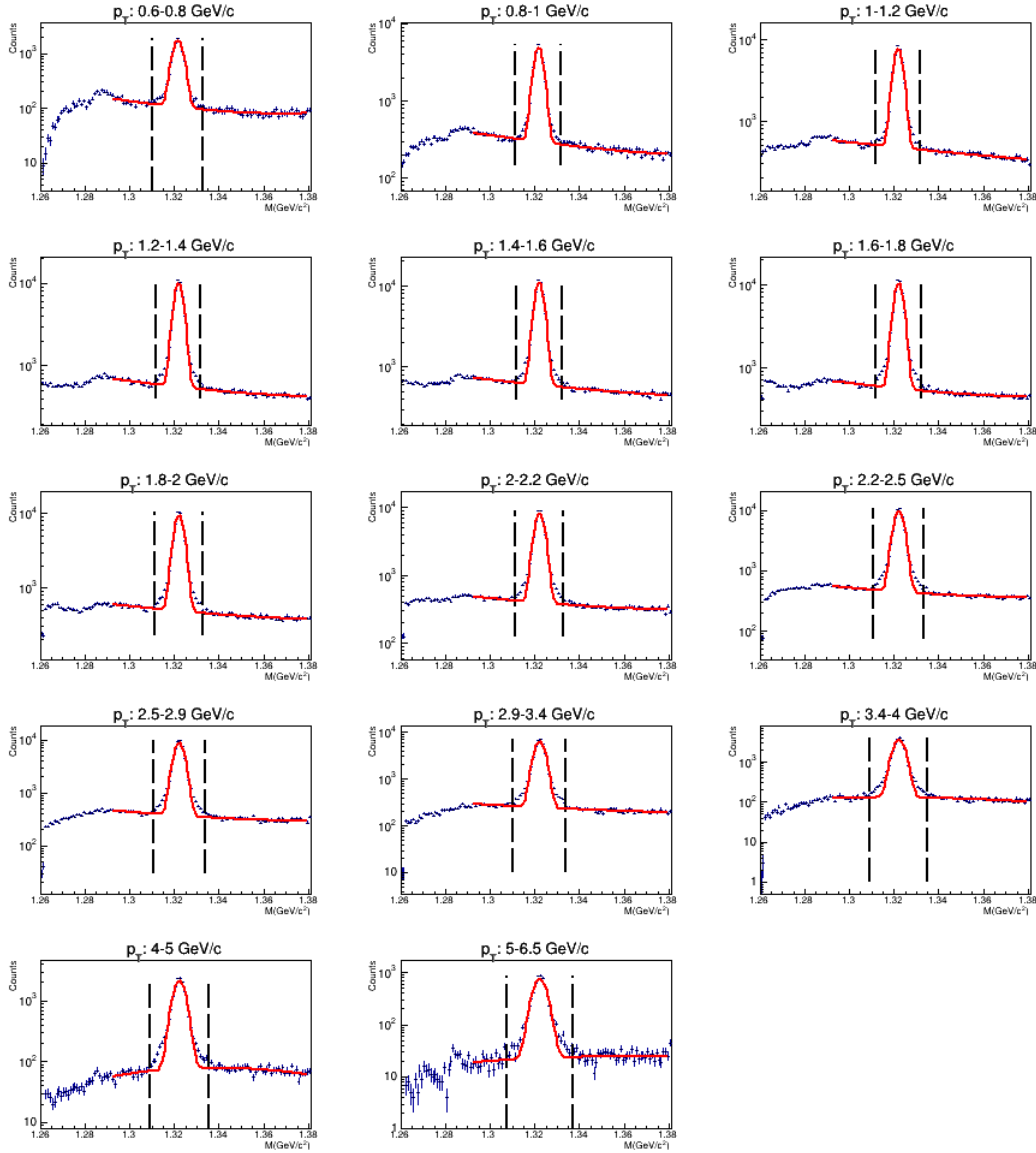


Figure A.5:  $\Xi^+$  Invariant mass spectra for all  $p_T$  bins for integrated multiplicity. These figures were obtained in this work.

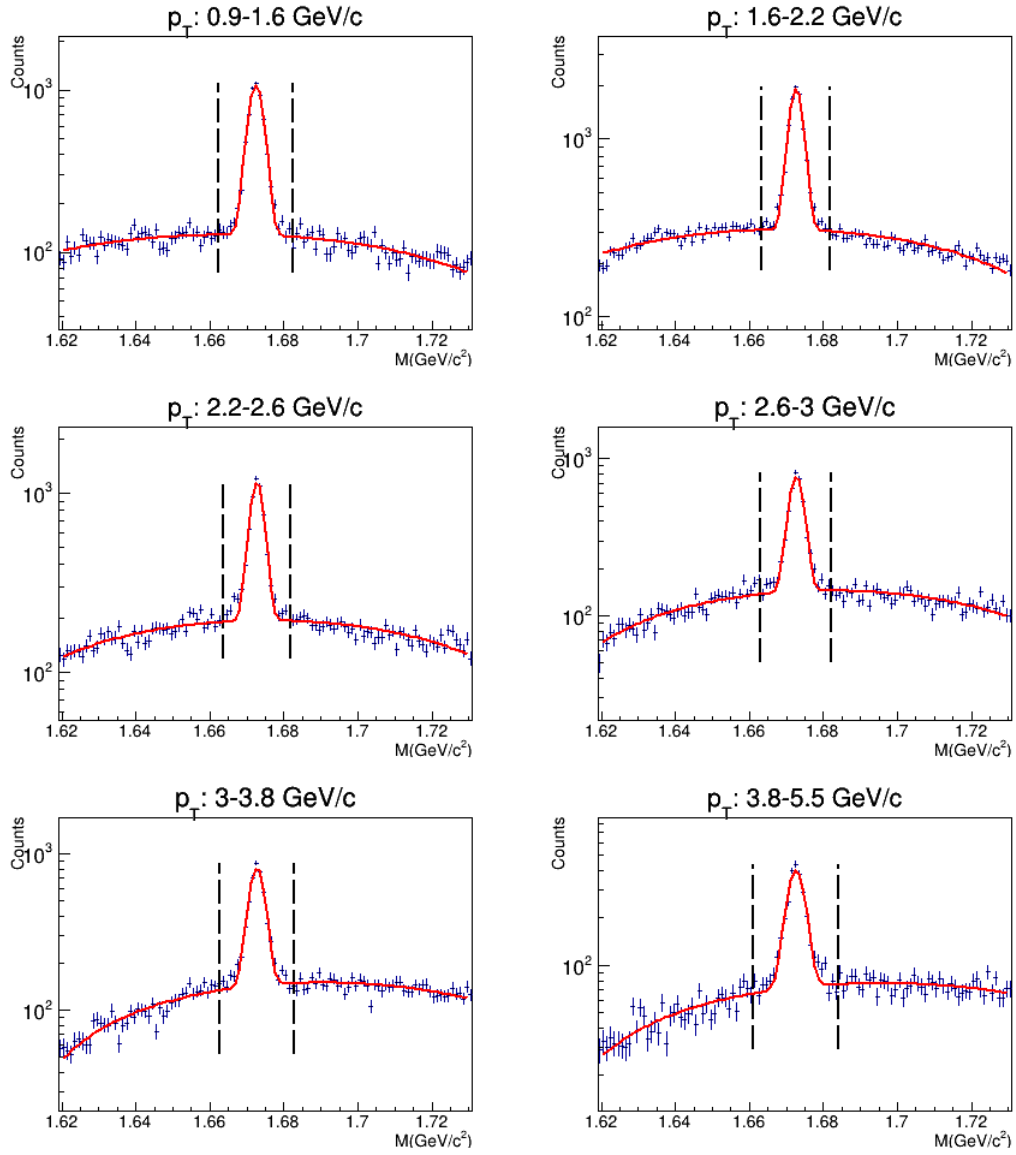


Figure A.6:  $\bar{\Omega}^-$  Invariant mass spectra for all  $p_T$  bins for integrated multiplicity. These figures were obtained in this work.

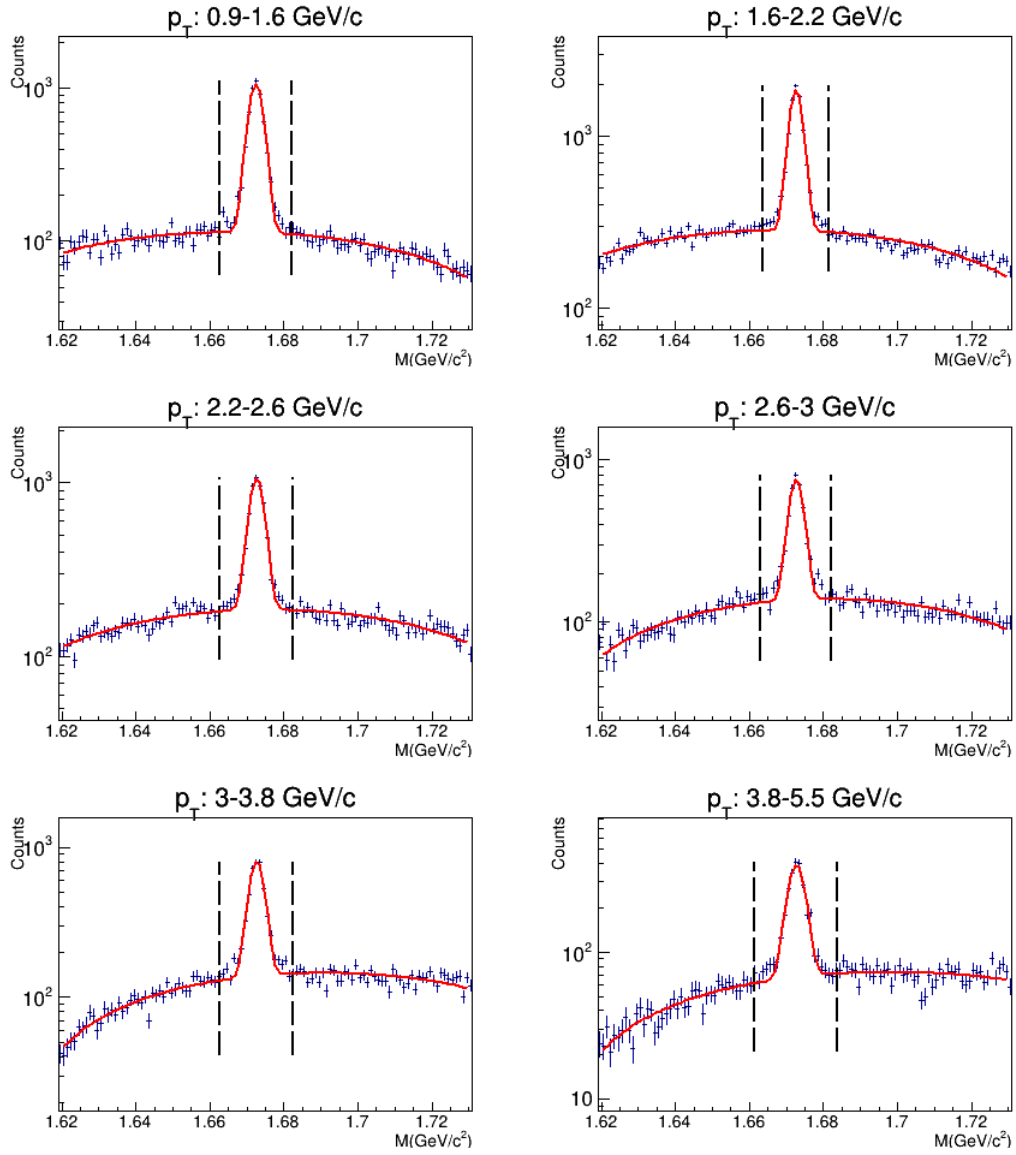


Figure A.7:  $\bar{\Omega}^+$  Invariant mass spectra for all  $p_T$  bins for integrated multiplicity. These figures were obtained in this work.

# Appendix B

## Cut studies



V0 cut studies in integrated multiplicity and  $p_T$

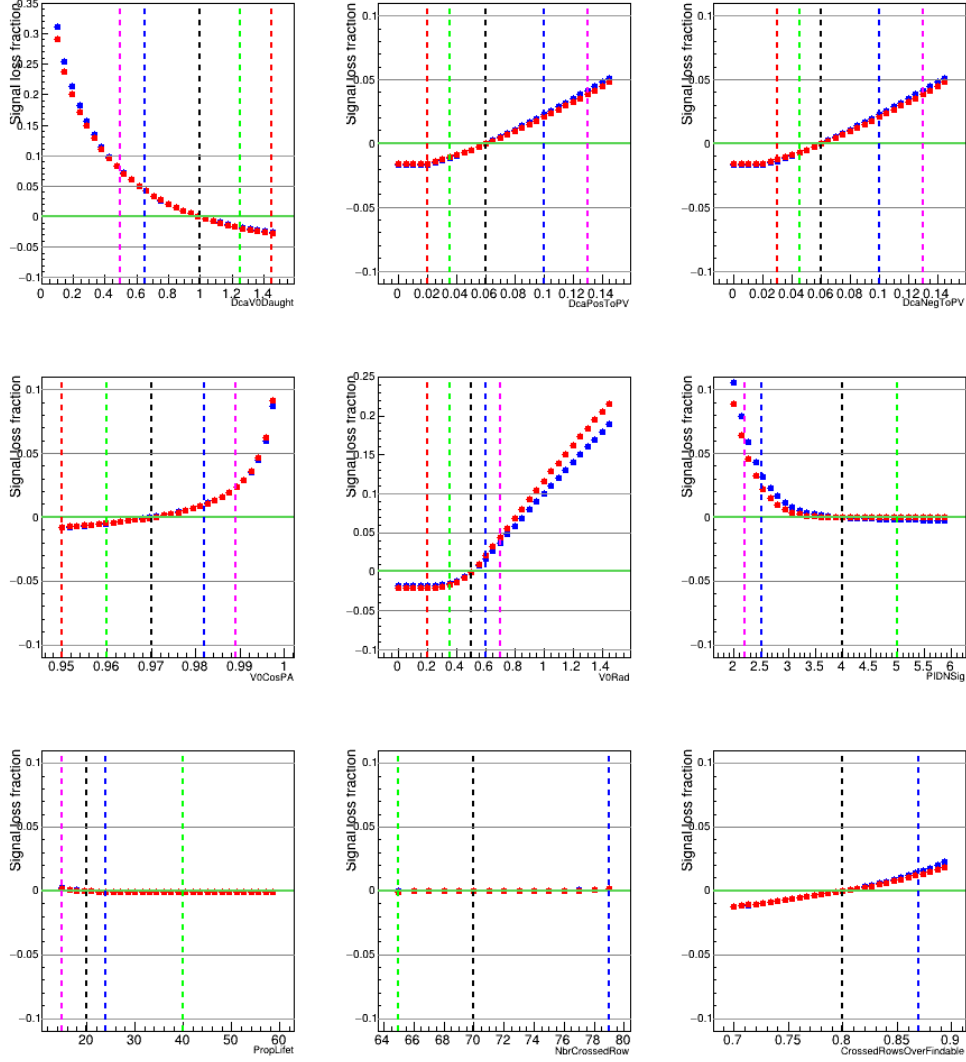


Figure B.1: The signal-loss fractions for  $K_s^0$  in integrated multiplicity and  $p_T$  are shown. The data are in blue and MC in red. The magenta, blue, green and red lines represent, respectively, the loosest, loose, tight and tightest cuts. The black dashed line corresponds to the default variable cut. These figures were obtained in this work.

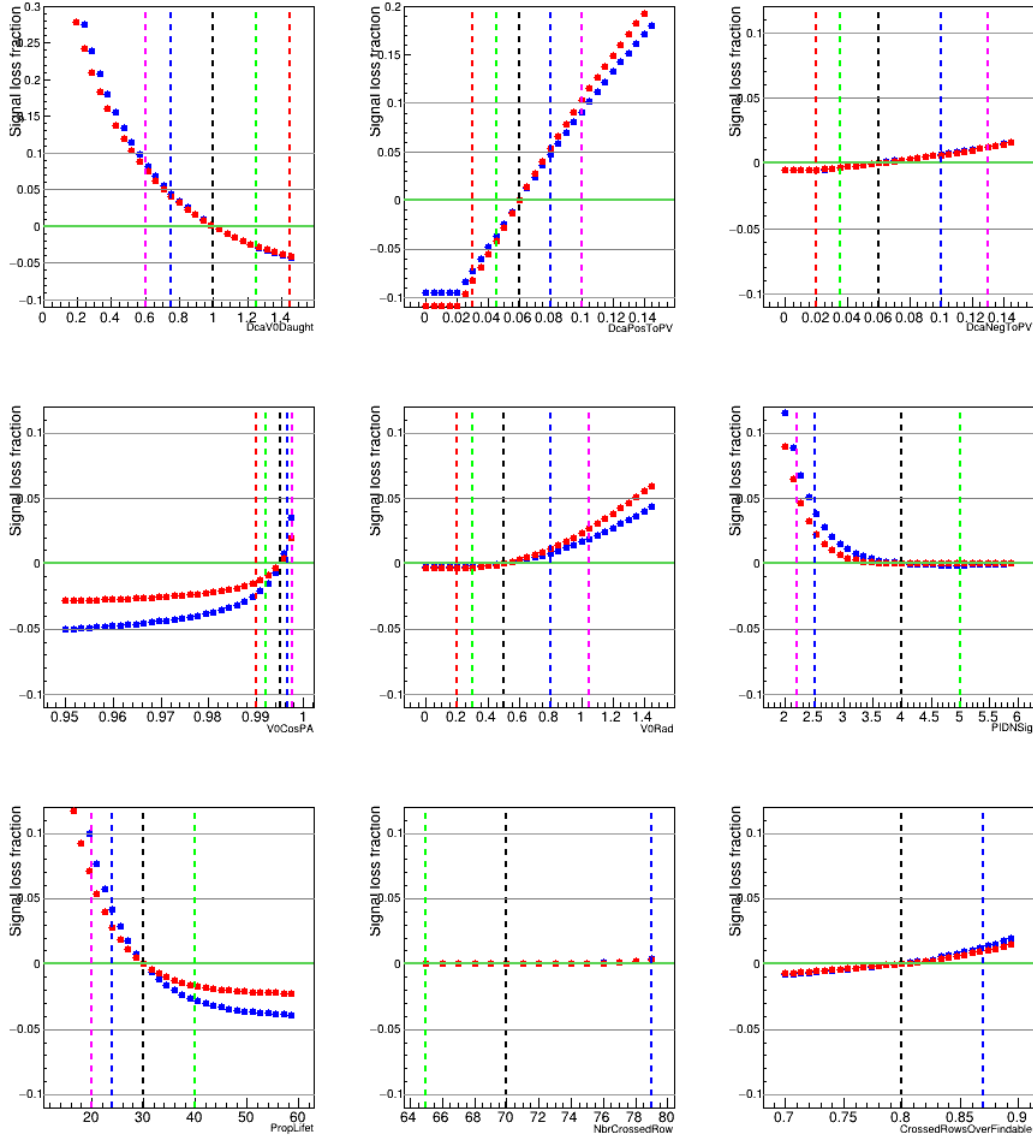


Figure B.2: The signal extraction fraction for  $\Lambda$  in integrated multiplicity and  $p_{\mathbf{T}}$  are shown. The data are in blue and MC in red. The magenta, blue, green and red lines represent, respectively, the loosest, loose, tight and tightest cuts. The black dashed line corresponds to the default variable cut. These figures were obtained in this work.

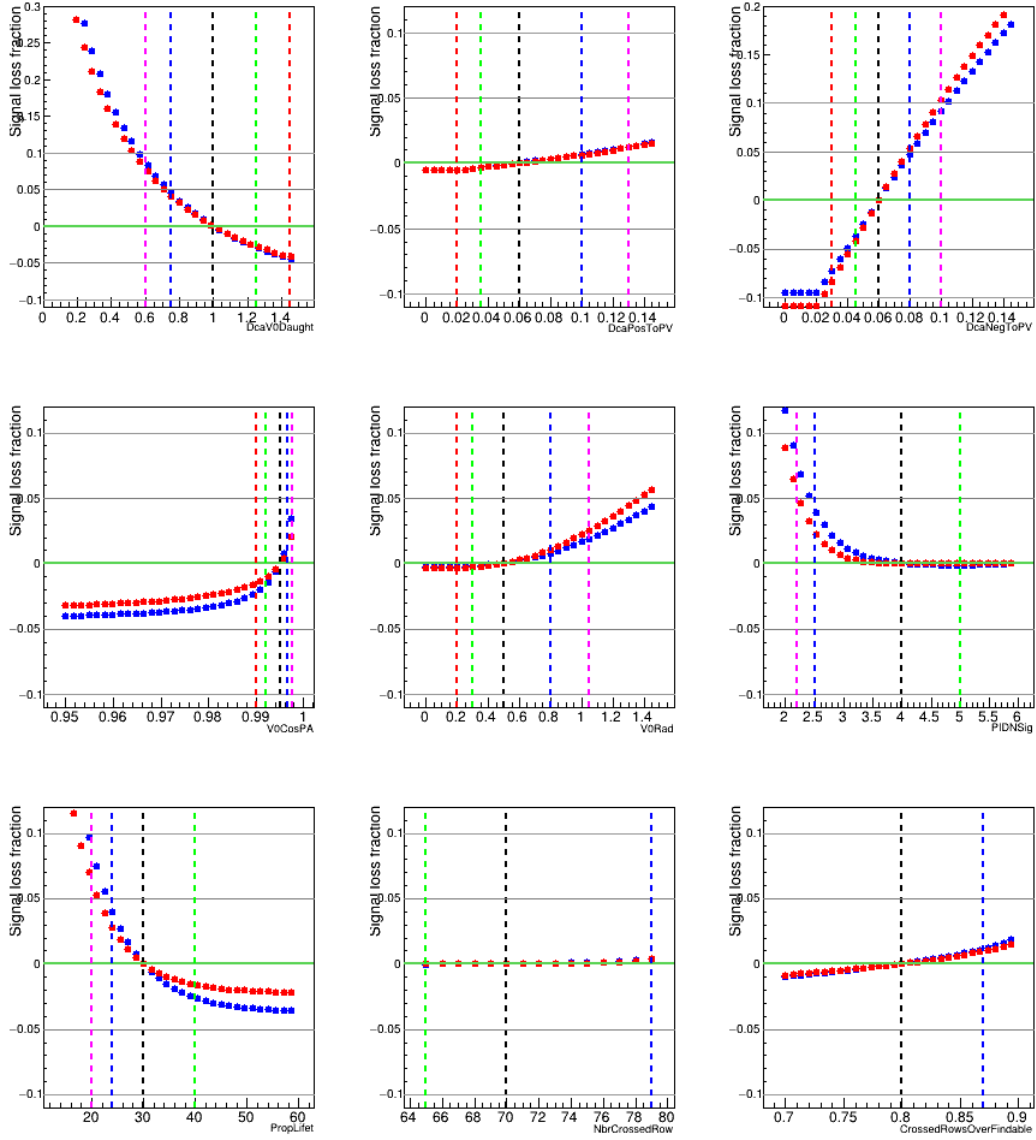


Figure B.3: The signal-loss fractions for  $\bar{\Lambda}$  in integrated multiplicity and  $p_T$  are shown. The data are in blue and MC in red. The magenta, blue, green and red lines represent, respectively, the loosest, loose, tight and tightest cuts. The black dashed line corresponds to the default variable cut. These figures were obtained in this work.

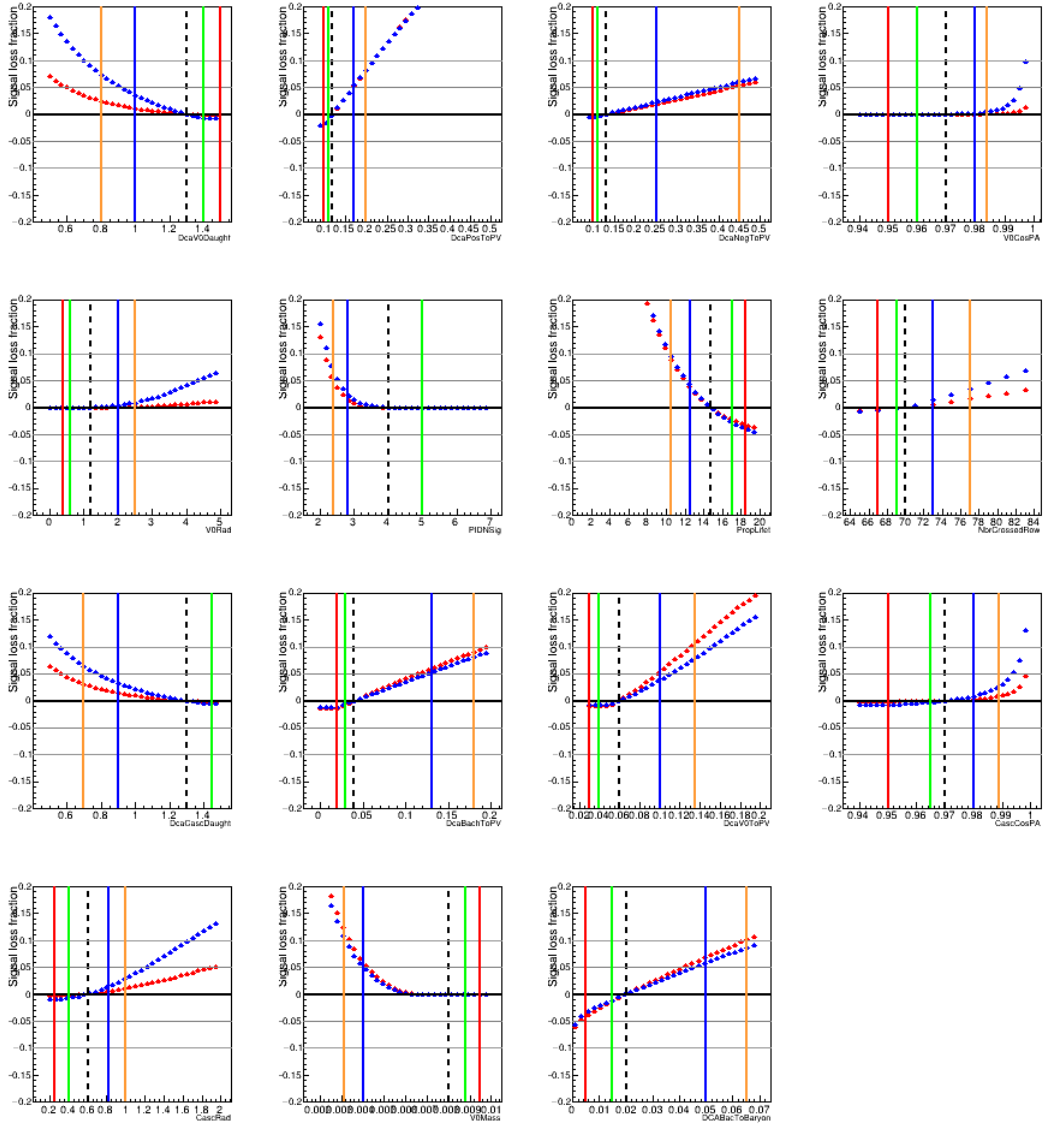
Cascade cut studies in integrated multiplicity and  $p_T$ 

Figure B.4: The signal-loss fractions for  $\Xi^-$  in integrated multiplicity and  $p_T$  are shown. The data are in blue and MC in red. The orange, blue, green and red lines represent, respectively, the loosest, loose, tight and tightest cuts. The black dashed line corresponds to the default variable cut. These figures were obtained in this work.

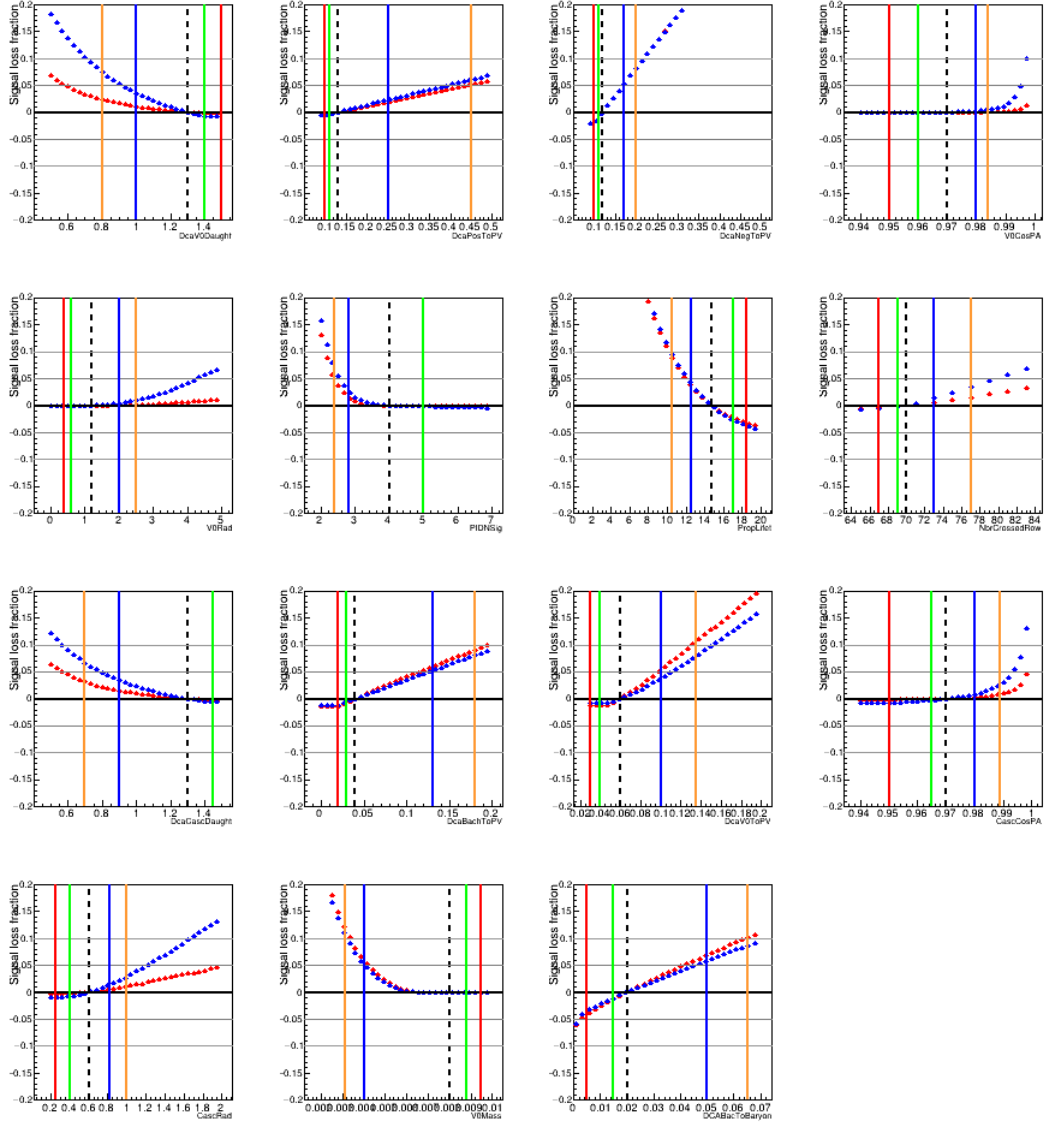


Figure B.5: The signal-loss fractions for  $\Xi^+$  in integrated multiplicity and  $p_T$  are shown. The data are in blue and MC in red. The orange, blue, green and red lines represent, respectively, the loosest, loose, tight and tightest cuts. The black dashed line corresponds to the default variable cut. These figures were obtained in this work.

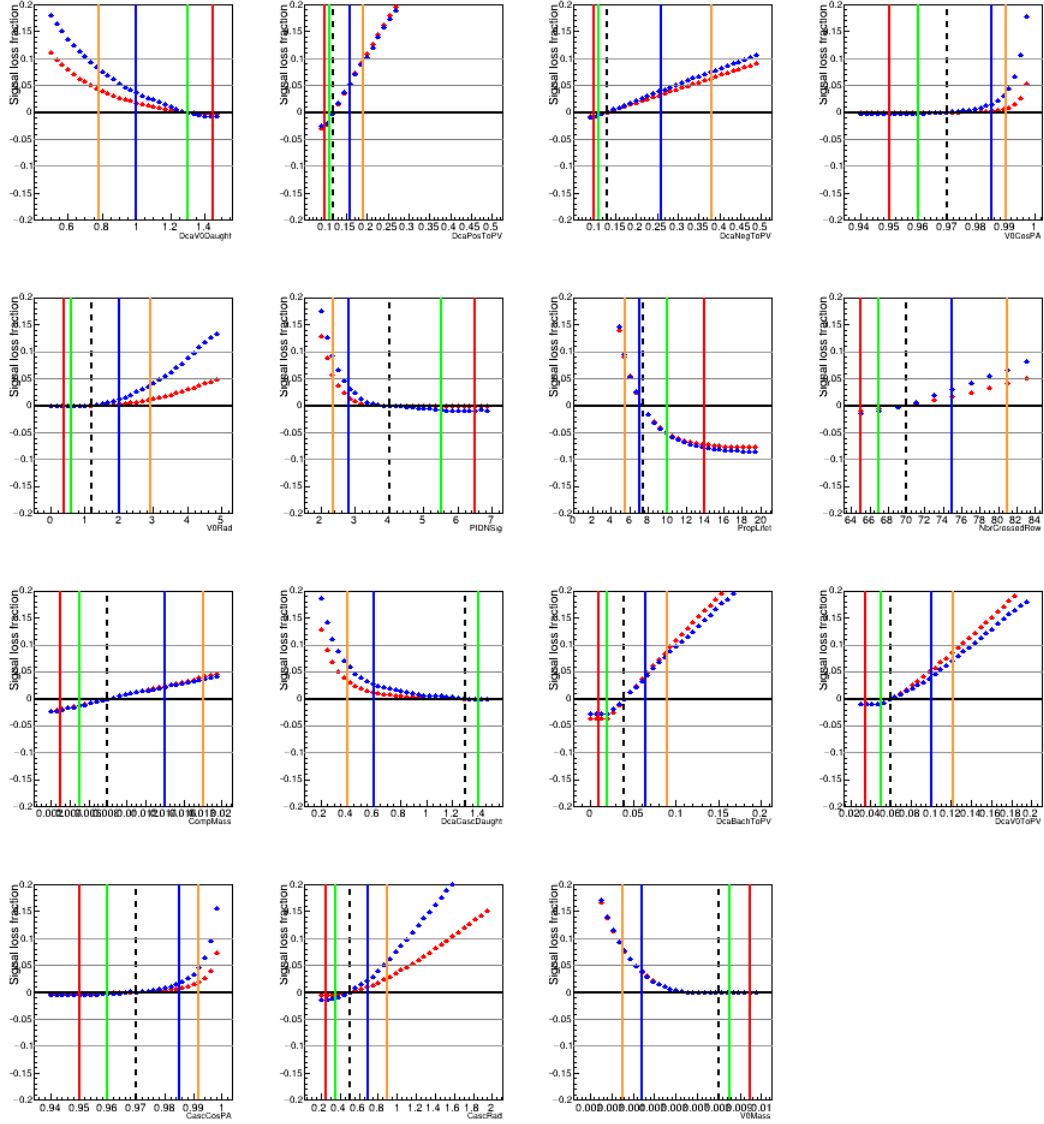


Figure B.6: The signal-loss fractions for  $\Omega^-$  in integrated multiplicity and  $p_T$  are shown. The data are in blue and MC in red. The orange, blue, green and red lines represent, respectively, the loosest, loose, tight and tightest cuts. The black dashed line corresponds to the default variable cut. These figures were obtained in this work.

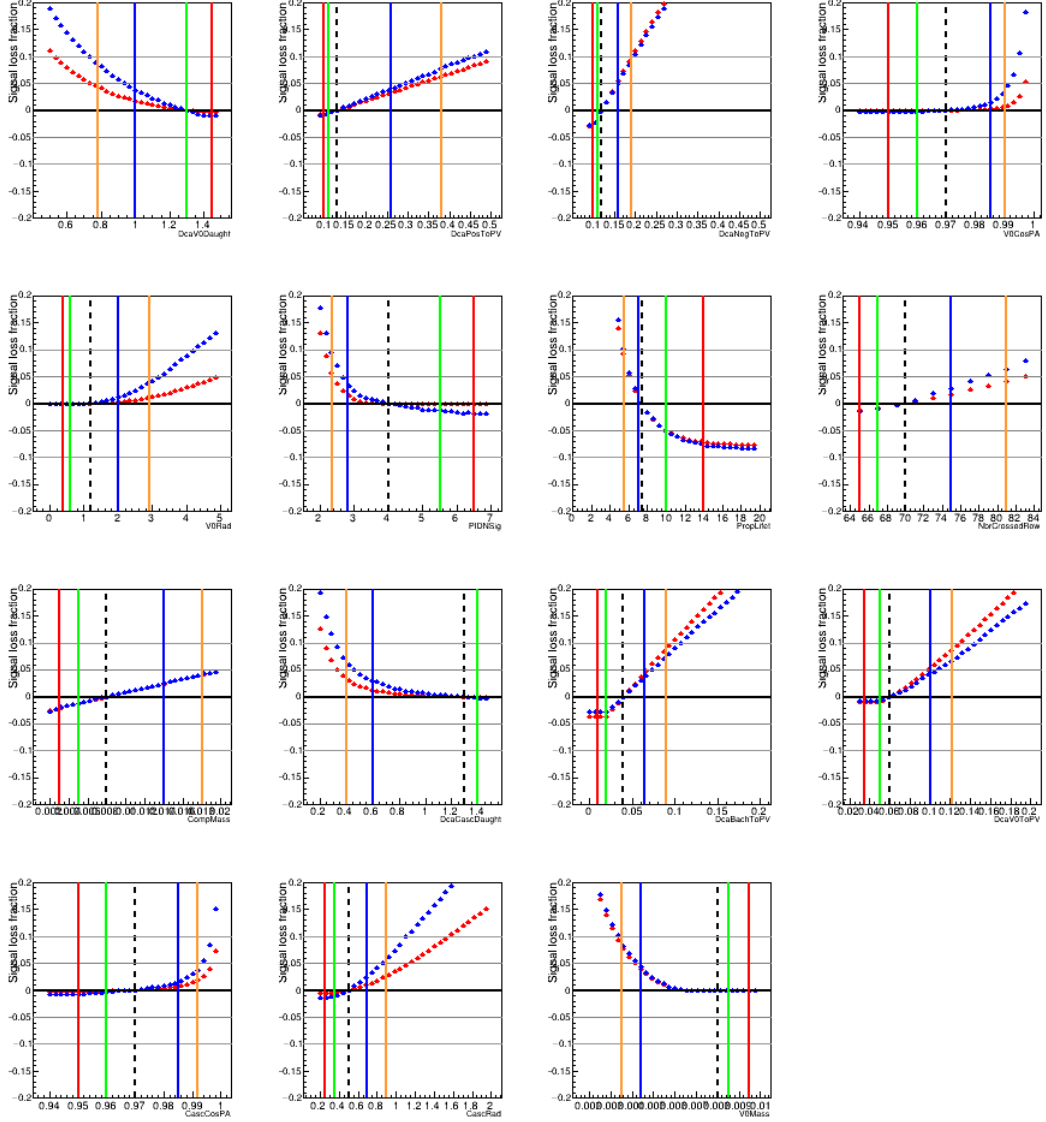


Figure B.7: The signal-loss fractions for  $\bar{\Omega}^+$  in integrated multiplicity and  $p_{\mathbf{T}}$  are shown. The data are in blue and MC in red. The orange, blue, green and red lines represent, respectively, the loosest, loose, tight and tightest cuts. The black dashed line corresponds to the default variable cut. These figures were obtained in this work.

# Appendix C

## Systematic uncertainties



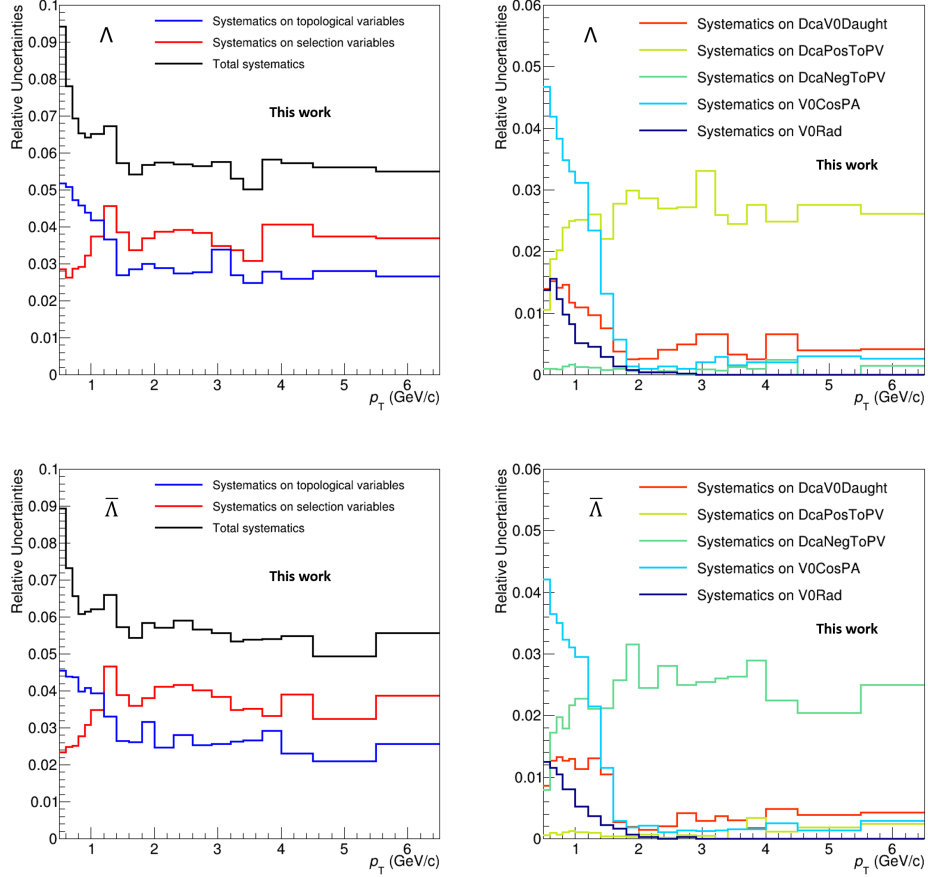


Figure C.1: Left panels show for  $\Lambda$  and  $\bar{\Lambda}$  in integrated multiplicity as a function of  $p_T$  the relative total systematic uncertainties in black, the relative systematic uncertainties due to the topological cuts in blue and the ones from selection variables in red. The right panels show for  $\Lambda$  and  $\bar{\Lambda}$  the single contribution to the relative systematic uncertainties from every topological variable.

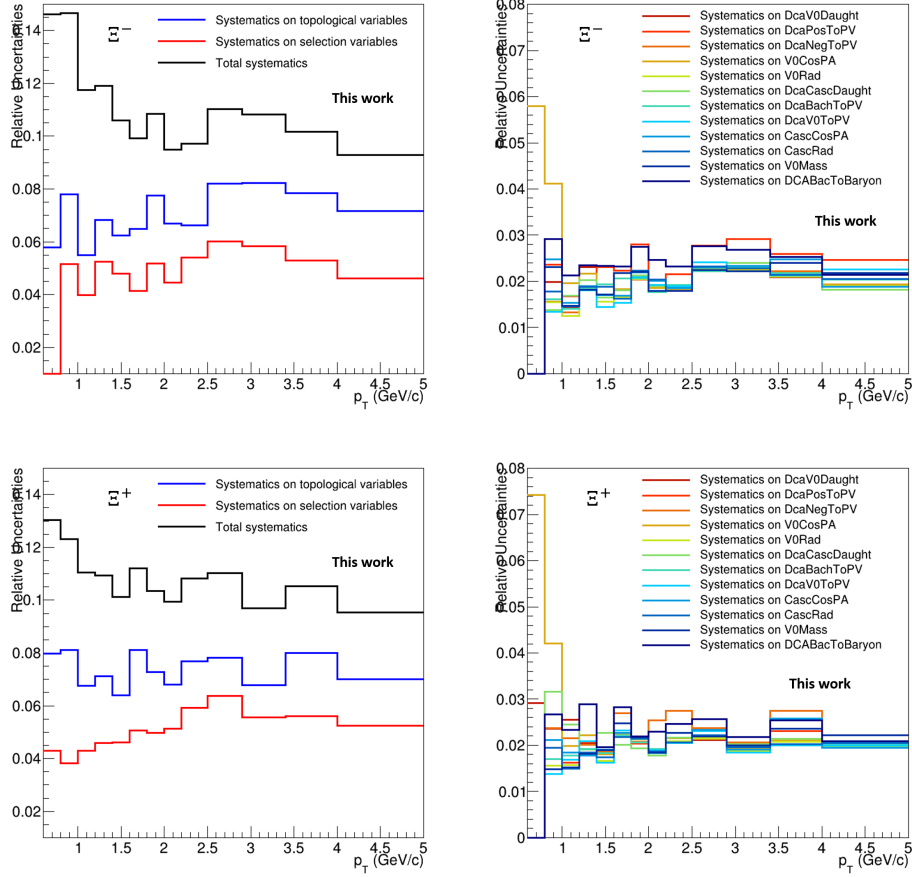


Figure C.2: The left panels show for  $\Xi^-$  and  $\Xi^+$  in integrated multiplicity as a function of  $p_{\mathbf{T}}$  the total systematic uncertainties in black, the systematic uncertainties due to the topological cuts in blue and the ones from selection variables in red. The right panels show for  $\Xi^-$  and  $\Xi^+$  the single contribution to the systematic uncertainties from every topological variable.

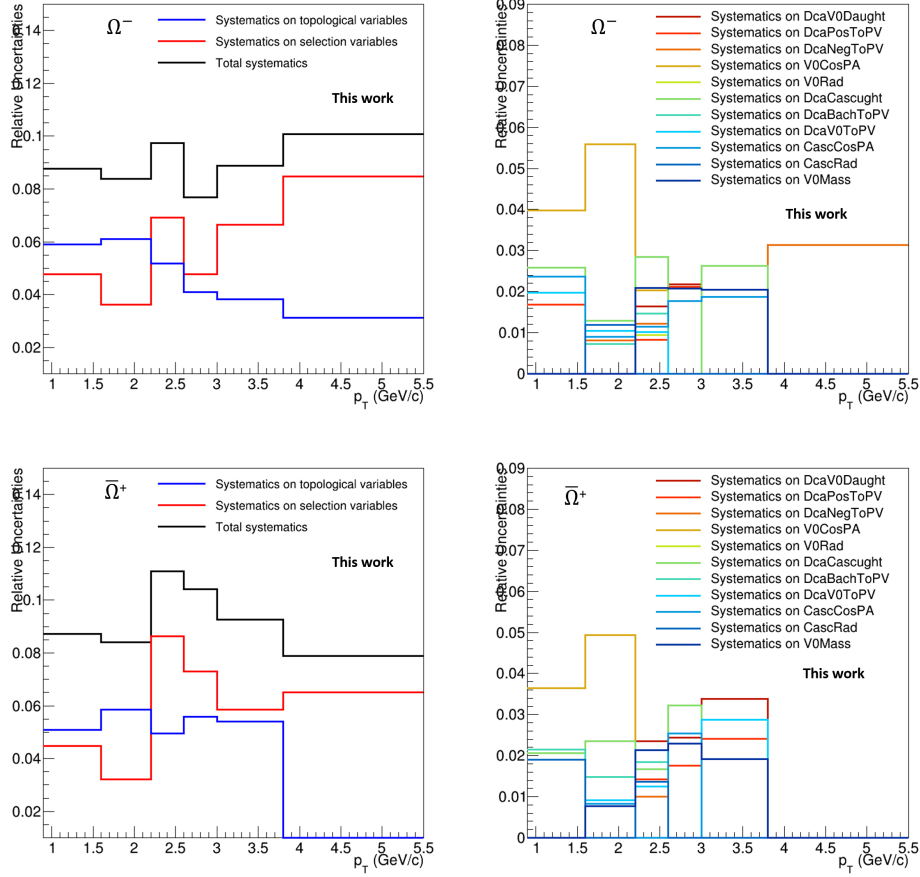


Figure C.3: The left panels show for  $\Omega^-$  and  $\bar{\Omega}^+$  in integrated multiplicity as a function of  $p_T$  the total systematic uncertainties in black, the systematic uncertainties due to the topological cuts in blue and the ones from selection variables in red. The right panels show for  $\Omega^-$  and  $\bar{\Omega}^+$  the single contribution to the systematic uncertainties from every topological variable.

## Systematic uncertainties on extrapolation

$\Lambda(\bar{\Lambda})$  and Cascade corrected spectra together with the five functions: Levy-Tsallis, Boltzmann,  $m_T$ -exponential, Fermi-Dirac, Blast-Wave.

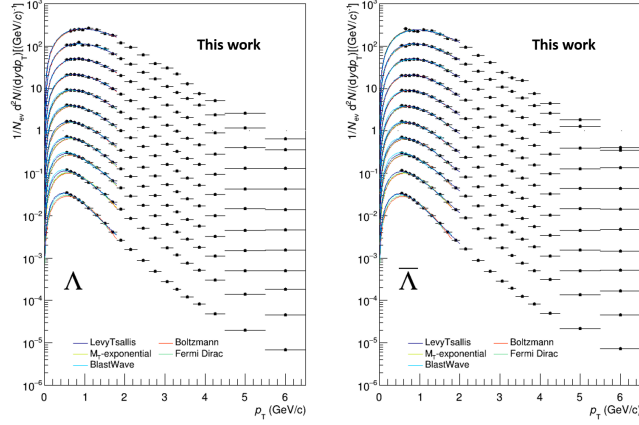


Figure C.4: The corrected spectra for  $\Lambda$  and  $\bar{\Lambda}$  are fitted with Levy-Tsallis, Boltzmann,  $m_T$ -exponential, Fermi Dirac and Blast Wave functions for  $p_T$  from 0 to 2 GeV/ $c$ .

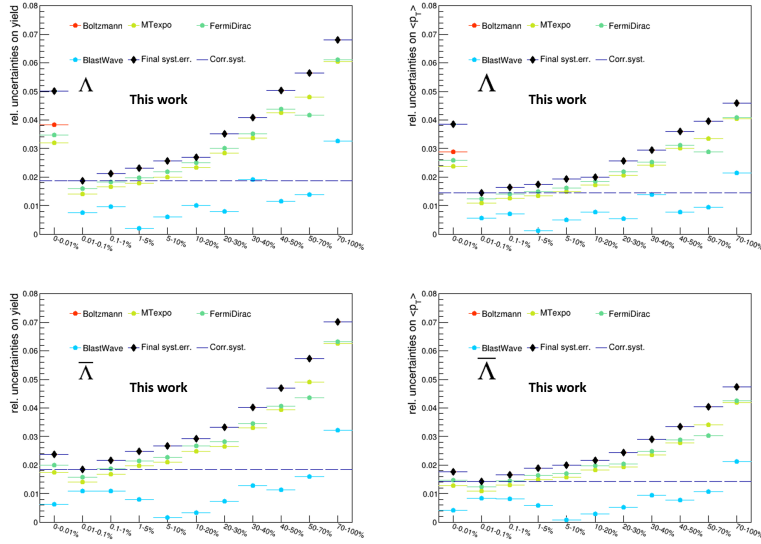


Figure C.5: Relative systematic uncertainties on  $p_T$ -integrated yield (left panel) and  $\langle p_T \rangle$  (right panel) for  $\Lambda$  and  $\bar{\Lambda}$ . The “correlated” vs multiplicity uncertainty component is indicated by the black dashed line.

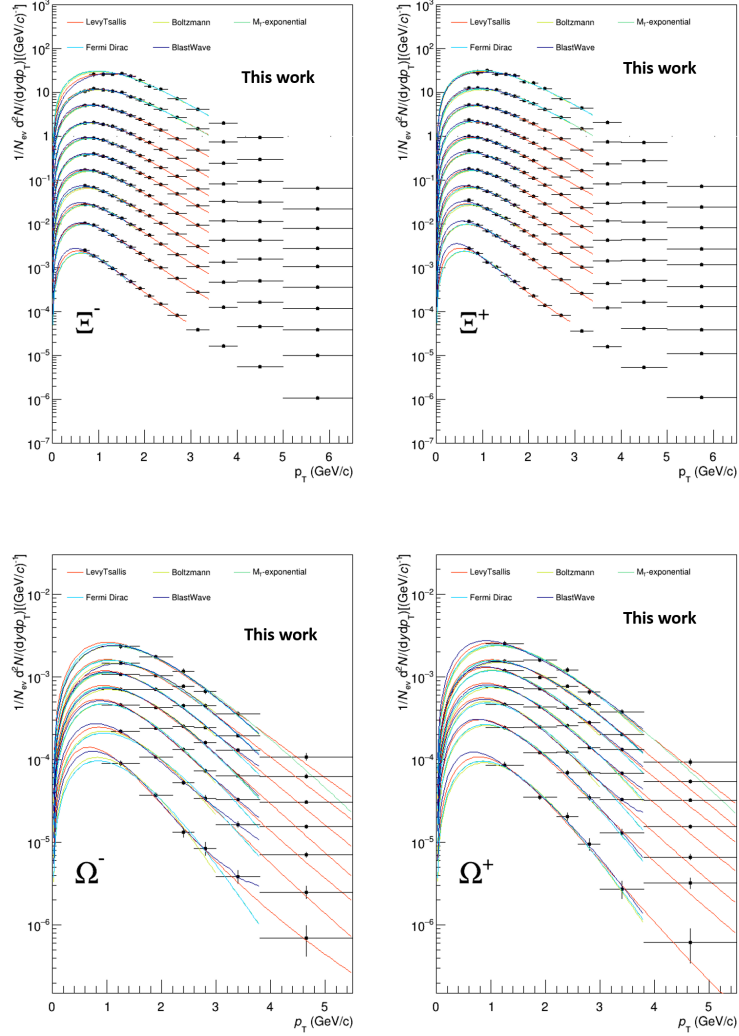


Figure C.6: The corrected spectra for  $\Xi^-$  and  $\Xi^+$  (top panels) and  $\Omega^-$  and  $\Omega^+$  (bottom panels) are fitted with Boltzmann, Levy-Tsallis,  $m_T$ -exponential, Fermi Dirac and Blast Wave functions for  $p_T$  from 0 to 3.5 GeV/c. Scalar factors are applied to better display the spectra but neither they nor the multiplicity classes are indicated since the focus is on the five fits.

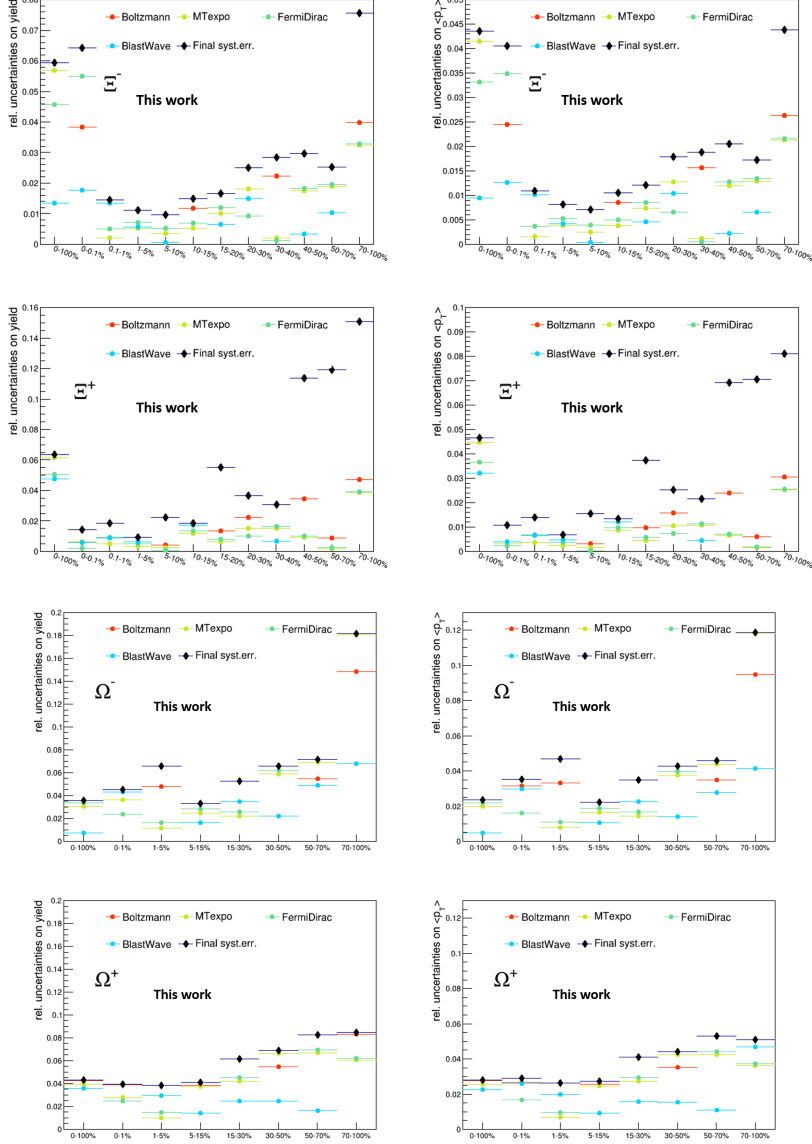


Figure C.7: Relative systematic uncertainties on  $p_T$ -integrated yield (left panel) and  $\langle p_T \rangle$  (right panel) for  $\Xi^-$ ,  $\Xi^+$ ,  $\Omega^-$  and  $\Omega^+$ .

## Total relative uncertainties

Figures C.8 and C.9 present the relative statistical, total systematic and uncorrelated systematic uncertainties on  $p_{\mathbf{T}}$ -integrated yields vs multiplicity classes for pp analysis at  $\sqrt{s} = 13$  TeV [56] in red, at  $\sqrt{s} = 7$  TeV [55] in blue and at  $\sqrt{s} = 5.02$  TeV in green for  $K_S^0$  (left panels) and  $\Lambda+\bar{\Lambda}$  (right panels) and for  $\Xi^++\Xi^-$  (left panels) and  $\bar{\Omega}^++\Omega^-$  (right panels).

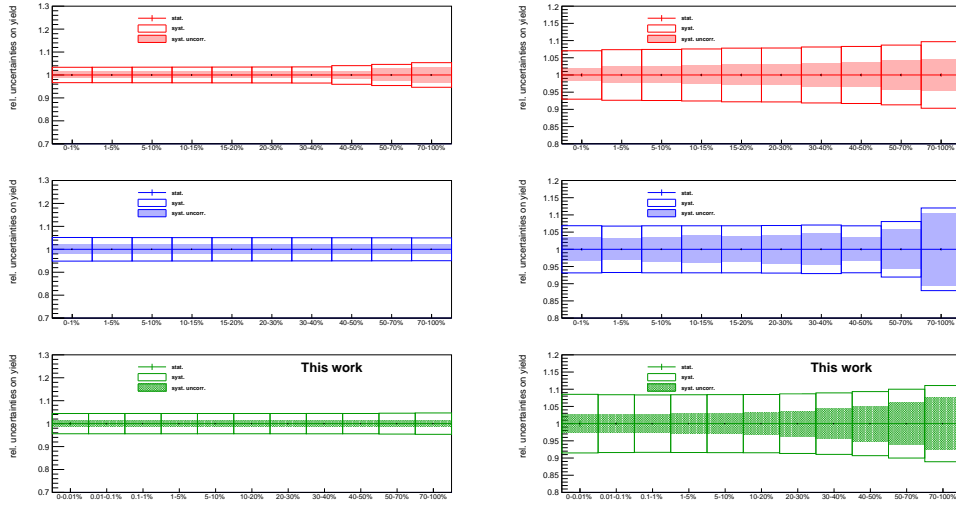


Figure C.8:  $K_S^0$  (left side) and  $\Lambda+\bar{\Lambda}$  (right side) relative uncertainties on  $p_{\mathbf{T}}$ -integrated yields at  $\sqrt{s} = 5.02$  TeV (green) vs multiplicity are shown compared with the previous results at  $\sqrt{s} = 7$  TeV [55] (blue) and  $\sqrt{s} = 13$  TeV [56] (red).

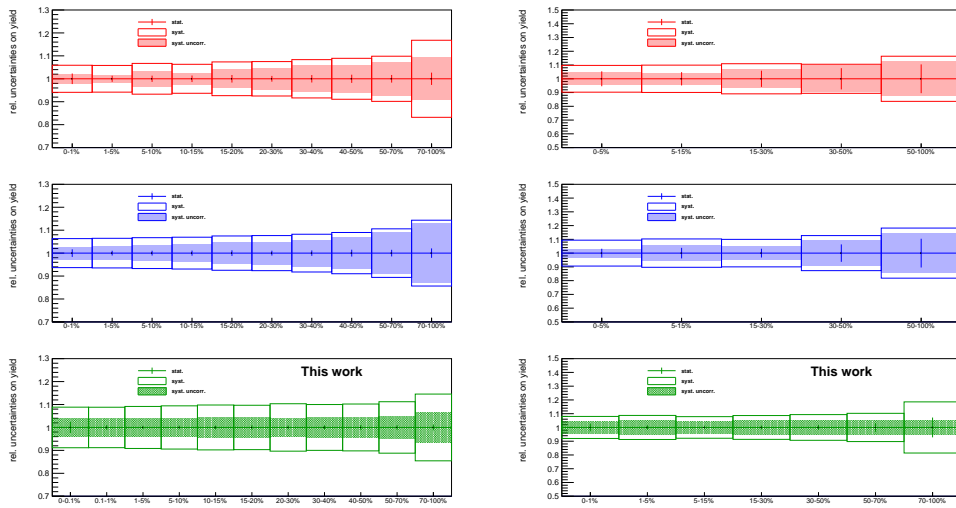


Figure C.9:  $\Xi^+ + \Xi^-$  (left side) and  $\bar{\Omega}^+ + \Omega^-$  (right side) relative uncertainties on  $p_T$ -integrated yields at  $\sqrt{s} = 5.02$  TeV (green) vs multiplicity are shown compared with the previous results at  $\sqrt{s} = 7$  TeV [55] (blue) and  $\sqrt{s} = 13$  TeV [56] (red).





# Bibliography

- [1] F. Halzen and A.D. Martin. Quarks and Leptons: an introductory course in modern particle physics. By John Wiley and Sons (1984). ISBN: 0471887412.
- [2] <https://argoncube.org/neutrinos.html>
- [3] E. Reya. Perturbative quantum chromodynamics. Physics Reports, Volume 69, Issue 3, 1981, Pages 195-333, ISSN 0370-1573. DOI: [https://doi.org/10.1016/0370-1573\(81\)90036-3](https://doi.org/10.1016/0370-1573(81)90036-3)
- [4] S. Bethke. The 2009 world average of  $\alpha_S$ . In European Physical Journal C 64, p. 689-703 (2009). DOI:<https://doi.org/10.1140/epjc/s10052-009-1173-1>
- [5] Quantum Chromodynamics - Particle Data Group. <https://pdg.lbl.gov/2019/reviews/rpp2019-rev-qcd.pdf>
- [6] Rajan Gupta. Introduction to lattice QCD: Course. pages 83–219, 1997.
- [7] N. Cabibbo and G. Parisi. Exponential hadronic spectrum and quark liberation. In Physics Letters B 59, p. 67-69 (1975). DOI: 10.1016/0370-2693(75)90158-6.
- [8] J.C. Collins and M.J. Perry. Superdense matter: neutrons or asymptotically free quarks? In Physical Review Letters 34, p. 1353-1356 (1975). DOI:DOI:<https://doi.org/10.1103/PhysRevLett.34.1353>
- [9] K. Yagi, T. Hatsuda and Y. Miake. Quark-Gluon Plasma. From Big Bang to Little Bang. By Cambridge University Press (2008). ISBN: 9780521089241.
- [10] A. Chodos, R.L. Jaffe, K. Johnson, C.B. Thorn, and V.F. Weisskopf. New extended model of hadrons. In Physical Review D 9, p. 3471-3495 (1974). DOI: <https://doi.org/10.1103/PhysRevD.9.3471>

- [11] D. Boyanovsky (2001). Phase transitions in the early and the present Universe: from the big bang to heavy ion collisions. DOI: 10.1007/978-94-010-0997-3\_1
- [12] Borsányi, S., Fodor, Z., Hoelbling, C. et al. Is there still any  $T_c$  mystery in lattice QCD? Results with physical masses in the continuum limit III. *J. High Energ. Phys.* 2010, 73 (2010). DOI: [https://doi.org/10.1007/JHEP09\(2010\)073](https://doi.org/10.1007/JHEP09(2010)073)
- [13] The Large Hadron Collider. <https://home.cern/science/accelerators/large-hadron-collider>.
- [14] Heister et al, Studies of QCD at  $e^+e^-$  Centre-of-mass Energies between 91 and 209 GeV. *The European Physical Journal. C, Particles and Fields* 35 (2004): 457-86. Web.
- [15] <https://www.bnl.gov/rhic/>
- [16] Kasza, Gábor and Csörgő, Tamás. Lifetime estimations from RHIC Au+Au data. *International Journal of Modern Physics A*, 1793-656X, Numb. 34, Vol. 26 1950147(2019). DOI: <https://doi.org/10.1142/S0217751X19501471>
- [17] CMS Collaboration. Measurement of the Pseudorapidity and Centrality Dependence of the Transverse Energy Density in Pb-Pb Collisions at  $\sqrt{s_{NN}} = 2.76$  TeV. *Phys. Rev. Lett.* 109 152303 (2012). DOI: <https://link.aps.org/doi/10.1103/PhysRevLett.109.152303>
- [18] <https://cerncourier.com/a/participants-and-spectators-at-the-heavy-ion-fireball/>
- [19] J. D. Bjorken. Highly Relativistic Nucleus-Nucleus Collisions: The Central Rapidity Region. *Phys. Rev. D* 27 (1983) 140–151. DOI: <https://doi.org/10.1103/PhysRevD.27.140>
- [20] <https://particlesandfriends.wordpress.com/2016/10/14/evolution-of-collisions-and-qgp/>
- [21] S. Conetti, LHC-B: A dedicated Beauty experiment for precision measurements of CP-violation, *Nuclear Physics B - Proceedings Supplements*, Volume 55, Issue 1, 1997, Pages 286-293, ISSN 0920-5632, DOI: [https://doi.org/10.1016/S0920-5632\(97\)00189-8](https://doi.org/10.1016/S0920-5632(97)00189-8).

- [22] CMS Collaboration. CMS: letter of intent by the CMS Collaboration for a general purpose detector at LHC. CERN-LHCC-92-003. LHCC-I-1. <https://cds.cern.ch/record/290808>
- [23] ATLAS Collaboration. ATLAS: Letter of intent for a general purpose p p experiment at the large hadron collider at CERN. CERN-LHCC-92-004. <http://cds.cern.ch/record/291061>
- [24] ALICE collaboration. ALICE: Technical proposal for a Large Ion collider Experiment at the CERN LHC. LHC Tech. Proposal. CERN, Geneva, 1995. <https://cds.cern.ch/record/293391/files/ce-000214817.pdf>
- [25] CMS Collaboration. Production of W and Z bosons in heavy-ion collisions with CMS. Nuclear Physics A, Volume 932, December 2014, Pages 459-465. DOI: <https://doi.org/10.1016/j.nuclphysa.2014.10.025>
- [26] ATLAS Collaboration. Medium-induced modification of Z-tagged charged particle yields in Pb+Pb collisions at 5.02 TeV with the ATLAS detector. [nucl-ex]<https://arxiv.org/abs/2008.09811>
- [27] R.L. Thews. Quarkonium production via recombination. Nucl.Phys., A783:301–308, 2007.
- [28] K. Aamodt et al. (ALICE Collaboration). Elliptic Flow of Charged Particles in Pb-Pb Collisions at  $\sqrt{s_{NN}} = 2.76$  TeV. Phys. Rev. Lett. 105, 252302, December 2010. DOI: <https://link.aps.org/doi/10.1103/PhysRevLett.105.252302>
- [29] Riabov, V. (2019). Overview of ALICE results on light flavour hadron production. Journal of Physics: Conference Series. 1390. 012026. DOI: 10.1088/1742-6596/1390/1/012026.
- [30] Khachatryan, V. et al. (CMS Collaboration). Observation of long-range near-side angular correlations in proton–proton collisions at the LHC. JHEP 9, 091 (2010). DOI: [https://doi.org/10.1007/JHEP09\(2010\)091](https://doi.org/10.1007/JHEP09(2010)091)
- [31] Khachatryan, V. et al. (CMS Collaboration). Evidence for collectivity in pp collisions at the LHC. Phys. Lett. B 765, 193–220 (2017). DOI: 10.1016/j.physletb.2016.12.009
- [32] Adam, J. et al. (ALICE Collaboration). Multi-strange baryon production in p–Pb collisions at  $\sqrt{s_{NN}} = 5.02$  TeV. Phys. Lett. B 758, 389–401 (2016). DOI: <https://doi.org/10.1016/j.physletb.2016.05.027>

- [33] Chatrchyan, S. et al. (CMS Collaboration). Observation of long-range near-side angular correlations in proton-lead collisions at the LHC. *Phys. Lett. B* 718, 795–814 (2013). DOI: <https://doi.org/10.1016/j.physletb.2012.11.025>
- [34] Aad, G. et al. (ATLAS Collaboration) Observation of associated near-side and away-side long-range correlations in  $\sqrt{s_{NN}} = 5.02$  TeV in proton-lead collisions with the ATLAS detector. *Phys. Rev. Lett.* 110, 182302 (2013). DOI: <https://link.aps.org/doi/10.1103/PhysRevLett.110.182302>
- [35] Aad, G. et al. (ATLAS Collaboration) Measurement with the ATLAS detector of multi-particle azimuthal correlations in p+Pb collisions at  $\sqrt{s_{NN}} = 5.02$  TeV. *Phys. Lett. B* 725, 60–78 (2013). DOI: <https://doi.org/10.1016/j.physletb.2013.06.057>
- [36] Chatrchyan, S. et al. (CMS Collaboration) Multiplicity and transverse momentum dependence of two- and four-particle correlations in pPb and PbPb collisions. *Phys. Lett. B* 724, 213–240 (2013). DOI: <https://doi.org/10.1016/j.physletb.2013.06.028>
- [37] Abelev, B. B. et al. (ALICE Collaboration). Long-range angular correlations of  $\pi$ , K and p in p–Pb collisions at  $\sqrt{s_{NN}} = 5.02$  TeV. *Phys. Lett. B* 726, 164–177 (2013). DOI: <https://doi.org/10.1016/j.physletb.2013.08.024>
- [38] Khachatryan, V. et al. (CMS Collaboration) Multiplicity and rapidity dependence of strange hadron production in pp, pPb, and PbPb collisions at the LHC. *Phys. Lett. B* 768, 103–129 (2017). DOI: <https://doi.org/10.1016/j.physletb.2017.01.075>
- [39] Abelev, B. et al. (ALICE Collaboration). Multiplicity dependence of pion, kaon, proton and lambda production in p–Pb collisions at  $\sqrt{s_{NN}} = 5.02$  TeV. *Phys. Lett. B* 728, 25–38 (2014). DOI: <https://doi.org/10.1016/j.physletb.2013.11.020>
- [40] Abelev, B. et al. (ALICE Collaboration) Long-range angular correlations on the near and away side in p–Pb collisions at  $\sqrt{s_{NN}} = 5.02$  TeV. *Phys. Lett. B* 719, 29–41 (2013). DOI: <https://doi.org/10.1016/j.physletb.2013.01.012>
- [41] J. Rafelski and B. Müller. Strangeness production in the Quark-Gluon Plasma. In *Physical Review Letters* 48, p.1066-1069 (1982). DOI: [10.1103/PhysRevLett.48.1066](https://doi.org/10.1103/PhysRevLett.48.1066).

- [42] Yin, Zhongbao. (2013). Strange and multi-strange particle production in Pb-Pb collisions at  $\sqrt{s_{NN}} = 2.76$  TeV with ALICE. *International Journal of Modern Physics: Conference Series*. DOI: <https://doi.org/10.1142/S2010194514602282>
- [43] STAR Collaboration. Enhanced strange baryon production in Au+Au collisions compared to p+p at  $\sqrt{s_{NN}} = 200$  GeV. In *Physical Review C* 77, n. 044908 (2008). DOI: [10.1103/PhysRevC.77.044908](https://doi.org/10.1103/PhysRevC.77.044908).
- [44] NA57 Collaboration. Strangeness enhancement at central rapidity in 40 A GeV/c Pb-Pb collisions. In *Journal of Physics G: Nuclear and Particle Physics* 37, n. 045105 (2010). DOI: [10.1088/0954-3899/37/4/045105](https://doi.org/10.1088/0954-3899/37/4/045105).
- [45] S. Hamieh, K. Redlich and A. Tounsi. Canonical Description of Strangeness Enhancement from p-A to Pb-Pb Collisions. In *Physics Letters B* 486, p. 61-66 (2000). DOI: [10.1016/S0370-2693\(00\)00762-0](https://doi.org/10.1016/S0370-2693(00)00762-0)
- [46] Redlich, K., Tounsi, A. Strangeness enhancement and energy dependence in heavy ion collisions. *Eur. Phys. J. C* 24, 589–594 (2002). DOI: <https://doi.org/10.1007/s10052-002-0983-1>
- [47] ALICE Collaboration., Adam, J., Adamová, D. et al. Enhanced production of multi-strange hadrons in high-multiplicity proton-proton collisions. *Nature Phys* 13, 535–539 (2017). DOI: <https://doi.org/10.1038/nphys4111>
- [48] Sjöstrand, T., Mrenna, S. and Skands, P. Z. A brief introduction to PYTHIA 8.1. *Comput. Phys. Commun.* 178, 852867 (2008). DOI: <https://doi.org/10.1016/j.cpc.2008.01.036>
- [49] Bierlich, C. and Christiansen, J. R. Effects of colour reconnection on hadron flavour observables. *Phys. Rev. D* 92, 094010 (2015). DOI: <https://doi.org/10.1103/PhysRevD.92.094010>
- [50] Pierog, T., Karpenko, I., Katzy, J., Yatsenko, E. and Werner, K. EPOS LHC: test of collective hadronization with LHC data. *Phys. Rev. C* 92, 034906 (2015). DOI: <https://doi.org/10.1103/PhysRevC.92.034906>
- [51] Andersson, Bo. (2005). The Lund model. *Camb. Monogr. Part. Phys. Nucl. Phys. Cosmol.* 7. DOI: [10.1017/CBO9780511524363](https://doi.org/10.1017/CBO9780511524363).
- [52] C. Bierlich, G. Gustafson, L. Lnnblad, H. Shah, The Angantyr model for Heavy-Ion Collisions in PYTHIA8. *JHEP* 10, 134 (2018). DOI: [https://doi.org/10.1007/JHEP10\(2018\)134](https://doi.org/10.1007/JHEP10(2018)134).

- [53] Ghosh, Premomoy & Muhuri, Sanjib. (2014). Do we see change of phase in proton-proton collisions at the Large Hadron Collider?. arXiv:1406.5811 [hep-ph]
- [54] <https://alice-figure.web.cern.ch/>
- [55] Adam, J. et al.(2017). Enhanced production of multi-strange hadrons in high-multiplicity proton-proton collisions. *Nature Physics*. 13. DOI: 10.1038/nphys4111.
- [56] ALICE collaboration. Multiplicity dependence of (multi-)strange hadron production in proton-proton collisions at  $\sqrt{s} = 13$  TeV. *Eur. Phys. J. C* 80, 167 (2020). DOI: 10.1140/epjc/s10052-020-7673-8
- [57] Adam, J. et al. Multi-strange baryon production in p-Pb collisions at  $\sqrt{s_{NN}} = 5.02$  TeV. *Nature Physics*, B, 758, 389–401 (2016). <https://arxiv.org/pdf/1512.07227.pdf>
- [58] <https://iopscience.iop.org/article/10.1088/1742-6596/1014/1/012010/pdf>
- [59] Cern accelerator complex. <https://stfc.ukri.org/research/particle-physics-and-particle-astronomy/large-hadron-collider/cern-accelerator-complex/>
- [60] <https://alice-figure.web.cern.ch/node/11218>
- [61] ALICE collaboration. ALICE ITS: the Run 1 to Run 2 transition and recent operational experience. *Proceedings of 24th International Workshop on Vertex Detectors*. DOI: 10.22323/1.254.0003
- [62] ALICE collaboration. ALICE Inner Tracking System (ITS): Technical Design Report. *Technical Design Report ALICE*. CERN, Geneva, 1999.
- [63] Dellacasa, G. and others. ALICE: Technical design report of the time projection chamber. CERN-OPEN-2000-183.
- [64] Gros, Philippe & Oskarsson, Anders. Identifying Charged Hadrons on the Relativistic Rise Using the ALICE TPC at LHC. CERN-THESIS-2011-036.
- [65] G. Charpak, F. Sauli. Multiwire proportional chambers and drift chambers. *Nuclear Instruments and Methods*. Volume 162, Issues 1–3, 1979, Pages 405-428, ISSN 0029-554X, DOI: [https://doi.org/10.1016/0029-554X\(79\)90726-2](https://doi.org/10.1016/0029-554X(79)90726-2)

- [66] P Cortese. ALICE transition-radiation detector: Technical Design Report. Technical Design Report ALICE (2001). CERN-LHCC-2001-021. <https://cds.cern.ch/record/519145>
- [67] <http://www-alice.gsi.de/trd/intro.html>
- [68] ALICE collaboration. ALICE Time-Of-Flight system (TOF): Technical Design Report. Technical Design Report ALICE. CERN, Geneva, 2000. CERN-LHCC-2002-016. <https://cds.cern.ch/record/545834>
- [69] <https://home.cern/science/accelerators/large-electron-positron-collider>
- [70] E Cerron Zeballos, I Crotty, D Hatzifotiadou, J Lamas Valverde, S Neupane, M.C.S Williams, A Zichichi. A new type of resistive plate chamber: The multigap RPC. Nuclear Instruments and Methods in Physics Research Section A: Accelerators, Spectrometers, Detectors and Associated Equipment, Volume 374, Issue 1, 1996, Pages 132-135, ISSN 0168-9002, DOI: [https://doi.org/10.1016/0168-9002\(96\)00158-1](https://doi.org/10.1016/0168-9002(96)00158-1).
- [71] François Piuz, W Klempt, L Leistam, J De Groot, and Jürgen Schükraft. ALICE high-momentum particle identification: Technical Design Report. Technical Design Report ALICE. CERN, Geneva, 1998. CERN-LHCC-98-19.
- [72] Nappi, E. & Seguinot, Jacques. (2005). Ring Imaging Cherenkov Detectors: The state of the art and perspectives. Nuovo Cimento Rivista Serie. 28. 1-130. DOI: 10.1393/ncr/i2006-10004-6.
- [73] Czerwinski, Dariusz & Deloff, Andrzej & Karpio, K. & Kozak, S. & Lukaszek, L. & Malinowski, H. & Siemiarczuk, Teodor & Stefanek, G. & Tykarski, L. & Wilk, G.. (1999). Alice Technical Design Report of the Photon Spectrometer PHOS.
- [74] ALICE collaboration. ALICE Electromagnetic Calorimeter Technical Design Report. Number CERN-LHCC-2008-014. ALICE-TDR-14. Geneva, Aug 2008.
- [75] <https://cerncourier.com/a/alice-joins-jet-set/>
- [76] ALICE Collaboration. ALICE forward detectors: FMD, TO and VO: Technical Design Report. Technical Design Report ALICE. CERN, Geneva, 2004. CERN-LHCC-2004-025.
- [77] <http://alicematters.web.cern.ch/q> = *ALICE<sub>c</sub>urrentITS*



- [78] ALICE Collaboration. ALICE Photon Multiplicity Detector (PMD): Technical Design Report. Technical Design Report ALICE. CERN, Geneva, 1999. CERN-LHCC-99-32.
- [79] M Gallio, W Klempt, L Leistam, J De Groot, and Jürgen Schükraft. ALICE Zero-Degree Calorimeter (ZDC): Technical Design Report. Technical Design Report ALICE. CERN, Geneva, 1999. CERN-LHCC-99-005. <https://cds.cern.ch/record/381433>
- [80] <https://www.bo.infn.it/alice-italia/Alice/ZDC/zdc.html>
- [81] Martinez, Ginés. The Muon Spectrometer of the ALICE experiment. Nuclear Physics A, Volume 749, 2005, Pages 313–319, 0375-9474. DOI: <http://dx.doi.org/10.1016/j.nuclphysa.2004.12.059>
- [82] [http://aliceinfo.cern.ch/Public/en/Chapter2/Chap2\\_dim\\_spec.html](http://aliceinfo.cern.ch/Public/en/Chapter2/Chap2_dim_spec.html)
- [83] Foka, Panagiota. (2013). Overview of results from ALICE at the CERN LHC. Journal of Physics: Conference Series. 455. 012004. DOI: 10.1088/1742-6596/455/1/012004.
- [84] Muller, Berndt & Schukraft, Jurgen & Wyslouch, Bolek. (2012). First Results from Pb+Pb collisions at the LHC. Annual Review of Nuclear and Particle Science. 62. DOI: 10.1146/annurev-nucl-102711-094910.
- [85] J. Aamodt, K. and et al. Two-pion Bose-Einstein correlations in Pb-Pb collisions at  $\sqrt{s_{NN}} = 2.76$  TeV with ALICE. Phys. Lett. B, Vol. 696, ISSN 0370-2693. DOI: <http://dx.doi.org/10.1016/j.physletb.2010.12.053>
- [86] Kalweit, Alexander. (2011). Particle Identification in the ALICE Experiment. Journal of Physics G-nuclear and Particle Physics - J PHYS G-NUCL PARTICLE PHYS. 38. DOI: 10.1088/0954-3899/38/12/124073.
- [87] Collaboration, ALICE. (2013). Centrality dependence of  $\pi$ ,  $K$ ,  $p$  production in Pb-Pb collisions at  $\sqrt{s_{NN}} = 2.76$  TeV. Phys.Rev.. C88.
- [88] Jacek Otwinowski. High- $p_T$  processes measured with ALICE at the LHC. proceedings from Xth Quark Confinement and the Hadron Spectrum. arXiv:1301.5285
- [89] ALICE Collaboration. The forward muon spectrometer of ALICE: addendum to the technical proposal for a Large Ion Collider experiment at the CERN LHC. LHC Tech. Proposal. CERN, Geneva, 1996.

- [90] Martino Gagliardi. The ALICE muon spectrometer: trigger detectors and quarkonia detection in p-p collisions. PhD thesis, Università degli studi di Torino, Dipartimento di Fisica Sperimentale.
- [91] Yu.N. Pestov. The Status of Spark Counters With a Localized Discharge. *Nucl.Instrum.Meth.*, A265:150–156, 1988.
- [92] M. Angelone, M. Pillon, F. Lacava, L. Pontecorvo, S. Veneziano, et al. Test of a resistive plate chamber under irradiation of photons and neutrons. *Nucl.Instrum.Meth.*, A355:399–405, 1995.
- [93] R. Arnaldi et al. Aging tests and chemical analysis of Resistive Plate Chambers for the trigger of the ALICE dimuon arm. *Nucl.Instrum.Meth.*, A533:112–115, 2004.
- [94] I. Crotty, J. Lamas Valverde, G. Laurenti, M.C.S. Williams, and A. Zichichi. The Non-spark mode and high rate operation of resistive parallel plate chambers. *Nucl.Instrum.Meth.*, A337:370–381, 1993.
- [95] R. Arnaldi, A. Baldit, V. Barret, N. Bastid, G. Blanchard, et al. Beam and ageing tests with a highly-saturated avalanche gas mixture for the ALICE p-p data taking. *Nucl.Phys.Proc.Suppl.*, 158:149–153, 2006.
- [96] Antonioli, P. and Kluge, A. and Riegler, W. Upgrade of the ALICE Read-out & Trigger System. CERN-LHCC-2013-019, ALICE-TDR-015, July 2013.
- [97] R. Arnaldi et al. (2005). Front-end electronics for the RPCs of the ALICE dimuon trigger. *Nuclear Science, IEEE Transactions on.* 52. 1176 - 1181. DOI: 10.1109/TNS.2005.852624.
- [98] Abelev, B. et al.(2014). Upgrade of the ALICE experiment: Letter of intent. *Journal of Physics G: Nuclear and Particle Physics.* 41. DOI: 10.1088/0954-3899/41/8/087001.
- [99] ALICE FoCal Collaboration. Letter of Intent: A Forward Calorimeter (FoCal) in the ALICE experiment. CERN-LHCC-2020-009. LHCC-I-036. <https://cds.cern.ch/record/2719928>
- [100] Uras, Antonio & Group, for. (2012). Muon physics in ALICE: The MFT upgrade project. *Journal of Physics Conference Series.* 446. DOI: 10.1088/1742-6596/446/1/012054.
- [101] Dupieux P. The muon trigger electronics upgrade: requirements and strategy, 2013. Joly B. Status of front-end electronics upgrade, 2013.

- [102] van der Meer, S. Calibration of the effective beam height in the ISR. CERN-ISR-PO-68-31. ISR-PO-68-31. <https://cds.cern.ch/record/296752>
- [103] Jouve, François & Rosnet, P & Royer, L. (2004). Front-End Electronics of the ALICE dimuon trigger. *IEEE Trans.Nucl.Sci.* 52 (2005) 1176-1181. DOI: 10.1109/TNS.2005.852624
- [104] Martino Gagliardi (2011). Measurement of reference cross sections in pp and Pb-Pb collisions at the LHC in van der Meer scans with the ALICE detector. *AIP Conference Proceedings.* 1422. DOI: 10.1063/1.3692205.
- [105] Livia Terlizzi. The ALICE Muon IDentifier. <https://arxiv.org/abs/2005.00285>
- [106] <https://pdg.lbl.gov/>
- [107] <https://pdg.lbl.gov/2006/reviews/pdf-files/montecarlo-web.pdf>
- [108] R. Brun, F. Bruyant, F. Carminati, S. Giani, M. Maire, A. McPherson, G. Patrick, and L. Urban. GEANT Detector Description and Simulation Tool. Geneva : CERN, 1993. - 430 p. DOI: 10.17181/CERN.MUHF.DMJ1
- [109] <http://home.thep.lu.se/~torbjorn/pythia81html/Welcome.html>
- [110] Agostinelli et al. (2002). GEANT4—a simulation toolkit. *Nuclear Instruments and Methods in Physics Research Section A: Accelerators, Spectrometers, Detectors and Associated Equipment.* 506. 250-303. DOI: 10.2172/799992.
- [111] [https://twiki.cern.ch/twiki/bin/viewauth/ALICE/ReferenceMultiplicity\\_dependent\\_pp\\_at\\_5\\_0](https://twiki.cern.ch/twiki/bin/viewauth/ALICE/ReferenceMultiplicity_dependent_pp_at_5_0).
- [112] <https://root.cern.ch/>
- [113] J. Alme et al. The ALICE TPC, a large 3-dimensional tracking device with fast readout for ultra-high multiplicity events. *Nucl.Instrum.Meth., Volume 622, Issue 1,2010, 316-367, ISSN 0168-9002.* DOI: <https://doi.org/10.1016/j.nima.2010.04.042>.
- [114] Elena Botta. Particle identification performance at ALICE. 5th Large Hadron Collider Physics Conference. arXiv:1709.00288v1 [nucl-ex]
- [115] ALICE Offline pages. <http://aliweb.cern.ch/Offline/>.

- [116] C. Tsallis. Possible generalization of Boltzmann-Gibbs statistics. In *Journal of Statistical Physics* 52, p. 479-487 (1988). DOI: 10.1007/BF01016429.
- [117] Adam, J. et al. Multiplicity dependence of light-flavor hadron production in pp collisions at  $\sqrt{s} = 7$  TeV. *Phys.Rev.C* 99 (2019) 2, 024906. DOI: 10.1103/PhysRevC.99.024906
- [118] Collaboration, ALICE. (2015). Pseudorapidity and transverse-momentum distributions of charged particles in proton-proton collisions at  $\sqrt{s} = 13$  TeV. *Physics Letters B.* 753. DOI: 10.1016/j.physletb.2015.12.030.
- [119] Castro, Xitzel. (2015). Strangeness production associated to a high- $p_T$  particle in Pb-Pb collisions at  $\sqrt{s_{NN}} = 2.76$  TeV with ALICE. *Journal of Physics: Conference Series.* 589. DOI: 10.1088/1742-6596/589/1/012018.
- [120] Abelev, B. et al. (ALICE Collaboration). Multiplicity dependence of pion, kaon, proton and lambda production in p-Pb collisions at . *Phys. Lett. B* 728, 25–38 (2014). DOI: 10.1016/j.physletb.2013.11.020
- [121] Massimiliano Marchisone. Performance of a resistive plate chamber equipped with a new prototype of amplified front-end electronics. *Journal of Instrumentation*, Volume 11, June 2016, 13th Workshop on Resistive Plate Chambers and Related Detectors (RPC2016).
- [122] SLUO Lectures on Statistics and Numerical Methods in HEP. [http://www-group.slac.stanford.edu/sluc/lectures/Stat\\_Lectures.html](http://www-group.slac.stanford.edu/sluc/lectures/Stat_Lectures.html).
- [123] Abelev, B and others. Technical Design Report for the Upgrade of the ALICE Inner Tracking System. CERN-LHCC-2013-024, ALICE-TDR-017. DOI: 10.1088/0954-3899/41/8/087002
- [124] Andreas Mathis. From gated to continuous readout - the GEM upgrade of the ALICE TPC. *Proceedings of the 5th International Conference on Micro-Pattern Gas Detectors (MPGD2017)*. <https://arxiv.org/abs/1803.04140>
- [125] Antonioli, P and Kluge, A and Riegler, W. Upgrade of the ALICE Readout & Trigger System. CERN-LHCC-2013-019. ALICE-TDR-015, Sep. 2013. <https://cds.cern.ch/record/1603472>